

POLITECNICO DI MILANO

Scuola di Ingegneria Industriale e dell'Informazione

Corso di Laurea Magistrale in Ingegneria Elettrica



**INVESTIGATIONS ON MECHANICAL AND ELECTRICAL
PROPERTIES OF SILICONE RUBBERS**

Relatore: Prof. Marco Faifer

Correlatore: Prof. Ronald Plath

Tesi di Laurea Magistrale di:
Alberto Dognini
Matr. 798828

Anno Accademico 2013-2014

This thesis is the result of my six months spent in Berlin, during which I got involved in a shared project of Technische Universität Berlin, BAM and IPH Berlin.

I would like to express my gratitude to Prof. Ronald Plath and Dr. Gerd Heidmann, for the opportunity to join the project and their careful assistance.

I state my warm and deep thanks to Dr. Chaiyaporn Lothongkam, for the precious support during my whole experience.

A sincere appreciation to Dr. Marcus Schuchardt and Ing. Roy Brusenbach, for the kind help and the forbearance with my many questions.

I would like to thank my supervisor, Prof. Marco Faifer, for his significant recommendations.

I am heartily thankful to my entire family, for giving me the possibility to study.

A special acknowledgment to Maria, for the important aid and the several suggestions.

Finally, a particular thought for Luciana, my dear aunt.

TABLE OF CONTENTS

INDEX OF FIGURES	iv
INDEX OF TABLES	ix
ABSTRACT	1
SOMMARIO	2
1 THE SILICONE RUBBER AS DIELECTRIC MATERIAL.....	3
1.1 Introduction	3
1.2 The Silicone Rubber.....	3
1.2.1 Compounding.....	4
1.2.2 Curing.....	4
1.2.3 Contamination.....	5
1.3 The Dielectric Materials	6
1.3.1 Relative Permittivity.....	6
1.3.2 Dipole Moment.....	7
1.3.3 Polarization Vector.....	8
1.3.4 Local Field and Clausius-Mossotti Equation.....	10
1.3.5 Electronic Polarization.....	11
1.3.6 Ionic Polarization.....	11
1.3.7 Orientational Polarization.....	12
1.3.8 Interfacial Polarization.....	13
1.3.9 Total Polarization.....	13
2 TENSILE STRENGTH TEST	14
2.1 Introduction	14
2.2 The Stress - Strain Curve.....	15
2.2.1 Elastic versus Plastic Deformation.....	15
2.2.2 Yield Points.....	17

2.2.3	True Stress and Strain.....	19
2.2.4	Toe Compensation.....	20
2.2.5	Influence of Strain Rate.....	21
2.2.6	Tensile Specimens.....	22
2.3	Testing Machine	22
2.3.1	Grips.....	23
2.3.2	Extensometers.....	24
2.4	Test Methodology	26
2.4.1	Sample Selection.....	26
2.4.2	Sample Preparation.....	26
2.4.3	Test Set-Up.....	26
2.4.4	Test Procedure.....	27
2.5	Development of the Test	28
2.5.1	Production of Samples.....	28
2.5.2	The Testing Process.....	31
2.6	The results	32
3	PARTIAL DISCHARGE MEASUREMENT.....	40
3.1	Introduction	40
3.2	Theory of Partial Discharge.....	40
3.2.1	Partial Discharge Models.....	41
3.2.2	PD pulse charge measurements.....	46
3.2.3	PD Signal Processing.....	49
3.2.4	Digital PD Measuring Instruments.....	52
3.2.5	Non-electrical PD Detection.....	53
3.3	The test cell.....	54
3.4	The measurement circuit	59
3.5	The samples	62
3.6	Development of the test.....	64

4	DISSIPATION FACTOR AND ELECTRIC PERMITTIVITY	72
4.1	Introduction	72
4.2	Theory of Dissipation Factor.....	72
4.2.1	General Aspects.....	72
4.2.2	The dissipation factor.....	77
4.2.3	Debye equations and Cole-Cole Plots.....	79
4.3	The Measurement Circuit	82
4.4	Development of the test.....	86
4.5	The Samples and the Results	89
4.5.1	ESA 7250 - Specimen D: air bubble effects.....	129
5	VOLUME RESISTIVITY	134
5.1	Introduction	134
5.2	The Electrical Conduction in Insulating Materials	134
5.3	The Volume Resistivity.....	136
5.3.1	The Standard Method.....	136
5.3.2	The Alternating Polarity Method.....	137
5.4	The Measurements	139
5.5	Computation of Activation Energy	151
6	POLARIZATION AND DEPolarIZATION CURRENT TEST	154
6.1	Introduction	154
6.2	Theory of PDC.....	154
6.3	The measurement circuit	159
6.4	The Results	162
7	CONCLUSIONS.....	169
	REFERENCES	171

INDEX OF FIGURES

Fig. 1.1	The molecular chains before and after the curing process	5
Fig. 1.2	Dielectric material placed in an electric field.....	8
Fig. 1.3	The non-uniform electric field inside a polarized dielectric	10
Fig. 1.4	Ionic chain without (a) and with (b) an applied field	12
Fig. 2.1	Determination of the modulus	16
Fig. 2.2	The offset yield strength.....	17
Fig. 2.3	Stress-strain curve of a linear polymer	18
Fig. 2.4	Stress-strain characteristic with yield stress greater than failure one	18
Fig. 2.5	Stress-strain characteristic with failure stress greater than yield one	19
Fig. 2.6	Toe compensation in a typical stress-strain curve	21
Fig. 2.7	HDPE stress-strain curve at increasing strain rates	21
Fig. 2.8	Typical Tensile Specimen (“dumb-bells”).....	22
Fig. 2.9	Scheme of an electromechanical twin-screw machine	23
Fig. 2.10	Systems for gripping the tensile specimens	24
Fig. 2.11	Scheme of an optical extensometer	25
Fig. 2.12	Silicone rubber during degasification process.....	29
Fig. 2.13	Die for dumb-bell test pieces.....	29
Fig. 2.14	Cutter used in the test.....	30
Fig. 2.15	Specimen during tensile strength test	31
Fig. 2.16	Graph of M 4642	33
Fig. 2.17	Graph of ESA 7250.....	34
Fig. 2.18	Graph of LR 7600/50	35
Fig. 3.1	Typical sizes of gaseous inclusions in solid dielectrics	41
Fig. 3.2	Network-based capacitive PD model.....	43
Fig. 3.3	Dipole model of a cavity discharge	44
Fig. 3.4	Field energy transferred to an electron and a positive ion	46
Fig. 3.5	PD measuring circuit.....	48
Fig. 3.6	PD bridge circuit for noise reduction.....	48
Fig. 3.7	Idealized PD pulse in time domain	49

Fig. 3.8 Frequency spectrum of PD pulse and bandwidth for measurements.....	50
Fig. 3.9 Block diagram of digital instruments with direct conversion of PD signal	53
Fig. 3.10 The upper plate (left) and the lower plate (right) of the test cell capacitor.....	54
Fig. 3.11 The electric field in the presence of guard ring	55
Fig. 3.12 Presence of parasitic capacitances in the test cell.....	56
Fig. 3.13 Scheme of the test cell's upper part	57
Fig. 3.14 Scheme of the circuit used in the test.....	59
Fig. 3.15 The Test Circuit	61
Fig. 3.16 The specimen D of Bluesil ESA 7250	64
Fig. 3.17 PD inception voltage with vacuum pump: Specimen A	67
Fig. 3.18 PD inception voltage with vacuum pump: Specimen B	68
Fig. 3.19 PD inception voltage with vacuum pump: Specimen C	68
Fig. 3.20 PD inception voltage with vacuum pump: Specimen D	69
Fig. 3.21 PD test with vacuum pump: Specimen D at higher voltage.....	69
Fig. 3.22 Fig. 3.20 PD inception voltage with vacuum pump: Specimen E	70
Fig. 3.23 Fig. 3.20 PD inception voltage with vacuum pump: Specimen F	70
Fig. 4.1 Sudden change of electric field and decrease of induced dipole moment	73
Fig. 4.2 Representation of the dielectric constant's components	75
Fig. 4.3 Frequency dependence of permittivity with many polarization mechanism	76
Fig. 4.4 Series and parallel equivalent circuits.....	78
Fig. 4.5 Current densities in the complex plane	79
Fig. 4.6 The Cole Cole plot for a single relaxation time	81
Fig. 4.7 Equivalent circuits for a material according to Debye equations	81
Fig. 4.8 Electric quantities in the complex plane	82
Fig. 4.9 Electric quantities in time domain	83
Fig. 4.10 Scheme of the circuit for dissipation factor and permittivity test.....	84
Fig. 4.11 Circuit's fragment of dissipation factor and permittivity test	85
Fig. 4.12 BamB03 – Dissipation factor	93
Fig. 4.13 BamB03 - Real Permittivity	93
Fig. 4.14 BamB03 - Imaginary Permittivity	93
Fig. 4.15 BamD02 - Dissipation factor.....	96
Fig. 4.16 BamD02 - Real Permittivity.....	96
Fig. 4.17 BamD02 - Imaginary Permittivity	96

Fig. 4.18 BamP01 - Dissipation factor	99
Fig. 4.19 BamP01 - Real Permittivity	99
Fig. 4.20 BamP01 - Imaginary Permittivity	99
Fig. 4.21 First protocol: Tan Delta comparison (500 V)	100
Fig. 4.22 First protocol: Real Permittivity comparison (500 V)	101
Fig. 4.23 First protocol: Imaginary Permittivity comparison (500 V)	102
Fig. 4.24 BamB02 - Tan Delta	105
Fig. 4.25 BamB02 - Real Permittivity	105
Fig. 4.26 BamB02 - Imaginary Permittivity	105
Fig. 4.27 BamD03 - Tan Delta	108
Fig. 4.28 BamD03 - Real Permittivity	108
Fig. 4.29 BamD03 - Imaginary Permittivity	108
Fig. 4.30 BamP03 - Tan Delta	111
Fig. 4.31 BamP03 - Real Permittivity	111
Fig. 4.32 BamP03 - Imaginary Permittivity	111
Fig. 4.33 Second protocol: Tan Delta comparison (500 V)	112
Fig. 4.34 Second protocol: Real Permittivity comparison (500 V)	113
Fig. 4.35 Second protocol: Imaginary Permittivity comparison (500 V)	114
Fig. 4.36 BamB05 - Tan Delta	117
Fig. 4.37 BamB05 - Real Permittivity	117
Fig. 4.38 BamB05 - Imaginary Permittivity	117
Fig. 4.39 BamD04 - Tan Delta	120
Fig. 4.40 BamD04 - Real Permittivity	120
Fig. 4.41 BamD04 - Imaginary Permittivity	120
Fig. 4.42 BamP02 - Tan Delta	123
Fig. 4.43 BamP02 - Real Permittivity	123
Fig. 4.44 BamP02 - Imaginary Permittivity	123
Fig. 4.45 Third protocol: Tan Delta comparison at 25°C	124
Fig. 4.46 Third protocol: Tan Delta comparison at 50°C	124
Fig. 4.47 Third protocol: Tan Delta comparison at 100°C	124
Fig. 4.48 Third protocol: Real Permittivity comparison at 25°C	126
Fig. 4.49 Third protocol: Real Permittivity comparison at 50°C	126
Fig. 4.50 Third protocol: Real Permittivity comparison at 100°C	126

Fig. 4.51 Third protocol: Imaginary Permittivity comparison at 25°C	127
Fig. 4.52 Third protocol: Imaginary Permittivity comparison at 50°C	128
Fig. 4.53 Third protocol: Imaginary Permittivity comparison at 100°C	128
Fig. 4.54 Comparison air bubble: Tan Delta at 25°C	131
Fig. 4.55 Comparison air bubble: Tan Delta at 50°C	131
Fig. 4.56 Comparison air bubble: Tan Delta at 100°C	131
Fig. 4.57 Comparison air bubble: Real Permittivity at 25°C	132
Fig. 4.58 Comparison air bubble: Real Permittivity at 50°C	133
Fig. 4.59 Comparison air bubble: Real Permittivity at 100°C	133
Fig. 5.1 Example of measured (standard) current and background one	137
Fig. 5.2 Example of Alternating-Polarity Method's quantities	138
Fig. 5.3 The electrometer "Keithley 6517B" connected to the test cell	139
Fig. 5.4 Volume resistivity - Temperature increase: ESA 7250	142
Fig. 5.5 Volume resistivity - Temperature decrease: ESA 7250	142
Fig. 5.6 Volume resistivity - Temperature cycle: BamB03	142
Fig. 5.7 Volume resistivity - Temperature cycle: BamB05	143
Fig. 5.8 Volume resistivity - Temperature cycle: BamB06	143
Fig. 5.9 Volume resistivity - Temperature increase:RT 601	144
Fig. 5.10 Volume resistivity - Temperature decrease:RT 601	145
Fig. 5.11 Volume resistivity - Temperature cycle: BamD02	145
Fig. 5.12 Volume resistivity - Temperature cycle: BamD03	145
Fig. 5.13 Volume resistivity - Temperature cycle: BamD04	146
Fig. 5.14 Volume resistivity - Temperature increase: Powersil 600	147
Fig. 5.15 Volume resistivity - Temperature decrease: Powersil 600	148
Fig. 5.16 Volume resistivity - Temperature cycle: BamP01	148
Fig. 5.17 Volume resistivity - Temperature cycle: BamP02	148
Fig. 5.18 Volume resistivity - Temperature cycle: BamP03	149
Fig. 5.19 Volume resistivity: temperature increase	150
Fig. 5.20 Volume resistivity: temperature decrease	150
Fig. 6.1 Scheme of the PDC measurements	155
Fig. 6.2 Polarization and depolarization currents due to a step charging voltage	158
Fig. 6.3 Scheme of PDC measuring system	159
Fig. 6.4 The polarization circuit	160

Fig. 6.5 The short-circuit circuit.....	161
Fig. 6.6 The depolarization circuit	161
Fig. 6.7 PDC test - Polarization: 25 °C.....	163
Fig. 6.8 PDC test - Polarization: 50 °C.....	163
Fig. 6.9 PDC test - Polarization: 100 °C.....	164
Fig. 6.10 PDC test - Depolarization: 25 °C.....	164
Fig. 6.11 PDC test - Depolarization: 50 °C.....	165
Fig. 6.12 PDC test - Depolarization: 100 °C.....	165
Fig. 6.13 Volume resistivity obtained from PDC test	168

INDEX OF TABLES

Tab. 2.1 Dimensions of die for dumb-bell test pieces.....	30
Tab. 2.2 Test results of M 4642	32
Tab. 2.3 Statistics of M 4642	32
Tab. 2.4 Test results of ESA 7250	33
Tab. 2.5 Statistics of ESA 7250	34
Tab. 2.6 Test results of LR 7600/50.....	34
Tab. 2.7 Statistics of LR 7600/50	35
Tab. 2.8 Statistical Process Control quantities for M 4642	38
Tab. 2.9 Statistical Process Control quantities for ESA 7250	38
Tab. 2.10 Statistical Process Control quantities for LR 7600/50.....	39
Tab. 3.1 Results of the first test (atmospheric pressure)	65
Tab. 3.2 Results of the second test (use of vacuum pump)	66
Tab. 4.1 The thicknesses of the samples ESA 7250	89
Tab. 4.2 The thicknesses of the samples RT 601.....	90
Tab. 4.3 The thicknesses of the samples Powersil 600	90
Tab. 4.4 BamB03 results, 500 V.....	91
Tab. 4.5 BamB03 results, 1000 V	91
Tab. 4.6 BamB03 results, 1500 V	92
Tab. 4.7 BamB03 results, 2000 V	92
Tab. 4.8 BamD02 results, 500 V.....	94
Tab. 4.9 BamD02 results, 1000 V.....	94
Tab. 4.10 BamD02 results, 1500 V.....	95
Tab. 4.11 BamD02 results, 2000 V.....	95
Tab. 4.12 BamP01 results, 500 V	97
Tab. 4.13 BamP01 results,1000 V	97
Tab. 4.14 BamP01 results, 1500 V	98
Tab. 4.15 BamP01 results, 2000 V	98
Tab. 4.16 BamB02 results, 500 V.....	103
Tab. 4.17 BamB02 results, 1000 V.....	103
Tab. 4.18 BamB02 results, 1500 V.....	104

Tab. 4.19 BamP01 results, 2000 V	104
Tab. 4.20 BamD03 results, 500 V.....	106
Tab. 4.21 BamD03 results, 1000 V.....	106
Tab. 4.22 BamD03 results, 1500 V.....	107
Tab. 4.23 BamD03 results, 2000 V.....	107
Tab. 4.24 BamP03 results, 500 V	109
Tab. 4.25 BamP03 results, 1000 V	109
Tab. 4.26 BamP03 results, 1500 V	110
Tab. 4.27 BamP03 results, 2000 V	110
Tab. 4.28 BamB05 results, 25°C	115
Tab. 4.29 BamB05 results, 50°C	115
Tab. 4.30 BamB05 results, 100°C.....	116
Tab. 4.31 BamD04 results, 25°C	118
Tab. 4.32 BamD04 results, 50°C	118
Tab. 4.33 BamD04 results, 100°C	119
Tab. 4.34 BamP02 results, 25°C.....	121
Tab. 4.35 BamP02 results, 50°C.....	121
Tab. 4.36 BamP02 results, 100°C.....	122
Tab. 4.37 Comparison with/without bubble, 25°C	129
Tab. 4.38 Comparison with/without bubble, 50°C	130
Tab. 4.39 Comparison with/without bubble, 100°C	130
Tab. 5.1 The accuracy of the ammeter	140
Tab. 5.2 The thicknesses of the samples ESA 7250	141
Tab. 5.3 Volume resistivity results of ESA 7250	141
Tab. 5.4 The thicknesses of the samples RT601	144
Tab. 5.5 Volume resistivity results of RT 601.....	144
Tab. 5.6 The thicknesses of the samples Powersil 600	146
Tab. 5.7 Volume resistivity results of Powersil 600	147
Tab. 5.8 Activation energies for ESA 7250.....	152
Tab. 5.9 Activation energies for RT 601.....	153
Tab. 5.10 Activation energies for Powersil 600	153
Tab. 6.1 The accuracy of the ammeter	162
Tab. 6.2 The thicknesses of the samples ESA 7250	162

ABSTRACT

Silicone is an extremely versatile rubber with central importance in industrial manufacturing, particularly in electrical engineering. This significant role is due to its many features, such as the good electrical insulating properties, the high inertness and non reactive behavior with most chemicals, the resistance to extreme environments and temperatures still maintaining its useful characteristics.

Nowadays, new kinds of silicone rubbers are continuously developed, which need characterization according to their specific application.

The first part of this study deals with the mechanical tensile strength; after a theoretical examination, the obtained results are presented and analyzed, concerning the tests conducted on different silicone rubbers in the company “IPH Berlin”.

The second part, regarding the investigation of electrical properties performed in the laboratories of “Technische Universität Berlin”, is introduced by a description of the employed test cell and a preliminary partial discharge measurement.

The dissipation factor test, from which the dielectric permittivity is computed, is based on the relationship between the test object and an ideal reference capacitor; the experiments are carried out varying three different parameters: the temperature, the frequency and the applied voltage.

The volume resistivity, obtained by using an electrometer with implementation of the alternating-polarity method, is investigated at different temperatures.

Finally, the polarization and depolarization current (PDC) test, at different temperatures, allows the evaluation of the dielectric response in the time domain.

These three dielectric tests are discussed and their results are inspected, yielding the characterization of different silicone rubbers and providing a reference for their future implementation in electrical components or a basis for a further scientific investigation.

SOMMARIO

Il silicone è una gomma estremamente versatile, largamente utilizzata nella produzione industriale e con un'importante funzione nell'ingegneria elettrica. Questo ruolo fondamentale è dovuto alle sue molteplici caratteristiche, come la proprietà di isolante elettrico, l'elevata inerzia in relazione a molteplici componenti chimici, la resistenza a condizioni termiche e ambientali estreme sempre mantenendo le specifiche peculiarità.

Al giorno d'oggi, nuove tipologie di silicone sono continuamente sviluppate, necessitando di una specifica analisi secondo i loro particolari utilizzi.

La prima parte di questo studio affronta il test meccanico di trazione uniassiale; dopo una spiegazione teorica, sono presentati e analizzati i risultati ottenuti, riguardanti gli esperimenti condotti su diverse gomme siliconiche nella società "IPH Berlin".

La seconda parte, attinente allo studio di proprietà elettriche effettuato nei laboratori della "Technische Universität Berlin", è introdotta da un'illustrazione della cella utilizzata per le diverse prove e da una misurazione di scariche parziali.

Il test riguardante il fattore di dissipazione, dal quale è calcolata la permittività, è basato sul confronto tra l'oggetto in prova e un condensatore ideale; l'esperimento è eseguito mediante la variazione di tre parametri: la frequenza, la temperatura e la tensione applicata. La resistività volumica, ottenuta con l'impiego di un elettrometro che utilizza il metodo cosiddetto "alternating-polarity", è analizzata a diverse temperature.

Infine, il test di "polarization and depolarization current" (PDC), effettuato a differenti temperature, permette la valutazione della risposta dielettrica nel dominio del tempo.

E' esaminato lo svolgimento degli esperimenti realizzati, in aggiunta all'analisi dei risultati, fornendo la caratterizzazione delle diverse gomme siliconiche e offrendo un riferimento per la loro implementazione in componenti elettrici, o un punto di partenza per ulteriori analisi in laboratorio.

1 THE SILICONE RUBBER AS DIELECTRIC MATERIAL

1.1 Introduction

The market for composite insulators is growing steadily. Compound designs typically use engineered polymers which offer higher mechanical strength, greater design flexibility, reduced weight, and lower breakage rates than ceramic components. The emerging shift to composites adds new importance to the debate over which polymeric material should be used for the housing. Insulator field experience and extensive, multi-stress lab testing of different elastomer formulations have shown silicone rubber behavior to be an advantage in these applications.

Silicone rubber compounds have characteristics of both inorganic and organic materials, and offer a number of advantages not found in other organic rubbers. They have fine electrical properties, good chemical stability, flame retardancy and superior resistance to heat and cold. Thus, they are used in nearly every industry to improve the quality and functionality of lots and lots of products.

1.2 The Silicone Rubber

Silicone rubber is an elastomer composed of silicone containing silicon together with carbon, hydrogen, and oxygen.

A polymer is composed of very large molecules that contain atoms arranged one after another in a chain-like manner, with each link of the chain being the same basic unit.

In the silicone rubber the basic unit is the siloxane (made by silicon and oxygen), forming the polysiloxanes. The chain-like arrangement repeats in regular cycles, so the structure can be written as repeating identical segments.

The raw material for silicone rubber is sand, which is converted into elemental silicon by heating with carbon. Conversion to chlorosilanes is by the direct processing of methyl chloride and elemental silicon, which gives a mixture of compounds that experiences a distillation. After a procedure involving water and a condensation procedure, the methyl siloxanes is formed, which is then polymerized to form the polydimethylsiloxane, used to make silicone rubber.

1.2.1 Compounding

The basic properties of elastomers are highly dependent on the polymers used in their manufacture. These properties can be modified, however, through the appropriate addition of compounding ingredients. Some are added to accelerate cross-linking, others improve processability, while others improve the properties of the finished product.

Some compounds are required to deliver the highest levels of performance in the end product, with cost being a secondary issue. In this case compounding requires the use of selected materials to give the required characteristics without the inclusion of non-essential ingredients which could compromise the performance.

In other applications, compounds may be designed to minimize cost, with extenders and diluents being added to reduce the proportion of high priced components in the mix. This inevitably leads to compromises in the mechanical and other properties, of course, but for certain applications this may be acceptable.

1.2.2 Curing

In its uncured state, silicone rubber is a highly-adhesive gel or liquid. In order to convert to a solid temperature-stable material it must be cured, or vulcanized, resulting in the cross-linking of elastomeric molecules (this connection is represented by the orange points in Fig. 1.1, indicated by the green arrow).

The curing process influences the elastic behavior. In fact, before the curing, the long molecular chains can slide past each other, exhibiting little elasticity; after it, the chains are cross-linked, which ensures they return to position when the deforming force is removed.

In a platinum-based silicone cure system, also called an *addition* system (because platinum is *added* to the system as a catalyst) two separate components must be mixed to catalyze the polymers: the one component, called also vulcanizing agent, contains a

platinum complex which must be mixed with the second, a hydride- and a vinyl-functional siloxane polymer, creating an ethyl bridge between the two.

Such silicone rubbers cure quickly, though the curing process can be accelerated by adding heat or pressure.

Moreover, silicone rubbers may be cured also with other methods, as a condensation cure system, a peroxide cure system, or an oxime cure system.

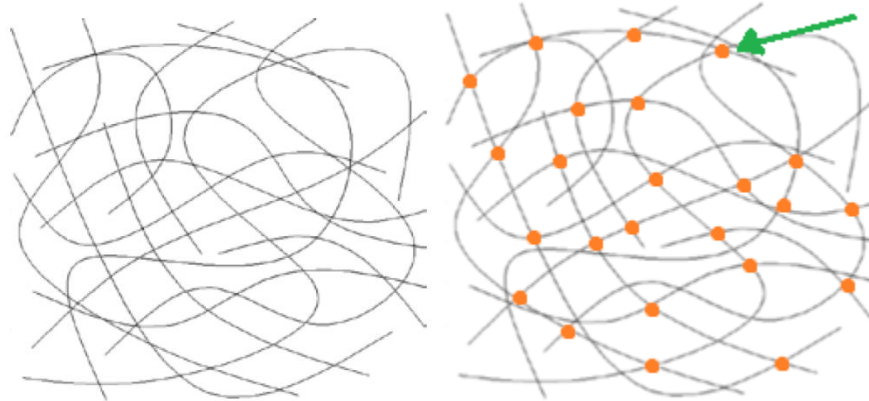


Fig. 1.1 The molecular chains before and after the curing process

For each analyzed material, it is extremely important to specify the curing conditions (time duration at the particular temperature), which can influence the test results. The silicone rubbers utilized in this work of thesis implemented the following specifications:

- Elastosil M4642 : 24 hours at 30 °C
- Bluesil ESA 7250 : 2 hours at 100 °C
- Lumisil LR 7600/50 : 2 hours at 120 °C
- Elastosil RT 601 : 45 minutes at 90 °C
- Powersil 600 : 24 hours at 30 °C

1.2.3 Contamination

Ceramic and glass have long been the materials of choice for high-voltage insulators and lightning arresters, offering good resistance to electrical stress and outdoor exposure without significant deterioration; however, one of their biggest problems in outdoor applications is airborne contamination (salt and pollution, for example) that settles on the insulator surface and leads to excessive leakage current, dry band arcing and eventually to flashover, [2].

On the other hand, composite insulators designed with silicone rubber have been found to reduce the need for maintenance in areas of moderate to high contamination. The surface of a silicone elastomer has a unique ability to interact with the contaminant and control leakage currents, interrupting the normal process that leads to contamination-induced flashover.

In addition, silicone rubber has demonstrated better hydrophobicity and lower surface energy than most organic polymers. The surface properties of silicone are such that the material recovers its hydrophobicity between contamination and/or corona episodes, while other materials progressively deteriorate.

1.3 The Dielectric Materials

A dielectric material is an electrical insulator that can be polarized by an applied electric field, often used to insulate conductors at different voltages.

The familiar parallel plate capacitor equation with free space as an insulator is given by $C = \frac{\epsilon_0 A}{d}$, where ϵ_0 is the absolute permittivity, A is the plate area, and d is the separation between the plates. If there is a material medium between the plates, then the capacitance, defined as the charge storage ability per unit voltage, increases by a factor of ϵ_r , called *dielectric constant of the medium* or *relative permittivity*. The increase in the capacitance is due to the polarization of the medium in which positive and negative charges are displaced with respect to their equilibrium positions. The opposite surfaces of the dielectric medium acquire opposite surface charge densities that are related to the amount of polarization in the material.

1.3.1 Relative Permittivity

We first consider a parallel plate capacitor with vacuum inside as the dielectric, connected to a constant voltage supply V , having the charge Q_0 on the plates. The capacitance C_0 of the parallel plate capacitor in free space is defined by:

$$C_0 = \frac{Q_0}{V}$$

The electric field, directed from high to low potential, is defined by $E = \frac{V}{d}$, where d is the separation of the plates.

Now, a slab of any nonconducting material is inserted into this parallel plate capacitor, with V kept the same (and also E). During the insertion of the dielectric slab, there is an external current flow indicating that there is additional charge being stored on the plates.

The charge on the electrodes increases from Q_0 to Q . Because there is now a greater amount of charge stored on the plates, the capacitance of the system is increased by the ratio Q to Q_0 . Consequently, the dielectric constant is given by:

$$\epsilon_r = \frac{C}{C_0} = \frac{Q}{Q_0}$$

1.3.2 Dipole Moment

An electrical dipole moment is simply a separation between a negative and positive charge of equal magnitude Q . If a is the vector from the negative to the positive charge, the electric dipole moment is defined as a vector by:

$$p = Qa$$

The region that contains the $+Q$ and $-Q$ charges has zero net charge; nonetheless it contains a dipole moment and gives rise to an electric field.

Considering a neutral atom, on average the center of negative charge of the electrons coincides with the positive nuclear charge, which means that the atom has no net dipole moment.

However, when this atom is placed in an external electric field, the electrons, being much lighter than the positive nucleus, become easily displaced, which results in the separation of the negative charge center from the positive one.

An induced dipole moment is developed and the atom is said polarized.

We define α as a quantity called *polarizability* to relate the induced dipole moment $p_{induced}$ to the field E causing it:

$$p_{induced} = \alpha E$$

Considering the displacement of electrons, the electronic polarization is taken into account and denoted as α_e .

1.3.3 Polarization Vector

When a material is placed in an electric field, the atoms and the molecules of the material become polarized, so we have a distribution of dipole moments in the material (Fig. 1.2a). Consider the polarized medium alone, as shown in Figure 1.2b. In the bulk of the material, the dipoles are aligned head to tail: every positive charge has a negative charge next to it and vice versa. But the charges of the dipoles appearing at the boundaries of the dielectric are not canceled by the opposite charges of any dipoles. There are therefore the surface charges $+Q_p$ and $-Q_p$ on the two faces that result from the polarization of the medium, called *surface polarization charges* (Fig. 1.2c).

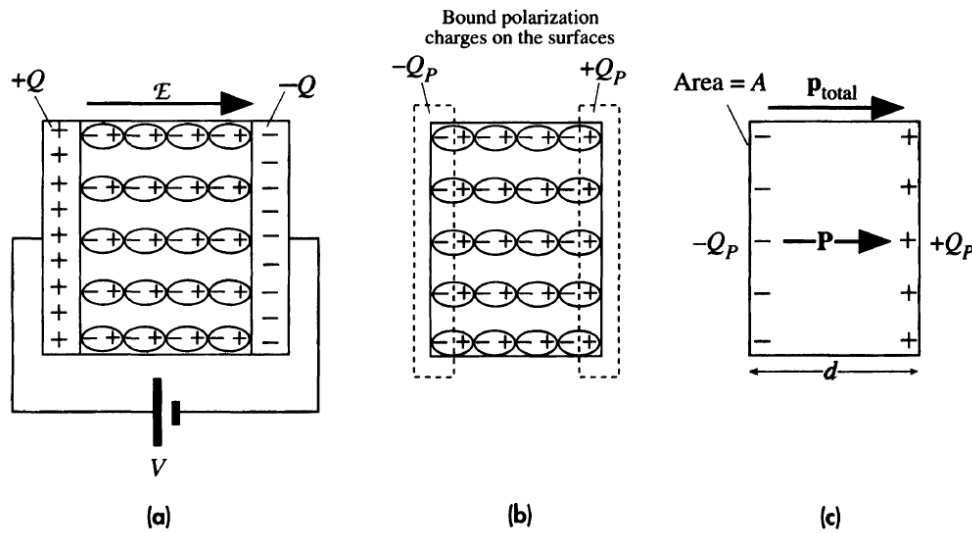


Fig. 1.2 Dielectric material placed in an electric field

The polarization of a medium is represented by a vector called polarization P , which direction is normal to the surface and the magnitude is defined as the total dipole moment per unit volume:

$$P = \frac{1}{Volume} [p_1 + p_2 + \dots + p_N]$$

where p_1, p_2, \dots, p_N are the dipole moments induced at N molecules in the volume.

Introducing the concept of total dipole moment as:

$$p_{total} = Q_p d$$

Indicating with σ_p is the *surface polarization charge density*, it follows:

$$P = \frac{p_{total}}{Volume} = \frac{Q_p d}{Ad} = \frac{Q_p}{A} = \sigma_p$$

To express the dependence of P on the field E , the quantity called *electric susceptibility* (χ_e) is introduced:

$$P = \chi_e \varepsilon_0 E$$

Recalling the quantity $p_{induced}$, we obtain:

$$P = N p_{induced} = N \alpha_e E \quad \rightarrow \quad \chi_e = \frac{1}{\varepsilon_0} N \alpha_e$$

It is important to recognize the difference between free and polarization (or bound) charges. The charges stored on the metal plates in Figure 1.2a are free because they result from the motion of free electrons in the metal. For example both Q_0 and Q , before and after the dielectric insertion, are free charges that arrive on the plates from the battery. The polarization charges $+Q_p$ and $-Q_p$, on the other hand, are bound to the molecules; they cannot move within the dielectric or on its surface.

The field E before the dielectric was inserted is given by:

$$E = \frac{V}{d} = \frac{Q_0}{C_0 d} = \frac{Q_0}{\varepsilon_0 A} = \frac{\sigma_0}{\varepsilon_0}$$

Where $\sigma_0 = \frac{Q_0}{A}$ is the free surface charge density without any dielectric medium between the plates.

After the insertion of the dielectric, the electric field remains the same, but the free charges on the plates are different. The free surface charge on the plates is now Q . In addition, there are bound polarization charges on the dielectric surfaces next to the plates.

The flow of current during the insertion of the dielectric is due to the additional free charges $Q - Q_0$ needed on the capacitor plates to neutralize the opposite polarity polarization charges Q_p appearing on the dielectric surfaces. The total charge due to that on the plate plus that appearing on the dielectric surface, $Q - Q_p$, must be the same as before, Q_0 , so that the electric field does not change inside the dielectric, that is:

$$Q - Q_p = Q_0 \quad \rightarrow \quad Q = Q_p + Q_0$$

Dividing by A and defining $\sigma = \frac{Q}{A}$ as the free surface charge density on the plates with the dielectric inserted it follows:

$$\sigma = \varepsilon_0 E + \sigma_p \quad \rightarrow \quad \sigma = \varepsilon_0 (1 + \chi_e) E$$

And recalling the previous equalities, it yields:

$$\epsilon_r = 1 + \chi_e \quad \rightarrow \quad \epsilon_r = 1 + \frac{N\alpha_e}{\epsilon_0}$$

The significance of the last equation is that it relates the microscopic polarization mechanism that determines α_e to the macroscopic property ϵ_r .

1.3.4 Local Field and Clausius-Mossotti Equation

The last equation, which relates ϵ_r to the electronic polarizability α_e , is only approximate because the electric field E is considered uniform within the whole dielectric.

However, the induced polarization depends on the actual field experienced by the polarized molecules within the dielectric and, due to the separation between negative and positive charges, the field is not constant on the atomic scale as we move through the insulating material (Fig. 1.3). The field experienced by an individual molecule is actually different than E , which represents the average field in the dielectric. As soon as the dielectric becomes polarized, the field at some arbitrary point depends not only on the charges on the plates (Q) but also on the orientations of all the other dipoles around this point in the dielectric, that depend on the crystal structure of the molecules. The actual field experienced by a molecule in a dielectric is defined as the local field and denoted by E_{loc} .

The Clausius-Mossotti equation is given by the following equation:

$$\frac{\epsilon_r - 1}{\epsilon_r + 2} = \frac{N\alpha_e}{3\epsilon_0}$$

It has been obtained considering the simplest case of a material with cubic crystal structure and it shows the relationship between the macroscopic property ϵ_r and the microscopic polarization phenomena α_e .

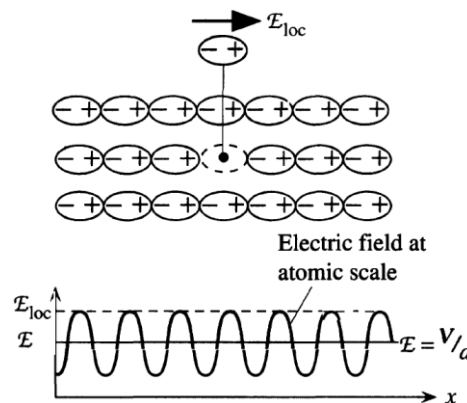


Fig. 1.3 The non-uniform electric field inside a polarized dielectric

1.3.5 Electronic Polarization

When a field is applied to a solid substance, the constituent atoms or molecules become polarized. The electron clouds within each atom become shifted by the field, and this gives rise to electronic polarization.

This type of electronic polarization within an atom, however, is quite small compared with the polarization due to the valence electrons in the covalent bonds within the solid, which are not rigidly tied to the positive ionic cores.

When an electric field is applied, the negative charge distribution associated with these valence electrons becomes readily shifted with respect to the positive charges of the ionic cores and the crystal exhibits polarization, or develops a polarization vector. The greater flexibility of electrons in covalent bonds compared with those in individual ionic cores is exhibited by the difference in their binding energy and is responsible for the large dielectric constants of covalent crystals.

1.3.6 Ionic Polarization

In addition to electronic polarization, other polarization mechanisms may also contribute to the relative permittivity; at first the ionic one is considered.

This type of polarization occurs in ionic crystals, having distinctly identifiable ions located at well defined lattice sites, so each pair of oppositely charged neighboring ions has a dipole moment.

In the absence of an applied field (Fig. 1.4a), the solid has no net polarization because the dipole moments of equal magnitude are lined up head to head and tail to tail so that the net dipole moment is zero.

The dipole moment p_+ in the positive x direction has the same magnitude as p_- in the negative x direction, so the net dipole moment, given by $(p_+ - p_-)$ is equal to zero.

In the presence of a field E along the x direction, however, the negative ions are pushed in the $-x$ direction and the positive ions in the $+x$ direction about their equilibrium positions (Fig. 1.4b). Consequently, the dipole moment p_+ in the $+x$ direction increases to p'_+ and the dipole moment p_- decreases to p'_- .

The net dipole moment is now no longer zero, per ion pair is now $(p'_+ - p'_-)$, which depends on the electric field E , as the induced average dipole moment per ion pair p_{av} .

The ionic polarizability α_i is defined in terms of the local field experienced by the ions:

$$p_{av} = \alpha_i E_{loc}$$

Generally, α_i is larger than the electronic polarizability α_e by a factor of 10 or more, which leads to ionic solids having large dielectric constants.

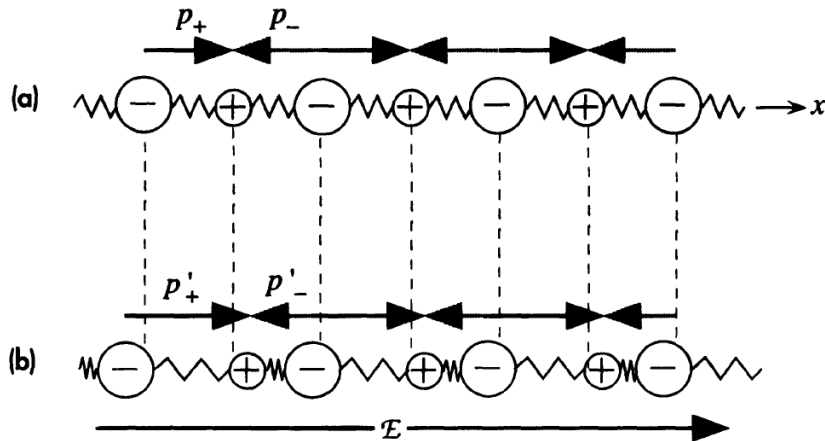


Fig. 1.4 Ionic chain without (a) and with (b) an applied field

1.3.7 Orientalional Polarization

Certain molecules possess a permanent dipole moments p_0 . In the liquid or gas phases these molecules, in the absence of an electric field, are randomly oriented as a result of thermal agitation. When an electric field E is applied, it tries to align the dipoles parallel to itself, facing the opposite force of the charges due to nearly rigid bond between them and, hence, applying a torque to the molecule.

This torque acts to rotate the molecule to align p_0 with E . If all the molecules were to simply rotate and align with the field, the polarization of the solid would be $P = Np_0$, where N is the number of molecules per unit volume.

However, due to their thermal energy, the molecules move around randomly and collide with each other and with the walls of the container. These collisions destroy the dipole alignments. Thus the thermal energy tries to randomize the orientations of the dipole moments. There is, nonetheless, a net average dipole moment per molecule p_{av} that is finite and directed along the field. Thus, the material exhibits net polarization, which leads to a dielectric constant that is determined by this *orientational polarization*.

To find the induced average dipole moment p_{av} along E , we need to know the average potential energy E_{dip} of a dipole placed in a field E and how this compares with the average

thermal energy per molecule; in order to know if the dipole manages to reach an alignment with the field or not.

It is possible to define a dipolar orientational polarizability α_d expressed as:

$$\alpha_d = \frac{1}{3} \frac{p_0^2}{kT}$$

In which k and T are the Boltzmann constant and the temperature, respectively. It is apparent that, in contrast to the electronic and ionic polarization, dipolar orientational polarization is strongly temperature dependent.

1.3.8 Interfacial Polarization

Interfacial polarization occurs whenever there is an accumulation of charge at an interface between two materials or between two regions within a material.

Invariably materials, however perfect, contain crystal defects, impurities, and various mobile charge carriers such as electrons, holes, or ionized host or impurity ions.

Under the presence of an applied field, small and mobile positive ions may migrate to the negative electrode. These positive ions pile up at the interface between the dielectric and the metal electrode and give rise to a positive space charge, which attracts more electrons to the negative electrode.

The term *interfacial polarization* arises because the positive charges accumulating at the interface and the remainder of negative charges in the bulk together constitute dipole moments that appear in the polarization vector P .

Another example is constituted by grain boundaries, that frequently lead to interfacial polarization as they can trap charges migrating under the influence of an applied field.

1.3.9 Total Polarization

In the presence of electronic, ionic, and orientational polarization mechanisms, the average induced dipole moment per molecule will be the sum of all the contributions in terms of the local field:

$$p_{av} = \alpha_e E_{loc} + \alpha_i E_{loc} + \alpha_d E_{loc}$$

Interfacial polarization cannot be simply added to the above equation as $\alpha_{if} E_{loc}$ because it occurs at interfaces and it is not related to an average polarization per molecule in the bulk.

2 TENSILE STRENGTH TEST

2.1 Introduction

Tensile tests, also known as tension tests, are performed for several reasons.

The results of these tests are used in selecting materials for engineering applications. Tensile properties frequently are included in material specifications to ensure quality. These properties often are measured during development of new materials and processes, so that different materials and processes can be compared. Finally, tensile properties often are used to predict the behavior of a material under other forms of loading.

Uniaxial tensile testing is the most commonly used for obtaining the mechanical characteristics of isotropic materials.

For anisotropic materials, such as composites materials and textiles, biaxial tensile testing is required.

The strength of a material and his elongation often are the primary concern. The strength of interest may be measured in terms of either the stress necessary to cause appreciable plastic deformation or the maximum stress that the material can withstand.

The elongation is defined in correspondence to the maximum force or as the largest elongation. These measures of strength and elongation are used, with appropriate caution (in the form of safety factors), in engineering design.

Also of interest is the material's ductility, which is a measure of how much it can be deformed before it fractures.

Rarely is ductility incorporated directly in design; rather, it is included in material specifications to ensure quality and toughness. Low ductility in a tensile test often is accompanied by low resistance to fracture under other forms of loading.

2.2 The Stress - Strain Curve

The test process involves placing the specimen in the machine and applying tension to it until it fractures.

The tensile force is recorded as a function of the increase in gage length; the data are manipulated, so that they are not specific to the geometry of the test sample.

Engineering stress, or nominal stress, s , is defined as:

$$s = F/A_0$$

where F is the tensile force applied, and A_0 is the initial cross-sectional area of the gage section.

Engineering strain, or nominal strain, e , is defined as:

$$e = \Delta L/L_0$$

where L_0 is the initial gage length and ΔL is the change in gage length ($L - L_0$).

When force-elongation data are converted to engineering stress and strain, a stress-strain curve, which is identical in shape to the force-elongation curve, can be plotted.

Regarding the final rupture, according to the norm ISO 37:2011(E), [12], we define the **tensile strength at break** as the “*tensile stress recorded at the moment of rupture*” and the **elongation at break** as the “*tensile strain in the test length at the breaking point*”.

2.2.1 Elastic versus Plastic Deformation

When a solid material is subjected to small stresses, the bonds between the atoms are stretched. When the stress is removed, the bonds relax and the material returns to its original shape. This reversible deformation is called *elastic deformation*. At higher stresses, planes of atoms slide over one another, in this case another deformation occurs, which is not recovered when the stress is removed, termed *plastic deformation*.

For most material, the initial portion of the curve is linear. The slope of this linear region is called **elastic modulus** or **Young’s modulus**:

$$E = s/e$$

This parameter indicates material’s stiffness.

Young's modulus is calculated by drawing a tangent to the initial linear portion of the stress-strain curve, selecting any point on this tangent, and dividing the tensile stress by the corresponding strain, for this reason it is also called *tangent modulus*.

Otherwise, for some materials (non linear thermoplastics) the *secant modulus* can be calculated (both methods are represented in Fig.2.1); it is the modulus value that is calculated at a specified strain value, 1% being the most common for rigid materials. Many technologists prefer working with secant modulus because of the uncertainty of fitting a tangent to the stress strain curves found in practice.

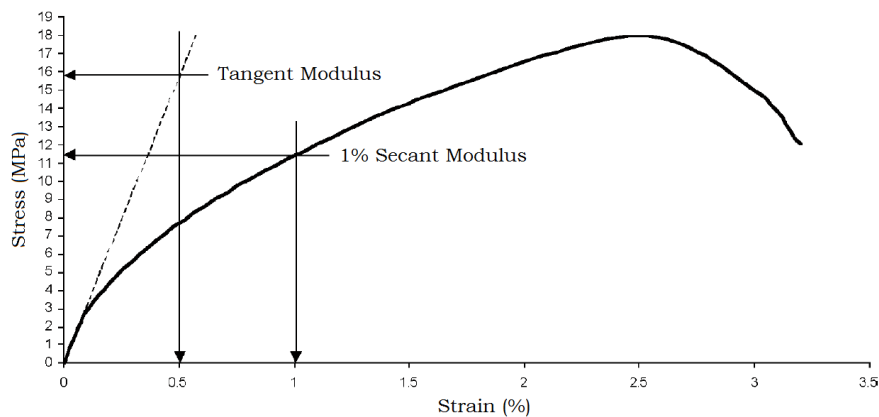


Fig. 2.1 Determination of the modulus

In the elastic range, the ratio, ν , between the magnitude of the lateral contraction strain and the axial strain is called **Poisson's ratio**, considering the tensile test in x-direction:

$$\nu = -\frac{e_y}{e_x}$$

In case of elastic strain very small, reasonably accurate measurement of Young's modulus and Poisson's ratio in a tensile test could require a very sensitive extensometer (or by velocity-of-sound measurements).

When the stress rises enough, the stress-strain behavior will cease to be linear and the strain will not disappear completely on unloading. The strain that remains is called plastic strain.

Once plastic deformation has begun, there will be both elastic and plastic contributions to the total strain, e_T , expressed as: $e_T = e_e + e_p$, where e_p is the plastic contribution and e_e is the elastic contribution.

It is tempting to define an *elastic limit* as the stress at which plastic deformation first occurs and a *proportional limit* as the stress at which the stress-strain curve first deviates from linearity. However, neither definition is very useful, because the measurements (and so the values of elastic and proportional limits) depend on the accuracy of the instruments in detecting the first deviation from linearity.

To avoid this problem, the onset of the plasticity could be described by an offset *yield strength*, which can be measured with great reproducibility. It can be found by constructing a straight line parallel to the initial linear portion of the stress-strain curve, with a defined offset (usually 0.2%, but other values can be used). The yield strength is the stress at which this line intersects the stress-strain curve (Fig. 2.2).

The advantage of defining yield strength in this way is that such a parameter is easily reproduced and does not depend heavily on the sensitivity of measurement.

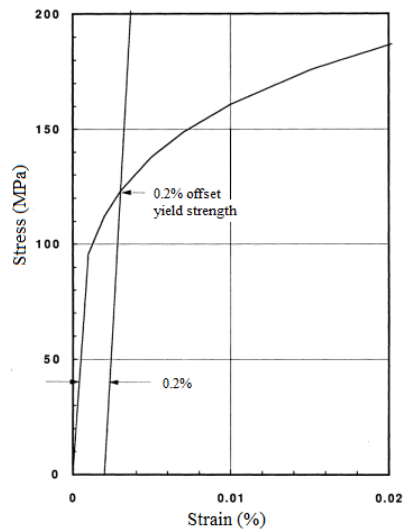


Fig. 2.2 The offset yield strength

2.2.2 Yield Points

For some materials, the stress-strain curves have initial maxima followed by lower stresses, in Fig. 2.3 the curve of a linear polymer is reported.

After the initial maximum, all the deformation at any instant is occurring within a relatively small region of the specimen. Continued elongation occurs by propagation of the deforming region along the gage section rather than by increased strain within the deforming region. Only after the entire gage section has been traversed by the band does the stress rise again.

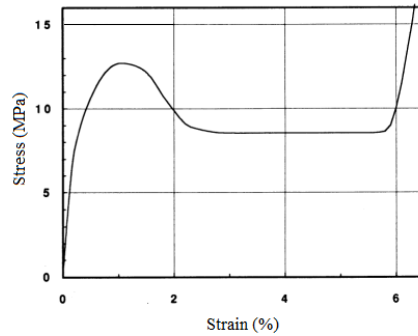


Fig. 2.3 Stress-strain curve of a linear polymer

According to the norm ISO 37:2011(E), the **tensile stress at yield** is defined as “*tensile stress at the first point on the stress-strain curve where some further increase in strain occurs without any increase in stress*” specifying that it “*might correspond either to a point of inflection or to a maximum*”; and, consequently, the **elongation at yield** is reported as “*tensile strain at the first point on the stress-strain curve where some further increase in strain is not accompanied by an increase in stress*”.

The **tensile strength** is the “*maximum tensile stress recorded in extending the test piece to breaking point*”.

Regarding the different materials, many kinds of curves are present.

The Fig. 2.4 shows the stress-strain relationship for a typical tough material with the failure stress lower than the yield stress, that corresponds to the tensile strength, in which the deformation starts to localize, forming a neck.

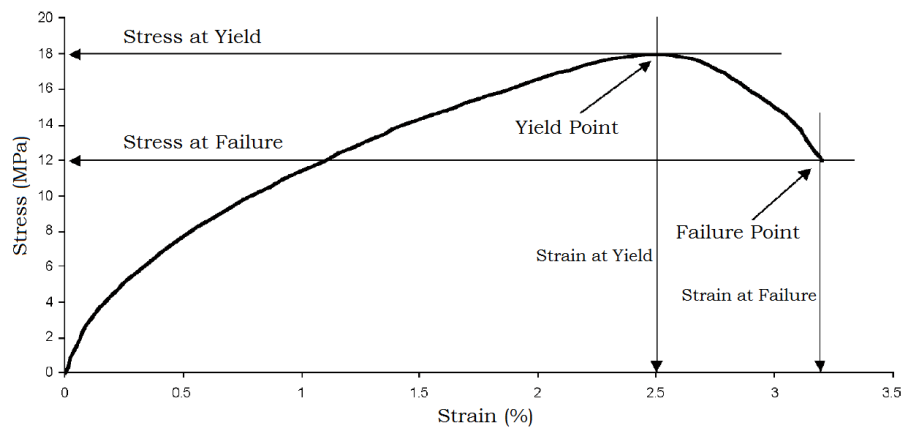


Fig. 2.4 Stress-strain characteristic with yield stress greater than failure one

Some tough materials will, after exhibiting a yield point, once again start to show an increase in stress with increasing strain and this characteristic is shown in Fig. 2.5.

In this case, the tensile strength is identified with the fracture strength.

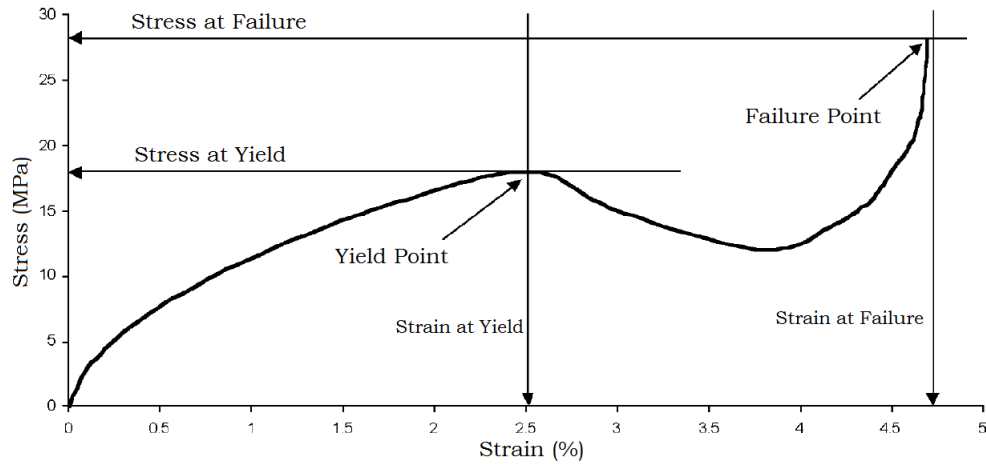


Fig. 2.5 Stress-strain characteristic with failure stress greater than yield one

Inflexible materials fracture before they neck. In this case, the fracture strength is the tensile strength.

Indeed, very brittle materials do not yield before fracture, they have tensile strengths but not yield strengths.

2.2.3 True Stress and Strain

The engineering stress-strain curve is based entirely on the original dimensions of the specimens, and in case of a ductile metal it does not give a true indication of the deformation characteristics, because the dimensions change continuously during the test.

Specimen pulled in tension becomes unstable and necks down; due to the rapid reduction of the specimen's cross-sectional area, the load required to continue deformation falls off.

The average stress based on the original area likewise decreases, and this produces the fall-off in the engineering stress-strain curve beyond the point of maximum load. Actually, the metal continues to strain harden to fracture, so that the stress required to produce further deformation should also increase. If the true stress, based on the actual cross-sectional area of the specimen, is used, the stress-strain curve increases continuously to fracture.

If the strain measurement is also based on instantaneous measurement, the curve that is obtained is known as true stress-strain curve.

The **true stress**, σ , is defined as:

$$\sigma = F/A$$

where A is the cross-sectional area at the time that the applied force is F .

Up to the point at which necking starts, **true strain**, ϵ , is defined as:

$$\epsilon = \ln \left(\frac{L}{L_0} \right)$$

This definition arises from taking an increment of the true strain, $d\epsilon$, as the incremental change in length, dL , divided by the length, L , at the time ($d\epsilon = dL/L$) and integrating.

As long as the deformation is uniform along the gage section, the true stress and strain can be calculated from the engineering quantities.

With constant volume and uniform deformation:

$$LA = L_0A_0$$

Thus, according to the definition of engineering strain,

$$A_0/A = 1 + e$$

The true stress can be written as:

$$\sigma = \left(F/A_0 \right) \cdot \left(A_0/A \right) = s(1 + e)$$

And the true strain:

$$\epsilon = \ln(1 + e)$$

At very low strains, the differences between true and engineering stress and strain are very small, and it does not really matter which one is used in computing the Young's modulus.

It must be emphasized that these expressions are valid as long as the deformation is uniform; once necking starts, the equations are still valid, but the cross-sectional area at the base of the neck must be measured directly rather than being inferred from the length measurements.

2.2.4 Toe Compensation

In a typical stress-strain curve there can be a toe region, (reported as AC in Fig. 2.6), which does not represent a property of the material. It is an artifact caused by a take-up of slack, and alignment or seating of the specimen. In order to obtain correct values of such parameters as modulus, strain, and yield point, this artifact must be compensated for to give the corrected zero point on the strain or extension axis. In the case of a material

exhibiting a linear behavior (as shown below), a continuation of the linear (CD) region of the curve is constructed through the zero-stress axis. The intersection (B) is the corrected zero-strain point from which all extensions or strains must be measured.

The elastic modulus can be determined by dividing the stress at any point along line CD (or its extension) by the strain at the same point (measured from point B, defined as zero-strain).

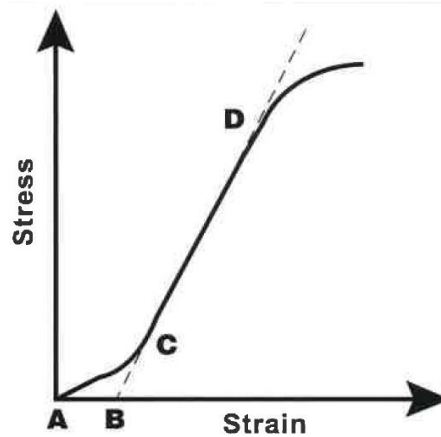


Fig. 2.6 Toe compensation in a typical stress-strain curve

2.2.5 Influence of Strain Rate

Viscoelastic materials exhibit time dependent behavior; this can cause problems with tensile testing and care should be taken to establish the rate of extension that tests were conducted. In Figure 2.7, the effects on the tensile stress-strain response of a high density polyethylene (HDPE) pulled at a number of different rates at 23 °C are shown. The strength, and as a consequence the modulus of the material, appears to increase with increasing rate of test.

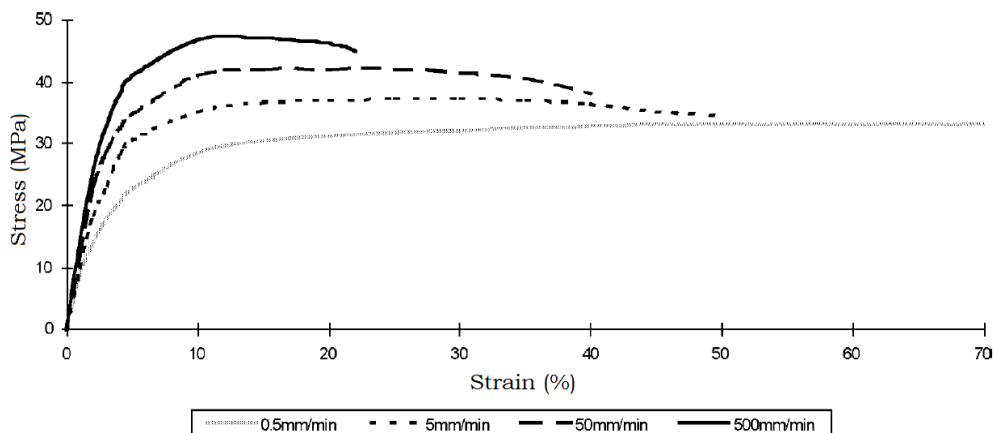


Fig. 2.7 HDPE stress-strain curve at increasing strain rates

Another interesting feature, is the lack of any discernible yield point in the low rates of test; it happens because the molecules of the HDPE, at this rate of extension, have sufficient time to align themselves just enough to accept the increase in deformation, whilst maintaining a constant resistance to the applied force (constant tensile stress).

2.2.6 Tensile Specimens

A tensile specimen is a standardized sample cross-section, the typical one is the so-called “dumb-bells”, which shape is shown in Fig. 2.8.

It has enlarged ends, or shoulders, for gripping. The important part of the specimen is the gage section. The cross-sectional area of the gage section is progressively reduced so that deformation and failure will be localized in this region.

The gage length is the region over which measurements are made and is centered within the reduced section. The distances between the ends of the gage section and the shoulders should be great enough so that the larger ends do not constrain deformation within the gage section, and the gage length should be great relative to its diameter. Otherwise, the stress state will be more complex than simple tension.

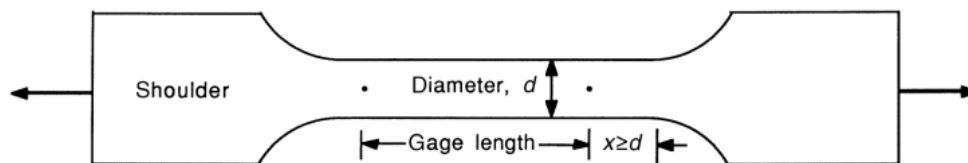


Fig. 2.8 Typical Tensile Specimen (“dumb-bells”)

2.3 Testing Machine

There are many types of testing machines. The most common are universal testing machines, which test materials in tension, compression or bending. The primary use of the this machine is to create the stress-strain diagram, further discussed.

The machine must have the proper capabilities for the test specimen being tested. There are three main parameters: force capacity, speed and accuracy. Force capacity refers to the fact that the machine must be able to generate enough force to fracture the specimen. The machine must be able to apply the force quickly or slowly enough to properly mimic the

actual application. Finally, the machine must be able to accurately measure the gauge length and forces applied.

Testing machines belong to two classes: electromechanical or hydraulic.

The electromechanical one uses an electric motor, gear reduction system and one, two or four screws to move the crosshead up or down. A range of crosshead speeds can be achieved by changing the speed of the motor. A microprocessor based closed-loop servo system can be implemented to accurately control the speed of the crosshead.

The scheme of an electromechanical twin-screw machine is showed in Fig. 2.9.

A hydraulic testing machine uses either a single- or dual-acting piston to move the crosshead up or down. In a manually operated machine, the operator adjusts a needle valve to control the rate of loading. In a closed loop hydraulic servo system, the needle valve is replaced by an electrically operated servo-valve for precise control.

In general, the electromechanical machine is capable of a wide range of test speeds and long crosshead displacements, whereas the hydraulic machine is a cost-effective solution for generating high forces.

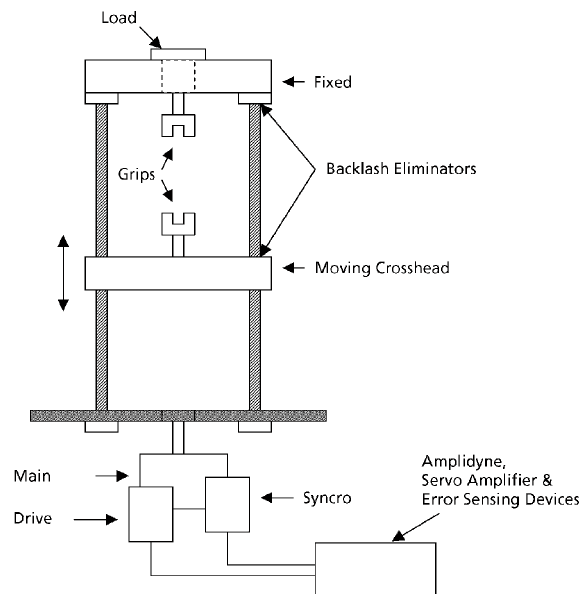


Fig. 2.9 Scheme of an electromechanical twin-screw machine

2.3.1 Grips

There are various ways of gripping the specimen, some of which are shown in Fig. 2.10.

For round specimens, these include threaded grips, serrated wedges, and, for butt end specimens, split collars constrained by a solid collar.

Sheet specimens may be gripped with pins or serrated wedges.

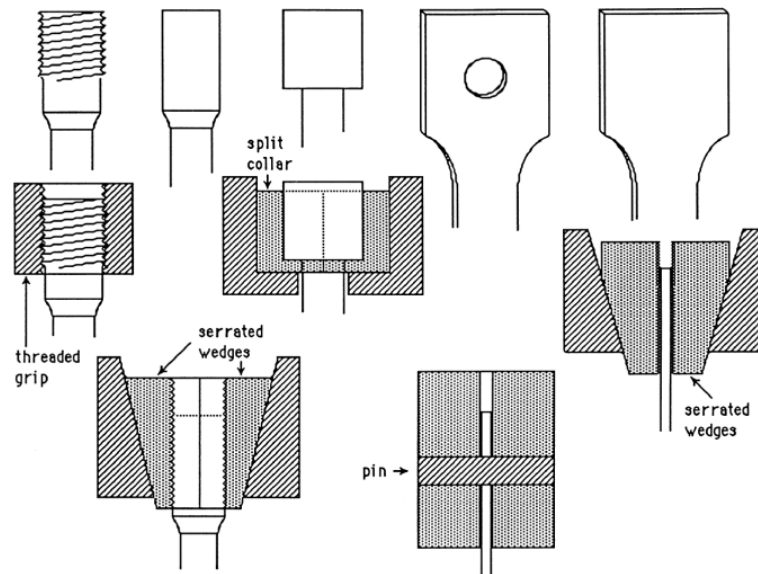


Fig. 2.10 Systems for gripping the tensile specimens

The following prescriptions must be ensured:

- The grip system is arranged such that the major axis of the test specimen coincides with the direction of pull through the centerline of the grip assembly.
- The specimen must be prevented from slipping relative to the grips and the grip must maintain or increase pressure on the test specimen as the force applied to the specimen increases.
- The grip system must not cause premature failure at the grips. This can be quite difficult at times when one is dealing with particularly brittle or unidirectional continuous fibre-filled material.

2.3.2 Extensometers

The standard ISO 37:2011(E) requires that the extensometer should measure the change in gauge length with an accuracy of 2%.

Many different types of extensometers can be used to monitor the strain in a tensile test; there two main categories: *contact* and *non-contact*.

CONTACT

For fairly hard plastics, the so called “grip on strain gauge” type, is suitable.

Four matched foil type resistance strain gauges are bonded to the curved spring steel, two on the outer surface and two on the inner surface. In this arrangement, as a specimen extends so the arms of the spring move further apart causing the gauges on the outer

surface of the spring to go into compression and the gauges on the inner surface of the spring to go into tension. The resultant variations in resistance are proportional to the level of strain in the specimen.

It has the advantage of low cost and ease to use, however it can influence small/delicate specimens.

NON-CONTACT

They use some form of light to illuminate and follow gauge marks which have been made on the specimen. Usually these gauge marks have been drawn, painted or even stuck onto the surface of the specimen prior to testing.

There are three primary types of non-contacting extensometer, optical, laser and video:

- **Optical extensometers** use either visible or infrared light to illuminate gauge marks on the specimen. Photoelectric sensing devices, using a servo mechanism, then follow the gauge marks as the specimen extends or contracts and the resulting movement is monitored using a displacement transducer. It is showed in Fig. 11.
- **Laser extensometers** use reciprocating or rotating mirrors to sweep a laser beam between the gauge marks on the specimen. It is based on the change of the angle subtended between the gauge marks and either the original gauge length.
- **Video extensometers** produce a real time image of the specimen and associated gauge marks. The resultant images are transmitted to a computer that then uses special software to process the images, comparing the original accurately measured gauge marks and their subsequent relative positions.

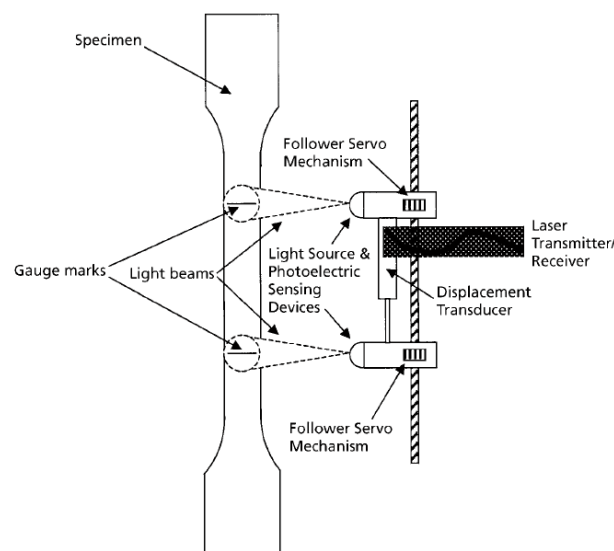


Fig. 2.11 Scheme of an optical extensometer

2.4 Test Methodology

The mechanical test is divided into four key elements, now presented.

2.4.1 Sample Selection

When a material is tested, the objective usually is to determine whether or not the material is suitable for its intended use.

The sample to be tested must fairly represent the body of material in question. In other words, it must be from the same source and have undergone the same processing steps.

It is often difficult to match exactly the test samples to the structure made from the material.

2.4.2 Sample Preparation

It should be remembered that a “sample” is a quantity of material that represents a larger lot. The sample usually is made into multiple “specimens” for testing. Test samples must be prepared properly to achieve accurate results.

First, as each sample is obtained, it should be identified as to material description, source, location and orientation with respect to the body of material, processing status at the time of sampling, and the date and time of the day that the sample was obtained.

Test specimens must be made carefully, with attention to several details. The specimen axis must be properly aligned with the material rolling direction, forging grain pattern, or composite layup; additionally, cold working of the test section must be minimized.

2.4.3 Test Set-Up

It requires that the equipment be properly matched to the test at hand.

The grips must properly fit the specimens; with wedge grips, placement of the specimen in the grip is critical to proper alignment. Ideally, the grip faces should be of the same width as the tab ends of the test bar, otherwise, lateral alignment is dependent only on the skill of the technician. The wedge grip inserts should be contained within the grip body or crosshead, and the specimen tabs should be fully engaged by the grips.

There are several potential problems that must be watched for during the test set-up, including specimen misalignment and worn grips.

The physical alignment of the two points of attachment of the specimen is important, because any off-center loading will exert bending loads on the specimen. This is critical in testing of brittle materials, and may cause problems even for ductile materials.

Alignment will be affected by the testing machine load frame, any grips and fixtures used, and the specimen itself. Misalignment may also induce load measurements errors due to the passage of bending forces through the load measuring apparatus.

Worn grips may contribute to off-center loading.

2.4.4 Test Procedure

The identity of each specimen should be verified, and pertinent identification should be accurately recorded for the test records and report.

The load-indicator zero and the plot-load-axis zero, if applicable, should be set before the specimen is placed in the grips, zeroes should never be reset later.

The specimen is placed in the grips and is secured by closing them.

In some cases, preload may be desirable and may be deliberately introduced. For materials for which the initial portion of the curve is linear, the strain zero may be corrected for preload by extending the initial strain portion of the stress-strain curve to zero load and measuring strain from that point.

The entire test must be monitored, in order to detect the eventual presence of problems. One common sign of trouble is a load-versus-strain plot in which the initial portion of the curve is not straight. This may indicate off-center loading of the specimen, improper installation of the extensometer, or the specimen was not straight to begin with.

Another potential trouble sign is a sharp drop in indicated load during the test. Such a drop may be characteristic of the material, but it also can indicate problems such as slippage between the specimen and the grips or stick-slip movement of the wedge grip inserts in the grip body. Slippage may be caused by worn inserts with dull teeth, particularly for hard, smooth specimens.

The stick-slip action in wedge grips is more common in testing of resilient materials, but it also can occur in testing of metals. If the sliding faces are not lubricated, they may move in unpredictable steps accompanied by drops in the load reading.

When wedge grips are used, the specimen must be installed so that the clamping force is contained within the grip body. Placing the specimen too near the open end of the grip body results in excessive stress on the grip and is a common cause of grip failure.

2.5 Development of the Test

In this section, the explanation of the tensile strength tests realized is carried out and the obtained results are presented.

The different analyzed silicone rubbers are:

- Elastosil M 4642
- Bluesil ESA 7250
- Lumisil LR 7600/50

The tests are conducted following the international standard **ISO 37:2011 (E)**, “**Rubber, vulcanized or thermoplastic – Determination of tensile stress-strain properties**”, [12].

The properties which can be determined are “tensile strength”, “elongation at tensile strength”, “tensile strength at break” and “elongation at break”.

The stresses are calculated assuming the area of the original cross-section and the initial distance between reference points within the length of the narrow portion is used to measure elongation.

According to this standard, **the type of test piece is the number 2**; so the standard thickness of the narrow portion shall be $2.0 \text{ mm} \pm 0.2 \text{ mm}$.

2.5.1 Production of Samples

All the silicone rubbers used for the mechanical tests have been produced in the company “Polymeric GmbH” in Berlin.

The two component of the polymer are mixed in a canister, according to their specific mixing ratios, and they undergo an initial degasification process, for approximately 20 minutes (a visual check of the bubble’s presence is conducted).

Afterwards, the liquid silicone is effused on a glass plate, enclosed by polycarbonate rectangular strips of 2 mm in height and it experiences another degasification phase (shown in Fig. 2.12), until the air bubbles are no longer visible in the vacuum state.

Later, a polycarbonate plate is superimposed; this operation requires particular attention and precision, in order to avoid the presence of air between the two materials that would mean a final silicone’s height less than 2 mm.

Finally, over the silicone are placed a glass sheet and a load of several kilos, to keep the set distance; then the material undergoes the curing in the oven, according to its specific conditions.



Fig. 2.12 Silicone rubber during degasification process

For every material, two sheets are produced and the used quantities (A+B components) range between 60 g and 90 g.

The specimens, dumb-bells, are obtained by cutting the sheets with a die, which dimensions are reported in Table 2.1 and Fig. 2.13, whereas the Fig. 2.14 shows the cutter used to trim the samples.

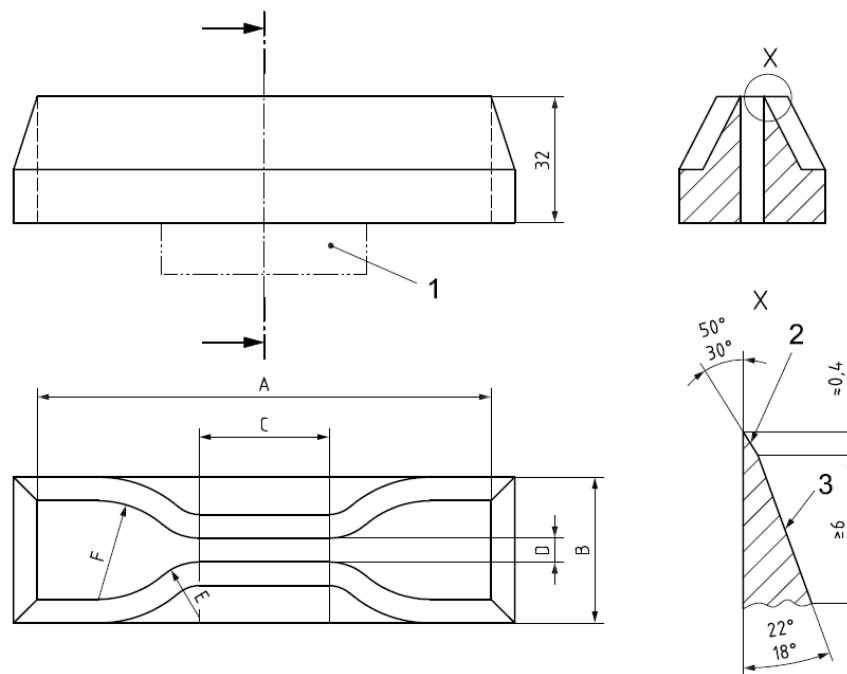


Fig. 2.13 Die for dumb-bell test pieces

Tab. 2.1 Dimensions of die for dumb-bell test pieces

Dimension	Type 2
A Overall length (minimum) ^a (mm)	75
B Width of ends (mm)	12,5 ± 1
C Length of narrow portion (mm)	25 ± 1
D Width of narrow portion (mm)	4 ± 0,1
E Transition radius outside (mm)	8 ± 0,5
F Transition radius inside (mm)	12,5 ± 1

Every specimen is numerated and its original position in the frame must be identified, obtaining the following numbers of pieces:

- Elastosil M 4642 : **15**
- Bluesil ESA 7250 : **13**
- Lumisil LR 7600/50 : **18**

**Fig. 2.14** Cutter used in the test

The thickness is measured in three points, in the middle and at each end of the narrow portion. The mean value is used to calculate the area of the cross section.

In any one dumb-bell, none of the three thickness measurements shall differ by more than 2% from the mean value.

Moreover, it is necessary to pay attention to the instrument used for these measurements: since the silicone is a quite soft material, using a device that applies a too high force can result in erroneous outcomes.

Finally, since the testing machine implements an optical extensometer, it is necessary to stick the two gauge marks at a distance of 20 mm, the test length.

According to the norm, the specimens remain at least 3 hours at the standard laboratory temperature, $(23 \pm 5) ^\circ\text{C}$, without humidity control, before the beginning of the test.

2.5.2 The Testing Process

The used machine is the electromechanical “Zwick Roell zmart.pro”; it has pneumatic grips with serrated wedges, by compressed air; a PC is connected to the machine and the test is realized with the software “testXpert II”.

The specimen is inserted in the grips, a great deal of care is needed in order to align it with the middle vertical axis and to avoid non-uniform distribution of tension over the cross-section. In addition, a pre-load of 0.1 N is applied to the samples, so that the test piece is not bent when the initial test length is measured.

The tests are conducted with a nominal rate of traverse of the moving grip of 250 mm/min; the Fig. 2.15 exhibits a specimen under test; in which it is possible to see the gauge marks brightened by the extensometer’s light.

Any test piece that breaks outside the test length (the gauge marks) shall be discarded, because a reliable result is not ensured. Moreover, a further critical analysis is made on the outcomes and eliminating those which values are too distant from the general behavior, revealing the presence of assignable causes and not only a natural chance variation.

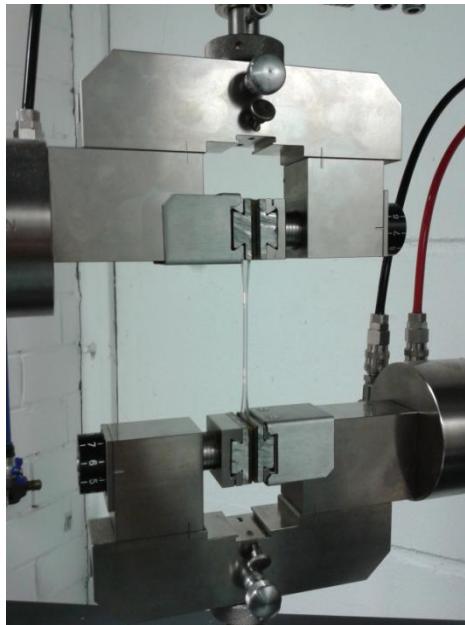


Fig. 2.15 Specimen during tensile strength test

2.6 The results

For each material, the software “TestXpert II” provides a test report, made by three components: the test results, the graph and the statistics.

The test results contains the data relative to each tested specimen; the area, S_0 , is computed by multiplying the particular thickness (mean value between the three measurements) and the width of the narrow portion (equal to 4 mm).

The initial test length is named L_0 and is measured by the extensometer.












With F_{max} and dL at F_{max} the maximum stress and elongation are indicated, respectively; whereas, the values recorded at the rupture are reported as F_{break} and dL at F_{break} .

The second component is the graph, which reports the stress-strain curves of every tested sample, built up with the stress-strain points recorded by the machine.

Finally, the statistics are presented. As indicated in the norm, the median for each main property is computed. Moreover, the estimated mean value and standard deviation have been reported; in calculating the mean value, the maximum and the minimum quantities have not been considered, following the procedure of specific mechanical test.

The results of **Elastosil M 4642**, based on eleven specimens, are reported in Tab. 2.2.

Tab. 2.2 Test results of M 4642

Legends	F_{max} N/mm ²	dL at F_{max} %	F_{Break} N/mm ²	dL at break %	S_0 mm ²	L_0 mm	Farbe	Alterung-Art
	6,6	333,63	6,58	334	8,26	20,19	orange/red	ungealtert
	7,4	367,62	7,12	368	8,27	19,89		
	6,6	335,71	6,55	336	8,30	19,49		
	7,0	365,68	6,98	366	8,30	19,87		
	6,6	335,58	6,57	336	8,17	20,21		
	7,0	354,82	6,73	355	8,19	19,70		
	6,4	331,57	6,44	332	8,14	19,99		
	6,8	337,71	6,78	338	8,15	19,89		
	7,2	358,61	7,20	359	8,07	19,91		
	6,8	342,89	6,84	343	8,04	19,96		
	6,9	357,98	6,89	358	8,21	19,92		

Tab. 2.3 Statistics of M 4642

n = 11	F_{max} N/mm ²	dL at F_{max} %	F_{Break} N/mm ²	dL at break %
median	6,8	342,89	6,78	343
mean value	6,8	346,96	6,78	347
standard deviation	0,3	13,66	0,24	13

The statistics of this material are presented in Tab. 2.3: whereas, in Fig. 2.16 its graph is shown. Apart from the initial small deflection, common to each tested material, in the M 4642 only one rising point of inflection appears clearly (around 100% in strain); in this case, due to their appearance, the curves are named “j-shaped”.

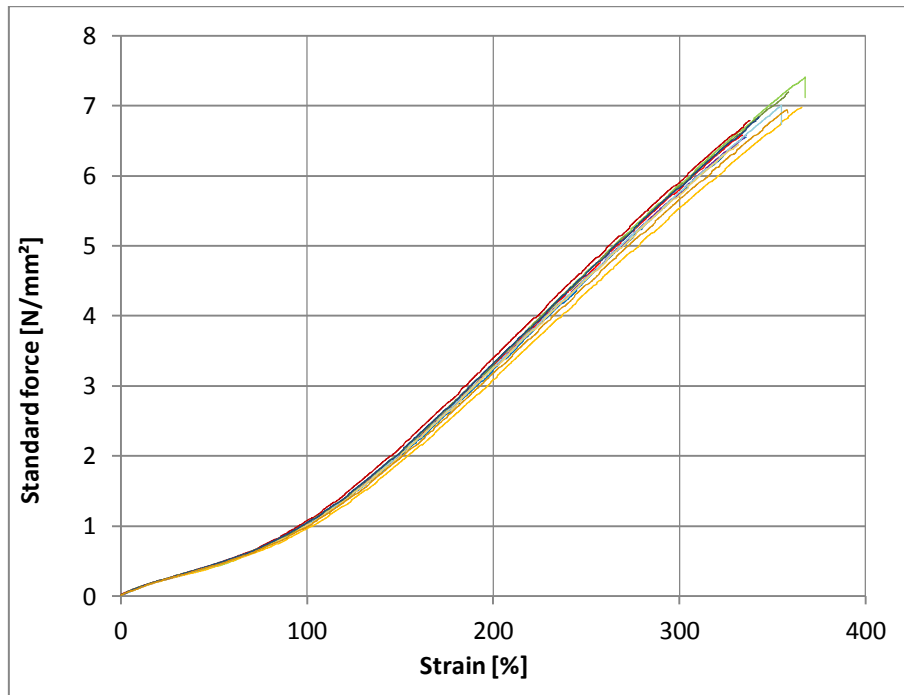


Fig. 2.16 Graph of M 4642

Considering the **Bluesil ESA 7250**, the outcomes of ten tested specimens constitute the test results that is proposed in Tab. 2.4.

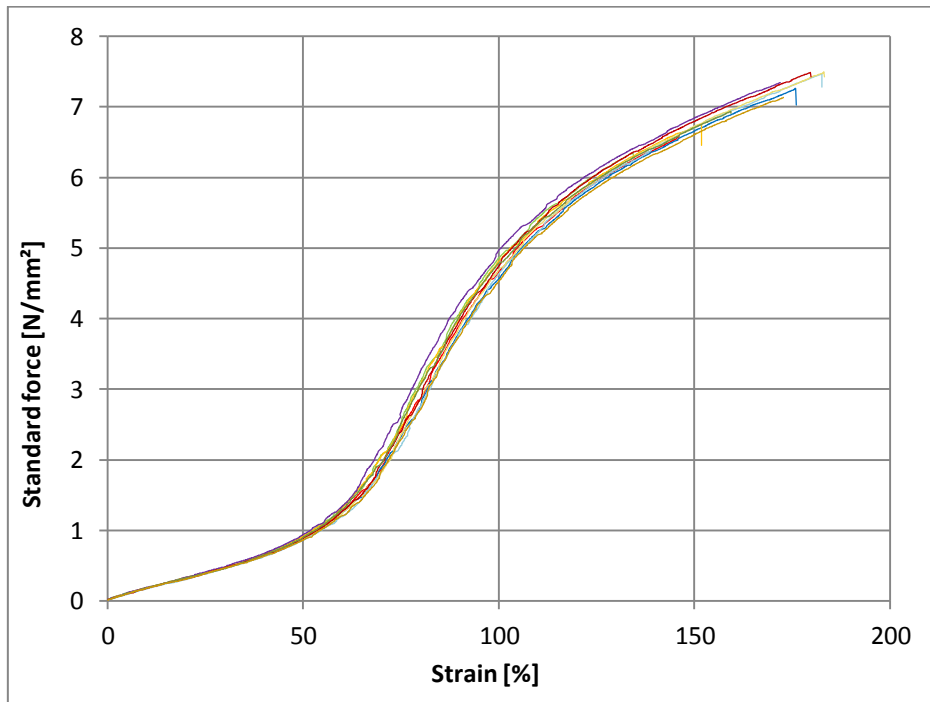
Tab. 2.4 Test results of ESA 7250

Legends	F_{\max} N/mm ²	dL at F_{\max} %	F_{Break} N/mm ²	dL at break %	S_0 mm ²	L_0 mm	Farbe	Alterung-Art
	6,6	146,16	6,58	146	8,36	20,71	transparent	ungealtert
	6,4	134,31	6,28	134	8,32	20,52		
	7,3	175,86	7,03	176	8,24	20,38		
	6,8	151,74	6,45	152	8,28	20,39		
	7,3	171,93	7,35	172	8,28	19,88		
	7,5	182,54	7,28	183	8,26	20,91		
	7,5	183,14	7,42	183	8,37	20,34		
	7,5	179,67	7,43	180	8,32	21,05		
	6,9	159,31	6,91	159	8,34	21,48		
	7,1	172,74	7,13	173	8,34	20,07		

Whereas, its statistics and the chart are presented in Tab. 2.5 and Fig. 2.17, respectively.

Tab. 2.5 Statistics of ESA 7250

n = 10	F_{\max} N/mm ²	dL at F_{\max} %	F_{Break} N/mm ²	dL at break %
median	7,2	172,34	7,08	173
mean value	7,1	167,57	7,02	168
standard deviation	0,4	16,92	0,42	17

**Fig. 2.17** Graph of ESA 7250

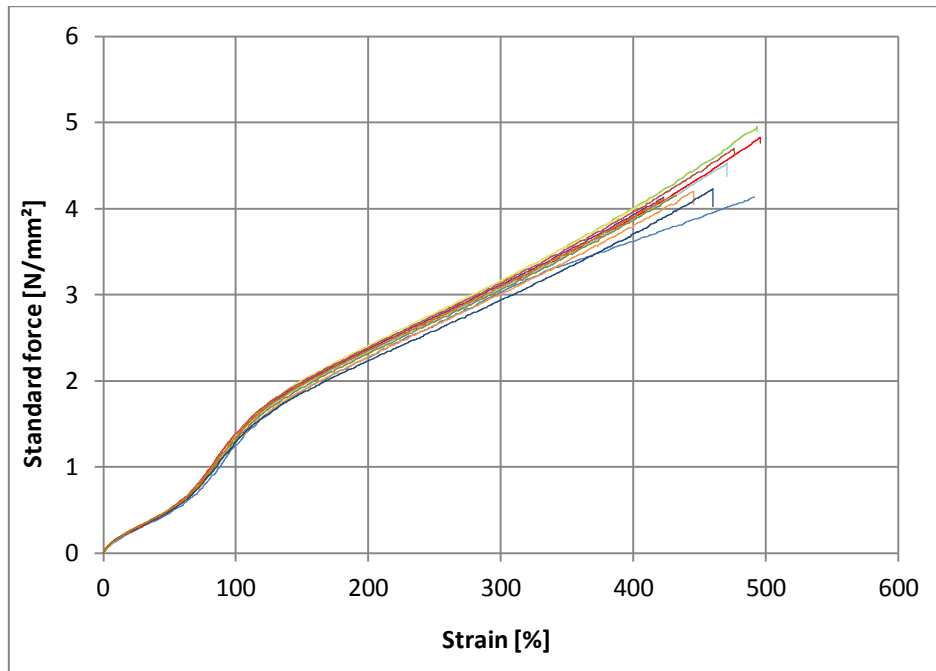
Finally, the results of **Lumisil LR 7600/50** are reported in Tab. 2.6 and its statistics are found in Tab. 2.7; in this case, eleven specimens constitute the report.

Tab. 2.6 Test results of LR 7600/50

Legends	F_{\max} N/mm ²	dL at F_{\max} %	F_{Break} N/mm ²	dL at break %	S_0 mm ²	L_0 mm	Farbe	Alterung-Art
	4,8	495,60	4,76	496	8,00	20,01	transparent	ungealtert
	4,9	493,16	4,89	493	7,66	19,88		
	4,1	491,34	4,13	491	7,73	19,75		
	4,2	445,58	4,04	446	7,52	19,70		
	4,1	422,86	4,13	423	7,60	19,77		
	4,5	470,62	4,38	471	7,70	19,98		
	4,1	413,92	4,12	414	7,68	19,18		
	4,7	476,06	4,61	476	7,76	20,47		
	4,1	431,48	4,15	432	7,80	19,79		
	4,2	459,80	4,02	460	8,08	19,60		
	4,1	423,38	4,11	423	7,56	19,89		

Tab. 2.7 Statistics of LR 7600/50

n = 11	F_{\max} N/mm ²	dL at F_{\max} %	F_{Break} N/mm ²	dL at break %
median	4,2	459,80	4,13	460
mean value	4,3	457,14	4,27	457
standard deviation	0,3	30,77	0,30	30

**Fig. 2.18** Graph of LR 7600/50

In the graphs related to LR 7600/50 (Fig. 2.18) and ESA 7250 (Fig. 2.17), two points of inflection (a rising one and a falling one) are recognized (unlike the M 4642 in Fig. 2.16). Because their particular form, in this case, the curves are named “s-shaped”.

Observing the different graphs, it is easily noticed that the silicone exhibits an unusual stress-strain curve. It does not present a first elastic part well separated by a following plastic one; in these silicone rubbers the two behavior are quite joined and, in different portions, one prevails on the other.

All the materials show an initial straight region, then a plastic behavior (commonly around 100% in strain) and still a linear one until the rupture; anyway, in the ESA 7250 the central plastic region is well-defined (Fig. 2.17), with respect to the other materials.

There are not yield points (in which an increase in strain is not accompanied by an increase in stress) along the curves; anyway some specimens exhibit a vertical drop in correspondence of the rupture.

This occurrence causes the difference between the stress at break and the maximum one. This vertical drop is not due to the formation of neck in the material, but to the limited resolution of the measuring system in following the instantaneous rupture; for this reason, evaluating the force, F_{\max} should be considered.

According to the final scope of the material, the researcher focuses his attention or on the maximum elongation or on the maximum stress expressed by the test's outcomes.

For example, considering a certain specific application, the LR 7600/50 could be suitable because its high elongation and the low endurable stress could not be considered for this implementation.

The different results given by the test of the same material can be due to many causes:

- The applied stress is not uniform in the cross-section, this could be because the specimen is not perfectly centered along the longitudinal and middle axes of the grips.
- The thickness varies along the narrow portion and only one value has been assumed to represent it.
- The curing process has not been uniform; in the oven, part of the sheet could be more or less exposed to the heat.
- There are tiny air bubbles not visible inside the silicone, that reduce the material's resistance.

The Young's modulus (presented in the paragraph 2.2.1) can be calculated from the values stress - strain, given by the software, used to build up the graphs in the first linear region; until the 30% of strain.

For each specimen, the following formula is implemented:

$$E_{n_s}(n) = \frac{s(n) - s(n - 1)}{e(n) - e(n - 1)}$$

In which n indicates the different points of the specimen's curve, assuming the values from 1 to N , and n_s is related to the particular specimen.

It is applied to each point of the curve having the corresponding strain between the first non-zero value until the 30%.

The mean value of these Young's moduli is computed (one for each specimen is obtained). Finally, the average value between the different specimens is computed, obtaining the Young's modulus for the material.

It is important to determine the uncertainty with which the Young's modulus is expressed. First of all, it is necessary to determine the uncertainty related to each specimen; this uncertainty is of type a , and it is given by the following formula:

$$u_a(E_{n_s}(n)) = \sqrt{\frac{s^2(E_{n_s}(n))}{N}}$$

in which $s^2(E_{n_s}(n))$ is the unbiased sample variance (with Bessel's correction).

Then, the uncertainties of each specimen must be combined, to find the error in the Young's modulus for a specific silicone, obtained with the error propagation theory:

$$u_{tot}(E_{n_s}(n)) = \sqrt{\frac{1}{N_s} \cdot \sum_{n_s=1}^{N_s} (u_a(E_{n_s}(n)))^2}$$

with N_s as number of specimens for each material (10 or 11, in our cases).

Finally, the calculated results are:

- M 4642 : 1.029 ± 0.015 MPa
- ESA 7250 : 1.677 ± 0.018 MPa
- LR 7600/50 : 1.202 ± 0.018 MPa

These outcomes are lower than other polymers, and in particular very tiny with comparison to different materials, usually in the order of $10^1 \div 10^2$ GPa.

This is a mathematical confirmation of the clear flexibility of the rubbers.

In order to verify the goodness and reliability of the obtained results, the "Statistical Process Control" is implemented.

It constitutes a method to verify if the outcomes will be statistically reasonable; in other words, if the procedure will be "in statistical control".

A process is said "in statistical control" if only chance causes are present, so the variations depend only on chance; if assignable causes occur it is named "out of control".

The determination of the process' condition is fulfilled with the concept of “natural tolerance”, which measure is considered the quantity “ 6σ ”, where σ is the standard deviation.

Assumed the distribution as normal, the process is said “in statistical control” if the values are included in the interval:

$$(\hat{\mu} - 3\hat{\sigma} ; \hat{\mu} + 3\hat{\sigma})$$

Where $\hat{\mu}$ is the estimated mean, with n as number of tested specimen:

$$\hat{\mu} = \frac{1}{n} \sum_{i=1}^n x_i$$

And $\hat{\sigma}$ is the estimated standard deviation, previously reported in the statistics:

$$\hat{\sigma} = \sqrt{\sum_{i=1}^n \frac{(x_i - \hat{\mu})^2}{n - 1}}$$

For every characteristic quantity (stress and strain, maximum and ultimate values) the estimated mean $\hat{\mu}$ and, consequently, the upper and lower limits are calculated, by using the test results from Tab. 2.2, Tab. 2.4 and Tab. 2.6.

These average values and limits for M 4642, ESA 7250 and LR 7600/50 are reported in Tab. 2.8, Tab. 2.9 and Tab. 2.10, respectively.

Tab. 2.8 Statistical Process Control quantities for M 4642

M4642	F_{max}	dL at F_{max}	F_{break}	dL at F_{break}
	[N/mm ²]	[%]	[N/mm ²]	[%]
Upper limit	7.7	388.42	7.53	389
Estimated Mean	6.8	347.44	6.79	348
Lower limit	6	306.45	6.05	307

Tab. 2.9 Statistical Process Control quantities for ESA 7250

ESA 7250	F_{max}	dL at F_{max}	F_{break}	dL at F_{break}
	[N/mm ²]	[%]	[N/mm ²]	[%]
Upper limit	8.3	216.51	8.24	217
Estimated Mean	7.1	165.74	6.99	166
Lower limit	5.9	114.97	5.73	115

Tab. 2.10 Statistical Process Control quantities for LR 7600/50

LR 7600/50	F_{max}	dL at F_{max}	F_{break}	dL at F_{break}
	[N/mm ²]	[%]	[N/mm ²]	[%]
Upper limit	5.3	549.01	5.21	549
Estimated Mean	4.3	456.71	4.3	457
Lower limit	3.4	364.41	3.39	365

Comparing the obtained outcomes, related to each specimen of every material, with the computed limits, it has been verified that all the results are included in their specific limits. Hence the process can be stated “in statistical control”, proving the statistical reliability of the test’s result.

3 PARTIAL DISCHARGE MEASUREMENT

3.1 Introduction

The partial discharge is a phenomenon due to the non-ideal behavior of dielectric materials, for which the medium experiences an incomplete transition of charges.

Its detection constitutes a valuable tool in electrical engineering, in order to prevent the decline and decay of insulating materials and to avoid their final breakage.

This chapter starts describing the partial discharge phenomenon and its measurement according to the theory. Then, the conducted test is presented: it consists in the inception voltage test and it provides significant information for the successive dielectric measurements. Moreover, in the next pages, the test cell (used for each experiment of this thesis) is presented and analyzed.

3.2 Theory of Partial Discharge

Electric discharges that do not completely bridge the electrodes are called *partial discharges* (PD). Although the magnitude of such discharges is usually small, they cause progressive deterioration and may lead to ultimate failure. It is therefore essential to detect their presence in a nondestructive control test.

In high voltage terminology, one differentiates between a “complete” and an “incomplete” breakdown of the insulation stressed by voltage application. During “complete” breakdown, the insulation collapses almost completely, bridging the electrodes by a low-ohmic resistance. However, during an “incomplete” breakdown, only a portion of the insulation collapses, resulting in “partial breakdown”. The still healthy portion of the insulation can withstand the voltage stress.

Partial discharges occurring in gases around electrodes of small radius of curvature (depending on several parameters as type of gas, pressure, polarity field distribution and

field strength) and those on the surface of solid insulating materials are known as “external” partial discharges.

On the other hand, partial discharges are considered “internal” if gas discharges occur as partial breakdowns in solid or liquid insulating materials.

Partial discharges usually begin in voids, cracks, or gas-filled cavities within a solid dielectric (Fig. 3.1a), at conductor-dielectric (solid or liquid) interfaces, or in bubbles within liquid dielectrics. PD can also occur along the boundary of different insulating materials (Fig. 3.1b).

It should be pointed out that, in the case of external partial discharges occurring at electrodes of small radius of curvature, it is not the possible damages to insulation which are of interest (as in the case of ageing due to internal partial discharges) but the high frequency disturbances arising out of these partial discharges, and quite often the energy dissipated (corona losses) together with its chemical after-effects. While investigating internal partial discharges, such external partial discharges in the test circuit represent disturbing parameters that must be recognized as such and eliminated.

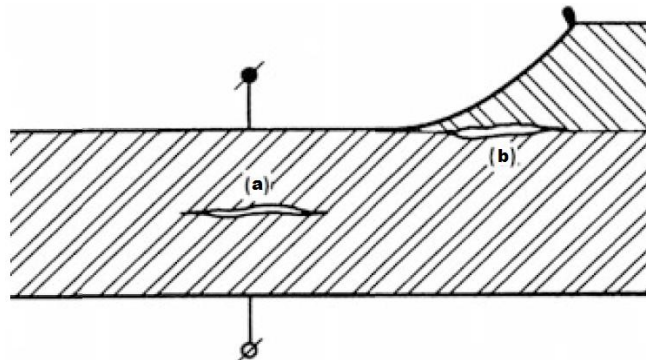


Fig. 3.1 Typical sizes of gaseous inclusions in solid dielectrics

3.2.1 Partial Discharge Models

As known, the electromagnetic transients due to PD events are only detectable at the terminals of HV apparatus. Therefore, it seems of interest if this external pulse charge is correlated with the internal pulse charge flowing through the PD defect.

To analyze the PD charge transfer, instead of realistic imperfections, simple cavity shapes are commonly investigated, such as spherical, elliptical and cylindrical cavities.

Generally, it can be distinguished between the (network-based) *capacitive model* and the *dipole PD model*.

Capacitive Model

This equivalent circuit has been originally proposed by Gemant & Philippoff as early as in 1932 and slightly modified after many years.

In this circuit, referred also as *abc-model*, C_a is the capacitance of the bulk dielectric between the electrodes of the test object, C_b is the stray capacitance of the healthy dielectric column between cavity and electrodes, and C_c is the cavity capacitance that is bridged by the spark gap F_c .

To analyze the PD charge transfer from the cavity to the terminals of the test sample, commonly a cylindrical dielectric column of constant diameter $2r_b$ is considered, as shown in Fig. 3.2a. For technical insulation, the condition $d_c \ll d_{b1} + d_{b2} \cong d_a$ is generally satisfied. Thus, the resulting capacitance of the solid dielectric column can simply be expressed by $C_b = \varepsilon_0 \varepsilon_r \pi \frac{r_b^2}{d_a}$.

In addition, equal radii are assumed for both the solid dielectric column and the cylindrical cavity, i.e. $r_c = r_b$, thus, the cavity capacitance is estimated by $C_c = \varepsilon_0 \pi \frac{r_b^2}{d_c}$. Assuming that the spark gap F_c breaks down at inception field strength E_i , the voltage collapse across the cavity capacitance can be approximated by $\Delta V_c \cong E_i d_c$. Based on this, the internal PD charge Q_c flowing through the gas-filled cavity ($\varepsilon_r=1$) can be expressed by:

$$Q_c \cong \Delta V_c C_c \cong E_i \varepsilon_0 \pi r_b^2$$

The transient current $i_b(t)$ and thus the charge Q_b flowing through the capacitances C_{b1} and C_{b2} are also flowing through the capacitance C_a , representing the bulk dielectric of the test sample, i.e. $Q_a = Q_b$. Therefore, the external charge Q_a detectable at the terminals of the test sample is:

$$Q_a = Q_b \cong \Delta V_c C_b \cong E_i \varepsilon_0 \varepsilon_r \pi r_b^2 \frac{d_c}{d_a}$$

Usually, the relative permittivity ε_r of the applied solid dielectrics is below 5, thus, the ratio between external detectable charge and internal charge flowing through the cavity becomes:

$$\frac{Q_a}{Q_c} \cong \varepsilon_r \frac{d_c}{d_a} \ll 1$$

Due to this relation, the external detectable charge is commonly referred to as apparent charge and it is not equal to the amount of that charge involved at the site of the discharge, which cannot be measured directly.

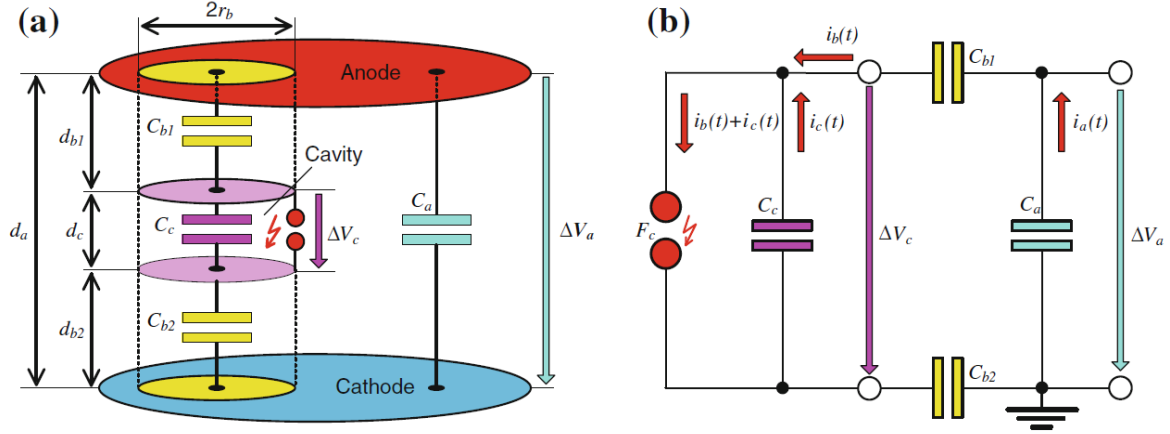


Fig. 3.2 Network-based capacitive PD model.

a Parallel-plane electrodes with circuit elements. **b** Capacitive equivalent circuit

The first mistake of this model is that the effective radius r_b increases drastically if a discharge channel (radius r_d) is formed, so the effective capacitance C_c is not any longer governed by the effective radius r_b of the solid dielectric column shown in Fig. 3.2a but by the radius r_d of the discharge channel developing inside the cavity, where the condition $r_d \ll r_b$ is always satisfied, yielding:

$$\frac{Q_a}{Q_c} \cong \epsilon_r \frac{d_c}{d_a} \left(\frac{r_b}{r_d} \right)^2$$

Hence, it cannot simply be claimed that the external PD charge is only a small fraction of the internal PD charge.

Another mistake is the assumption that the applied test voltage induces charge carriers at the anode-side and cathode-side cavity boundary. That means the internal charge has already been produced just before PD event is ignited, which is in contrast to the physics of gas discharges.

Dipole PD Model

The main difference with respect the previous model is that the cavity is not discharged via a spark gap but charged due to the creation of charge carriers as consequence of ionization

processes in the gas-filled cavity. As the charge carriers of both polarities are deposited at the anode-side and cathode-side cavity boundary, a dipole moment is established, as illustrated in Fig. 3.3a. The space charge field, commonly referred to as Poisson field, opposes the electrostatic field caused by the applied test voltage, commonly referred to as Laplacian field. As a consequence, the ionization of gas molecules is quenched immediately after the PD event has been ignited, where the time interval is usually in the nanosecond range.

The current $i_c(t)$ caused by the charge carriers moving inside the cavity continues like a displacement current $i_b(t)$ through the solid dielectric column (the capacitances C_{b1} and C_{b2}). From this follows that the external PD charge Q_a detectable at the terminals of the test sample must be equal to the internal PD charge Q_c flowing through the cavity, which is in contrast to the apparent charge concept presented previously.

Moreover, it shall be assumed that the Laplace field between the electrodes remains constant during the time duration of a PD event which is usually in the order of nanoseconds. Thus, only the Poisson field caused by the separation of the charge carriers of opposite polarity has to be considered to estimate the PD charge transfer.

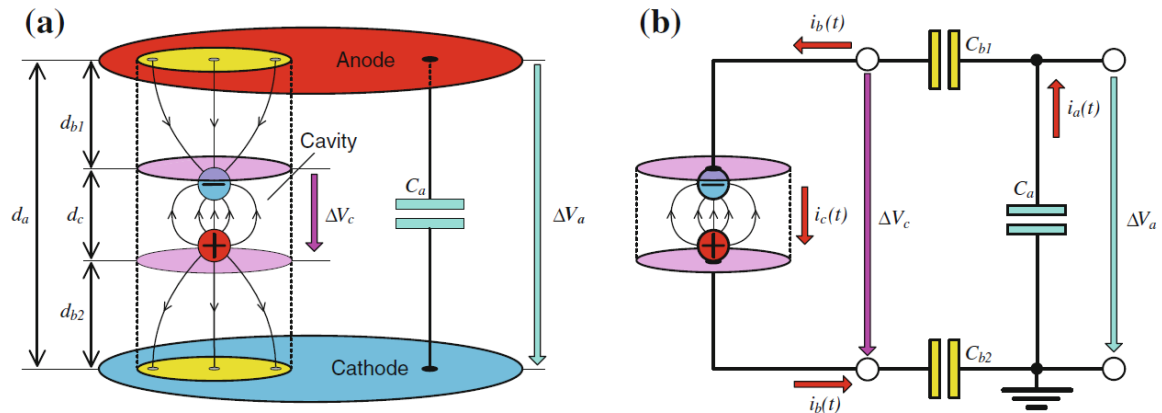


Fig. 3.3 Dipole model of a cavity discharge
a Space charge field - **b** Circuit elements

The movement of a single electron and the associated positive ion are considered, where the propagation to the electrodes is hampered by two dielectric layers of spacing d_c , as illustrated in Fig. 3.4. Assuming that at inception field strength E_i , only a single electron carrying the elementary charge $-e$ is liberated from a neutral molecule at position $x = x_i$, the electron is attracted by the anode due to the Coulomb force $F = -eE_ix_i$.

Thus, after travelling the maximum possible distance x_i , the field energy transferred to the electron becomes:

$$W_e = F \int_{x_i}^0 dx = -e \cdot E_i(0 - x_i) = eE_i x_i$$

In an analogue manner, the energy transferred from the field to the associated positive ion carrying the elementary charge e is:

$$W_p = F \int_{x_i}^0 dx = -e \cdot E_i(d_c - x_i)$$

Hence, the total field energy transferred to both the electron and the associated positive ion after approaching the dielectric layers becomes:

$$W_t = W_e + W_p = eE_i d_c$$

It is obvious that this equation is independent from the actual site x_i where the electron is liberated from a neutral molecule. Thus, also the field energy transferred to an electron avalanche created by the ionization of n_i molecules is given by:

$$W_a = eE_i d_c n_i$$

Imagining that the test sample is disconnected from the HV test supply just before a PD event is ignited at the inception voltage V_i , the energy desired for the movement of the charge carriers is delivered from the test sample capacitance C_a , as shown in Fig. 3.3b.

If the movement of the charge carriers occurs within a time interval t_d , the energy balance theorem can be expressed as follows:

$$W_a = V_i \int_0^{t_d} i_a(t) \cdot dt = V_i Q_a = eE_i n_i d_c = P_m E_i$$

where the term $P_m = en_i d_c$ represents the dipole moment and E_i the inception field strength.

Separating the charge Q_a delivered from the electrodes of the test sample, one gets:

$$Q_a = en_i d_c \frac{E_i}{V_i} = P_m \frac{E_i}{V_i}$$

Considering the last two equations, it can thus be concluded that the external charge Q_a detectable at the terminals of the test sample seems to be a reasonable quantity to assess the PD severity, which is in contrast to the traditional apparent charge concept. In this context, it seems to be noticeable that the detectable external PD charge Q_a increases with the cavity length d_c and thus with the danger for an insulation breakdown, even if the number n_i of molecules ionized in case of a single PD event remains constant.

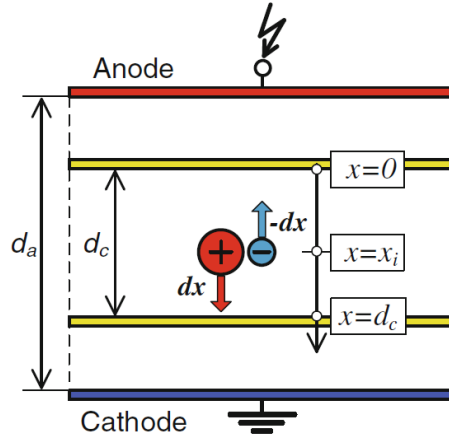


Fig. 3.4 Field energy transferred to an electron and a positive ion

3.2.2 PD pulse charge measurements

The high-frequency PD current pulses are strongly distorted when travelling from the origin to the electrodes of the test object. Different to this, the time integral of the transient PD current and thus the pulse charge is more or less invariant.

As the PD transients are characterized by time parameters in the nanosecond range, the leads between test object and HV test supply can be considered as disconnected due to its extremely high inductive impedance. Consequently, the charge Q_c flowing through the PD defect is almost completely delivered from the test object capacitance C_a , which is associated with a voltage collapse ΔV_a across the electrodes of the test object. Consequently, the pulse charge Q_c flowing through the PD defect, which is delivered from the electrodes of the test object, can be expressed as follows:

$$Q_c = Q_a = \Delta V_a \cdot C_a$$

After the fast PD process is quenched, the transient PD current approaches zero so that the impedance of the connection leads is drastically reduced. Thus, the test object capacitance C_a will be recharged by the HV test supply, i.e. the former voltage step ΔV_a is inverted.

That means the time integral of the charging current can also be approximated by $Q_c = Q_a$, even if the shape of this charging current is very different from that of the original PD current. This fact offers the possibility to measure the pulse charge flowing through the PD defect by means of a measuring impedance, if connected between the LV electrode of the test object and the ground.

The measuring circuit should be bridged by a coupling capacitor C_k to ensure a short duration of the recharging process, and thus, well-reproducible PD measurements. Moreover, an appropriately designed HV inductor should be connected between HV test supply and test object to reject electromagnetic noises coming from the voltage supply.

For a direct measurement of the pulse charge, the measuring impedance could be equipped with a measuring capacitance C_m . Under this condition, the magnitude of voltage jump appearing across C_m is direct proportional to the pulse charge to be measured. At alternating test voltages, however, the capacitive load current through the test object might become substantially higher than the signal of the charge; to overcome this crucial problem, the measuring capacitance C_m can be shunted by a measuring resistor R_m .

To suppress the disturbing signal due to the capacitive load current through the test object, a measuring resistor R_m equal to the characteristic impedance of the measuring cable (which is commonly 50 Ω) is employed and shunted by an appropriately designed inductance.

In general, the measuring impedance is connected in series with the coupling capacitor C_k (as shown in Fig. 3.5), and not with the test object, in order to avoid that unexpected breakdowns could exceed the kA range, and also because the ground connection lead of the test object cannot be interrupted in many cases.

In addition, an inductance L_s is placed, to carry the alternating load current through the coupling capacitor. The over-voltage protection unit O_p is required to suppress fast over-voltages due to an insulation breakdown, which could damage not only the measuring impedance but also the measuring instrument.

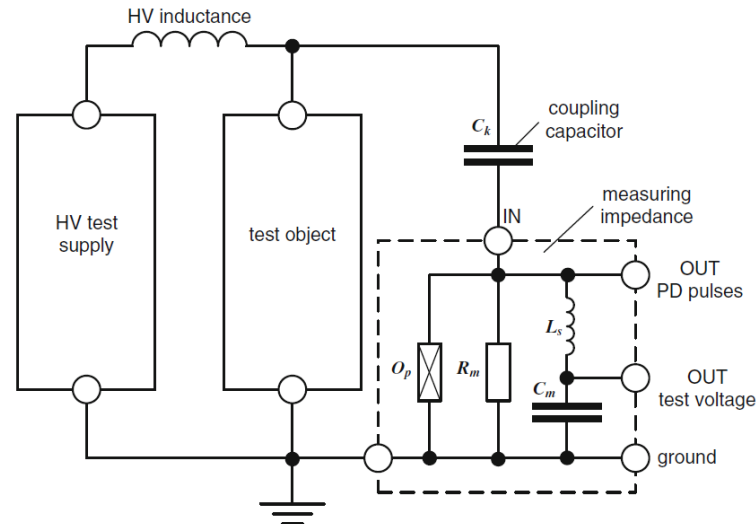


Fig. 3.5 PD measuring circuit

Electromagnetic noises disturbing sensitive PD measurements can be eliminated at certain extent if the so-called balanced PD bridge is adopted (shown in Fig. 3.6). Here, the adjustable measuring impedances Z_{m1} and Z_{m2} are installed in the ground connection leads of the test object, providing the measuring branch, and the coupling capacitor, providing the reference branch. Adjusting Z_{m1} and Z_{m2} accordingly, the bridge can be balanced. That means the common mode noises appearing at the high-voltage terminals are more or less suppressed by the differential amplifier so that only the PD signal originating in the test object appears at the output and is thus measured by the PD instrument.

Anyway, the design is complex because both branches must have an equivalent frequency response over the full investigated bandwidth and, so, it is not generally employed in practice.

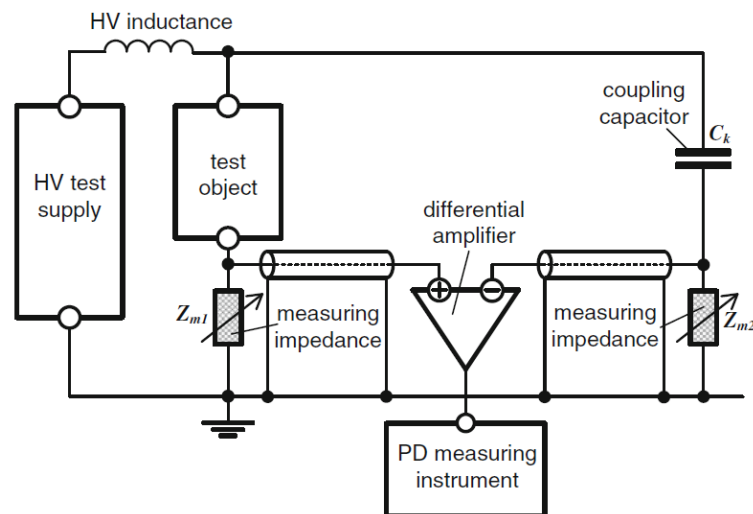


Fig. 3.6 PD bridge circuit for noise reduction

3.2.3 PD Signal Processing

As discussed previously, the time integral of the transient PD current flowing through the connection leads of the test object is more or less correlated with that charge amount flowing through the PD defect. That means the pulse charge is invariant even if the transient current is substantially distorted due to attenuation, dispersion and reflection phenomena when travelling through large test objects. Thus, the transient voltage appearing across a resistive measuring impedance must be integrated to measure the pulse charge.

Investigations on several types of specimen have revealed that PD in solid insulating materials have a rise time of a few ns and a half-value time of some tens of ns. Partial discharges in oil result in current pulses with appreciably longer rise times in the region of 1 μ s and half-value times of some μ s.

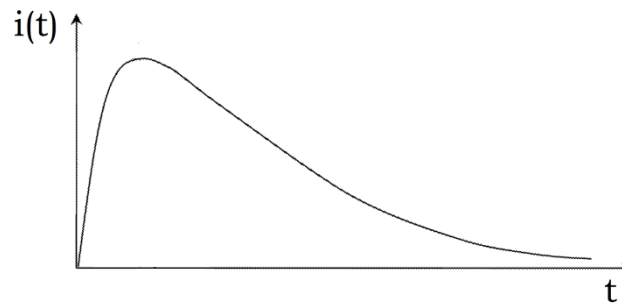


Fig. 3.7 Idealized PD pulse in time domain

The figure 3.7 shows the simplified waveform $i(t)$ of a partial discharge pulse as a superposition of two exponential functions. The charge of the current pulse is obtained as the area below the current/time curve as:

$$Q = \int_0^{\infty} i(t) \cdot dt$$

The spectrum of this current pulse can be obtained by Fourier analysis, idealized in Fig. 3.8. The amplitude frequency spectrum is approximately constant up to a certain frequency and equal to the DC component at the frequency $f = 0$.

For the theoretical limiting case of an infinitely small pulse (the Dirac pulse), the spectral amplitude density is known to be constant up to infinitely high frequencies.

It may be stated that the shorter the PD pulses, the higher are the frequencies to which the spectrum extends and the smaller the values of the DC component.

The expression for the complex spectrum of the current pulse is:

$$F(\omega) = \int_{-\infty}^{+\infty} i(t) \cdot e^{-j\omega t} \cdot dt$$

we have, for $\omega = 2\pi f = 0$, the relation:

$$Q = F(0)$$

i.e. the pulse charge Q corresponds to the DC component $F(0)$ of the spectral amplitude density.

For the range of frequencies in which the spectral amplitude density is nearly constant, the important conclusion is that Q is the same as the spectral amplitude density $F(f)$.

The measurement can conveniently be achieved by a so-called *quasi-integration* using a band-pass filter, i.e. if the signal processing is performed in a frequency range where the amplitude–frequency spectrum of the captured PD pulses is nearly constant, in which $F(f) = Q$.

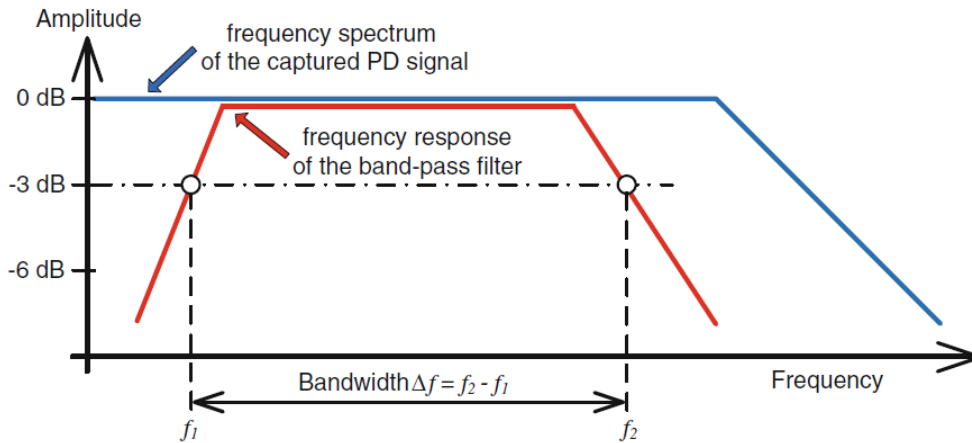


Fig. 3.8 Frequency spectrum of PD pulse and bandwidth for measurements

An idealized measuring system with lower and upper cutoff frequencies f_1 and f_2 is considered in which the transfer factor A has a constant amplitude A_0 .

The mid-band frequency of the system (or the resonance frequency of the narrow-band system) is:

$$f_0 = \frac{f_1 + f_2}{2}$$

and the bandwidth:

$$\Delta f = f_2 - f_1$$

If the Dirac pulse is applied as input to the system, the output signal (impulse response) is:

$$s(t) = 2A_0F(f_0)\{f_2 si[2\pi f_2(t - t_0)] - f_1 si[2\pi f_1(t - t_0)]\}$$

where the function $si(x) = \frac{\sin(x)}{x}$ is the travel time of the system and $F(f_0)$ is the spectral amplitude density of the Dirac pulse at the mid-band frequency of the system.

The maximum value of the impulse response works out to:

$$s_{max} = 2A_0F(f_0)\Delta f$$

The impulse response is thus practically determined by the properties of the measuring system. Information about the pulse exciting the measuring system is contained only in $F(f_0)$ and hence in the maximum value of the impulse response.

The result derived for the Dirac pulse can also be applied to the PD pulse, provided its amplitude density is constant at least up to the upper cutoff frequency f_2 . Since $F(f_0) = Q$, the maximum value of the response signal of the PD pulse charge is proportional to:

$$s_{max} \sim F(f_0) = Q$$

Depending on the bandwidth of the measuring system, two characteristic response signals can now be distinguished.

Wide-band instruments

For wide-band PD measurements on technical test objects, the following frequency parameters are recommended in the Amendment to IEC 60270-2000:

- Lower limit frequency: $30 \text{ kHz} \leq f_1 \leq 100 \text{ kHz}$
- Upper limit frequency: $130 \text{ kHz} \leq f_2 \leq 1 \text{ MHz}$

Characteristic for the band-limited signal processing is still the widening of the impulse response compared to the original impulse.

For the limiting case of $f_1 = 0$ (ideal low-pass), the mean duration of the impulse response can be given as:

$$\tau' = \frac{1}{2f_2} = \frac{1}{2\Delta f}$$

According to this, the bandwidth of a PD meter determines its resolution capacity for fast repetitive PD pulses. To avoid impermissible superposition of the impulse responses in the measuring instruments, it must be ensured that the spacing of the pulses among themselves and between the reflected ones, as encountered for instance in long cables, be appreciably smaller than τ' .

Narrow-band instruments

Using the narrow-band PD signal processing, IEC 60270-2000 suggests the following data:

- Resonance frequency: $50 \text{ kHz} \leq f_0 \leq 1 \text{ MHz}$
- Bandwidth: $9 \text{ kHz} \leq \Delta f \leq 30 \text{ kHz}$

The average duration of the AC signal oscillating with frequency f_0 is:

$$\tau = \frac{1}{\Delta f}$$

The maximum repetition rate of PD pulses that do not still result in superposition errors is thus significantly lower than using the selectively wideband instruments.

In some instruments, the resonance frequency can be varied over a wide range. This is of advantage while trying to avoid interferences appearing frequently only within certain limited frequency ranges or finding out resonance locations in the measuring and test circuits. Disadvantageous is that PD pulses cannot be distinguished according to their polarities since both positive and negative PD pulses result in the same response signal.

3.2.4 Digital PD Measuring Instruments

Due to the achievements in digital signal processing (DSP), the traditional analogue PD measurement is increasingly replaced by the advanced digital technique.

Currently, two basic measuring principles are in use.

The first one utilizes an analogue pre-processing unit to establish the charge signal of the PD pulses, an electronic integrator. After that, a digital signal processing is performed, where a comparatively low sampling rate is required for the A/D conversion.

Another option, reported in Fig. 3.9, is the initial use of a very fast A/D converter to digitize the PD signal captured from the test object. Then, the band-pass filtering required for the quasi-integration of the PD pulses is commonly performed by an adjustable digital filter and a numerical integrator.

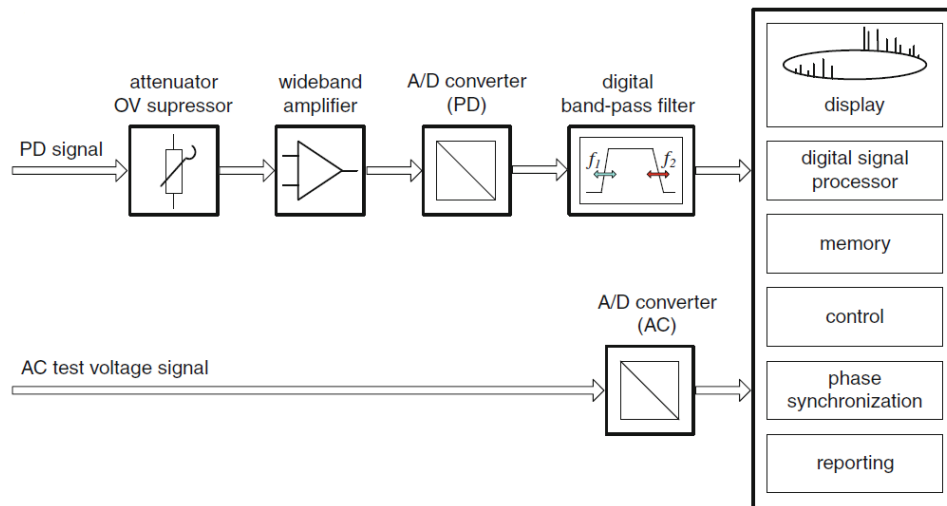


Fig. 3.9 Block diagram of digital instruments with direct conversion of PD signal

3.2.5 Non-electrical PD Detection

Partial electrical breakdowns cause not only high frequency electrical transient phenomena and currents in the supply networks but also give indication of breakdown occurrences in gases and liquids by means of optical, acoustical and chemical effects.

Optical and acoustic methods of establishing the presence of partial discharges are applied specially in case of external and surface discharges, but in case of transparent materials also the internal ones could be detected.

Keywords in this connection are: residual-light amplifier, night-view equipment, directional microphones with amplifiers in sonic and ultrasonic range.

In view of the relatively low levels of energy involved, determination of partial discharges based upon chemical effects presupposes comparatively long duration and totally enclosed surroundings.

3.3 The test cell

The characterized silicone rubbers need to be placed in a test cell, a **circular parallel plates capacitor**, in order to interact with the measurement circuit.

This instrument is now presented and its use in the tests is described. It is noticeable that the same capacitor will be used also for the next experiments (explained in the successive chapters).

The edges of the plates are not sharp, but rounded; in this way the electric field on the borders is not strictly concentrated and it becomes more homogeneous.

The upper plate corresponds to the high voltage electrode (shown in Fig. 3.10-left), whereas the lower plate is divided in two components: the inner part is the low voltage electrode (the gold circle in figure 3.10-right) and the external portion is the guard ring (the silver part in fig. 3.10-right).



Fig. 3.10 The upper plate (left) and the lower plate (right) of the test cell capacitor

The inner part (low voltage electrode) is also said “charge collecting electrode”, because it is connected to the measurement device; a narrow insulating gap separates it from the guard ring (or guard electrode) and the voltage applied to these two components is the same.

With this geometry and voltage arrangement the guard electrode serves two major purposes, although they are directly linked:

- First, it ensures that the electric field lines near the edge of the collecting electrode remain straight, perpendicular to both the low voltage electrode and the high voltage one, so that the gathering volume is accurately defined by the area of the collecting electrode and the electrode separation, as it is represented in Fig. 3.11. If no guard electrode is used, the field lines near the edge of the low voltage electrode will tend to bow out, resulting in a poorly defined charge gathering volume.
- Secondly, maintaining the same voltage on the collecting electrode and the guard ring minimizes the extent of charge leakage outside the collecting volume, because there is no significant driving potential to promote this additional charge collection by the LV electrode.

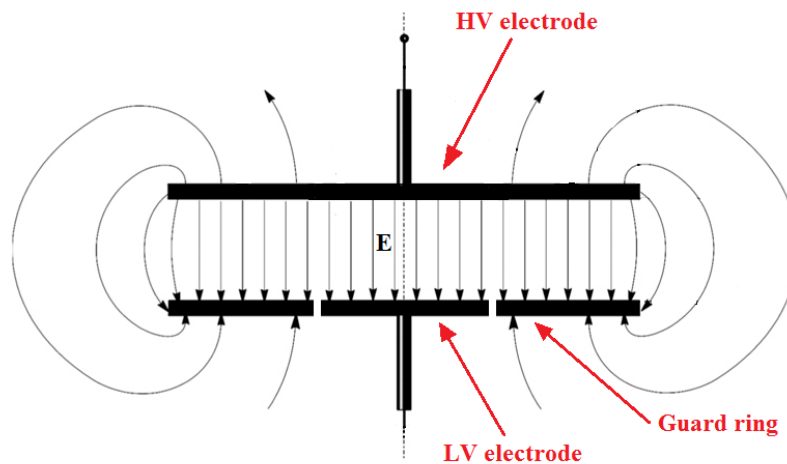


Fig. 3.11 The electric field in the presence of guard ring

To understand this last consideration we consider the example reported in Fig. 3.12, in which the two components are not kept at equal voltage.

During a test with alternating current, the measurement device (connected between the LV electrode and ground) has its own voltage drop (V_{meas}); the presence of parasitic capacitances in air (called C_{par}), between the guard ring (directly connected to ground) and the collecting electrode, warps the measure because additional charges (related to the current i_{par}) interact with the collecting volume.

Hence, it is necessary to supply the guard ring with a voltage source equal to the drop on the measurement device.

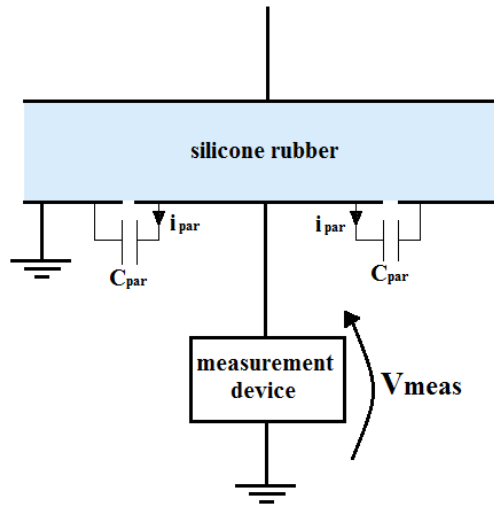


Fig. 3.12 Presence of parasitic capacitances in the test cell

This instrument owns two relevant advantages: the specimen can be heated, developing the test at higher temperature, and the pressure inside the cell can be varied with an additional pump, also inserting a particular gas material.

The lower plate rests on a solid base, the upper plate is mounted on the supports and it is vertically adjustable. The vertical adjustment works via a hydraulic system which, at the same time, can press the electrode against the other one.

The hydraulic system works with an oil pump, that is directly connected to the top of the test cell. The oil is pressed against an internal piston, normally kept in the high position by a spring, and it moves down in the cylinder. The piston is mechanically connected to the high voltage electrode; another spring (also called “membrane”) links up this electrode to the body of the test cell. The relative scheme is illustrated in Fig. 3.13.

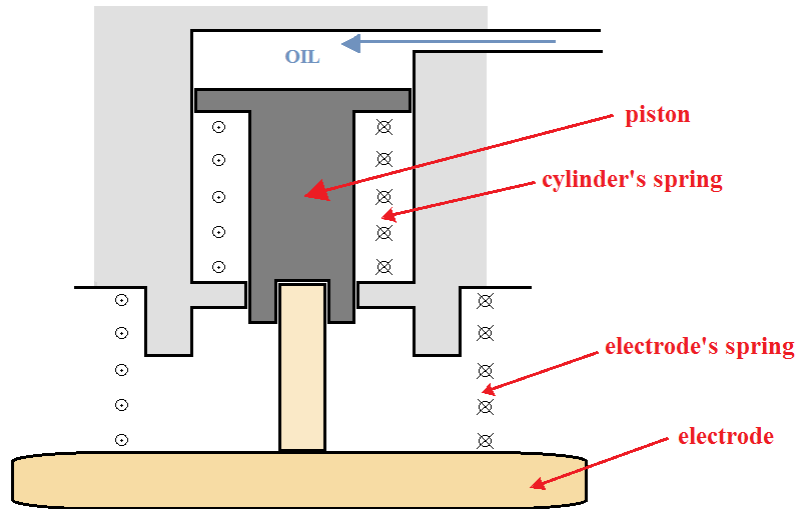


Fig. 3.13 Scheme of the test cell's upper part

When the oil is pumped, its pressure indicated by the gauge (installed on the pump) remains at zero value until the moving electrode reaches the specimen. Only at this point the oil's pressure starts to increase.

An important aspect of these measurements is the pressure which the plates are touching the material surface with. A too low pressure may not be enough for the electrodes to touch the surface well, in an uniform way; but using a too high pressure may deform the specimen and reduce excessively the thickness, especially when working with flexible polymer materials. Harder materials do not expect a so great dependence, because an high pressure warps them less significantly.

The norms do not report a precise value for every kind of material; anyway, the standard ASTM D 257 suggests that adequate contacts have been found with values ranging from 140 to 700 kPa, [20].

The relationship between oil's and electrode's pressures (P_{oil} and P_{sil}) is found, considering that the force exercised from the oil on the piston (F_{piston}) is equal to that one from the electrode to the silicone (F_{sil}):

$$F_{piston} = F_{sil}$$

$$P_{piston} \cdot A_{piston} = P_{sil} \cdot A_{sil}$$

$$P_{sil} = \frac{P_{piston} \cdot A_{piston}}{A_{sil}} = \frac{P_{piston} \cdot (D_{piston})^2}{(D_{sil})^2} = \frac{P_{oil} \cdot (D_{piston})^2}{(D_{sil})^2}$$

Where A_{sil} and A_{piston} indicate the area of silicone and piston, respectively; D_{sil} and D_{piston} are the relative diameters.

The term P_{oil} indicates the pressure of the oil measured by the pump's gauge.

With:

- $D_{sil} = 120$ mm (specimens for the PD test)
- $D_{piston} = 40$ mm
- $P_{oil} = 20 \frac{kg}{cm^2} = 1961.33$ kPa

we obtain:

$$P_{sil} = \frac{P_{oil}}{9} = 217.9 \text{ kPa}$$

The pressure applied is maintained in the lower part of the norm's range, due to the high flexibility of the material used.

A key point is the determination of the accuracy related to the calculated pressure, which will be used in the following chapters.

The caliber used to measure the piston's diameter has a resolution of 0.1 mm, and that one related to the silicone's diameter is 1 mm.

Regarding the oil's pressure, this is indicated by an analogic pressure gauge, having the resolution of $\pm 1 \frac{kg}{cm^2}$.

The errors are considered with an uniform distribution, so the uncertainty (of type *b*) is given by:

$$u = \frac{a}{\sqrt{3}}$$

where *a* indicates the resolution.

In our specific cases, we obtain:

- $u(D_{piston}) = 0.028$ mm
- $u(D_{sil}) = 0.28$ mm
- $u(P_{oil}) = 56$ kPa

These uncertainties are combined in order to obtain that related to the silicone's pressure, applying the following formula:

$$u(P_{sil}) = P_{silicone} \sqrt{\left(\frac{u(P_{oil})}{P_{oil}}\right)^2 + 4\left(\frac{u(D_{sil})}{D_{sil}}\right)^2 + 4\left(\frac{u(D_{piston})}{D_{piston}}\right)^2} = 6.3 \text{ kPa}$$

in which the error propagation theory has been implemented, assuming independent variables.

Finally, we can express the pressure applied to the silicone as:

$$P_{sil} = 217.9 \pm 6.3 \text{ kPa}$$

3.4 The measurement circuit

In this paragraph the electric circuit for partial discharge test is presented (Fig. 3.14), describing the different components.

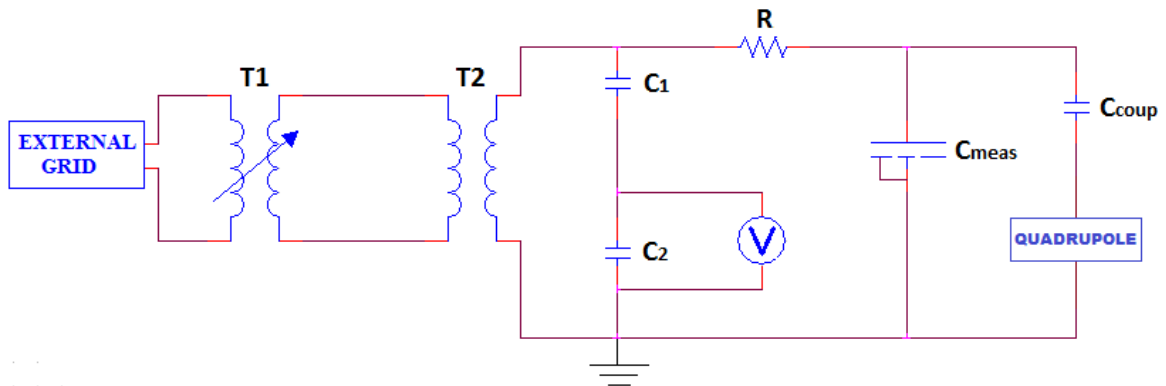


Fig. 3.14 Scheme of the circuit used in the test

The different components of the circuit are:

- **T1**, the adjustable transformer, or regulating transformer, which is not placed in the test room (constituting a Faraday cage). The voltage on the primary winding is fixed at 400 V, while on the secondary winding a tap changer acts, varying the voltage from 0 to 400 V. The tap changer is directly commanded by the control panel, in order to modify the test voltage.

- **T2**, denoting the step-up (or high-voltage) transformer, which is placed in the test room. The secondary voltage varies from 0 to 380 kV, according to the position of the T1's tap changer. The iron core, on which the two windings are wound, is immersed into oil and the external body is made by epoxy resin and paper.
- **C₁** and **C₂**, the two capacitors that, together with the voltmeter connected to **C₂**, constitute the capacitive voltage divider, used for the measuring of the test voltage, applied to the sample. Naming V_{test} as the voltage applied to the sample, the voltage measured by the voltmeter (V_{meas}) is:

$$V_{meas} = V_{test} \cdot \frac{C_1}{C_1 + C_2}$$

In our case, the capacitance C_2 is much higher than the C_1 one.

The two capacitors and the voltmeter compose an unique device.

- **R**, denoting a resistor, with a resistance equal to 6.1 kΩ, used to prevent interferences in the measurement from the voltage divider and from the high voltage capacitor.
- **C_{meas}**, indicating the test cell that contains the specimen. For this specific test it is necessary to short-circuit the guard ring and the collecting electrode, because the measurement device is not connected in series to the low voltage electrode. The test's results are related not only to the collecting electrode, but to the entire test cell.
- **C_{coup}**, the coupling capacitor, having a capacitance of 1 nF. It is used for the measurements of partial discharges in the circuit. In fact, this capacitor constitutes a very fast source of charges (faster than the high voltage transformer), to compensate the effects of partial discharges (movement of charges) in the circuit. Hence, this behavior of the coupling capacitor represents the key point for the partial discharges measurements.
- **Quadrupole**, symbolizing the equipment for the measurements of partial discharges. It is directly connected to the coupling capacitor and it is made by two branches: one for the voltage measurement (at low frequency, 50Hz) and the other for the partial discharges one (at high frequency, in the range of few nanoseconds).

Two cables (for the voltage and for the partial discharges) ensure the attachment between the quadrupole and the MPD, the device that effectively analyzes partial discharges, fed by a low voltage battery (of 12 V). Finally, a PC is connected to the MPD via optical fibers and an USB station (transforming the optical signal in digital one).

The test room containing the circuit is shown in Fig. 3.15

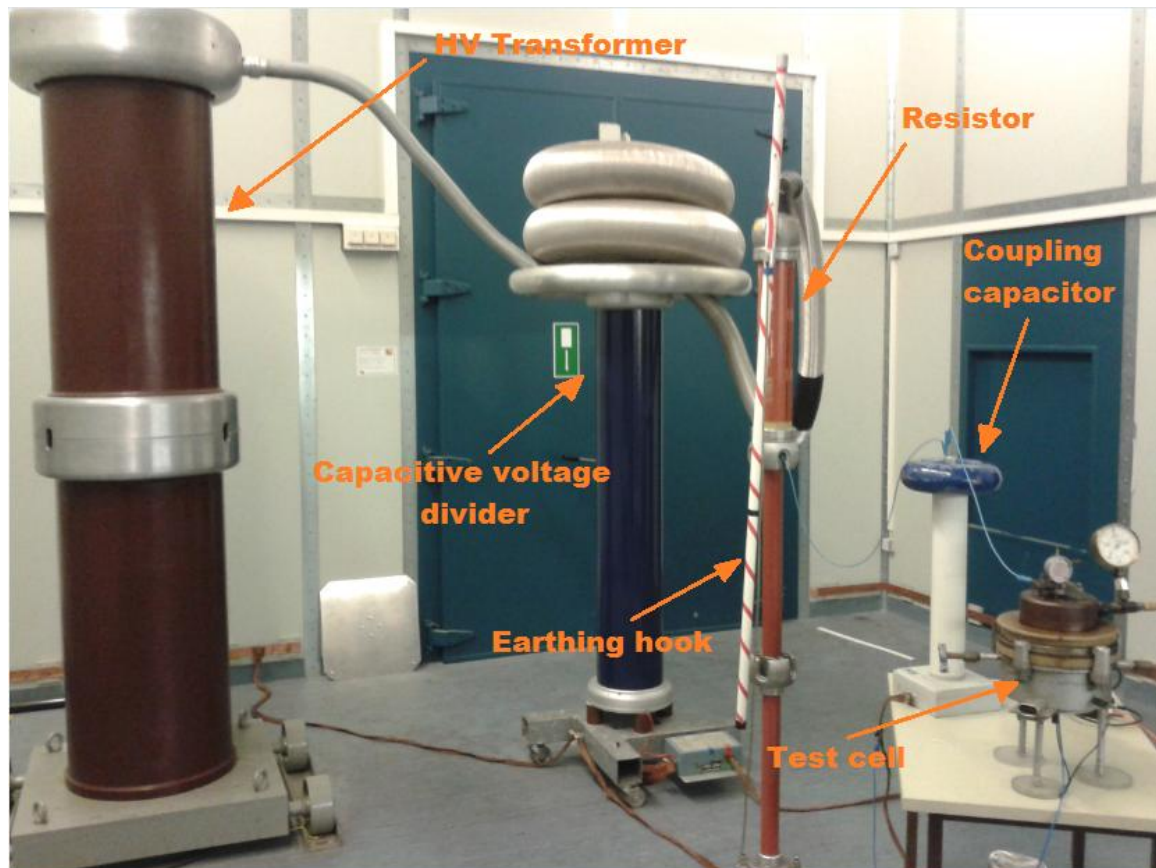


Fig. 3.15 The Test Circuit

In the figure 3.15 the **earthing hook** is also shown: it is a bar constituting a resistance that has a metallic hook on the upper part and a connection to ground in the bottom.

It is used after the test, for the purpose of security, to dissipate the charges that remained on the different components and it is kept connected during the adjustments of the circuit.

The partial discharges are detected by the MPD, connected to the coupling capacitor; hence they can theoretically take place in every part of the circuit.

In practice, all the circuit's devices (capacitors, resistor and transformer) are assured partial discharges free, so the origin is the specimen in the test cell.

3.5 The samples

For this measurements 6 samples are tested. The specimens, which material is the Bluesil ESA 7250, have been produced by two companies: “Polymeric GmbH” and “BAM – Bundesanstalt für Materialforschung und –prüfung”, both in Berlin.

The samples are round, with a diameter of 120 mm and different average thicknesses:

- Specimen A: 1.214 ± 0.012 mm
- Specimen B : 1.656 ± 0.011 mm
- Specimen C : 1.702 ± 0.013 mm
- Specimen D : 1.761 ± 0.012 mm
- Specimen E : 2.050 ± 0.011 mm
- Specimen F : 2.753 ± 0.020 mm

Each specimen’s average thickness is obtained by measuring the thickness in 6 equidistant points and computing their mean value.

Their uncertainties are calculated combining the uncertainty of type *a*, due to the variance of the 6 thickness measurements, and that one of type *b*, due to the resolution of the instrument, Δ , equal to 0.001 mm. The implemented formula is:

$$u_c(d) = \sqrt{\left(\frac{\Delta}{\sqrt{12}}\right)^2 + \frac{s^2(d)}{6}}$$

The error distribution is assumed uniform, and $s^2(d)$ is the unbiased sample variance.

Due to the electrodes’ pressure, the thickness varies; this is an important issue that must be considered.

To determine the real thickness, what we would need is a stress-strain curve of compressive mechanical test; the solution is in the tensile strength test.

In fact, in the initial portion, the stress-strain curves of these two test coincide; so we can consider the Young’s modulus obtained in our mechanical tests for this purpose.

$$\text{strain obtained} = \frac{\text{stress applied}}{\text{Young's modulus of ESA 7250}} = \frac{0.2179 \text{ MPa}}{1.677 \text{ MPa}} = 0.1299$$

Hence, there is a reduction of 12.99% in the specimen thickness.

The implemented formula is:

$$d' = d \left(1 - \frac{P_{sil}}{E} \right)$$

where d and d' are the thicknesses before and after the reduction, respectively; P_{sil} is the pressure applied on the silicone and E is the Young's modulus.

Following the propagation error theory, the uncertainty on the new thickness is:

$$u(d') = \sqrt{\left(\frac{\partial d'}{\partial d}\right)^2 (u_c(d))^2 + \left(\frac{\partial d'}{\partial P_{sil}}\right)^2 (u(P_{sil}))^2 + \left(\frac{\partial d'}{\partial E}\right)^2 (u_{tot}(E))^2}$$

that yields:

$$u(d') = \sqrt{\left(\left(1 - \frac{P_{sil}}{E}\right) \cdot u_c(d)\right)^2 + \left(\frac{d \cdot u(P_{sil})}{E}\right)^2 + \frac{(d \cdot P_{sil} \cdot u_{tot}(E))^2}{E^4}}$$

in which $u_{tot}(E)$ is the uncertainty of the Young's modulus (equal to 0.018 MPa).

The thicknesses of the specimens in the test cell become:

- Specimen A: 1.057 ± 0.012 mm
- Specimen B : 1.440 ± 0.012 mm
- Specimen C : 1.481 ± 0.013 mm
- Specimen D : 1.532 ± 0.012 mm
- Specimen E : 1.783 ± 0.012 mm
- Specimen F : 2.395 ± 0.020 mm

In the middle of the specimen D has been put (intentionally, during the production) an air bubble, in order to detect its influence on the test results.

The Fig. 3.16 shows the sample D, in which the air bubble is visible.

The specimen B presents two big air bubbles in the external part, near the edge, which, being outside the collecting volume, have not influence in the other dielectric tests.

The production follows the same process described for the mechanical test, but in this case the different shape and, eventually, the lower thickness, made it more difficult.



Fig. 3.16 The specimen D of Bluesil ESA 7250

3.6 Development of the test

The goal of the test is to find the minimum inception voltage of partial discharges for every specimen.

The test voltage is increased very slowly (leaving the necessary time at the circuit to respond to the variation) until the first partial discharges arise.

The importance of these inception voltages is related to the successive tests ($\tan\delta$, PDC and volume resistivity); in fact these found values will be the maximum applied voltages in the next measurements; in this way we will be sure that the results will not be affected by partial discharges' distortion.

Moreover, this test is conducted in order to verify if there is a linear dependence between the voltage applied and the thickness of the sample; hence, if the inception voltage can be characterized by the electric field applied.

First of all it is necessary to calibrate the measuring device. A calibrator is utilized, that puts in a defined fixed charge. This value is inserted in the software, that computes the ratio between the measured and the real charge, said "divider factor", used during the whole test.

Initially, a measurement is done without any sample in the test cell. Up to 4.4 kV the partial discharges have not been detected, it means that the circuit and, in particular, the test cell do not interfere the experiment. Hence, all the discharges' occurrences come from the specimen under test.

The first test is entirely conducted at atmospheric pressure.

The results obtained are shown in Tab. 3.1. Considering the material as homogeneous and indicating V_{inc} as the inception voltage, the corresponding electric field has been computed:

$$E_{inc} = \frac{V_{inc}}{d'}$$

In order to express the uncertainty of the calculated E_{inc} , the inception voltage is assumed with a resolution of 0.5 kV (in this case as the operator resolution) with a triangular error distribution, obtaining:

$$u(V_{inc}) = \frac{0.25}{\sqrt{6}} \cong 0.1 \text{ kV}$$

Then, the following formula is applied:

$$u(E_{inc}) = E_{inc} \sqrt{\left(\frac{u(V_{inc})}{V_{inc}}\right)^2 + \left(\frac{u(d')}{d'}\right)^2}$$

Tab. 3.1 Results of the first test (atmospheric pressure)

Specimen	Thickness [mm]	Inception Voltage [kV]	Electric field [V/m]
A	1.057 ± 0.012	2.3 ± 0.1	2.18 ± 0.09
B	1.440 ± 0.012	2.2 ± 0.1	1.53 ± 0.07
C	1.481 ± 0.013	2.6 ± 0.1	1.76 ± 0.07
D	1.532 ± 0.012	2.7 ± 0.1	1.77 ± 0.07
E	1.783 ± 0.012	2.8 ± 0.1	1.57 ± 0.06
F	2.395 ± 0.020	3.0 ± 0.1	1.25 ± 0.05

As it can be noted, the inception of partial discharges does not strictly depend on the electric field, that assumes different values as the thickness changes.

Without considering the sample B (in which the low inception voltage could be attributed to the two big bubbles), we can notice a decrease in the electric field, as the thickness enhances.

One problem could be constituted by the remaining air between the electrodes and the specimens, when the high voltage plate is pressed down by the oil's pressure, causing surface partial discharges.

For this reason, another test is developed, using a pump to remove air and create the vacuum inside the test cell;

This pump is activated when the test cell is strictly closed; after the vacuum creation, the high voltage electrode is decreased until the oil's pressure reaches $20 \frac{\text{kg}}{\text{cm}^2}$.

In this conditions it is important to avoid a possible dielectric breakdown because, according to the Paschen's law, the breakdown voltage is lower at low pressure than at atmospheric pressure (because the pump does not create a perfect vacuum state).

In addition, the applied voltage to Specimen D has been slightly increased (with respect to the inception one), in order to investigate the phenomenon in presence of an air bubble.

The results of the test and the computed electric field are reported in Tab. 3.2.

Tab. 3.2 Results of the second test (use of vacuum pump)

Specimen	Thickness [mm]	Inception Voltage [kV]	Electric field [V/m]
A	1.057 ± 0.012	2.2 ± 0.1	2.08 ± 0.10
B	1.440 ± 0.012	2.8 ± 0.1	1.94 ± 0.07
C	1.481 ± 0.013	2.2 ± 0.1	1.49 ± 0.07
D	1.532 ± 0.012	3.2 ± 0.1	2.10 ± 0.07
E	1.783 ± 0.012	2.3 ± 0.1	1.29 ± 0.06
F	2.395 ± 0.020	3.3 ± 0.1	1.38 ± 0.05

Even if, in general, the inception voltage and the corresponding electric field are slightly increased, there is not absolutely linearity between the voltage and the thickness, as it noted from the values assumed by the electric field (and the specimen B, in this case, presents a quite high value).

The reason can be found in this consideration: as the thickness (and so the volume) enhances, the probability to have microvoids or defects increases; these elements constitute one of the main sources of partial discharges.

The figures in the following pages, from Fig. 3.17 to Fig. 3.23, illustrate the PD pictures of the second test, with vacuum pump, obtained by the software.

In every graph, the occurrence of partial discharge are marked with a blue point (the intensity makes the color change). On the y-axis the value of the charge is represented, whereas the x-axis represents the phase of occurrence.

The full strip in the bottom of the graph indicates the noises detected by the measurement device; a partial discharge (and then the inception voltage) is recognized when this band is exceeded.

The following considerations about the graphs are hypothesis based on the pattern's evaluation and cannot be established with absolute certainty.

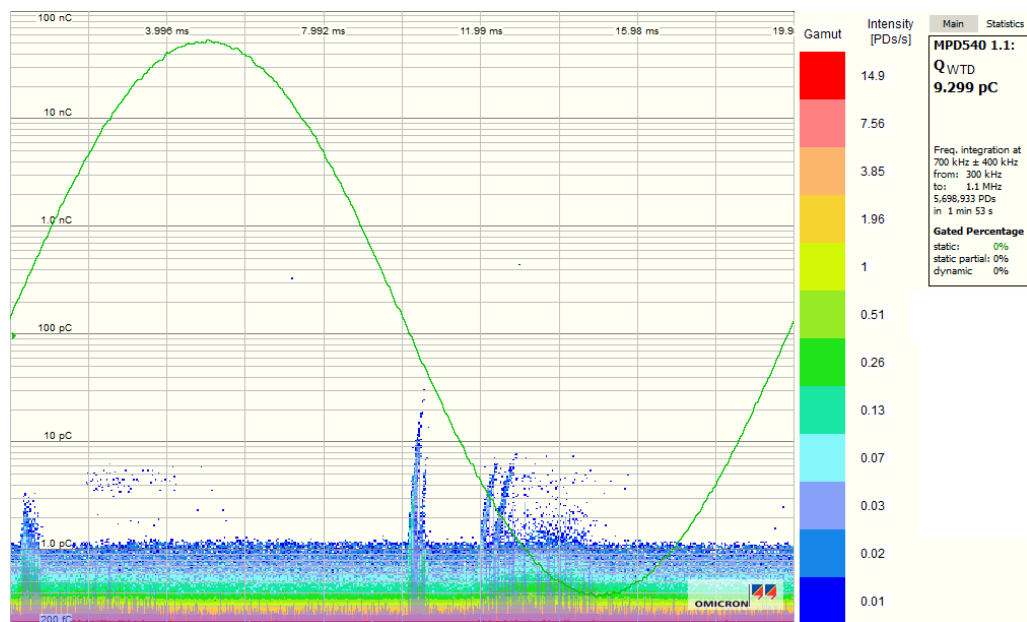


Fig. 3.17 PD inception voltage with vacuum pump: Specimen A

The graph in Fig. 3.17 shows the presence of different phenomena, maybe surface and inner discharges, because the occurrences are more intensive near the crossing point of the voltage wave (at 180°), tending to concentrate in narrow columns, and they do not take place exactly below the voltage peaks.

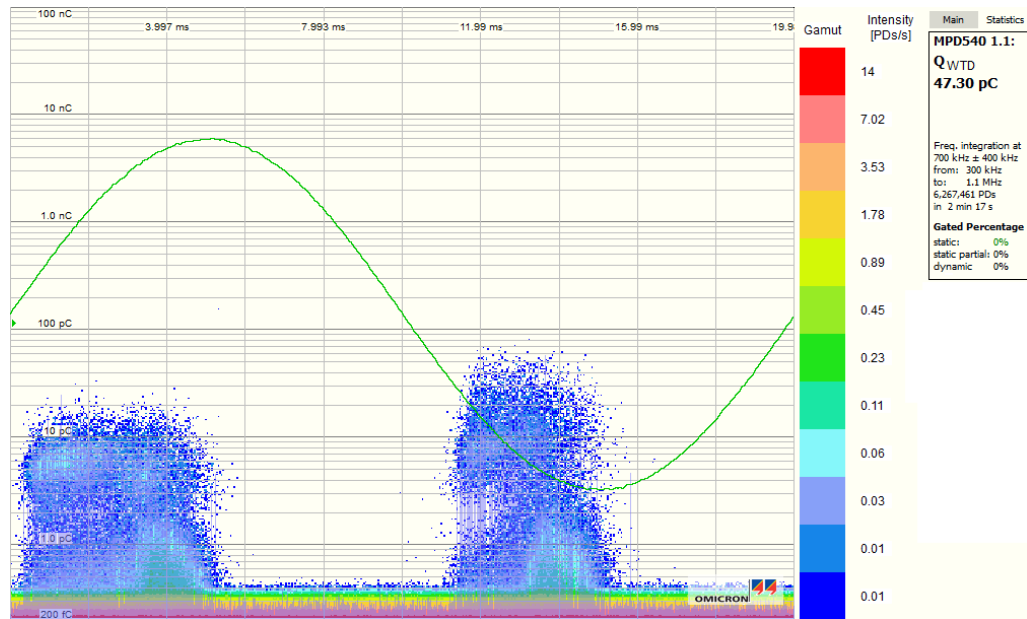


Fig. 3.18 PD inception voltage with vacuum pump: Specimen B

According to Fig. 3.18, in Specimen B the presence of the bubbles is well detected. The partial discharges increase fast and are inclined to concentrate in restricted regions; their similar amplitude suggests the existence of inner discharges.

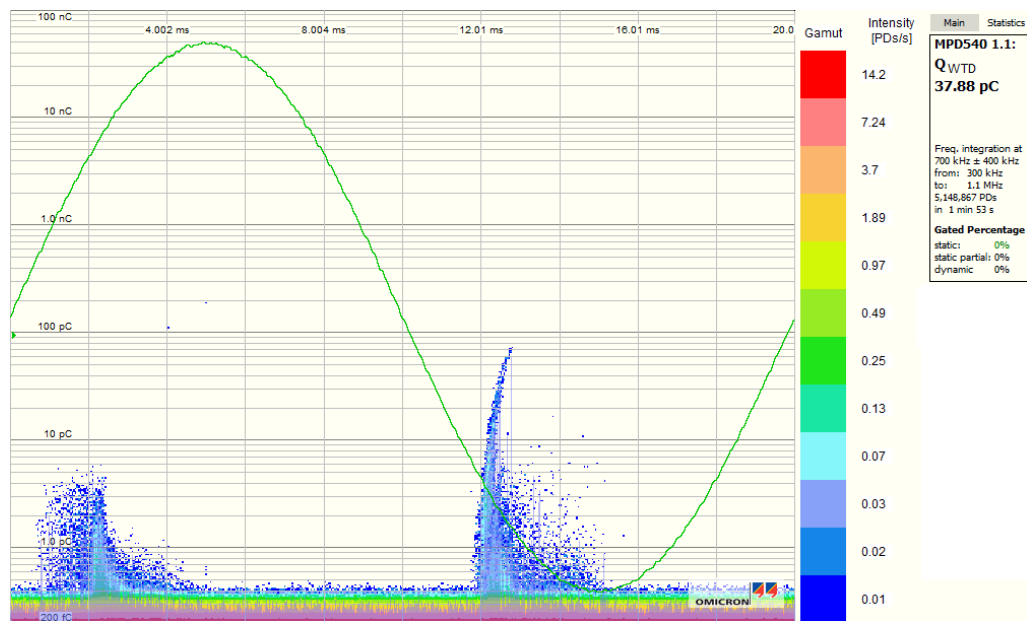


Fig. 3.19 PD inception voltage with vacuum pump: Specimen C

Looking at the picture in Fig. 3.19, the concentration of partial discharges in Specimen C is probably due to surface occurrences, which could take place near the low voltage side, being the discharges more intensive during the negative half-wave.

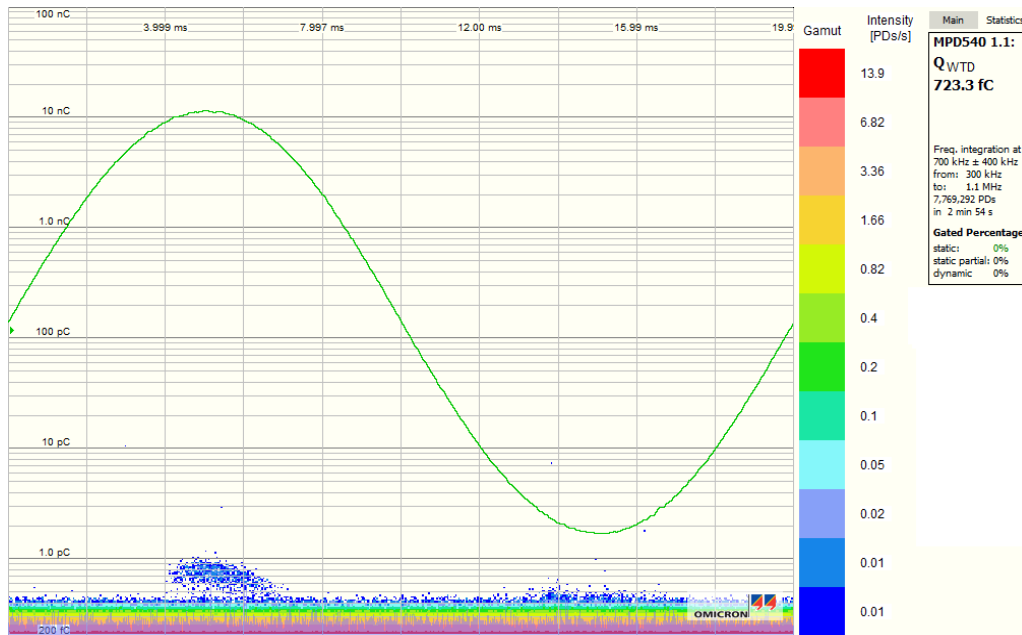


Fig. 3.20 PD inception voltage with vacuum pump: Specimen D

Regarding the Fig. 3.20, the presence of discharges exactly at the voltage peak would suggest the presence of corona effect, but from the next picture (same specimen at higher voltage, Fig. 3.21) it is possible to state that it is only the inception of the void.

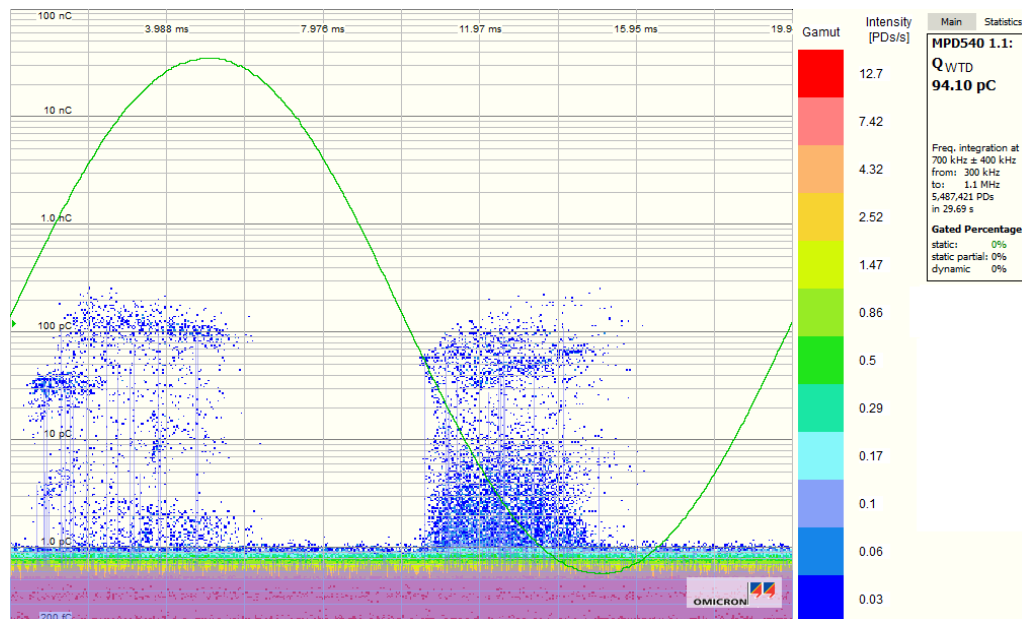


Fig. 3.21 PD test with vacuum pump: Specimen D at higher voltage

Moreover, the Fig. 3.21 shows the increase of voltage applied to the Specimen D. The partial discharges, initially spread, increase fast and tend to concentrate in confined regions of the graph, displaying the influence of air bubble on PD occurrence.

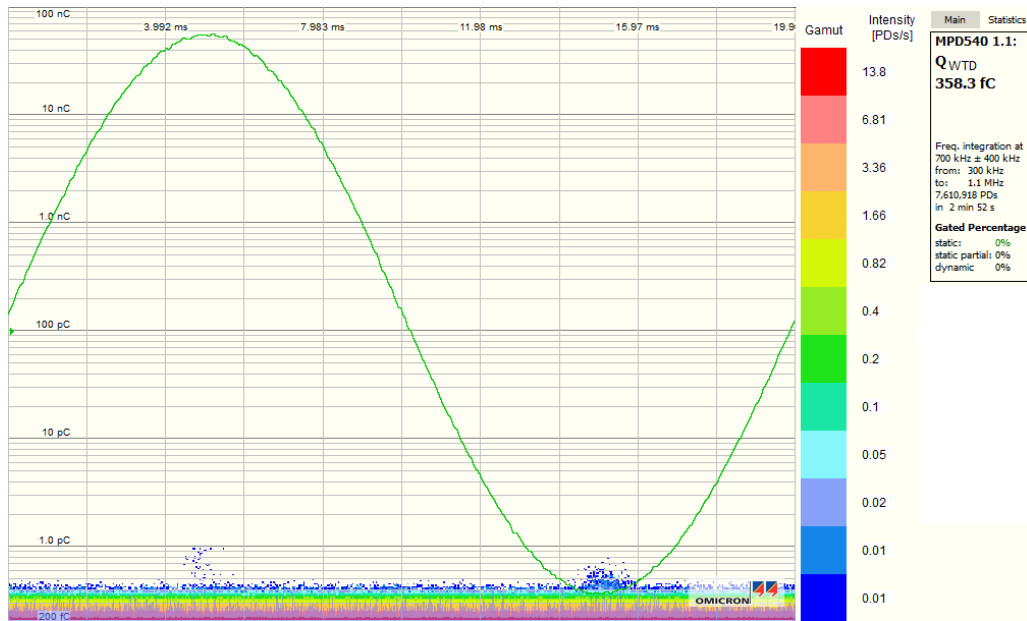


Fig. 3.22 Fig. 3.20 PD inception voltage with vacuum pump: Specimen E

Also in Specimen E (as reported in Fig. 3.22), the PD occurrences exactly at the voltage peaks recommend the presence of corona discharge (maybe on the low potential side, because at the positive voltage peak the discharges have higher and spreader values).

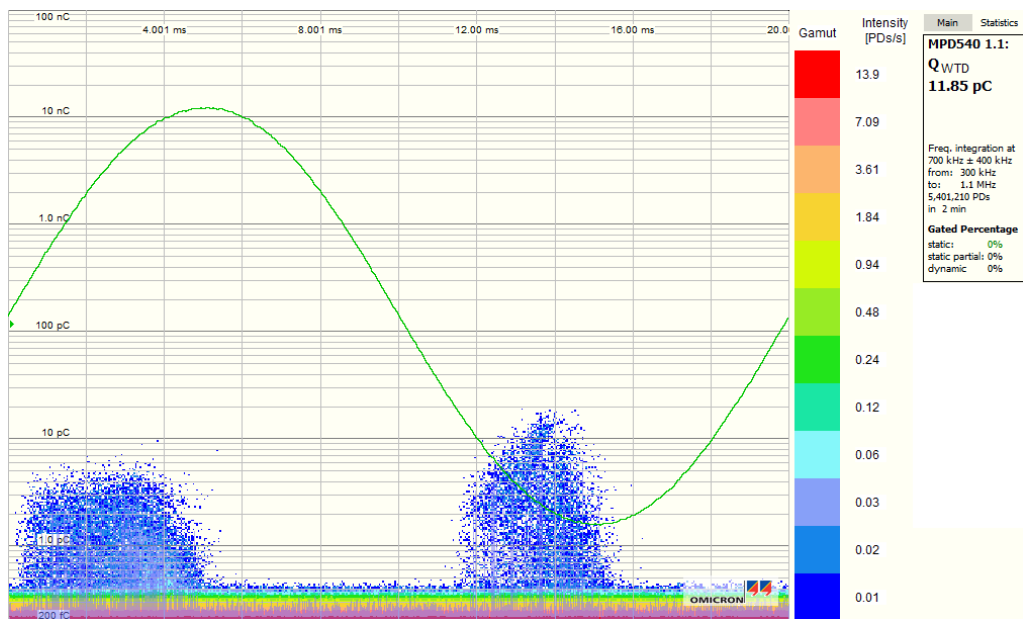


Fig. 3.23 Fig. 3.20 PD inception voltage with vacuum pump: Specimen F

Finally, the pattern presented in Fig. 3.23, shows distributions not symmetric around the voltage peaks and with slightly different height, suggesting the occurrence of surface or inner discharges in Specimen F.

With this presented test, the test cell and its response to different applied voltages have been analyzed; in addition, we could determine the inception voltage of partial discharges for silicone rubber and its behavior on the variation of specimen's thickness.

It constitutes an important basis for the successive dielectric tests, described in the next chapters, that will be carried out at atmospheric pressure (considering the general outcomes of the two PD experiments).

In fact, measuring specimens of similar thickness, the absence of partial discharges up to 2 kV can be ensured. In this way this phenomenon is ruled out from the obtained results.

4 DISSIPATION FACTOR AND ELECTRIC PERMITTIVITY

4.1 Introduction

Dissipation factor and permittivity are fundamental characteristics in typifying dielectric materials, allowing the evaluation of their losses and polarization properties.

They are initially presented in this chapter according to a theoretical point of view; then, after the explanation of the measurement, their determination is carried out for three kinds of silicone rubber, calculating the real and imaginary components of permittivity and analyzing the obtained results.

The tests are conducted assuming as parameters the temperature, the voltage applied and the frequency, that are varied according to three different protocols.

Finally, the influence of an air bubble (injected during the manufacturing into the specimen) on these dielectric properties is reported and compared with the standard results.

4.2 Theory of Dissipation Factor

The static dielectric constant that has been presented in the first chapter is an effect of polarization under DC conditions. When the applied field, or the voltage across a parallel plate capacitor, is a sinusoidal signal, then the polarization of the medium under these AC conditions leads to an AC dielectric constant that is generally different than the static case.

4.2.1 General Aspects

It is considered, as an example, the orientational polarization involving dipolar molecules. The sinusoidally varying field changes magnitude and direction continuously, and it tries to line up the dipoles one way and then the other way and so on.

In the ideal behavior, all the molecules of the material can follow the field completely without any delay.

If the instantaneous induced dipole moment p per molecule can instantaneously follow the field variations (E), then at any instant:

$$p = \alpha_d E$$

In which α_d is the polarizability, that has its expected maximum value from DC conditions.

There are two factors opposing the immediate alignment of the dipoles with the field.

First is that thermal agitation tries to randomize the dipole orientations. Collisions in the gas phase, random jolting from lattice vibrations in the liquid and solid phases, for example, aid the randomization of the dipole orientations.

Second, the molecules rotate in a viscous medium by virtue of their interactions with neighbors, which is particularly strong in the liquid and solid states and means that the dipoles cannot respond instantaneously to the changes in the applied field. If the field changes too rapidly, then the dipoles cannot follow the field and, as a consequence, remain randomly oriented.

At high frequencies, therefore, α_d will be zero as the field cannot induce a dipole moment. At low frequencies, of course, the dipoles can respond rapidly to follow the field and α_d has its maximum value. It is clear that α_d changes from its maximum value to zero as the frequency of the field is increased. We need to find the behavior of α_d as a function of frequency so that we can determine the dielectric constant ϵ_r by the Clausius-Mossotti equation.

Suppose that after a prolonged application, corresponding to dc conditions, the applied field across the dipolar gaseous medium is suddenly decreased from E_0 to E at a time we define as zero, as shown in Fig. 4.1. Decreasing the field, so the induced DC dipole moment per molecule should be smaller and given by $\alpha_d(0)E$ where $\alpha_d(0)$ is α_d at $\omega = 0$, DC conditions. Therefore, the induced dipole moment per molecule has to decrease, or relax, from $\alpha_d(0)E_0$ to $\alpha_d(0)E$.

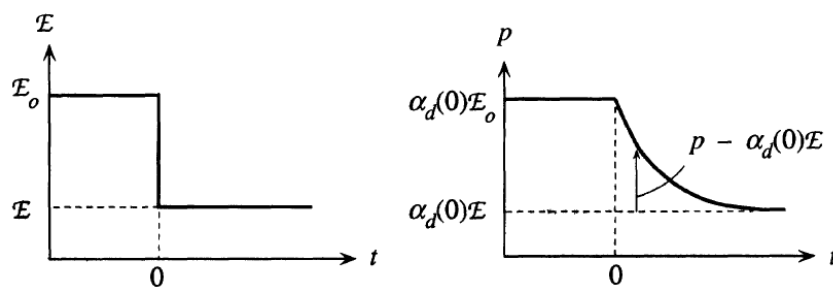


Fig. 4.1 Sudden change of electric field and decrease of induced dipole moment

In a gas medium the molecules would be moving around randomly and their collisions with each other and the walls of the container randomize the induced dipole per molecule. Thus the decrease, or the relaxation process, in the induced dipole moment is achieved by random collisions. Assuming that τ is the average time, called the relaxation time, between molecular collisions, then this is the mean time it takes per molecule to randomize the induced dipole moment.

If p is the instantaneous induced dipole moment, then $p - \alpha_d(0)E$ is the excess dipole moment, which must eventually disappear to zero through random collisions as $t \rightarrow \infty$.

It would take an average τ seconds to eliminate the excess dipole moment $p - \alpha_d(0)E$.

The derivative of the induced dipole moment, thus its rate of change, is then:

$$\frac{dp}{dt} = -\frac{p - \alpha_d(0)E}{\tau}$$

where the negative sign represents a decrease.

This last equation can be used to obtain the dipolar polarizability under AC conditions.

Considering an AC electric field in exponential representation:

$$E = E_0 e^{j\omega t}$$

Hence, it is obtained:

$$\frac{dp}{dt} = -\frac{p}{\tau} + \frac{\alpha_d(0)}{\tau} E_0 e^{j\omega t}$$

Solving this equation the induced dipole moment is:

$$p = \alpha_d(\omega) E_0 e^{j\omega t}$$

Where $\alpha_d(\omega)$ is given by:

$$\alpha_d(\omega) = \frac{\alpha_d(0)}{1 + j\omega\tau}$$

and represents the orientational polarizability under AC field conditions.

Polarizability $\alpha_d(\omega)$ is a complex number, indicating that p and E are out of phase.

At low frequencies, $\omega\tau \ll 1$, $\alpha_d(\omega)$ is nearly $\alpha_d(0)$, and p is in phase with E .

The rate of relaxation $1/\tau$ is much faster than the frequency of the field or the rate at which the polarization is being changed; p then closely follows E .

At very high frequencies, $\omega t \gg 1$, the rate of relaxation $1/\tau$ is much slower than the frequency of the field and p can no longer follow the variations in the field.

Recalling the following equation, with N as number of molecules in the volume:

$$\epsilon_r = 1 + \frac{N\alpha_d(\omega)}{\epsilon_0}$$

the dielectric constant is determined:

$$\epsilon_r = \epsilon'_r - j\epsilon''_r$$

where ϵ'_r is the real part and ϵ''_r is the imaginary part, both being frequency dependent, shown in Fig. 4.2.

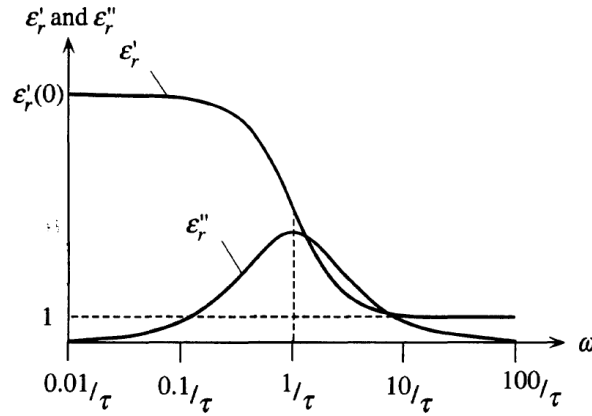


Fig. 4.2 Representation of the dielectric constant's components

The real part ϵ'_r decreases from its maximum value $\epsilon'_r(0)$, corresponding to $\alpha_d(0)$, to 1 at high frequencies when $\alpha_d \rightarrow 0$.

The imaginary part ϵ''_r is zero at low and high frequencies but peaks when $\omega t = 1$.

The real part ϵ'_r represents the relative permittivity that we would use in calculating the capacitance, as for example in $C = \epsilon_0 \epsilon'_r \frac{S}{d}$; it is related to an ideal, lossless, capacitor (in which the current is shifted 90° in advance with respect to the voltage across its terminals) that behaves only the reactive power.

The imaginary part ϵ''_r represents the energy lost in the dielectric medium due to the collisions of the dipoles in orienting according to the actual electric field, the polarization losses. It is related only to active power.

The active power, due to polarization effect, dissipated in the dielectric medium peaks when $\omega = 1/\tau$. The rate of energy storage by the field is determined by ω whereas the rate

of energy transfer to molecular collisions is determined by $1/\tau$. When $\omega = 1/\tau$, the two processes, energy storage by the field and energy transfer to random collisions, are then occurring at the same rate, and hence energy is being transferred to heat most efficiently (reported in Fig. 4.2). The peak in ϵ_r'' versus ω is called a relaxation peak, which is at a frequency when the dipole relaxations are at the right rate for maximum power dissipation. This process is known as dielectric resonance.

Although we considered only orientational polarization, in general a dielectric medium will also exhibit other polarization mechanisms and certainly electronic polarization since there will always be electron clouds around individual atoms, or electrons in covalent bonds.

If we were to consider the ionic polarizability in ionic solids, we would also find a ionic polarizability α_i to be frequency dependent and a complex number.

In this case, lattice vibrations in the crystal, typically at frequencies ω_i in the infrared region of the electromagnetic spectrum, will dissipate the energy stored in the induced dipole moments just as energy was dissipated by molecular collisions in the gaseous dipolar medium. Thus, the energy loss will be greatest when the frequency of the polarizing field is the same as the lattice vibration frequency, $\omega = \omega_i$, which tries to randomize the polarization.

We can represent the general features of the frequency dependence of the real and imaginary parts of the dielectric constant as in Figure 4.3. Although the figure shows distinctive peaks in ϵ_r'' and transition features in ϵ_r' , in reality these peaks and various features are broader. First, there is no single well-defined lattice vibration frequency but instead an allowed range of frequencies, just as in solids where there is an allowed range of energies for the electron. Moreover, the polarization effects depend on the crystal orientation.

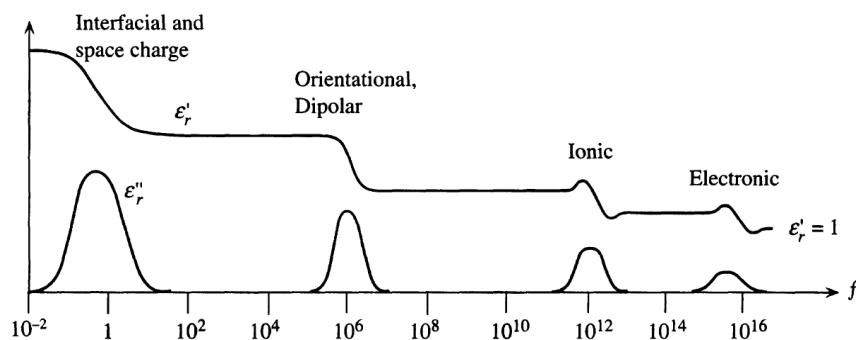


Fig. 4.3 Frequency dependence of permittivity with many polarization mechanism

4.2.2 The dissipation factor

Hence, applying a certain voltage V to a real capacitor the resulting current does not lead it of exactly 90° , but of a lower value: $90^\circ - \delta$, equal to the power factor φ . The current can be divided into two components: one in phase with the voltage, I_δ , and the other one in advance of 90° , I_C .

We define the relative magnitude of I_δ with respect to I_C through a quantity, $\tan\delta$, called the loss tangent (or loss factor, or dissipation factor), as:

$$\tan\delta = \frac{I_\delta}{I_C}$$

I_C is the current that would flow in an ideal lossless capacitor, and thus related to the real permittivity ε_r' ; I_δ is the current associated to the polarization losses, through the imaginary permittivity ε_r'' , and to the intrinsic conductivity of the material, σ , usually very tiny in an insulating material.

Multiplying the currents by the applied voltage, we obtain the real and imaginary power of the real capacitor:

$$P_\delta = VI_\delta \qquad Q_C = VI_C$$

Hence, it follows:

$$\tan\delta = \frac{P_\delta}{Q_C}$$

Considering these last conclusions, at any given frequency a capacitor with losses can be represented either by capacitance C_S and resistance R_S in series, or by capacitance C_P and resistance R_P in parallel.

For the equivalent parallel circuit, it yields:

$$\tan\delta = \frac{P_\delta}{Q_C} = \frac{\frac{V^2}{R_P}}{\omega C_P V^2} = \frac{1}{\omega C_P R_P}$$

And for the series circuit:

$$\tan\delta = \frac{P_\delta}{Q_C} = \frac{R_S I^2}{\frac{I^2}{\omega C_S}} = \omega C_S R_S$$

It should be pointed out that the agreement between these two models is reached only at a certain frequency, as illustrated in Fig. 4.4.

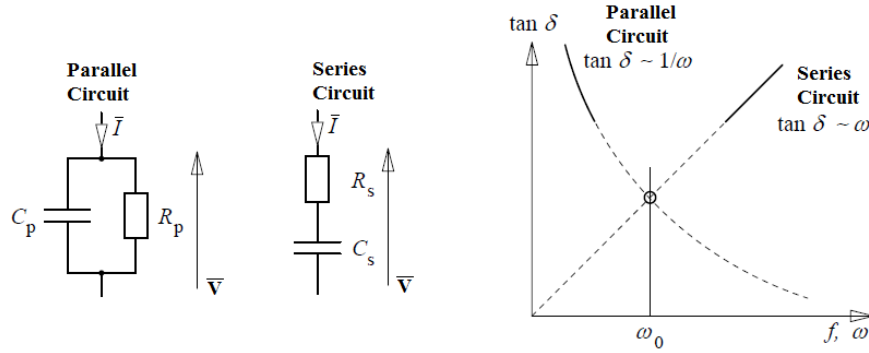


Fig. 4.4 Series and parallel equivalent circuits

Between the series and parallel components, the following relations hold:

$$C_P = \frac{C_S}{1 + \tan^2 \delta} \quad R_P = \frac{1 + \tan^2 \delta}{\tan^2 \delta} R_S \quad \omega \cdot C_S \cdot R_S = \frac{1}{\omega \cdot C_P \cdot R_P}$$

As said, the loss factor $\tan \delta$ represents the influence of polarization and conductive losses on the capacitive character.

For the sake of strictness, another kind of loss that influences the dissipation factor is constituted by the partial discharges; in our analysis, according to the conclusions of the third chapter, we will neglect this component.

Thus, the following equations will be considered:

$$\tan \delta = \tan \delta_L + \tan \delta_{pol}$$

In which $\tan \delta_L$ represents the conductive losses component and $\tan \delta_{pol}$ the polarization one.

In the same way, the total current density is the sum of the conductive current density:

$$\bar{J}_C = \sigma \bar{E}$$

and the displacement one:

$$j\omega \bar{D} = j\omega \epsilon_0 \epsilon_r \bar{E} = \omega \epsilon_0 \epsilon_r'' \bar{E} + j\omega \epsilon_0 \epsilon_r' \bar{E}$$

As reported in the complex plane of Fig. 4.5.

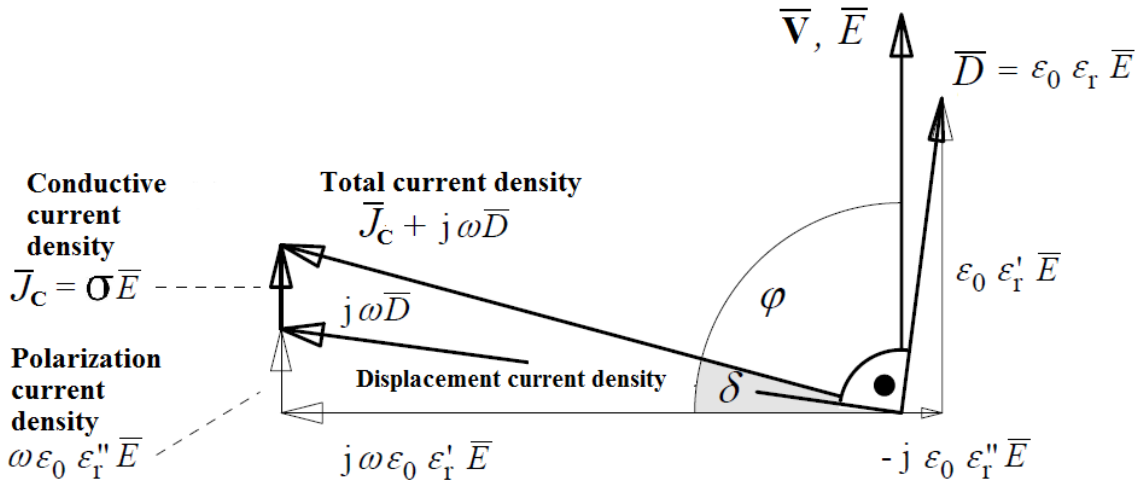


Fig. 4.5 Current densities in the complex plane

Then, the dissipation factor can be expressed as:

$$\tan \delta = \frac{\sigma + \omega \epsilon_0 \epsilon_r''}{\omega \epsilon_0 \epsilon_r'}$$

In which the two contributions are:

$$\tan \delta_L = \frac{\sigma}{\omega \epsilon_0 \epsilon_r'}$$

$$\tan \delta_{Pol} = \frac{\epsilon_r''}{\epsilon_r'}$$

4.2.3 Debye equations and Cole-Cole Plots

Consider now a dipolar dielectric in which there are both orientational and electronic polarizations, α_d and α_e , respectively, contributing to the overall polarizability, [7].

Electronic polarization α_e will be independent of frequency over the typical frequency range of operation of a dipolar dielectric, well below optical frequencies.

At high frequencies, orientational polarization will be too sluggish to respond, $\alpha_d = 0$, and the ϵ_r will be $\epsilon_{r\infty}$, (the subscript 'infinity', simply means high frequencies where orientational polarization is negligible). The dielectric constant and polarizabilities are generally related through:

$$\epsilon_r = 1 + \frac{N}{\epsilon_0} \alpha_e + \frac{N}{\epsilon_0} \alpha_d(\omega) = \epsilon_{r\infty} + \frac{N}{\epsilon_0} \alpha_d(\omega)$$

where we have combined 1 and α_e terms to represent the high frequency ϵ_r as $\epsilon_{r\infty}$.

Further $\frac{N}{\epsilon_0} \alpha_d(0)$ determines the contribution of orientational polarization to the static dielectric constant ϵ_{rdc} , so that $\frac{N}{\epsilon_0} \cdot \alpha_d(0)$ is simply $(\epsilon_{rdc} - \epsilon_{r\infty})$.

Substituting for the frequency dependence of $\alpha_d(\omega)$ and writing ϵ_r in terms of real and imaginary parts, we obtain:

$$\epsilon_r' - j\epsilon_r'' = \epsilon_{r\infty} + \frac{N}{\epsilon_0} \cdot \frac{\alpha_d(0)}{1 + j\omega\tau} = \epsilon_{r\infty} + \frac{\epsilon_{rdc} - \epsilon_{r\infty}}{1 + j\omega\tau}$$

We can eliminate the complex denominator and equate real and imaginary parts to obtain what are known as **Debye equations**:

$$\epsilon_r' = \epsilon_{r\infty} + \frac{\epsilon_{rdc} - \epsilon_{r\infty}}{1 + (\omega\tau)^2}$$

And

$$\epsilon_r'' = \frac{(\epsilon_{rdc} - \epsilon_{r\infty}) \cdot \omega\tau}{1 + (\omega\tau)^2}$$

The imaginary part ϵ_r'' that represents the dielectric loss exhibits a peak at $\omega = \frac{1}{\tau}$ which is called Debye loss peak.

Many dipolar gases and some liquids with dipolar molecules exhibit this type of behavior. In the case of solids the peak is typically much broader because we cannot represent the losses in terms of just one single well-defined relaxation time τ ; the relaxation in the solid is usually represented by a distribution of relaxation times.

In dielectric studies of materials it is quite common to find a plot of the imaginary part (ϵ_r'') versus the real part (ϵ_r') as a function of frequency ω .

Such plots are called **Cole-Cole plots** after their originators. The Debye equations obviously provide the necessary values for ϵ_r' and ϵ_r'' to be plotted for the present simple dipolar relaxation mechanism that has only a single relaxation time τ .

In fact, by simply putting in $\tau = 1$ second, we can calculate and plot ϵ_r'' versus ϵ_r' for $\omega = 0$ (DC) to $\omega \rightarrow \infty$ as show in Figure 4.6. The result is a semicircle.

While for certain substances, such as gases and some liquids, the Cole-Cole plots do indeed generate a semicircle, for many dielectrics, the curve is typically flattened and asymmetric, and not a semicircle.

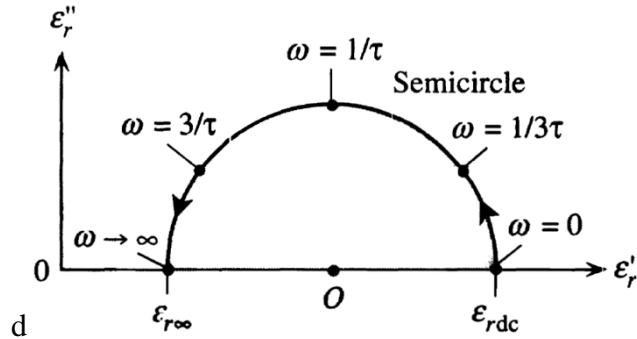


Fig. 4.6 The Cole Cole plot for a single relaxation time

The Debye equations lead to a particular RC circuit representation of a dielectric material that is quite useful. Suppose that we have a resistance R_S in series with a capacitor C_S , both of which are in parallel with the capacitor C_∞ as in Figure 4.7 a. The equivalent admittance of this circuit corresponds to the Debye equations. In parallel is present a resistance R_∞ , that takes into account the non-zero conductivity of the dielectric material.

If A is the area and d is the thickness of a parallel plate capacitor with a dipolar dielectric, then:

$$C_\infty = \epsilon_0 \epsilon_r \frac{A}{d} \quad R_\infty = \frac{d}{\sigma A} \quad C_S = \frac{\epsilon_0 (\epsilon_{rdc} - \epsilon_\infty) A}{d} \quad R_S = \frac{\tau}{C_S}$$

Notice that, in this circuit model, R_S , C_S , R_∞ and C_∞ do not depend on the frequency, which is only true for an ideal Debye dielectric, so with a single relaxation time τ .

For a material with many relaxation times, additional branches are added in parallel, as reported in Figure 4.7 b.

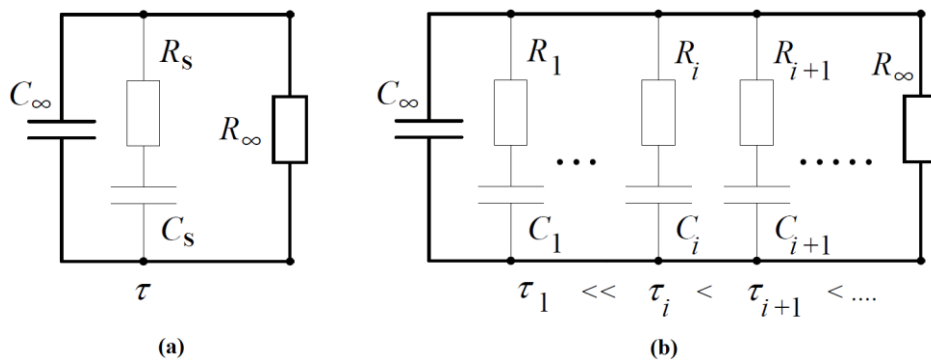


Fig. 4.7 Equivalent circuits for a material according to Debye equations with a single relaxation time (a) and with many ones (b).

4.3 The Measurement Circuit

The tests have been conducted in laboratories of the Technische Universität in Berlin.

The basic idea is the comparison between an ideal capacitor and the test one. In fact, the ideal capacitor is considered without losses, and hence its impedance (Z_{ref}) coincides with the imaginary part, constituted by the capacitive reactance (X_{Cref}), neglecting the ohmic component.

$$Z_{ref} = j \cdot X_{Cref} = j \cdot \frac{1}{\omega \cdot C_{ref}}$$

Applying a certain voltage \bar{V} to this capacitor the corresponding current across its terminals (\bar{I}_{ref}) will be exactly shifted by 90° in advance.

Considering the test capacitor, we deal with losses, represented by a resistance (R_X); so its impedance (Z_X) is made by a real and an imaginary part (with capacitive reactance X_{CX}).

$$Z_X = R_X + j \cdot X_{CX} = R_X + j \cdot \frac{1}{\omega C_X}$$

Consequently, the corresponding current (\bar{I}_X) is shifted in advance with respect to the applied voltage by an angle lower than 90° , complement of δ , obtaining two components: the capacitive current (\bar{I}_{XC}) and the resistive one (\bar{I}_{XR}).

The Figure 4.8 shows these considered quantities in the complex plane.

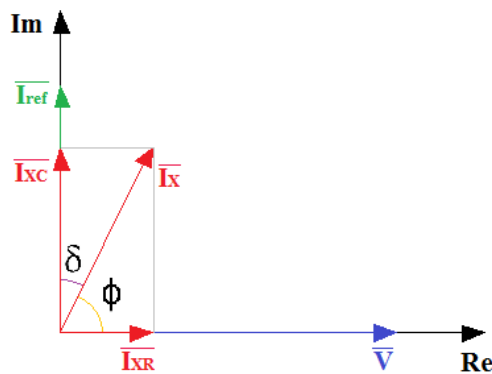


Fig. 4.8 Electric quantities in the complex plane

Since the angle δ represents the phase difference between $\overline{I_X}$ and $\overline{I_{XC}}$, considering that the currents $\overline{I_{ref}}$ and $\overline{I_{XC}}$ have the same phase it is possible to compute δ (from which the dissipation factor $\tan\delta$ is acquired) as the phase shift between $\overline{I_X}$ and $\overline{I_{ref}}$.

The Figure 4.9 displays the considered quantities in time domain.

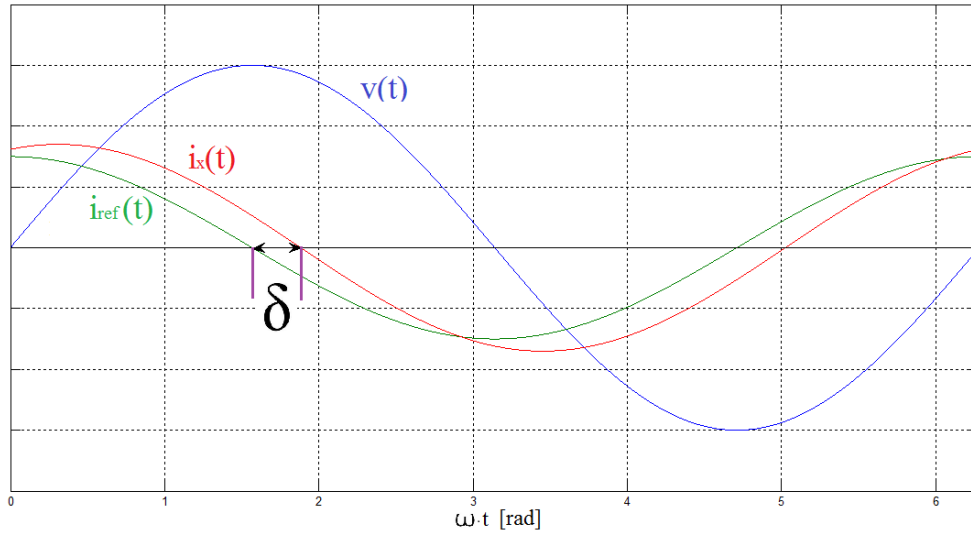


Fig. 4.9 Electric quantities in time domain

Hence, the measurement circuit operates in order to determine the instants of zero crossing related to the currents in the two capacitors. Its scheme is represented in Figure 4.10.

The system computes also the currents amplitudes that, together with the $\tan\delta$ value, allow to determine the capacitance and the resistance of the equivalent circuit of the test capacitor.

In particular, for the parallel equivalent circuit, the following equations are implemented:

$$\tan\delta = \frac{I_{XR}}{I_{XC}} = \frac{1}{\omega C_X R_X} \quad I_{XR} = \frac{V}{R_X} \quad I_{XC} = j\omega C_X V$$

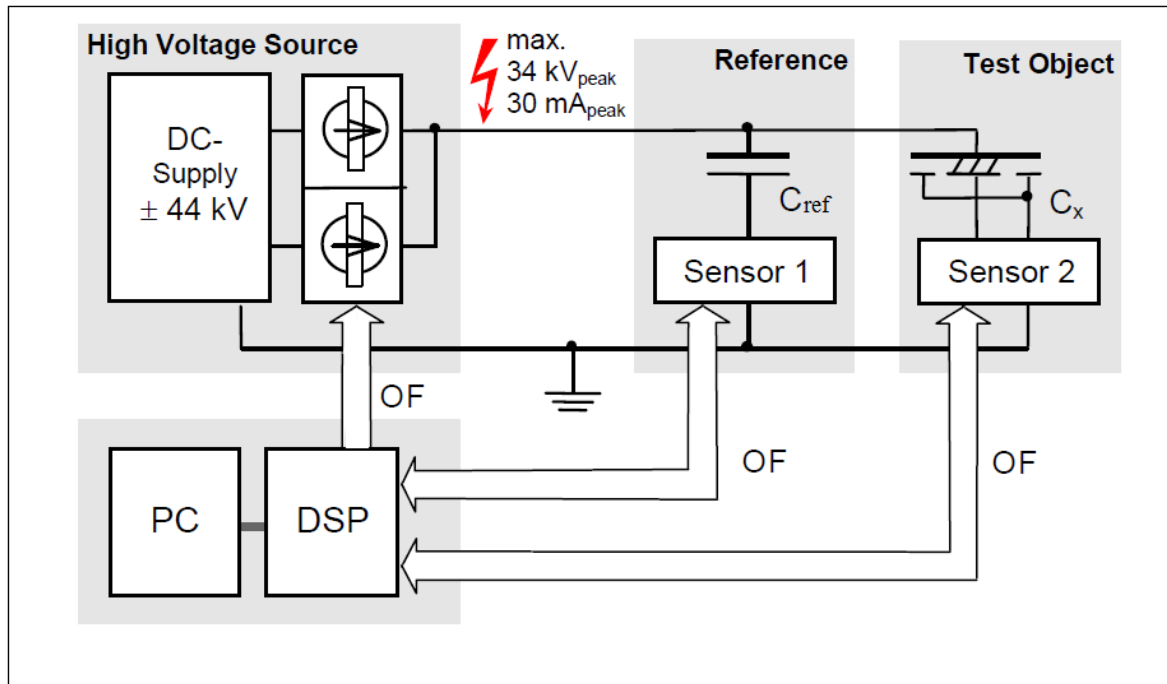


Fig. 4.10 Scheme of the circuit for dissipation factor and permittivity test

The different components of the circuit are:

- The **High Voltage Source**, in turn it is constituted by two high voltage transformers, a Graetz bridge rectifier (full-wave rectification with 4 diodes) and a bipolar high voltage inverter, realized with many transistors in cascade. The high voltage inverter is controlled digitally via two floating power sources. The maximum output voltage and current are $24 \text{ kV}_{\text{eff}}$ and $20 \text{ mA}_{\text{eff}}$, respectively; in a frequency range from 1 mHz to 1 kHz. This power supply is properly a current source, so it requires the values of the circuit's impedances in order to supply the desired potential. It is connected between the high voltage side of the two capacitors and ground, and the adjustment is operated by the PC via the optical fiber.
- The **Reference Capacitor**, produced by "Tettex AG Instruments" and insulated with compressed gas (SF6 at 4,5 bar). It presents a dissipation factor, $\tan\delta$, lower than $1 \cdot 10^{-5}$.
- The **Test Object**, corresponding to the test cell presented in the paragraph 3.3, linked in parallel with the reference capacitor. During this test, the guard ring is not

short-circuited with the inner electrode, but directly connected to ground; in this way, only the current from the measuring electrode is considered in the outcomes.

- A pair of coupled **Sensors**, connected in series to each capacitor. In their analog part, capacitive voltage dividers are present and followed by an operational amplifier integrator (with adjustable capacitance); then the measurement signal is digitized by a 16-bit A/D converter with a sampling rate of 64 kHz.
- The **DSP** receives the digital data from both sensors via optical fibers; it computes the Fast Fourier Transform, obtaining the current signals in frequency domain.
- Finally, the **PC** acquires the data from the DSP and the results are computed. It is controlled by the software “LDV5”, with which the specific instructions are transmitted to the generator.

Furthermore, a resistive voltage divider is present on the Graetz bridge and the high voltage circuit is integrated with resistances and capacitances due to filtering function and to discharge the potential after the test.

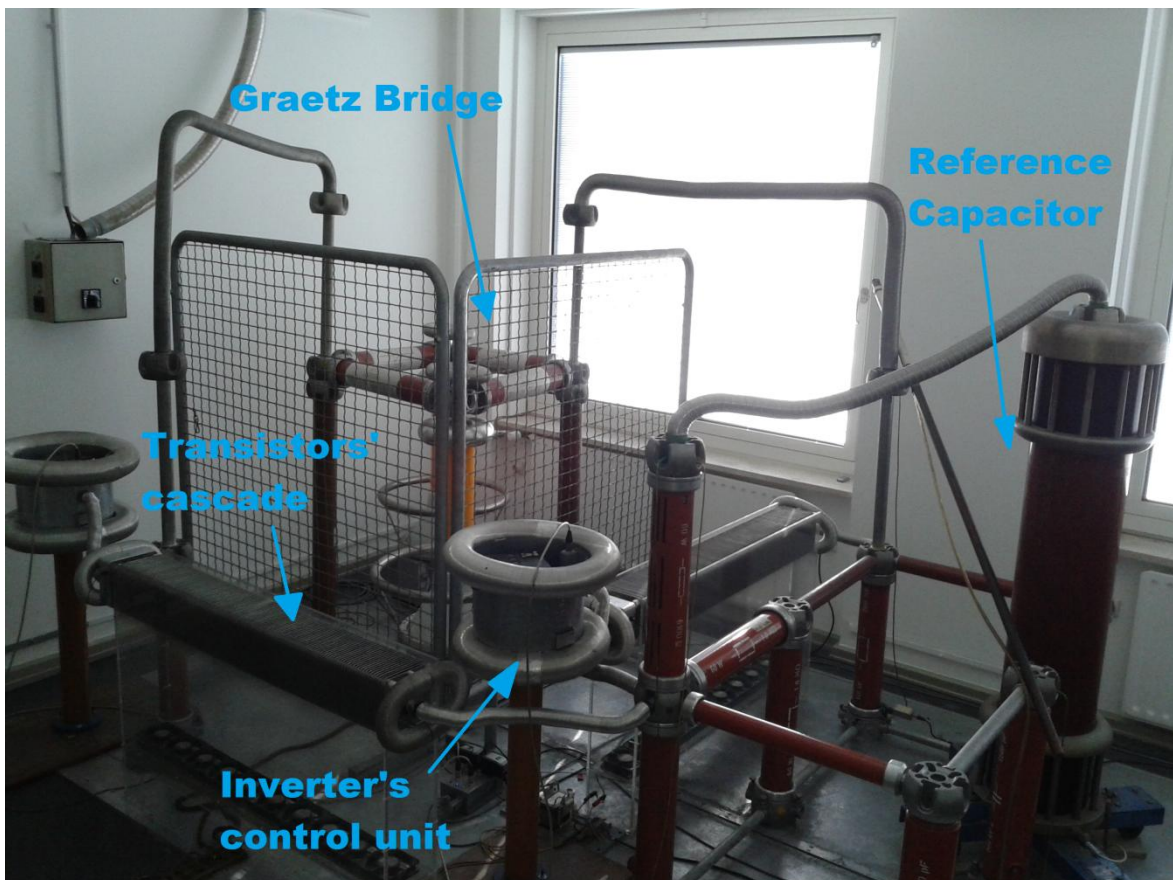


Fig. 4.11 Circuit's fragment of dissipation factor and permittivity test

4.4 Development of the test

At the beginning of each measurement is necessary to supply to the generator the value of the circuit's impedance, in particular the stray capacitance (corresponding to the unavoidable and unwanted capacitance between the circuit components simply due to their proximity); in this way, the real voltage applied to the capacitors is always the desired one. Anyway, because of the guard electrode, the collected current is only due to the inner impedance of the sample.

For each material, three specimens were tested and everyone experienced different procedures. The analysis of this test focused on the determination of the dissipation factor and permittivity in function of voltage applied, frequency and temperature.

Then, for each specimen one of this parameters was kept constant, varying the remaining two.

- The first protocol is at **Constant Frequency**, kept at 50 Hz. The temperature is progressively increased from room temperature (25 °C) up to 100 °C; in this range five tests are carried out. Then, after a break of 30 minutes, the temperature is decreased and the measurements are made at the same steps.

In this way a temperature cycle is realized (that must be concluded in one day), investigating if this could affect the dielectric properties.

At each temperature, the measurement is realized at four different voltage levels: 500 V, 1 kV, 1.5 kV and 2 kV.

- The second protocol is at **Constant Temperature**, that is maintained at room temperature (25 °C). A frequency ramp is realized, from 0.1 Hz to 1 kHz, with nine steps; at each one, a measurement is realized at the same voltage levels: 500 V, 1 kV, 1.5 kV and 2 kV.

The generator cannot provide a sinusoidal waveform with high voltage level at the high frequencies; in these cases it was not possible to get the results.

- Finally, the last protocol is conducted at **Constant Voltage**, of 500 V. Three temperatures have been investigated: room temperature (25°C), 50 °C and 100 °C; at each one the frequency ramp is realized, following the same steps of the second protocol.

The test temperature is controlled by an external device, the temperature controller, electrically connecting it to the lower part of the test cell, where the heat is developed by a resistance. The controller maintains the temperature at the desired value, making use of a thermocouple.

When the set temperature is reached, to wait for 40 minutes in this condition is advisable; in this way the whole test cell remains thermally stable.

Moreover, it was experienced that the temperature controller must be electrically disconnected during the measurement, because it interferes with the test circuit at 50 Hz, producing distorted results.

From the software, these outcomes are obtained:

- The **dissipation factor**, $\tan\delta$, with:

$$u(\tan\delta) = 1\% \cdot \tan\delta + 10^{-5}$$

- The **capacitance of the equivalent parallel circuit**, C_X , having the uncertainty:

$$u(C_X) = 0.1\% \cdot C_X + 1 \text{ pF}$$

In addition, other quantities are computed and reported:

- The **real part of permittivity**, ε'_r , acquired from the definition of capacitance (being the only part of permittivity that contributes to it) as:

$$\varepsilon'_r = \frac{C_X d'}{\varepsilon_0 A}$$

considering A as the area of the inner electrode, $7853.9 \pm 4.5 \text{ mm}^2$ (having measured the diameter with an instrument of 0.1 mm in resolution), and d' as the reduced thickness.

Its uncertainty is calculated with the following formula:

$$u(\varepsilon'_r) = \varepsilon'_r \cdot \sqrt{\left(\frac{u(C_X)}{C_X}\right)^2 + \left(\frac{u(A)}{A}\right)^2 + \left(\frac{u(d')}{d'}\right)^2}$$

- The **conductive losses component of the dissipation factor**, $\tan\delta_L$, starting from the expression reported in the paragraph 4.2.2:

$$\tan\delta_L = \frac{\sigma}{\omega\varepsilon_0\varepsilon_r'} = \frac{1}{2\pi f\varepsilon_0\varepsilon_r'\rho}$$

The volume resistivity ρ corresponds to the value directly obtained with the specific volume resistivity test, described in the next chapter, for the exact specimen at each temperature (in these cases, the volume resistivity and the dissipation factor tests are conducted simultaneously).

The uncertainty corresponds to the expression below:

$$u(\tan\delta_L) = \tan\delta_L \cdot \sqrt{\left(\frac{u(f)}{f}\right)^2 + \left(\frac{u(\rho)}{\rho}\right)^2 + \left(\frac{u(\varepsilon_r')}{\varepsilon_r'}\right)^2}$$

in which $u(f)$ is assumed following the constructor declaration:

$$u(f) = 0.1\% \cdot f + 1 \text{ mHz}$$

- The **polarization losses component of the dissipation factor**, $\tan\delta_{Pol}$, using this formulation:

$$\tan\delta_{Pol} = \tan\delta - \tan\delta_L$$

for which the uncertainty is:

$$u(\tan\delta_{Pol}) = \sqrt{(u(\tan\delta))^2 + (u(\tan\delta_L))^2}$$

- The **imaginary part of permittivity**, ε_r'' , calculated from the definition of $\tan\delta_{Pol}$:

$$\varepsilon_r'' = \tan\delta_{Pol} \cdot \varepsilon_r'$$

and, consequently:

$$u(\varepsilon_r'') = \varepsilon_r'' \cdot \sqrt{\left(\frac{u(\varepsilon_r')}{\varepsilon_r'}\right)^2 + \left(\frac{u(\tan\delta_{Pol})}{\tan\delta_{Pol}}\right)^2}$$

4.5 The Samples and the Results

For this kind of test, three different silicone rubber materials have been investigated:

- Bluesil ESA 7250
- Elastosil RT 601
- Powersil 600

As stated before, for each material three specimens are produced and tested, according to the described protocols.

The average thickness of a specimen is computed with six measures. The thickness slightly differs along the same sample but it varies more between different specimens, because the mode of production.

The diameter is 130 mm for all the samples, its uncertainty is computed considering a uniform error distribution and the resolution of 1 mm of the instrument.

All the samples have been produced in the company BAM –“Bundesanstalt für Materialforschung und –prüfung” in Berlin.

All the tests have been fulfilled with oil pressure at $20 \frac{\text{kg}}{\text{cm}^2}$. Hence, the thickness of the specimens during the measure is determined with the procedure explained in the paragraph 3.5 (also regarding the uncertainty calculation).

Considering the material Bluesil ESA 7250, it should be noted that, due to the different silicone diameter, the relative reduction is different with respect to the specimens of the partial discharge test.

The three samples are called BamB02, BamB03 and BamB05; their thicknesses are reported in Table 4.1.

Tab. 4.1 The thicknesses of the samples ESA 7250

Specimen	Reduced Thickness [mm]	Protocol
BAMB03	1.946 ± 0.013	Constant Frequency
BAMB02	1.864 ± 0.011	Constant Temperature
BAMB05	1.861 ± 0.012	Constant Voltage

In this work of thesis, the tensile strength test has not been conducted on the silicone Elastosil RT 601; hence, in order to get the Young's modulus, the results contained in the "IPH Berlin" database are considered, obtaining:

$$E_{RT601} = 1.760 \pm 0.023 \text{ MPa}$$

Still following the explanation of paragraph 3.5, in Table 4.2 the reduced thicknesses of RT 601 samples are reported, with the type of applied protocol.

Tab. 4.2 The thicknesses of the samples RT 601

Specimen	Reduced Thickness [mm]	Protocol
BAMD02	2.021 ± 0.013	Constant Frequency
BAMD03	2.000 ± 0.012	Constant Temperature
BAMB04	1.859 ± 0.014	Constant Voltage

Also the Young's modulus of Powersil 600 has been obtained thanks to mechanical test results in the IPH database:

$$E_{Powersil600} = 0.692 \pm 0.011 \text{ MPa}$$

The specimens used for this test are shown in Table 4.3, together with the reduced thicknesses and the specific protocol.

Tab. 4.3 The thicknesses of the samples Powersil 600

Specimen	Reduced Thickness [mm]	Protocol
BAMP01	1.660 ± 0.026	Constant Frequency
BAMP03	1.612 ± 0.023	Constant Temperature
BAMP02	1.596 ± 0.024	Constant Voltage

The considerations that are going to be presented regarding the obtained values are directly based on the obtained outcomes just reported; for a more specific inspection of these hypothesis, a greater number of samples would be necessary.

Initially, the results of the first protocol (constant frequency) are presented; those related to **ESA 7250** are reported in four tables, from Tab. 4.4 to Tab. 4.7. Their graphs, containing the main quantities, include both the increase and decrease of temperature (the tendency is indicated by arrows) and are illustrated from Fig. 4.12 to Fig. 4.14.

Tab. 4.4 BamB03 results, 500 V

Temp [°C]	Test at 500 V											
	C _x [pF]	u(C _x) [pF]	tanδ	u(tanδ)	tanδ _L	u(tanδ _L)	tanδ _{pol}	u(tanδ _{pol})	ε _r '	u(ε _r ')	ε _r ''	u(ε _r '')
25	92.4	1.1	5.17E-04	1.5E-05	2.151E-06	3.4E-08	5.15E-04	1.5E-05	2.585	0.035	1.331E-03	4.3E-05
40	90.0	1.1	8.14E-04	1.8E-05	5.132E-06	8.1E-08	8.09E-04	1.8E-05	2.519	0.035	2.036E-03	5.4E-05
60	87.6	1.1	1.884E-03	2.9E-05	1.361E-05	2.2E-07	1.870E-03	2.9E-05	2.451	0.035	4.585E-03	9.6E-05
80	85.1	1.1	5.088E-03	6.1E-05	3.498E-05	5.7E-07	5.053E-03	6.1E-05	2.382	0.034	1.203E-02	2.3E-04
100	82.4	1.1	1.382E-02	1.5E-04	7.40E-05	1.2E-06	1.375E-02	1.5E-04	2.305	0.034	3.168E-02	5.8E-04
Break 30 mins												
100	81.7	1.1	1.601E-02	1.7E-04	8.52E-05	1.4E-06	1.592E-02	1.7E-04	2.288	0.034	3.642E-02	6.7E-04
80	83.2	1.1	7.539E-03	8.5E-05	4.985E-05	8.3E-07	7.489E-03	8.5E-05	2.327	0.034	1.743E-02	3.2E-04
60	85.2	1.1	3.105E-03	4.1E-05	2.149E-05	3.5E-07	3.083E-03	4.1E-05	2.384	0.034	7.35E-03	1.4E-04
40	88.3	1.1	1.060E-03	2.1E-05	7.94E-06	1.3E-07	1.052E-03	2.1E-05	2.470	0.035	2.599E-03	6.3E-05
25	91.9	1.1	5.08E-04	1.5E-05	2.808E-06	4.4E-08	5.05E-04	1.5E-05	2.573	0.035	1.299E-03	4.3E-05

Tab. 4.5 BamB03 results, 1000 V

Temp. [°C]	Test at 1000 V											
	C _x [pF]	u(C _x) [pF]	tanδ	u(tanδ)	tanδ _L	u(tanδ _L)	tanδ _{pol}	u(tanδ _{pol})	ε _r '	u(ε _r ')	ε _r ''	u(ε _r '')
25	92.4	1.1	5.20E-04	1.5E-05	2.151E-06	3.4E-08	5.18E-04	1.5E-05	2.585	0.035	1.339E-03	4.3E-05
40	90.0	1.1	8.28E-04	1.8E-05	5.132E-06	8.1E-08	8.23E-04	1.8E-05	2.518	0.035	2.072E-03	5.4E-05
60	87.6	1.1	1.918E-03	2.9E-05	1.361E-05	2.2E-07	1.904E-03	2.9E-05	2.451	0.035	4.668E-03	9.7E-05
80	85.1	1.1	5.200E-03	6.2E-05	3.498E-05	5.7E-07	5.165E-03	6.2E-05	2.382	0.034	1.230E-02	2.3E-04
100	82.4	1.1	1.413E-02	1.5E-04	7.40E-05	1.2E-06	1.405E-02	1.5E-04	2.305	0.034	3.239E-02	5.9E-04
Break 30 mins												
100	81.7	1.1	1.636E-02	1.7E-04	8.52E-05	1.4E-06	1.627E-02	1.7E-04	2.287	0.034	3.722E-02	6.8E-04
80	83.2	1.1	7.702E-03	8.7E-05	4.985E-05	8.3E-07	7.652E-03	8.7E-05	2.327	0.034	1.781E-02	3.3E-04
60	85.2	1.1	3.166E-03	4.2E-05	2.149E-05	3.5E-07	3.145E-03	4.2E-05	2.384	0.034	7.50E-03	1.5E-04
40	88.3	1.1	1.077E-03	2.1E-05	7.94E-06	1.3E-07	1.069E-03	2.1E-05	2.470	0.035	2.640E-03	6.3E-05
25	91.9	1.1	5.09E-04	1.5E-05	2.808E-06	4.4E-08	5.06E-04	1.5E-05	2.573	0.035	1.302E-03	4.3E-05

4. DISSIPATION FACTOR AND ELECTRIC PERMITTIVITY

Tab. 4.6 BamB03 results, 1500 V

Temp [°C]	Test at 1500 V											
	C _x [pF]	u(C _x) [pF]	tanδ	u(tanδ)	tanδ _L	u(tanδ _L)	tanδ _{pol}	u(tanδ _{pol})	ε _r '	u(ε _r ')	ε _r ''	u(ε _r '')
25	92.4	1.1	5.26E-04	1.5E-05	2.151E-06	3.4E-08	5.23E-04	1.5E-05	2.585	0.035	1.353E-03	4.4E-05
40	90.0	1.1	8.41E-04	1.8E-05	5.132E-06	8.1E-08	8.36E-04	1.8E-05	2.518	0.035	2.105E-03	5.5E-05
60	87.6	1.1	1.970E-03	3.0E-05	1.361E-05	2.2E-07	1.956E-03	3.0E-05	2.451	0.035	4.795E-03	9.9E-05
80	85.1	1.1	5.348E-03	6.3E-05	3.498E-05	5.7E-07	5.313E-03	6.3E-05	2.382	0.034	1.265E-02	2.4E-04
100	82.3	1.1	1.449E-02	1.5E-04	7.40E-05	1.2E-06	1.441E-02	1.5E-04	2.304	0.034	3.321E-02	6.1E-04
Break 30 mins												
100	81.7	1.1	1.676E-02	1.8E-04	8.52E-05	1.4E-06	1.667E-02	1.8E-04	2.287	0.034	3.814E-02	7.0E-04
80	83.2	1.1	7.902E-03	8.9E-05	4.985E-05	8.3E-07	7.852E-03	8.9E-05	2.327	0.034	1.827E-02	3.4E-04
60	85.2	1.1	3.254E-03	4.3E-05	2.149E-05	3.5E-07	3.233E-03	4.3E-05	2.384	0.034	7.71E-03	1.5E-04
40	88.3	1.1	1.102E-03	2.1E-05	7.94E-06	1.3E-07	1.094E-03	2.1E-05	2.470	0.035	2.702E-03	6.4E-05
25	91.9	1.1	5.18E-04	1.5E-05	2.808E-06	4.4E-08	5.15E-04	1.5E-05	2.573	0.035	1.326E-03	4.3E-05

Tab. 4.7 BamB03 results, 2000 V

Temp [°C]	Test at 2000 V											
	C _x [pF]	u(C _x) [pF]	tanδ	u(tanδ)	tanδ _L	u(tanδ _L)	tanδ _{pol}	u(tanδ _{pol})	ε _r '	u(ε _r ')	ε _r ''	u(ε _r '')
25	92.4	1.1	5.29E-04	1.5E-05	2.151E-06	3.4E-08	5.27E-04	1.5E-05	2.585	0.035	1.362E-03	4.4E-05
40	90.0	1.1	8.65E-04	1.9E-05	5.132E-06	8.1E-08	8.60E-04	1.9E-05	2.518	0.035	2.165E-03	5.6E-05
60	87.6	1.1	2.030E-03	3.0E-05	1.361E-05	2.2E-07	2.016E-03	3.0E-05	2.451	0.035	4.94E-03	1.0E-04
80	85.1	1.1	5.502E-03	6.5E-05	3.498E-05	5.7E-07	5.467E-03	6.5E-05	2.382	0.034	1.302E-02	2.4E-04
100	82.3	1.1	1.486E-02	1.6E-04	7.40E-05	1.2E-06	1.479E-02	1.6E-04	2.304	0.034	3.407E-02	6.2E-04
Break 30 mins												
100	81.7	1.1	1.718E-02	1.8E-04	8.52E-05	1.4E-06	1.709E-02	1.8E-04	2.287	0.034	3.910E-02	7.1E-04
80	83.2	1.1	8.113E-03	9.1E-05	4.985E-05	8.3E-07	8.064E-03	9.1E-05	2.327	0.034	1.876E-02	3.5E-04
60	85.2	1.1	3.350E-03	4.3E-05	2.149E-05	3.5E-07	3.328E-03	4.3E-05	2.384	0.034	7.94E-03	1.5E-04
40	88.3	1.1	1.133E-03	2.1E-05	7.94E-06	1.3E-07	1.125E-03	2.1E-05	2.470	0.035	2.779E-03	6.6E-05
25	91.9	1.1	5.25E-04	1.5E-05	2.808E-06	4.4E-08	5.23E-04	1.5E-05	2.573	0.035	1.345E-03	4.3E-05

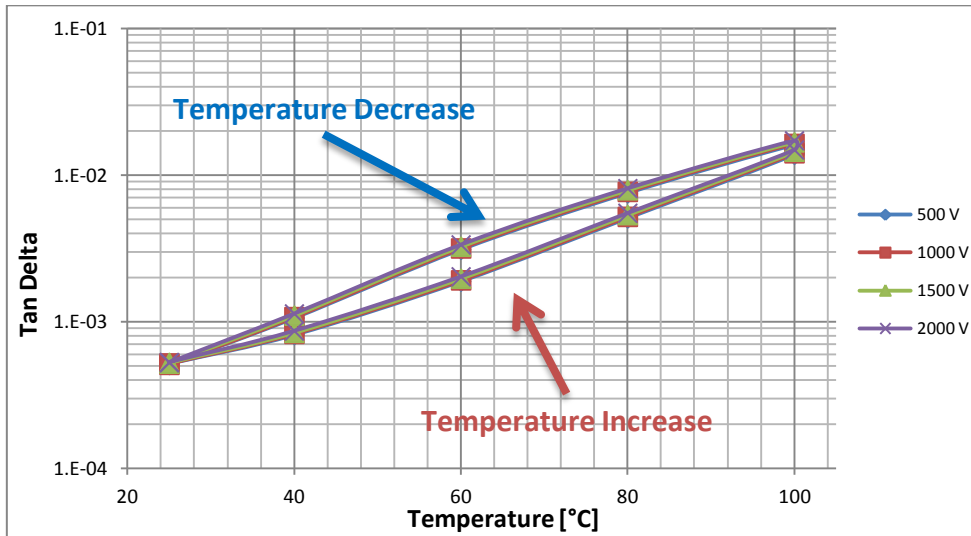


Fig. 4.12 BamB03 – Dissipation factor

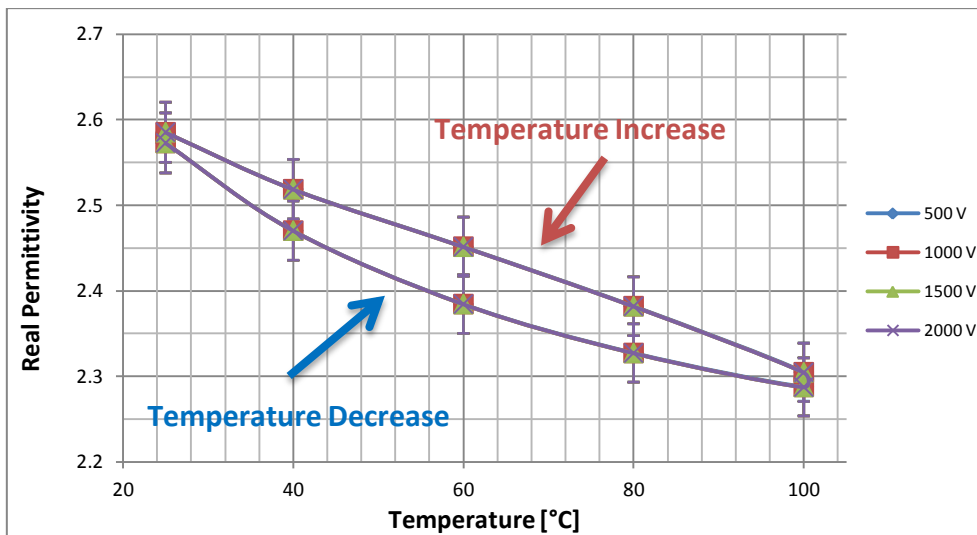


Fig. 4.13 BamB03 - Real Permittivity

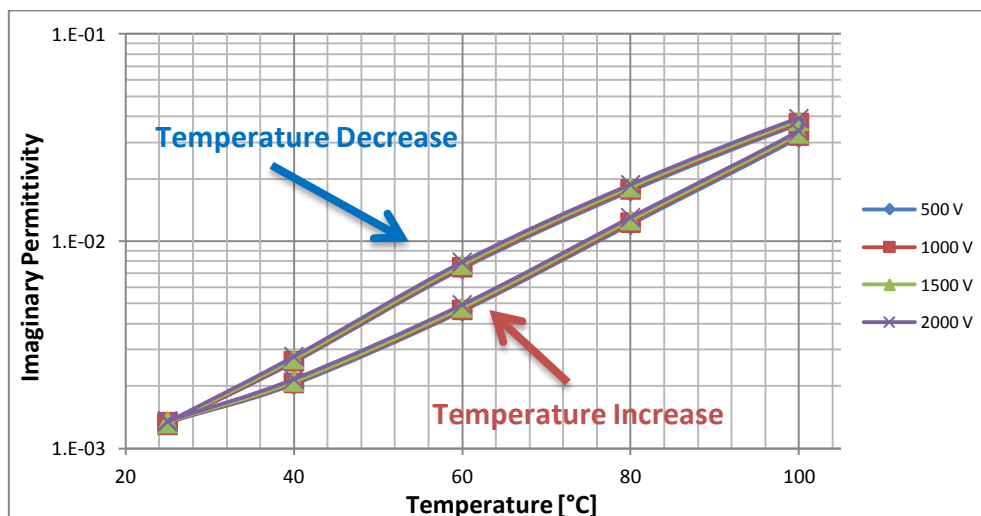


Fig. 4.14 BamB03 - Imaginary Permittivity

The specimen of **RT 601** (BamD02) provides the results found from Tab. 4.8 to Tab. 4.11.

Tab. 4.8 BamD02 results, 500 V

Temp (°C)	Test at 500 V											
	C_x [pF]	$u(C_x)$ [pF]	$\tan\delta$	$u(\tan\delta)$	$\tan\delta_L$	$u(\tan\delta_L)$	$\tan\delta_{pol}$	$u(\tan\delta_{pol})$	ϵ_r'	$u(\epsilon_r')$	ϵ_r''	$u(\epsilon_r'')$
25	89.1	1.1	1.66E-04	1.2E-05	5.033E-08	9.7E-10	1.66E-04	1.2E-05	2.589	0.036	4.30E-04	3.1E-05
40	87.3	1.1	1.78E-04	1.2E-05	1.017E-07	1.7E-09	1.78E-04	1.2E-05	2.536	0.036	4.51E-04	3.1E-05
60	84.7	1.1	1.85E-04	1.2E-05	2.100E-07	3.5E-09	1.84E-04	1.2E-05	2.463	0.035	4.54E-04	3.0E-05
80	82.3	1.1	2.07E-04	1.2E-05	2.115E-07	3.6E-09	2.07E-04	1.2E-05	2.393	0.035	4.94E-04	3.0E-05
100	79.7	1.1	3.34E-04	1.3E-05	1.924E-07	3.3E-09	3.34E-04	1.3E-05	2.317	0.035	7.74E-04	3.3E-05
Break 30 mins												
100	79.2	1.1	3.94E-04	1.4E-05	1.965E-07	3.4E-09	3.94E-04	1.4E-05	2.301	0.035	9.07E-04	3.5E-05
80	80.7	1.1	3.69E-04	1.4E-05	1.762E-07	3.0E-09	3.69E-04	1.4E-05	2.346	0.035	8.65E-04	3.5E-05
60	82.7	1.1	2.67E-04	1.3E-05	1.373E-07	2.4E-09	2.67E-04	1.3E-05	2.402	0.035	6.42E-04	3.2E-05
40	85.4	1.1	1.88E-04	1.2E-05	6.10E-08	1.2E-09	1.88E-04	1.2E-05	2.481	0.035	4.66E-04	3.0E-05
25	88.4	1.1	1.93E-04	1.2E-05	2.380E-08	4.6E-10	1.93E-04	1.2E-05	2.570	0.036	4.96E-04	3.1E-05

Tab. 4.9 BamD02 results, 1000 V

Temp. (°C)	Test at 1000 V											
	C_x [pF]	$u(C_x)$ [pF]	$\tan\delta$	$u(\tan\delta)$	$\tan\delta_L$	$u(\tan\delta_L)$	$\tan\delta_{pol}$	$u(\tan\delta_{pol})$	ϵ_r'	$u(\epsilon_r')$	ϵ_r''	$u(\epsilon_r'')$
25	89.1	1.1	1.71E-04	1.2E-05	5.033E-08	9.7E-10	1.71E-04	1.2E-05	2.590	0.036	4.42E-04	3.1E-05
40	87.3	1.1	1.86E-04	1.2E-05	1.017E-07	1.7E-09	1.86E-04	1.2E-05	2.536	0.036	4.71E-04	3.1E-05
60	84.7	1.1	1.85E-04	1.2E-05	2.100E-07	3.5E-09	1.85E-04	1.2E-05	2.463	0.035	4.55E-04	3.0E-05
80	82.3	1.1	2.09E-04	1.2E-05	2.115E-07	3.6E-09	2.09E-04	1.2E-05	2.393	0.035	5.00E-04	3.0E-05
100	79.7	1.1	3.43E-04	1.3E-05	1.924E-07	3.3E-09	3.43E-04	1.3E-05	2.317	0.035	7.95E-04	3.3E-05
Break 30 mins												
100	79.2	1.1	4.03E-04	1.4E-05	1.965E-07	3.4E-09	4.03E-04	1.4E-05	2.301	0.035	9.27E-04	3.5E-05
80	80.7	1.1	3.76E-04	1.4E-05	1.762E-07	3.0E-09	3.76E-04	1.4E-05	2.346	0.035	8.82E-04	3.5E-05
60	82.7	1.1	2.68E-04	1.3E-05	1.373E-07	2.4E-09	2.68E-04	1.3E-05	2.402	0.035	6.44E-04	3.2E-05
40	85.4	1.1	2.02E-04	1.2E-05	6.10E-08	1.2E-09	2.02E-04	1.2E-05	2.481	0.035	5.00E-04	3.1E-05
25	88.4	1.1	1.96E-04	1.2E-05	2.380E-08	4.6E-10	1.96E-04	1.2E-05	2.570	0.036	5.04E-04	3.2E-05

4. DISSIPATION FACTOR AND ELECTRIC PERMITTIVITY

Tab. 4.10 BamD02 results, 1500 V

Temp (°C)	Test at 1500 V											
	C _x [pF]	u(C _x) [pF]	tanδ	u(tanδ)	tanδ _L	u(tanδ _L)	tanδ _{pol}	u(tanδ _{pol})	ε _r '	u(ε _r ')	ε _r ''	u(ε _r '')
25	89.1	1.1	1.71E-04	1.2E-05	5.033E-08	9.7E-10	1.71E-04	1.2E-05	2.590	0.036	4.44E-04	3.1E-05
40	87.3	1.1	1.86E-04	1.2E-05	1.017E-07	1.7E-09	1.86E-04	1.2E-05	2.536	0.036	4.71E-04	3.1E-05
60	84.7	1.1	1.91E-04	1.2E-05	2.100E-07	3.5E-09	1.90E-04	1.2E-05	2.463	0.035	4.69E-04	3.0E-05
80	82.3	1.1	2.13E-04	1.2E-05	2.115E-07	3.6E-09	2.13E-04	1.2E-05	2.393	0.035	5.09E-04	3.0E-05
100	79.7	1.1	3.45E-04	1.3E-05	1.924E-07	3.3E-09	3.45E-04	1.3E-05	2.317	0.035	8.00E-04	3.3E-05
Break 30 mins												
100	79.2	1.1	4.09E-04	1.4E-05	1.965E-07	3.4E-09	4.09E-04	1.4E-05	2.301	0.035	9.41E-04	3.5E-05
80	80.7	1.1	3.81E-04	1.4E-05	1.762E-07	3.0E-09	3.80E-04	1.4E-05	2.346	0.035	8.93E-04	3.5E-05
60	82.7	1.1	2.74E-04	1.3E-05	1.373E-07	2.4E-09	2.74E-04	1.3E-05	2.402	0.035	6.58E-04	3.2E-05
40	85.4	1.1	2.17E-04	1.2E-05	6.10E-08	1.2E-09	2.17E-04	1.2E-05	2.481	0.035	5.39E-04	3.1E-05
25	88.4	1.1	1.99E-04	1.2E-05	2.380E-08	4.6E-10	1.99E-04	1.2E-05	2.570	0.036	5.11E-04	3.2E-05

Tab. 4.11 BamD02 results, 2000 V

Temp (°C)	Test at 2000 V											
	C _x [pF]	u(C _x) [pF]	tanδ	u(tanδ)	tanδ _L	u(tanδ _L)	tanδ _{pol}	u(tanδ _{pol})	ε _r '	u(ε _r ')	ε _r ''	u(ε _r '')
25	89.1	1.1	1.72E-04	1.2E-05	5.033E-08	9.7E-10	1.72E-04	1.2E-05	2.590	0.036	4.46E-04	3.1E-05
40	87.3	1.1	1.88E-04	1.2E-05	1.017E-07	1.7E-09	1.88E-04	1.2E-05	2.536	0.036	4.77E-04	3.1E-05
60	84.7	1.1	1.91E-04	1.2E-05	2.100E-07	3.5E-09	1.91E-04	1.2E-05	2.463	0.035	4.70E-04	3.0E-05
80	82.3	1.1	2.14E-04	1.2E-05	2.115E-07	3.6E-09	2.14E-04	1.2E-05	2.393	0.035	5.11E-04	3.0E-05
100	79.7	1.1	3.51E-04	1.4E-05	1.924E-07	3.3E-09	3.51E-04	1.4E-05	2.317	0.035	8.13E-04	3.4E-05
Break 30 mins												
100	79.2	1.1	4.17E-04	1.4E-05	1.965E-07	3.4E-09	4.17E-04	1.4E-05	2.301	0.035	9.59E-04	3.6E-05
80	80.7	1.1	3.86E-04	1.4E-05	1.762E-07	3.0E-09	3.86E-04	1.4E-05	2.346	0.035	9.04E-04	3.5E-05
60	82.7	1.1	2.79E-04	1.3E-05	1.373E-07	2.4E-09	2.79E-04	1.3E-05	2.402	0.035	6.71E-04	3.2E-05
40	85.4	1.1	2.38E-04	1.2E-05	6.10E-08	1.2E-09	2.38E-04	1.2E-05	2.481	0.035	5.91E-04	3.2E-05
25	88.4	1.1	2.09E-04	1.2E-05	2.380E-08	4.6E-10	2.09E-04	1.2E-05	2.570	0.036	5.36E-04	3.2E-05

The main results of RT 601 are shown in the next figures, from Fig. 4.15 to fig. 4.17.

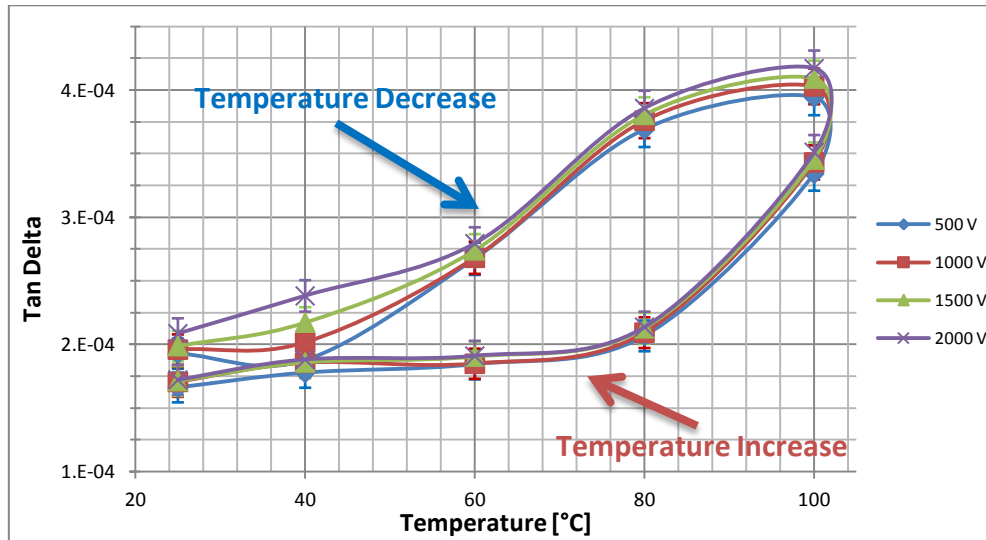


Fig. 4.15 BamD02 - Dissipation factor

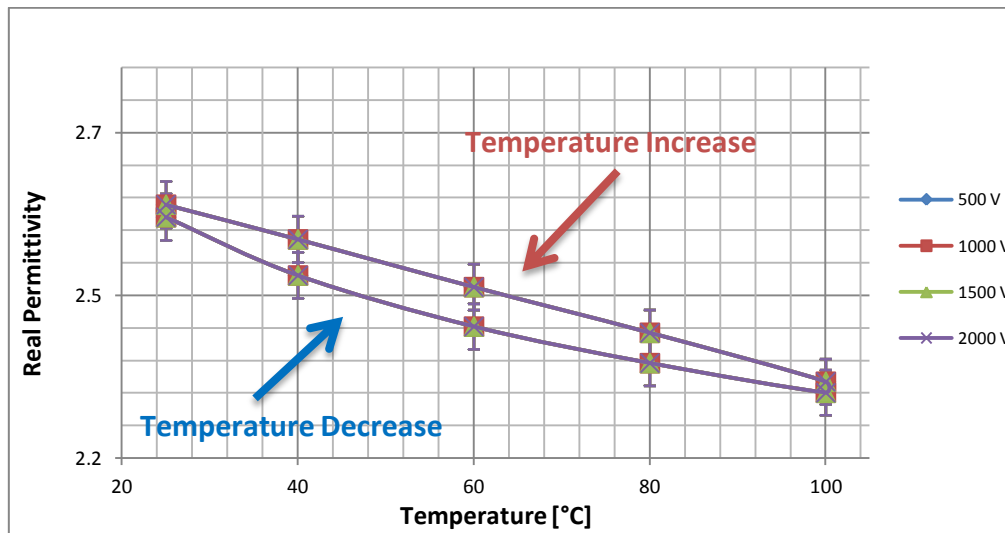


Fig. 4.16 BamD02 - Real Permittivity

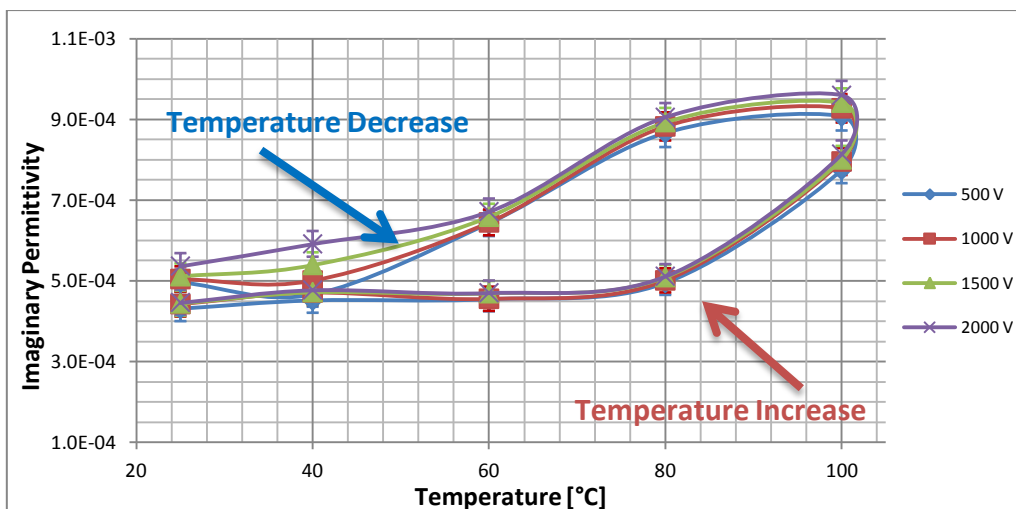


Fig. 4.17 BamD02 - Imaginary Permittivity

The results of **Powersil 600** at constant frequency are presented in the next tables, from Tab. 4.12 to Tab. 4.15.

Tab. 4.12 BamP01 results, 500 V

Temp (°C)	Test at 500 V											
	C _x [pF]	u(C _x) [pF]	tanδ	u(tanδ)	tanδ _L	u(tanδ _L)	tanδ _{pol}	u(tanδ _{pol})	ε _r '	u(ε _r ')	ε _r ''	u(ε _r '')
25	88.0	1.1	5.24E-04	1.5E-05	2.904E-09	8.2E-11	5.24E-04	1.5E-05	2.101	0.042	1.101E-03	3.9E-05
40	85.8	1.1	7.28E-04	1.7E-05	5.76E-09	1.6E-10	7.28E-04	1.7E-05	2.048	0.041	1.491E-03	4.6E-05
60	84.2	1.1	1.015E-03	2.0E-05	1.419E-08	4.0E-10	1.015E-03	2.0E-05	2.009	0.041	2.038E-03	5.8E-05
80	82.0	1.1	1.468E-03	2.5E-05	3.91E-08	1.1E-09	1.468E-03	2.5E-05	1.958	0.040	2.874E-03	7.6E-05
100	80.6	1.1	1.962E-03	3.0E-05	9.60E-08	2.6E-09	1.962E-03	3.0E-05	1.924	0.040	3.775E-03	9.6E-05
Break 30 mins												
100	80.9	1.1	1.978E-03	3.0E-05	9.85E-08	2.6E-09	1.978E-03	3.0E-05	1.930	0.040	3.818E-03	9.7E-05
80	82.6	1.1	1.544E-03	2.5E-05	5.33E-08	1.5E-09	1.544E-03	2.5E-05	1.972	0.040	3.044E-03	8.0E-05
60	84.6	1.1	1.067E-03	2.1E-05	1.502E-08	4.2E-10	1.067E-03	2.1E-05	2.020	0.041	2.156E-03	6.0E-05
40	86.9	1.1	7.51E-04	1.8E-05	7.52E-09	2.1E-10	7.51E-04	1.8E-05	2.074	0.042	1.559E-03	4.8E-05
25	89.0	1.1	5.63E-04	1.6E-05	4.17E-09	1.2E-10	5.63E-04	1.6E-05	2.125	0.042	1.197E-03	4.1E-05

Tab. 4.13 BamP01 results, 1000 V

Temp (°C)	Test at 1000 V											
	C _x [pF]	u(C _x) [pF]	tanδ	u(tanδ)	tanδ _L	u(tanδ _L)	tanδ _{pol}	u(tanδ _{pol})	ε _r '	u(ε _r ')	ε _r ''	u(ε _r '')
25	88.0	1.1	5.25E-04	1.5E-05	2.904E-09	8.2E-11	5.25E-04	1.5E-05	2.101	0.042	1.104E-03	3.9E-05
40	85.8	1.1	7.21E-04	1.7E-05	5.76E-09	1.6E-10	7.21E-04	1.7E-05	2.048	0.041	1.477E-03	4.6E-05
60	84.2	1.1	1.012E-03	2.0E-05	1.419E-08	4.0E-10	1.012E-03	2.0E-05	2.009	0.041	2.033E-03	5.8E-05
80	82.0	1.1	1.461E-03	2.5E-05	3.91E-08	1.1E-09	1.461E-03	2.5E-05	1.958	0.040	2.862E-03	7.6E-05
100	80.6	1.1	1.966E-03	3.0E-05	9.60E-08	2.6E-09	1.966E-03	3.0E-05	1.924	0.040	3.781E-03	9.7E-05
Break 30 mins												
100	80.9	1.1	1.982E-03	3.0E-05	9.86E-08	2.6E-09	1.982E-03	3.0E-05	1.930	0.040	3.826E-03	9.8E-05
80	82.6	1.1	1.546E-03	2.5E-05	5.33E-08	1.5E-09	1.546E-03	2.5E-05	1.972	0.040	3.049E-03	8.0E-05
60	84.6	1.1	1.071E-03	2.1E-05	1.502E-08	4.2E-10	1.071E-03	2.1E-05	2.020	0.041	2.163E-03	6.1E-05
40	86.9	1.1	7.51E-04	1.8E-05	7.52E-09	2.1E-10	7.51E-04	1.8E-05	2.074	0.042	1.558E-03	4.8E-05
25	89.0	1.1	5.69E-04	1.6E-05	4.17E-09	1.2E-10	5.69E-04	1.6E-05	2.125	0.042	1.208E-03	4.1E-05

4. DISSIPATION FACTOR AND ELECTRIC PERMITTIVITY

Tab. 4.14 BamP01 results, 1500 V

Temp (°C)	Test at 1500 V											
	C _x [pF]	u(C _x) [pF]	tanδ	u(tanδ)	tanδ _L	u(tanδ _L)	tanδ _{pol}	u(tanδ _{pol})	ε _r '	u(ε _r ')	ε _r ''	u(ε _r '')
25	88.0	1.1	5.24E-04	1.5E-05	2.904E-09	8.2E-11	5.24E-04	1.5E-05	2.101	0.042	1.100E-03	3.9E-05
40	85.8	1.1	7.24E-04	1.7E-05	5.76E-09	1.6E-10	7.24E-04	1.7E-05	2.048	0.041	1.483E-03	4.6E-05
60	84.2	1.1	1.013E-03	2.0E-05	1.419E-08	4.0E-10	1.013E-03	2.0E-05	2.009	0.041	2.035E-03	5.8E-05
80	82.0	1.1	1.464E-03	2.5E-05	3.91E-08	1.1E-09	1.464E-03	2.5E-05	1.958	0.040	2.866E-03	7.6E-05
100	80.6	1.1	1.969E-03	3.0E-05	9.60E-08	2.6E-09	1.969E-03	3.0E-05	1.924	0.040	3.787E-03	9.7E-05
Break 30 mins												
100	80.9	1.1	1.981E-03	3.0E-05	9.86E-08	2.1E-09	1.981E-03	3.0E-05	1.930	0.040	3.823E-03	9.8E-05
80	82.6	1.1	1.550E-03	2.5E-05	5.33E-08	1.1E-09	1.550E-03	2.5E-05	1.972	0.040	3.055E-03	8.0E-05
60	84.6	1.1	1.067E-03	2.1E-05	1.502E-08	3.0E-10	1.067E-03	2.1E-05	2.020	0.041	2.156E-03	6.0E-05
40	86.9	1.1	7.53E-04	1.8E-05	7.52E-09	1.5E-10	7.53E-04	1.8E-05	2.074	0.042	1.562E-03	4.8E-05
25	89.0	1.1	5.68E-04	1.6E-05	4.172E-09	8.3E-11	5.68E-04	1.6E-05	2.125	0.042	1.207E-03	4.1E-05

Tab. 4.15 BamP01 results, 2000 V

Temp (°C)	Test at 2000 V											
	C _x [pF]	u(C _x) [pF]	tanδ	u(tanδ)	tanδ _L	u(tanδ _L)	tanδ _{pol}	u(tanδ _{pol})	ε _r '	u(ε _r ')	ε _r ''	u(ε _r '')
25	88.0	1.1	5.22E-04	1.5E-05	2.904E-09	8.2E-11	5.22E-04	1.5E-05	2.101	0.042	1.097E-03	3.9E-05
40	85.8	1.1	7.27E-04	1.7E-05	5.76E-09	1.6E-10	7.27E-04	1.7E-05	2.048	0.041	1.489E-03	4.6E-05
60	84.2	1.1	1.012E-03	2.0E-05	1.419E-08	4.0E-10	1.012E-03	2.0E-05	2.009	0.041	2.032E-03	5.8E-05
80	82.0	1.1	1.462E-03	2.5E-05	3.91E-08	1.1E-09	1.462E-03	2.5E-05	1.958	0.040	2.864E-03	7.6E-05
100	80.6	1.1	1.962E-03	3.0E-05	9.60E-08	2.6E-09	1.962E-03	3.0E-05	1.924	0.040	3.775E-03	9.6E-05
Break 30 mins												
100	80.9	1.1	1.985E-03	3.0E-05	9.86E-08	2.6E-09	1.985E-03	3.0E-05	1.930	0.040	3.830E-03	9.8E-05
80	82.6	1.1	1.549E-03	2.5E-05	5.33E-08	1.5E-09	1.549E-03	2.5E-05	1.972	0.040	3.055E-03	8.0E-05
60	84.6	1.1	1.067E-03	2.1E-05	1.502E-08	4.2E-10	1.067E-03	2.1E-05	2.021	0.041	2.155E-03	6.0E-05
40	86.9	1.1	7.51E-04	1.8E-05	7.52E-09	2.1E-10	7.51E-04	1.8E-05	2.074	0.042	1.558E-03	4.8E-05
25	89.0	1.1	5.67E-04	1.6E-05	4.17E-09	1.2E-10	5.67E-04	1.6E-05	2.125	0.042	1.206E-03	4.1E-05

The graphs illustrating the Powersil 600 results correspond to three figures, from Fig. 4.18 to Fig. 4.20.

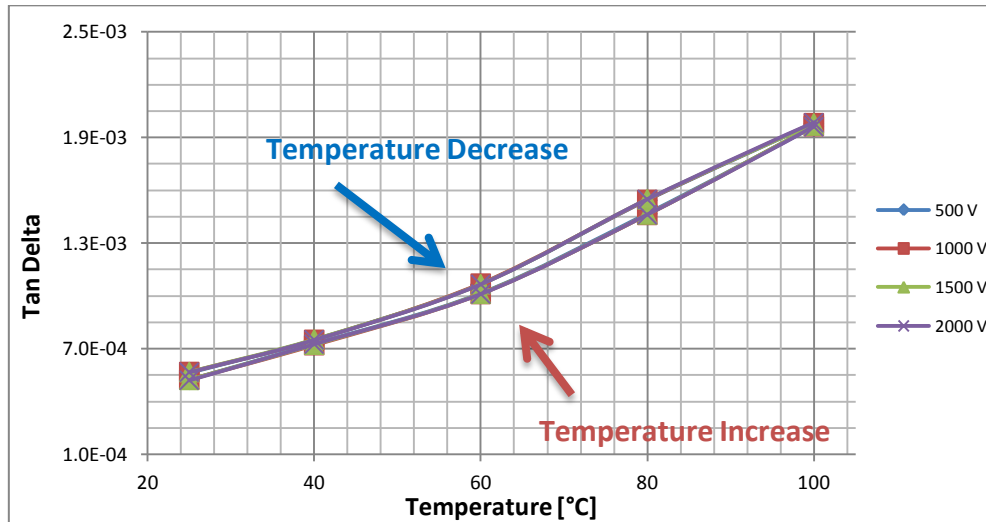


Fig. 4.18 BamP01 - Dissipation factor

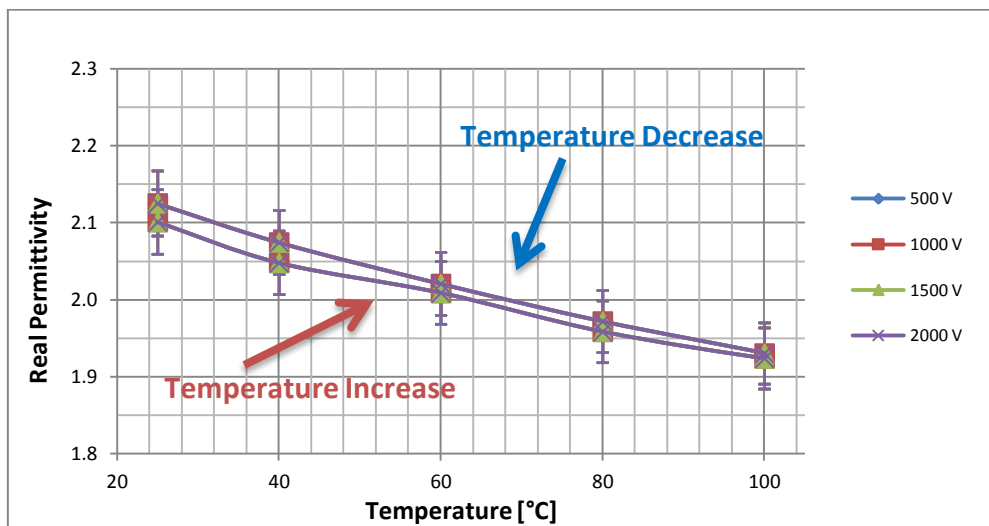


Fig. 4.19 BamP01 - Real Permittivity

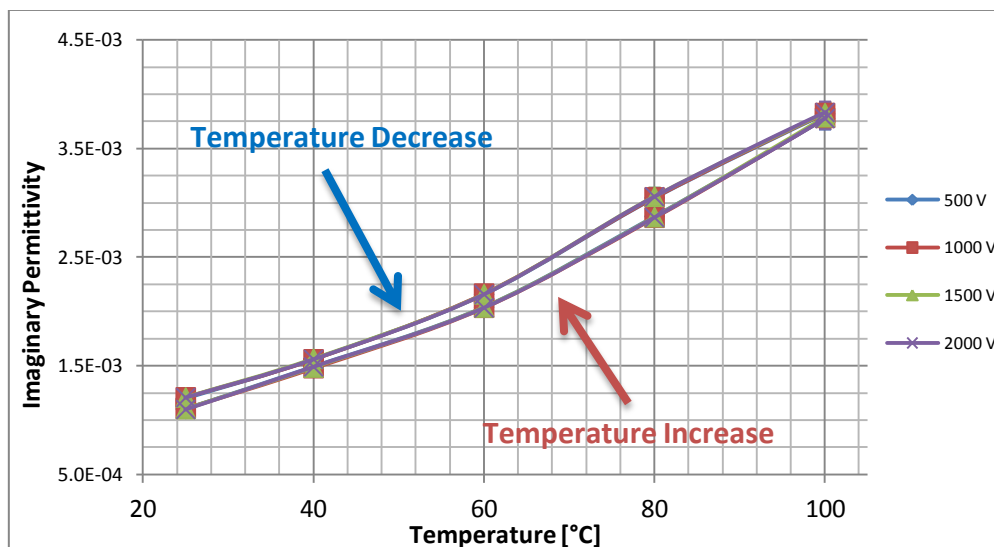


Fig. 4.20 BamP01 - Imaginary Permittivity

The first noticeable aspect is the independence of the quantities from the voltage applied (except a small difference in the $\tan\delta$ of RT 601, Fig. 4.15), which, at least for our range, is not sufficient to modify the polarization mechanism.

In order to show the comparison between the different materials, three graphs are presented (from Fig. 4.21 to Fig. 4.23), in which the dissipation factor and the two components of permittivity are illustrated, considering the results with the applied voltage equal to 500 V.

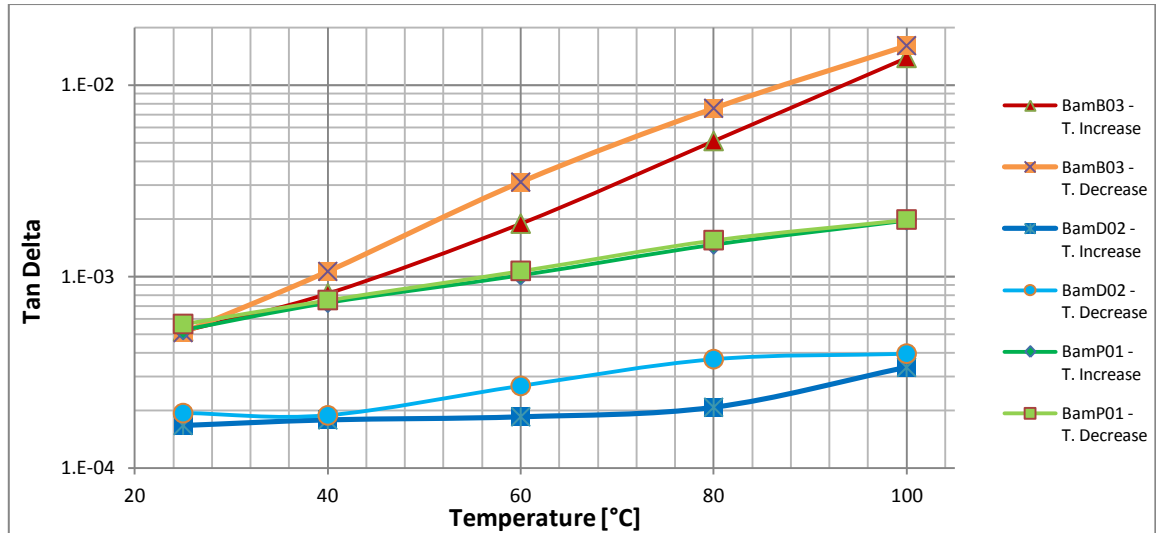


Fig. 4.21 First protocol: Tan Delta comparison (500 V)

As shown in Fig. 4.21, the **dissipation factor** clearly increases with the temperature growth for all the materials, proving that the collisions due to thermal causes contributes to the material's losses.

For the ESA 7250, also reported in Fig. 4.12, this increase is quite clear (more than one order of magnitude), it tends to be exponential and, in the cycle of temperatures, no differences are found in $\tan\delta$ between the growth and reduction of temperature.

Between the tested materials, it presents the highest loss factor (particularly at high temperatures).

Its volume resistivity is high, so the dissipation factor is similar to $\tan\delta_{pol}$ (Tab. 4.4).

In the RT 601 the smallest increase of $\tan\delta$ is reported (concentrated from 80°C to 100°C) and, in general, this loss tangent is the lowest analyzed one (Fig. 4.21).

The material shows an unstable behavior: the different values in the two parts of temperature cycle are evident and they can be due to chemical modification of the polymer, that can need time to return to the original configuration, as seen in Fig. 4.15.

Cause the very high resistivity, the dissipation factor can be identified with $\tan\delta_{pol}$; looking at $\tan\delta_L$ in Tab. 4.8, it depends a lot on the temperature (definitely more than the polarization component).

The Powersil 600 presents a linear increase in the dissipation factor, showing a less sensitivity for the temperature with respect to ESA 7250 (Fig. 4.21); moreover, in the temperature cycle the difference is tiny: Powersil 600 seems to adapt quickly to the temperature change.

The volume resistivity of Powersil 600 is very small, consequently the $\tan\delta_L$ can be neglected in evaluating the dissipation factor, referring to Tab. 4.12.

Also this conductive component increases with the temperature much more than $\tan\delta_{pol}$, as it is noticeable in ESA 7250 and to a lesser extent RT 601.

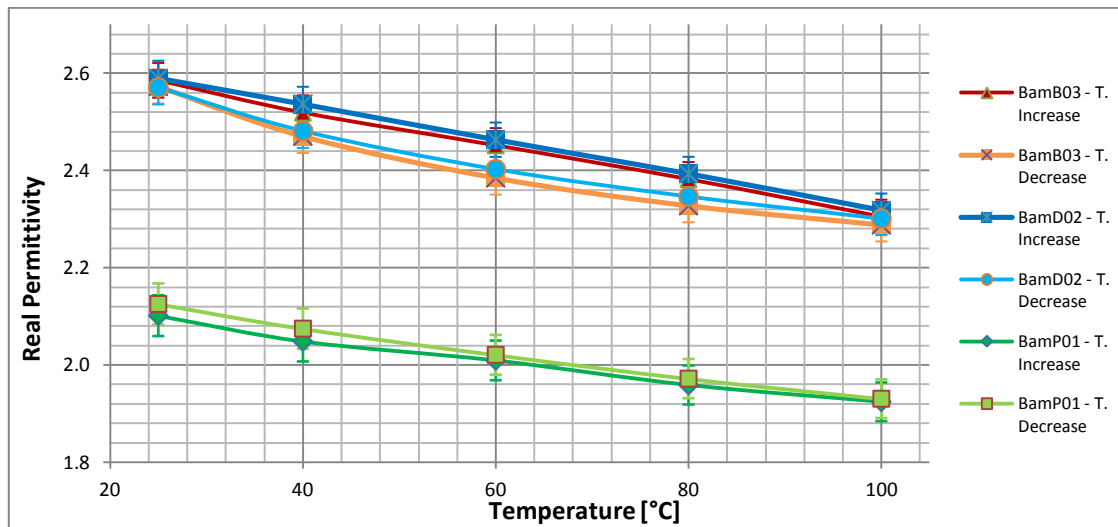


Fig. 4.22 First protocol: Real Permittivity comparison (500 V)

Considering the **real part of permittivity**, it decreases with the temperature in all the material, as illustrated in Fig. 4.22. The polarizability is opposed and overcome by the thermal agitation that randomizes the silicone's constituents, which are more free to move and do not follow the alternating electric field.

For the cycles of ESA 7250 and RT 601 (also shown in Fig. 4.13 and 4.16, respectively), the return to room temperature involves a lower ϵ'_r , due to less polarizable elements in this transition of temperature, while for Powersil 600 this behavior is opposite (Fig. 4.19).

The ESA 7250 and RT 601 start from a similar value but this last silicone has a smaller dependence on the temperature, decreasing of a lower quantity.

Powersil 600 presents the lowest polarizability between the analyzed silicones.

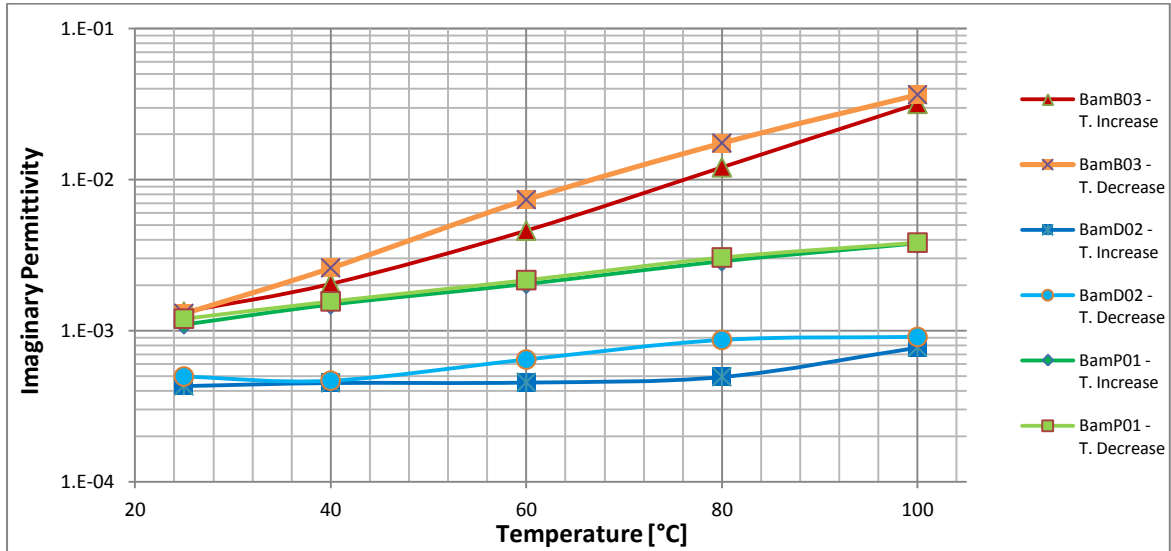


Fig. 4.23 First protocol: Imaginary Permittivity comparison (500 V)

Regarding the **imaginary part of permittivity** (Fig. 4.23), it follows the behavior of the dissipation factor (which can be assumed coincident with $\tan\delta_{pol}$), because the parallel capacitance (and then the real component of permittivity) is much more stable.

In general, looking at the real permittivity and the $\tan\delta$ (Fig. 4.21 and Fig. 4.23), it can be stated that, with the increase of temperature, despite the decrease of medium's polarization (due to randomization of dipoles/molecules, that do not follow the electric field) the losses increases, because the collisions inside the material.

In the following pages, the results of the second protocol, conducted at constant temperature, are reported in tables and correlated charts.

The outcomes of **ESA 7250**, referred to the specimen BamB02, are found in the next tables, from Tab. 4.16 to 4.19.

Tab. 4.16 BamB02 results, 500 V

Freq [Hz]	Test at 500 V											
	C _x [pF]	u(C _x) [pF]	tanδ	u(tanδ)	tanδ _L	u(tanδ _L)	tanδ _{pol}	u(tanδ _{pol})	ε _r '	u(ε _r ')	ε _r ''	u(ε _r '')
0.1	96.7	1.1	1.075E-01	1.1E-03	1.015E-03	1.8E-05	1.065E-01	1.1E-03	2.593	0.033	2.761E-01	4.5E-03
1	96.3	1.1	1.095E-02	1.2E-04	1.019E-04	1.5E-06	1.084E-02	1.2E-04	2.582	0.033	2.800E-02	4.7E-04
10	96.3	1.1	1.389E-03	2.4E-05	1.020E-05	1.5E-07	1.378E-03	2.4E-05	2.581	0.033	3.558E-03	7.7E-05
50	96.3	1.1	5.52E-04	1.6E-05	2.040E-06	3.0E-08	5.50E-04	1.6E-05	2.580	0.033	1.420E-03	4.4E-05
100	96.2	1.1	4.74E-04	1.5E-05	1.020E-06	1.5E-08	4.73E-04	1.5E-05	2.580	0.033	1.220E-03	4.1E-05
150	96.2	1.1	4.43E-04	1.4E-05	6.802E-07	9.9E-09	4.42E-04	1.4E-05	2.580	0.033	1.140E-03	4.0E-05
350	96.2	1.1	4.20E-04	1.4E-05	2.916E-07	4.2E-09	4.20E-04	1.4E-05	2.579	0.033	1.082E-03	3.9E-05
500	96.2	1.1	4.02E-04	1.4E-05	2.041E-07	3.0E-09	4.02E-04	1.4E-05	2.579	0.033	1.036E-03	3.9E-05
1000	96.2	1.1	3.71E-04	1.4E-05	1.021E-07	1.5E-09	3.71E-04	1.4E-05	2.578	0.033	9.56E-04	3.7E-05

Tab. 4.17 BamB02 results, 1000 V

Freq [Hz]	Test at 1000 V											
	C _x [pF]	u(C _x) [pF]	tanδ	u(tanδ)	tanδ _L	u(tanδ _L)	tanδ _{pol}	u(tanδ _{pol})	ε _r '	u(ε _r ')	ε _r ''	u(ε _r '')
0.1	96.7	1.1	1.115E-01	1.1E-03	1.015E-03	1.8E-05	1.105E-01	1.1E-03	2.592	0.033	2.864E-01	4.7E-03
1	96.3	1.1	1.120E-02	1.2E-04	1.019E-04	1.5E-06	1.110E-02	1.2E-04	2.582	0.033	2.866E-02	4.8E-04
10	96.3	1.1	1.389E-03	2.4E-05	1.020E-05	1.5E-07	1.379E-03	2.4E-05	2.581	0.033	3.560E-03	7.7E-05
50	96.3	1.1	5.55E-04	1.6E-05	2.040E-06	3.0E-08	5.52E-04	1.6E-05	2.580	0.033	1.425E-03	4.4E-05
100	96.2	1.1	4.66E-04	1.5E-05	1.020E-06	1.5E-08	4.65E-04	1.5E-05	2.580	0.033	1.199E-03	4.1E-05
150	96.2	1.1	4.44E-04	1.4E-05	6.802E-07	9.9E-09	4.44E-04	1.4E-05	2.580	0.033	1.144E-03	4.0E-05
350	96.2	1.1	4.19E-04	1.4E-05	2.916E-07	4.2E-09	4.18E-04	1.4E-05	2.579	0.033	1.079E-03	3.9E-05
500	96.2	1.1	4.11E-04	1.4E-05	2.041E-07	3.0E-09	4.11E-04	1.4E-05	2.579	0.033	1.059E-03	3.9E-05
1000	96.2	1.1	3.69E-04	1.4E-05	1.021E-07	1.5E-09	3.69E-04	1.4E-05	2.578	0.033	9.51E-04	3.7E-05

4. DISSIPATION FACTOR AND ELECTRIC PERMITTIVITY

Tab. 4.18 BamB02 results, 1500 V

Freq [Hz]	Test at 1500 V											
	C _x [pF]	u(C _x) [pF]	tanδ	u(tanδ)	tanδ _L	u(tanδ _L)	tanδ _{pol}	u(tanδ _{pol})	ε _r '	u(ε _r ')	ε _r ''	u(ε _r '')
0.1	96.7	1.1	1.156E-01	1.2E-03	1.016E-03	1.8E-05	1.146E-01	1.2E-03	2.592	0.033	2.970E-01	4.9E-03
1	96.3	1.1	1.159E-02	1.3E-04	1.019E-04	1.5E-06	1.149E-02	1.3E-04	2.582	0.033	2.966E-02	5.0E-04
10	96.3	1.1	1.410E-03	2.4E-05	1.020E-05	1.5E-07	1.400E-03	2.4E-05	2.581	0.033	3.614E-03	7.8E-05
50	96.3	1.1	5.59E-04	1.6E-05	2.040E-06	3.0E-08	5.57E-04	1.6E-05	2.580	0.033	1.438E-03	4.4E-05
100	96.2	1.1	4.70E-04	1.5E-05	1.020E-06	1.5E-08	4.69E-04	1.5E-05	2.580	0.033	1.209E-03	4.1E-05
150	96.2	1.1	4.44E-04	1.4E-05	6.802E-07	9.9E-09	4.43E-04	1.4E-05	2.580	0.033	1.143E-03	4.0E-05
350	96.2	1.1	4.19E-04	1.4E-05	2.916E-07	4.2E-09	4.19E-04	1.4E-05	2.579	0.033	1.080E-03	3.9E-05
500	96.2	1.1	4.11E-04	1.4E-05	2.041E-07	3.0E-09	4.11E-04	1.4E-05	2.579	0.033	1.059E-03	3.9E-05
1000	96.2	1.1	3.73E-04	1.4E-05	1.021E-07	1.5E-09	3.73E-04	1.4E-05	2.578	0.033	9.62E-04	3.8E-05

Tab. 4.19 BamP01 results, 2000 V

Freq [Hz]	Test at 2000 V											
	C _x [pF]	u(C _x) [pF]	tanδ	u(tanδ)	tanδ _L	u(tanδ _L)	tanδ _{pol}	u(tanδ _{pol})	ε _r '	u(ε _r ')	ε _r ''	u(ε _r '')
0.1	96.7	1.1	1.200E-01	1.2E-03	1.016E-03	1.8E-05	1.189E-01	1.2E-03	2.591	0.033	3.082E-01	5.0E-03
1	96.3	1.1	1.204E-02	1.3E-04	1.019E-04	1.5E-06	1.194E-02	1.3E-04	2.582	0.033	3.082E-02	5.2E-04
10	96.3	1.1	1.442E-03	2.4E-05	1.020E-05	1.5E-07	1.432E-03	2.4E-05	2.581	0.033	3.696E-03	7.9E-05
50	96.3	1.1	5.64E-04	1.6E-05	2.040E-06	3.0E-08	5.62E-04	1.6E-05	2.580	0.033	1.450E-03	4.4E-05
100	96.2	1.1	4.71E-04	1.5E-05	1.020E-06	1.5E-08	4.70E-04	1.5E-05	2.580	0.033	1.213E-03	4.1E-05
150	96.2	1.1	4.45E-04	1.4E-05	6.802E-07	9.9E-09	4.44E-04	1.4E-05	2.580	0.033	1.146E-03	4.0E-05
350	96.2	1.1	4.18E-04	1.4E-05	2.916E-07	4.2E-09	4.18E-04	1.4E-05	2.579	0.033	1.078E-03	3.9E-05
500	96.2	1.1	4.11E-04	1.4E-05	2.041E-07	3.0E-09	4.11E-04	1.4E-05	2.579	0.033	1.060E-03	3.9E-05
1000	96.2	1.1	3.65E-04	1.4E-05	1.021E-07	1.5E-09	3.65E-04	1.4E-05	2.578	0.033	9.42E-04	3.7E-05

The graphs of ESA 7250, related to dissipation factor and the two components of permittivity, are shown from Fig. 4.24 to Fig. 4.26.

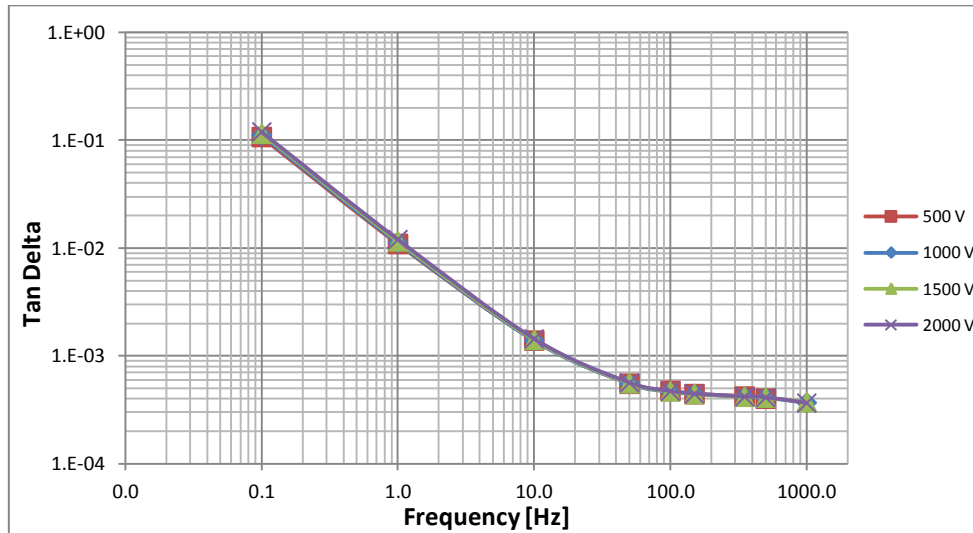


Fig. 4.24 BamB02 - Tan Delta

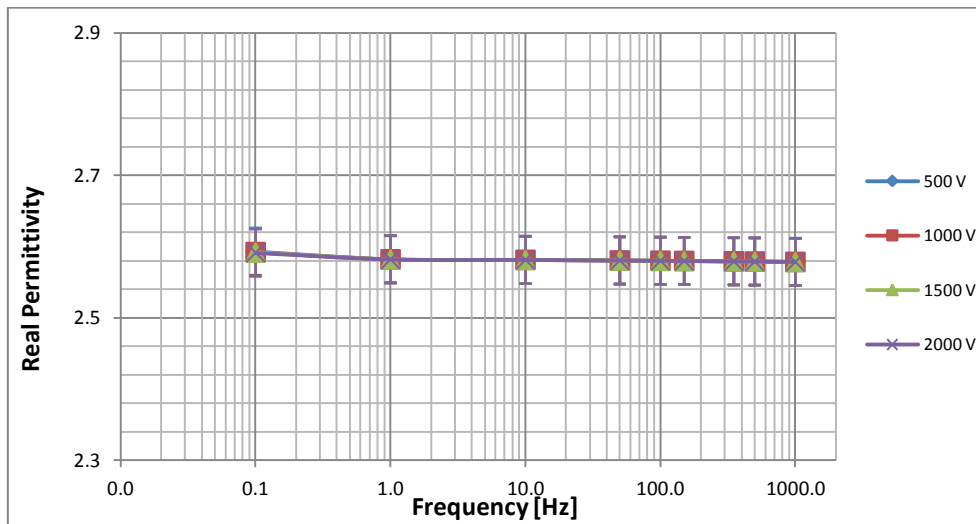


Fig. 4.25 BamB02 - Real Permittivity

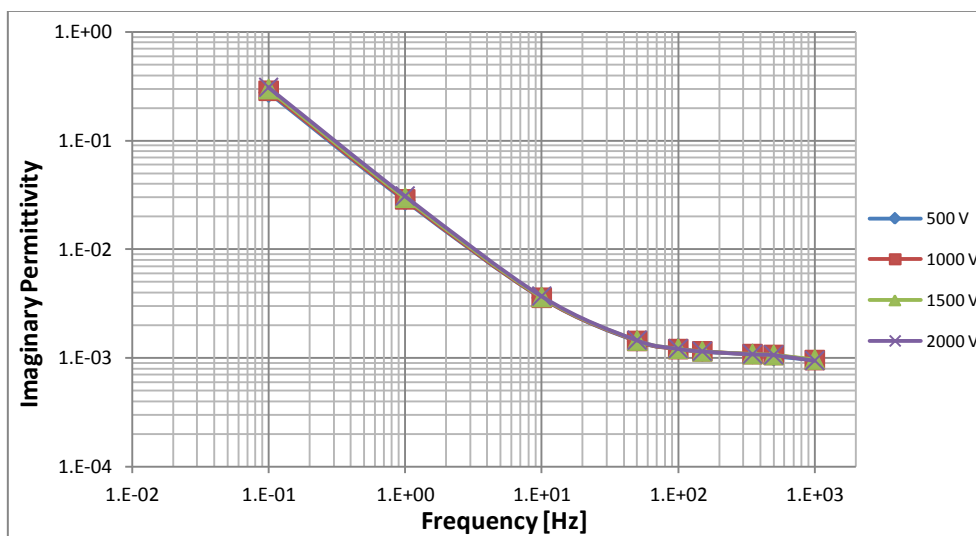


Fig. 4.26 BamB02 - Imaginary Permittivity

For the second protocol, the results of **RT 601** are presented in four tables, from Tab. 4.20 to Tab. 4.23, showing the dependence on voltage and frequency.

Tab. 4.20 BamD03 results, 500 V

Freq [Hz]	Test at 500 V											
	C_x [pF]	$u(C_x)$ [pF]	$\tan\delta$	$u(\tan\delta)$	$\tan\delta_L$	$u(\tan\delta_L)$	$\tan\delta_{pol}$	$u(\tan\delta_{pol})$	ϵ_r'	$u(\epsilon_r')$	ϵ_r''	$u(\epsilon_r'')$
0.1	92.5	1.1	4.356E-03	5.4E-05	4.90E-05	1.0E-06	4.307E-03	5.4E-05	2.659	0.035	1.145E-02	2.1E-04
1	92.4	1.1	1.004E-03	2.0E-05	4.900E-06	9.2E-08	9.99E-04	2.0E-05	2.658	0.035	2.657E-03	6.4E-05
10	92.4	1.1	2.48E-04	1.2E-05	4.900E-07	9.2E-09	2.47E-04	1.2E-05	2.658	0.035	6.57E-04	3.4E-05
50	92.4	1.1	2.17E-04	1.2E-05	9.80E-08	1.8E-09	2.17E-04	1.2E-05	2.658	0.035	5.76E-04	3.3E-05
100	92.4	1.1	2.41E-04	1.2E-05	4.902E-08	9.2E-10	2.41E-04	1.2E-05	2.657	0.035	6.39E-04	3.4E-05
150	92.4	1.1	2.65E-04	1.3E-05	3.268E-08	6.1E-10	2.65E-04	1.3E-05	2.657	0.035	7.03E-04	3.5E-05
350	92.4	1.1	3.00E-04	1.3E-05	1.401E-08	2.6E-10	3.00E-04	1.3E-05	2.657	0.035	7.97E-04	3.6E-05
500	92.4	1.1	3.24E-04	1.3E-05	9.81E-09	1.8E-10	3.24E-04	1.3E-05	2.657	0.035	8.60E-04	3.7E-05
1000	92.4	1.1	3.34E-04	1.3E-05	4.904E-09	9.2E-11	3.34E-04	1.3E-05	2.656	0.035	8.88E-04	3.7E-05

Tab. 4.21 BamD03 results, 1000 V

Freq [Hz]	Test at 1000 V											
	C_x [pF]	$u(C_x)$ [pF]	$\tan\delta$	$u(\tan\delta)$	$\tan\delta_L$	$u(\tan\delta_L)$	$\tan\delta_{pol}$	$u(\tan\delta_{pol})$	ϵ_r'	$u(\epsilon_r')$	ϵ_r''	$u(\epsilon_r'')$
0.1	92.5	1.1	6.434E-03	7.4E-05	4.90E-05	1.0E-06	6.385E-03	7.4E-05	2.659	0.035	1.698E-02	3.0E-04
1	92.4	1.1	1.007E-03	2.0E-05	4.900E-06	9.2E-08	1.002E-03	2.0E-05	2.658	0.035	2.664E-03	6.4E-05
10	92.4	1.1	2.58E-04	1.3E-05	4.901E-07	9.2E-09	2.58E-04	1.3E-05	2.658	0.035	6.85E-04	3.5E-05
50	92.4	1.1	2.30E-04	1.2E-05	9.80E-08	1.8E-09	2.30E-04	1.2E-05	2.658	0.035	6.10E-04	3.4E-05
100	92.4	1.1	2.49E-04	1.2E-05	4.902E-08	9.2E-10	2.49E-04	1.2E-05	2.657	0.035	6.62E-04	3.4E-05
150	92.4	1.1	2.65E-04	1.3E-05	3.268E-08	6.1E-10	2.65E-04	1.3E-05	2.657	0.035	7.04E-04	3.5E-05
350	92.4	1.1	3.07E-04	1.3E-05	1.401E-08	2.6E-10	3.07E-04	1.3E-05	2.657	0.035	8.16E-04	3.6E-05
500	92.4	1.1	3.22E-04	1.3E-05	9.81E-09	1.8E-10	3.22E-04	1.3E-05	2.657	0.035	8.55E-04	3.7E-05
1000	92.4	1.1	3.36E-04	1.3E-05	4.904E-09	9.2E-11	3.36E-04	1.3E-05	2.656	0.035	8.92E-04	3.7E-05

4. DISSIPATION FACTOR AND ELECTRIC PERMITTIVITY

Tab. 4.22 BamD03 results, 1500 V

Freq [Hz]	Test at 1500 V											
	C _x [pF]	u(C _x) [pF]	tanδ	u(tanδ)	tanδ _L	u(tanδ _L)	tanδ _{pol}	u(tanδ _{pol})	ε _r '	u(ε _r ')	ε _r ''	u(ε _r '')
0.1	92.5	1.1	7.901E-03	8.9E-05	4.90E-05	1.0E-06	7.852E-03	8.9E-05	2.659	0.035	2.088E-02	3.6E-04
1	92.4	1.1	1.024E-03	2.0E-05	4.900E-06	9.2E-08	1.019E-03	2.0E-05	2.658	0.035	2.708E-03	6.5E-05
10	92.4	1.1	2.74E-04	1.3E-05	4.900E-07	9.2E-09	2.73E-04	1.3E-05	2.658	0.035	7.26E-04	3.5E-05
50	92.4	1.1	2.44E-04	1.2E-05	9.80E-08	1.8E-09	2.44E-04	1.2E-05	2.658	0.035	6.48E-04	3.4E-05
100	92.4	1.1	2.60E-04	1.3E-05	4.902E-08	9.2E-10	2.60E-04	1.3E-05	2.657	0.035	6.91E-04	3.5E-05
150	92.4	1.1	2.76E-04	1.3E-05	3.268E-08	6.1E-10	2.76E-04	1.3E-05	2.657	0.035	7.32E-04	3.5E-05
350	92.4	1.1	3.18E-04	1.3E-05	1.401E-08	2.6E-10	3.18E-04	1.3E-05	2.657	0.035	8.46E-04	3.7E-05
500	92.4	1.1	3.33E-04	1.3E-05	9.81E-09	1.8E-10	3.33E-04	1.3E-05	2.657	0.035	8.85E-04	3.7E-05
1000	92.4	1.1	3.49E-04	1.3E-05	4.904E-09	9.2E-11	3.49E-04	1.3E-05	2.656	0.035	9.26E-04	3.8E-05

Tab. 4.23 BamD03 results, 2000 V

Freq [Hz]	Test at 2000 V											
	C _x [pF]	u(C _x) [pF]	tanδ	u(tanδ)	tanδ _L	u(tanδ _L)	tanδ _{pol}	u(tanδ _{pol})	ε _r '	u(ε _r ')	ε _r ''	u(ε _r '')
0.1	92.5	1.1	9.01E-03	1.0E-04	4.90E-05	1.0E-06	8.97E-03	1.0E-04	2.659	0.035	2.384E-02	4.1E-04
1	92.4	1.1	1.068E-03	2.1E-05	4.900E-06	9.2E-08	1.063E-03	2.1E-05	2.659	0.035	2.827E-03	6.7E-05
10	92.4	1.1	2.92E-04	1.3E-05	4.900E-07	9.2E-09	2.91E-04	1.3E-05	2.658	0.035	7.74E-04	3.6E-05
50	92.4	1.1	2.59E-04	1.3E-05	9.80E-08	1.8E-09	2.59E-04	1.3E-05	2.658	0.035	6.87E-04	3.5E-05
100	92.4	1.1	2.76E-04	1.3E-05	4.902E-08	9.2E-10	2.76E-04	1.3E-05	2.657	0.035	7.33E-04	3.5E-05
150	92.4	1.1	2.90E-04	1.3E-05	3.268E-08	6.1E-10	2.90E-04	1.3E-05	2.657	0.035	7.70E-04	3.6E-05
350	92.4	1.1	3.28E-04	1.3E-05	1.401E-08	2.6E-10	3.28E-04	1.3E-05	2.657	0.035	8.72E-04	3.7E-05
500	92.4	1.1	3.46E-04	1.3E-05	9.81E-09	1.8E-10	3.46E-04	1.3E-05	2.657	0.035	9.19E-04	3.8E-05
1000	92.4	1.1	3.53E-04	1.4E-05	4.904E-09	9.2E-11	3.53E-04	1.4E-05	2.656	0.035	9.38E-04	3.8E-05

The charts of silicone RT 601, related to BamD02 results, are illustrated in the next figures, from Fig. 4.27 to Fig. 4.29.

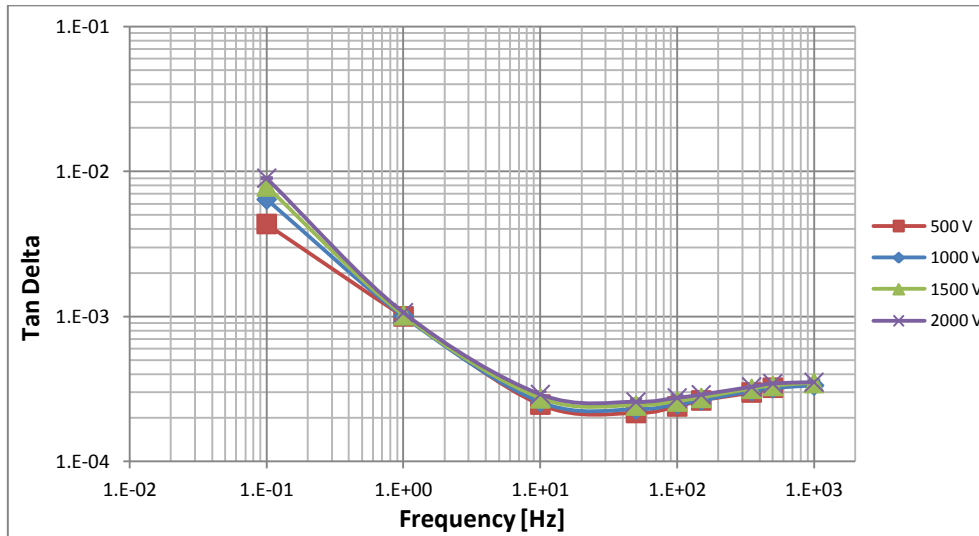


Fig. 4.27 BamD03 - Tan Delta

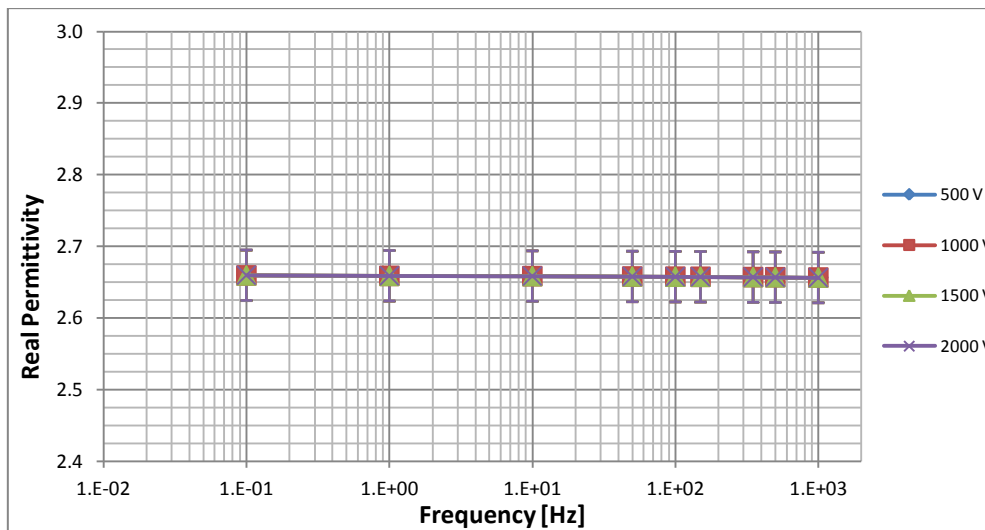


Fig. 4.28 BamD03 - Real Permittivity

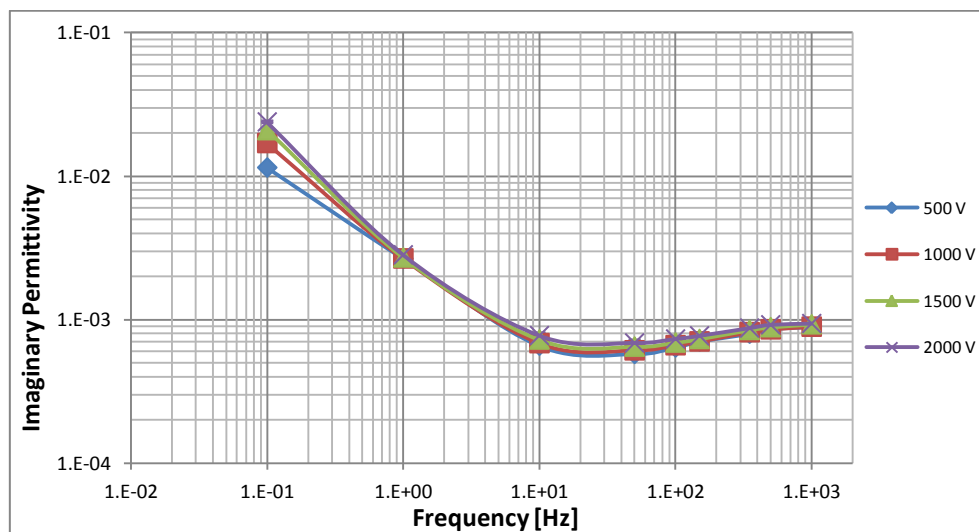


Fig. 4.29 BamD03 - Imaginary Permittivity

The last specimen of the second protocol is the BamP03 of **Powersil 600**, which provides the outcomes from Tab. 4.26 to tab. 4.29.

Tab. 4.24 BamP03 results, 500 V

Freq [Hz]	Test at 500 V											
	C_x [pF]	$u(C_x)$ [pF]	$\tan\delta$	$u(\tan\delta)$	$\tan\delta_L$	$u(\tan\delta_L)$	$\tan\delta_{pol}$	$u(\tan\delta_{pol})$	ϵ_r'	$u(\epsilon_r')$	ϵ_r''	$u(\epsilon_r'')$
0.1	95.5	1.1	2.332E-03	3.3E-05	1.747E-06	4.9E-08	2.330E-03	3.3E-05	2.215	0.041	5.16E-03	1.2E-04
1	95.2	1.1	1.726E-03	2.7E-05	1.753E-07	4.6E-09	1.726E-03	2.7E-05	2.207	0.040	3.809E-03	9.2E-05
10	95.0	1.1	8.57E-04	1.9E-05	1.756E-08	4.6E-10	8.57E-04	1.9E-05	2.203	0.040	1.888E-03	5.4E-05
50	95.0	1.1	5.17E-04	1.5E-05	3.515E-09	9.3E-11	5.17E-04	1.5E-05	2.202	0.040	1.138E-03	3.9E-05
100	95.0	1.1	4.36E-04	1.4E-05	1.758E-09	4.6E-11	4.36E-04	1.4E-05	2.201	0.040	9.59E-04	3.6E-05
150	95.0	1.1	3.87E-04	1.4E-05	1.172E-09	3.1E-11	3.87E-04	1.4E-05	2.201	0.040	8.52E-04	3.4E-05
350	94.9	1.1	2.96E-04	1.3E-05	5.02E-10	1.3E-11	2.96E-04	1.3E-05	2.201	0.040	6.52E-04	3.1E-05
500	94.9	1.1	2.54E-04	1.3E-05	3.517E-10	9.3E-12	2.54E-04	1.3E-05	2.201	0.040	5.60E-04	2.9E-05
1000	94.9	1.1	1.63E-04	1.2E-05	1.759E-10	4.6E-12	1.63E-04	1.2E-05	2.200	0.040	3.58E-04	2.6E-05

Tab. 4.25 BamP03 results, 1000 V

Freq [Hz]	Test at 1000 V											
	C_x [pF]	$u(C_x)$ [pF]	$\tan\delta$	$u(\tan\delta)$	$\tan\delta_L$	$u(\tan\delta_L)$	$\tan\delta_{pol}$	$u(\tan\delta_{pol})$	ϵ_r'	$u(\epsilon_r')$	ϵ_r''	$u(\epsilon_r'')$
0.1	95.5	1.1	2.348E-03	3.3E-05	1.747E-06	4.9E-08	2.346E-03	3.3E-05	2.215	0.041	5.20E-03	1.2E-04
1	95.2	1.1	1.808E-03	2.8E-05	1.753E-07	4.6E-09	1.808E-03	2.8E-05	2.207	0.040	3.990E-03	9.6E-05
10	95.0	1.1	8.76E-04	1.9E-05	1.756E-08	4.6E-10	8.76E-04	1.9E-05	2.203	0.040	1.929E-03	5.4E-05
50	95.0	1.1	5.33E-04	1.5E-05	3.515E-09	9.3E-11	5.33E-04	1.5E-05	2.202	0.040	1.173E-03	4.0E-05
100	95.0	1.1	4.38E-04	1.4E-05	1.758E-09	4.6E-11	4.38E-04	1.4E-05	2.201	0.040	9.65E-04	3.6E-05
150	95.0	1.1	3.89E-04	1.4E-05	1.172E-09	3.1E-11	3.89E-04	1.4E-05	2.201	0.040	8.57E-04	3.4E-05
350	94.9	1.1	3.01E-04	1.3E-05	5.02E-10	1.3E-11	3.01E-04	1.3E-05	2.201	0.040	6.63E-04	3.1E-05
500	94.9	1.1	2.63E-04	1.3E-05	3.517E-10	9.3E-12	2.63E-04	1.3E-05	2.201	0.040	5.80E-04	3.0E-05
1000	94.9	1.1	1.62E-04	1.2E-05	1.759E-10	4.6E-12	1.62E-04	1.2E-05	2.200	0.040	3.57E-04	2.6E-05

Tab. 4.26 BamP03 results, 1500 V

Freq [Hz]	Test at 1500 V											
	C_x [pF]	$u(C_x)$ [pF]	$\tan\delta$	$u(\tan\delta)$	$\tan\delta_L$	$u(\tan\delta_L)$	$\tan\delta_{pol}$	$u(\tan\delta_{pol})$	ϵ_r'	$u(\epsilon_r')$	ϵ_r''	$u(\epsilon_r'')$
0.1	95.5	1.1	2.380E-03	3.4E-05	1.747E-06	4.9E-08	2.379E-03	3.4E-05	2.215	0.041	5.268E-03	1.2E-04
1	95.2	1.1	1.814E-03	2.8E-05	1.753E-07	4.6E-09	1.814E-03	2.8E-05	2.207	0.040	4.004E-03	9.6E-05
10	95.0	1.1	8.99E-04	1.9E-05	1.756E-08	4.6E-10	8.99E-04	1.9E-05	2.203	0.040	1.981E-03	5.5E-05
50	95.0	1.1	5.52E-04	1.6E-05	3.515E-09	9.3E-11	5.52E-04	1.6E-05	2.202	0.040	1.215E-03	4.1E-05
100	95.0	1.1	4.58E-04	1.5E-05	1.758E-09	4.6E-11	4.58E-04	1.5E-05	2.201	0.040	1.009E-03	3.7E-05
150	95.0	1.1	4.08E-04	1.4E-05	1.172E-09	3.1E-11	4.08E-04	1.4E-05	2.201	0.040	8.99E-04	3.5E-05
350	94.9	1.1	3.17E-04	1.3E-05	5.02E-10	1.3E-11	3.17E-04	1.3E-05	2.201	0.040	6.97E-04	3.2E-05
500	94.9	1.1	2.73E-04	1.3E-05	3.517E-10	9.3E-12	2.73E-04	1.3E-05	2.201	0.040	6.00E-04	3.0E-05
1000	94.9	1.1	1.74E-04	1.2E-05	1.759E-10	4.6E-12	1.74E-04	1.2E-05	2.200	0.040	3.83E-04	2.7E-05

Tab. 4.27 BamP03 results, 2000 V

Freq [Hz]	Test at 2000 V											
	C_x [pF]	$u(C_x)$ [pF]	$\tan\delta$	$u(\tan\delta)$	$\tan\delta_L$	$u(\tan\delta_L)$	$\tan\delta_{pol}$	$u(\tan\delta_{pol})$	ϵ_r'	$u(\epsilon_r')$	ϵ_r''	$u(\epsilon_r'')$
0.1	95.5	1.1	2.506E-03	3.5E-05	1.747E-06	4.9E-08	2.504E-03	3.5E-05	2.215	0.041	5.55E-03	1.3E-04
1	95.2	1.1	1.825E-03	2.8E-05	1.753E-07	4.6E-09	1.825E-03	2.8E-05	2.207	0.040	4.029E-03	9.7E-05
10	95.0	1.1	9.16E-04	1.9E-05	1.756E-08	4.6E-10	9.16E-04	1.9E-05	2.203	0.040	2.017E-03	5.6E-05
50	95.0	1.1	5.73E-04	1.6E-05	3.515E-09	9.3E-11	5.73E-04	1.6E-05	2.202	0.040	1.263E-03	4.2E-05
100	95.0	1.1	4.75E-04	1.5E-05	1.758E-09	4.6E-11	4.75E-04	1.5E-05	2.201	0.040	1.046E-03	3.8E-05
150	95.0	1.1	4.25E-04	1.4E-05	1.172E-09	3.1E-11	4.25E-04	1.4E-05	2.201	0.040	9.36E-04	3.6E-05
350	94.9	1.1	3.30E-04	1.3E-05	5.02E-10	1.3E-11	3.30E-04	1.3E-05	2.201	0.040	7.27E-04	3.2E-05
500	94.9	1.1	2.85E-04	1.3E-05	3.517E-10	9.3E-12	2.85E-04	1.3E-05	2.201	0.040	6.26E-04	3.1E-05
1000	94.9	1.1	1.79E-04	1.2E-05	1.759E-10	4.6E-12	1.79E-04	1.2E-05	2.200	0.040	3.93E-04	2.7E-05

Regarding the BamP03, three graphs illustrate its obtained quantities: from Fig. 4.30 to Fig. 4.32.

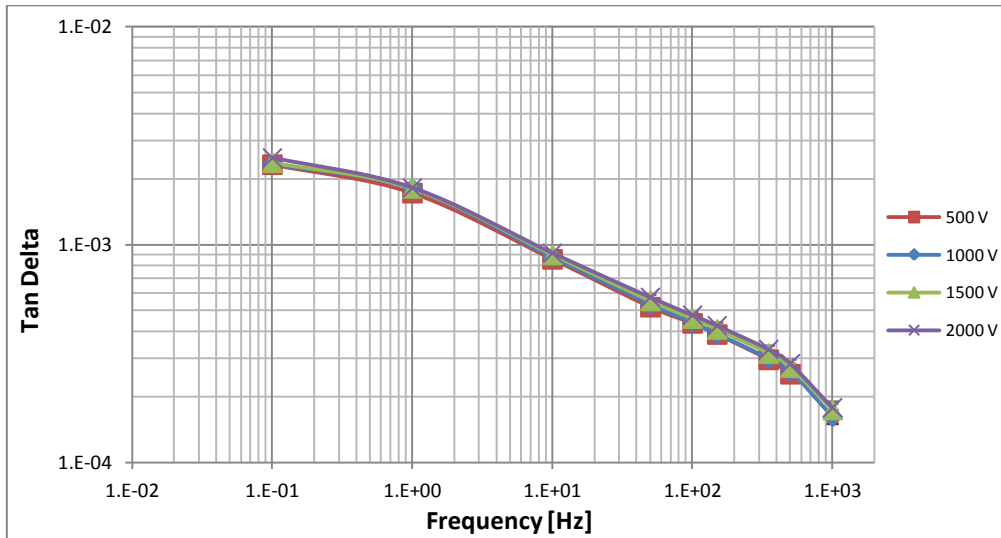


Fig. 4.30 BamP03 - Tan Delta

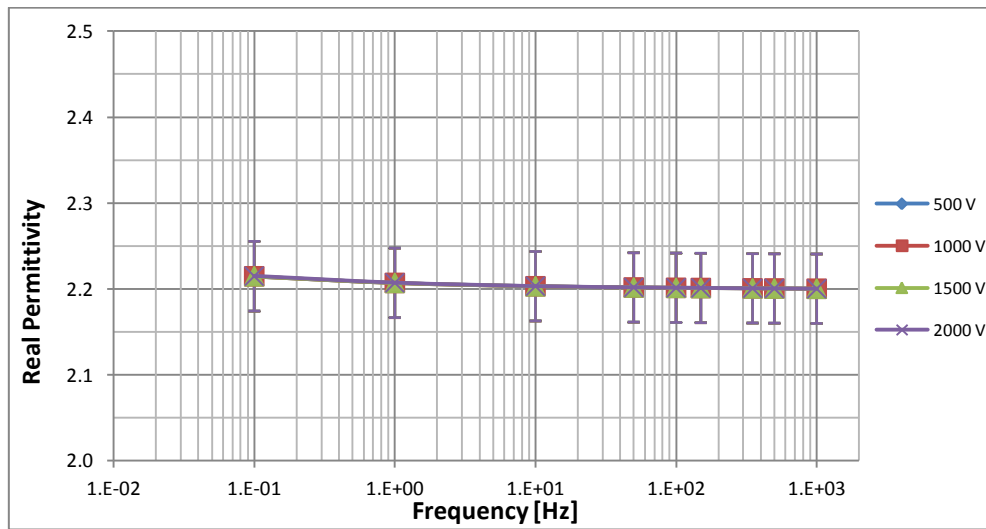


Fig. 4.31 BamP03 - Real Permittivity

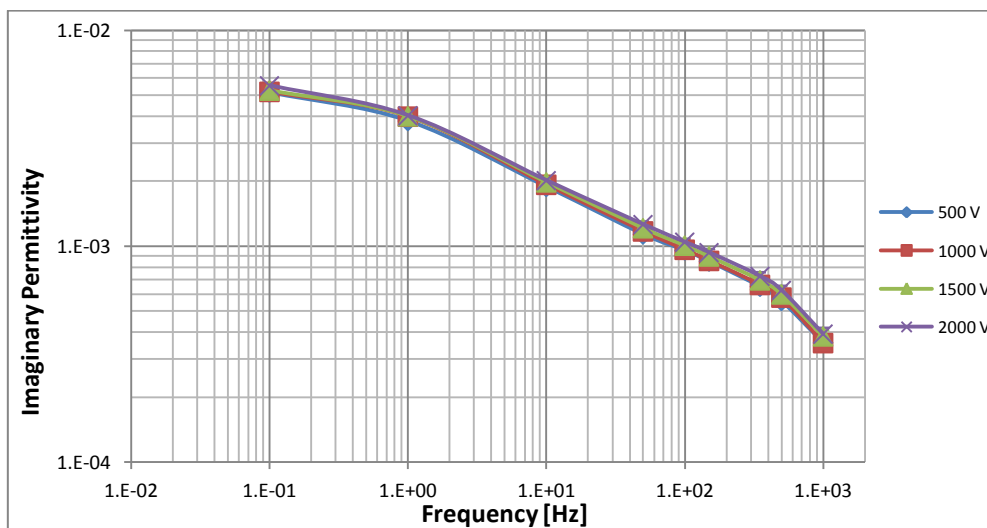


Fig. 4.32 BamP03 - Imaginary Permittivity

In the following graphs (from Fig. 4.33 to Fig. 4.35) the different silicone rubbers are compared, according to the outcomes of principal quantities at 500 V.

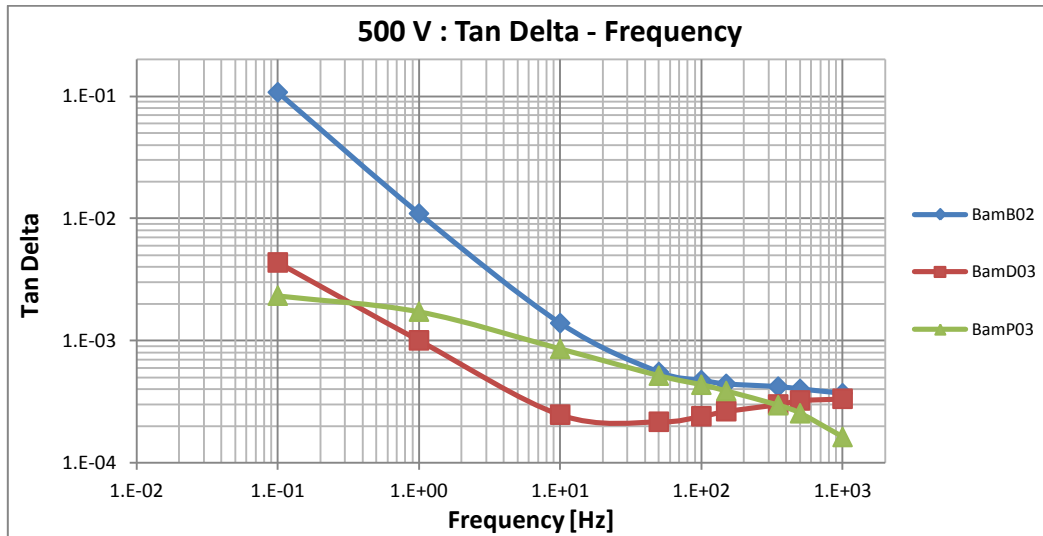


Fig. 4.33 Second protocol: Tan Delta comparison (500 V)

Starting with the **dissipation factor** considerations, the only correlation with the voltage applied is detectable only at 0.1 Hz (a small growth of $\tan\delta$ when the voltage increases); in general, for the other frequencies, also considering the computed uncertainties, the dissipation factor does not show a dependence on the voltage in all the tested materials (considering the results from Tab. 4.16 to Tab. 4.27).

In general, the behavior of $\tan\delta$ with respect to the frequency is different in each silicone (referring to Fig. 4.33). In the initial portion of frequencies (0.1 – 50 Hz), the dissipation factors of all the specimens reduces considerably; it is the most pronounced effect, which shows the reduction of collisions (and, hence, heat dissipation) of big/heavy elements that do not follow the alternating electric field.

After this fall, continuing to increase the frequency, ESA 7250 reaches a quite stable (only a very small reduction is detected, Fig. 4.24). The $\tan\delta_{pol}$ decreases in the same manner, while $\tan\delta_L$ continues to reduce more intensely (according to its basic expression).

About the RT 601, after the initial reduction its dissipation factor (coincident with $\tan\delta_{pol}$) tends to slightly increase with the frequency (Fig. 4.27); anyway, the conductive component $\tan\delta_L$ continues to reduce (the only variable in its formula is the frequency). Remaining C_x stable with the frequency, the number of polarized molecules is the same, but the intensity and quantity of collisions vary, according to Tab. 4.20.

The dissipation factor of Powersil 600 has a small reduction moving the initial frequencies on (with respect to the other silicones) and it continues to decrease (with an higher slope at high frequencies), as illustrated in Fig. 4.30 and Fig. 4.33. At the end, the $\tan\delta$ reduces of one order of magnitude. The tiny decrease of the dielectric constant could not be asserted, due to its uncertainty; or the reductions of these two quantities could suggest an overcome of resonance frequency ($\omega = 1/\tau$) of a polarization mechanism.

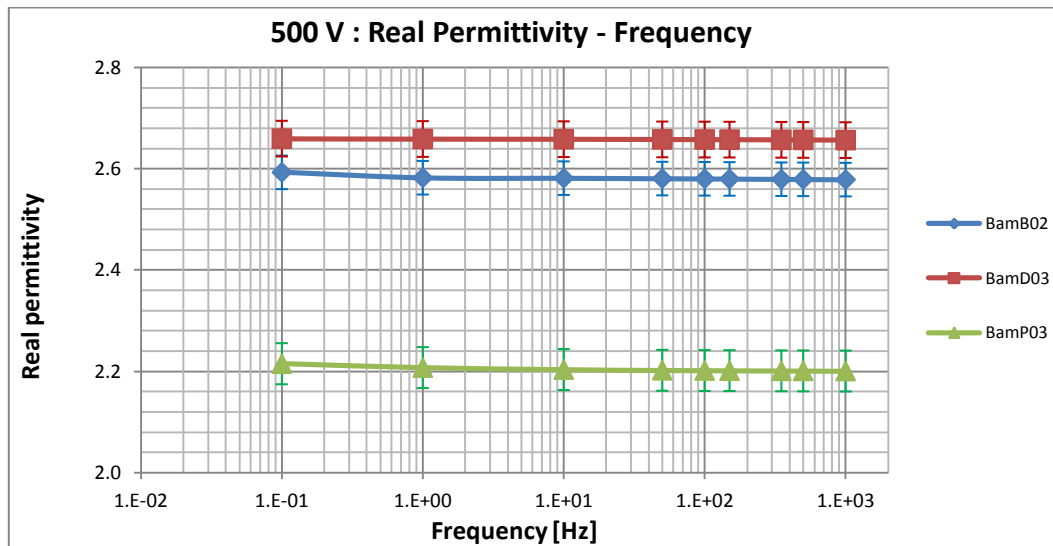


Fig. 4.34 Second protocol: Real Permittivity comparison (500 V)

Considering the **real part of permittivity**, it remains definitely constant over the range of test frequencies; in fact, the computed uncertainties conceal the minimal reduction of ESA 7250 and Powersil 600 (in particular at 0.1 Hz), shown in Fig. 4.25 and Fig. 4.28.

It suggests that the elements experiencing the polarization are the same, with the same mechanism; in particular, this regularity up to 1 kHz may indicate that only small elements are involved in the medium's polarization.

The highest dielectric constants belong to ESA 7250 and RT 601 (Fig. 4.34), as reported in the first protocol.

The **imaginary part of permittivity**, shown in Fig. 4.35, essentially corresponds to the loss tangent, being ϵ_r' constant in this test.

It depends a lot on the frequency and it generally decreases with it; molecules or dipoles that do not contribute to polarization, but subjected to the alternating field by producing heat from collisions, lose their involvement with losses at high frequencies.

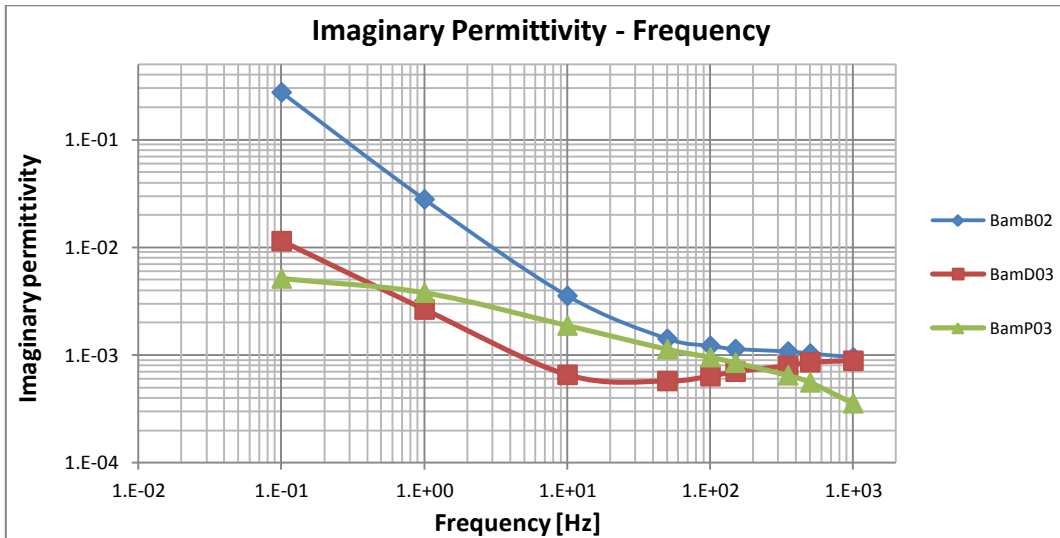


Fig. 4.35 Second protocol: Imaginary Permittivity comparison (500 V)

Also in the second protocol, it is noticeable the independence between the polarization of these dielectric materials and their losses: the elements experiencing the polarization are the same at different frequencies, but their losses strictly depend on it.

The Powersil 600 and RT 601 present the least interaction with the frequency in the analyzed silicones, opposed by the ESA7250 (that reaches a dissipation factor about 10^{-1} at 0.1 Hz), as indicated from Fig. 4.33 to Fig. 4.35.

The last protocol of loss tangent test is conducted at constant voltage, equal to 500 V.

The results of **ESA 7250**, related to the specimen BamB05, are reported in the next three tables, from Tab. 4.28 to Tab. 4.30.

Tab. 4.28 BamB05 results, 25°C

Freq [Hz]	Temperature at 25 °C											
	C _x [pF]	u(C _x) [pF]	tanδ	u(tanδ)	tanδ _L	u(tanδ _L)	tanδ _{pol}	u(tanδ _{pol})	ε _r '	u(ε _r ')	ε _r ''	u(ε _r '')
0.1	97.4	1.1	7.214E-02	7.3E-04	8.76E-04	1.6E-05	7.126E-02	7.3E-04	2.607	0.034	1.858E-01	3.1E-03
1	97.3	1.1	7.315E-03	8.3E-05	8.77E-05	1.3E-06	7.227E-03	8.3E-05	2.605	0.034	1.882E-02	3.3E-04
10	97.3	1.1	9.60E-04	2.0E-05	8.77E-06	1.3E-07	9.51E-04	2.0E-05	2.604	0.034	2.478E-03	6.0E-05
50	97.3	1.1	4.47E-04	1.4E-05	1.755E-06	2.6E-08	4.45E-04	1.4E-05	2.603	0.034	1.160E-03	4.1E-05
100	97.2	1.1	3.98E-04	1.4E-05	8.78E-07	1.3E-08	3.97E-04	1.4E-05	2.603	0.034	1.034E-03	3.9E-05
150	97.2	1.1	3.90E-04	1.4E-05	5.853E-07	8.8E-09	3.89E-04	1.4E-05	2.602	0.034	1.013E-03	3.9E-05
350	97.2	1.1	3.81E-04	1.4E-05	2.509E-07	3.8E-09	3.81E-04	1.4E-05	2.602	0.034	9.911E-04	3.8E-05
500	97.2	1.1	3.71E-04	1.4E-05	1.756E-07	2.6E-09	3.70E-04	1.4E-05	2.602	0.034	9.637E-04	3.8E-05
1000	97.2	1.1	3.25E-04	1.3E-05	8.78E-08	1.3E-09	3.25E-04	1.3E-05	2.601	0.034	8.457E-04	3.6E-05

Tab. 4.29 BamB05 results, 50°C

Freq [Hz]	Temperature at 50 °C											
	C _x [pF]	u(C _x) [pF]	tanδ	u(tanδ)	tanδ _L	u(tanδ _L)	tanδ _{pol}	u(tanδ _{pol})	ε _r '	u(ε _r ')	ε _r ''	u(ε _r '')
0.1	95.5	1.1	4.278E-01	4.3E-03	3.630E-03	6.6E-05	4.241E-01	4.3E-03	2.555	0.034	1.084E+00	1.8E-02
1	93.4	1.1	4.517E-02	4.6E-04	3.711E-04	5.7E-06	4.479E-02	4.6E-04	2.499	0.033	1.119E-01	1.9E-03
10	93.3	1.1	4.700E-03	5.7E-05	3.713E-05	5.7E-07	4.663E-03	5.7E-05	2.498	0.033	1.165E-02	2.1E-04
50	93.3	1.1	1.121E-03	2.1E-05	7.43E-06	1.1E-07	1.114E-03	2.1E-05	2.497	0.033	2.782E-03	6.5E-05
100	93.2	1.1	7.01E-04	1.7E-05	3.717E-06	5.7E-08	6.98E-04	1.7E-05	2.495	0.033	1.741E-03	4.8E-05
150	93.2	1.1	5.54E-04	1.6E-05	2.478E-06	3.8E-08	5.52E-04	1.6E-05	2.495	0.033	1.377E-03	4.3E-05
350	93.2	1.1	3.82E-04	1.4E-05	1.062E-06	1.6E-08	3.81E-04	1.4E-05	2.494	0.033	9.51E-04	3.7E-05
500	93.2	1.1	3.39E-04	1.3E-05	7.44E-07	1.1E-08	3.38E-04	1.3E-05	2.494	0.033	8.43E-04	3.5E-05
1000	93.1	1.1	2.68E-04	1.3E-05	3.721E-07	5.7E-09	2.67E-04	1.3E-05	2.492	0.033	6.66E-04	3.3E-05

Tab. 4.30 BamB05 results, 100°C

Freq [Hz]	Temperature at 100 °C											
	C_x [pF]	$u(C_x)$ [pF]	$\tan\delta$	$u(\tan\delta)$	$\tan\delta_L$	$u(\tan\delta_L)$	$\tan\delta_{pol}$	$u(\tan\delta_{pol})$	ϵ_r'	$u(\epsilon_r')$	ϵ_r''	$u(\epsilon_r'')$
0.1	129.6	1.1	3.276E+00	3.3E-02	2.371E-02	3.9E-04	3.253E+00	3.3E-02	3.469	0.038	1.128E+01	1.7E-01
1	94.4	1.1	5.658E-01	5.7E-03	3.258E-03	5.0E-05	5.625E-01	5.7E-03	2.525	0.034	1.420E+00	2.4E-02
10	87.4	1.1	6.705E-02	6.8E-04	3.519E-04	5.6E-06	6.670E-02	6.8E-04	2.338	0.033	1.560E-01	2.7E-03
50	87.2	1.1	1.362E-02	1.5E-04	7.05E-05	1.1E-06	1.355E-02	1.5E-04	2.333	0.033	3.161E-02	5.6E-04
100	87.1	1.1	6.955E-03	8.0E-05	3.531E-05	5.6E-07	6.919E-03	8.0E-05	2.330	0.033	1.612E-02	2.9E-04
150	87.1	1.1	4.686E-03	5.7E-05	2.354E-05	3.7E-07	4.663E-03	5.7E-05	2.330	0.033	1.086E-02	2.0E-04
350	87.0	1.1	2.094E-03	3.1E-05	1.009E-05	1.6E-07	2.084E-03	3.1E-05	2.329	0.033	4.855E-03	9.9E-05
500	87.1	1.1	1.485E-03	2.5E-05	7.06E-06	1.1E-07	1.478E-03	2.5E-05	2.330	0.033	3.442E-03	7.5E-05
1000	86.6	1.1	8.23E-04	1.8E-05	3.551E-06	5.6E-08	8.20E-04	1.8E-05	2.317	0.033	1.899E-03	5.0E-05

The graphs related to the results of ESA 7250 are illustrated in the next three figures, from Fig. 4.36 to Fig. 4.38.

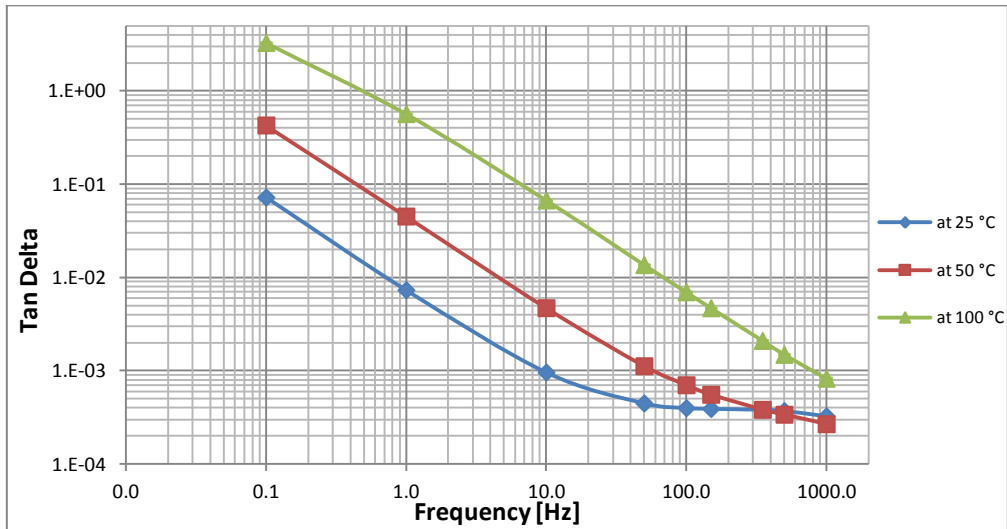


Fig. 4.36 BamB05 - Tan Delta

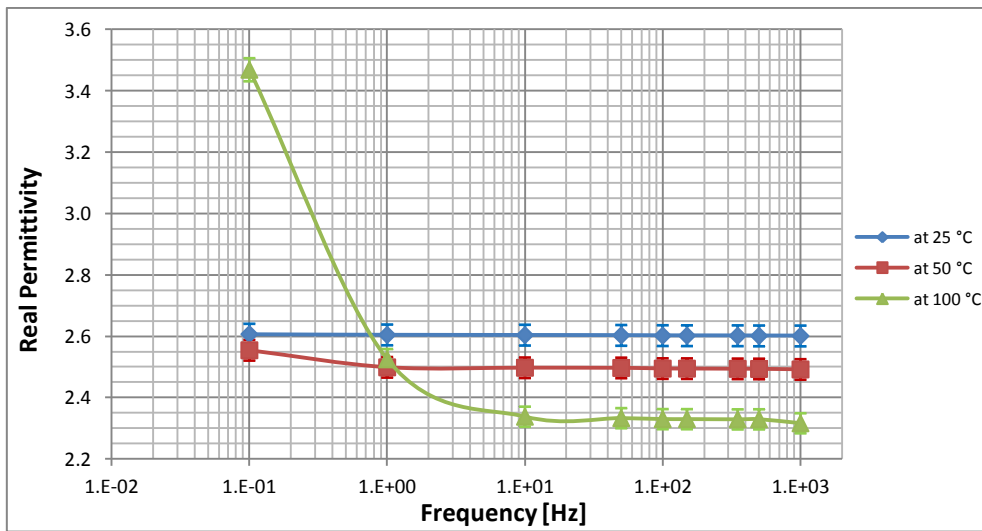


Fig. 4.37 BamB05 - Real Permittivity

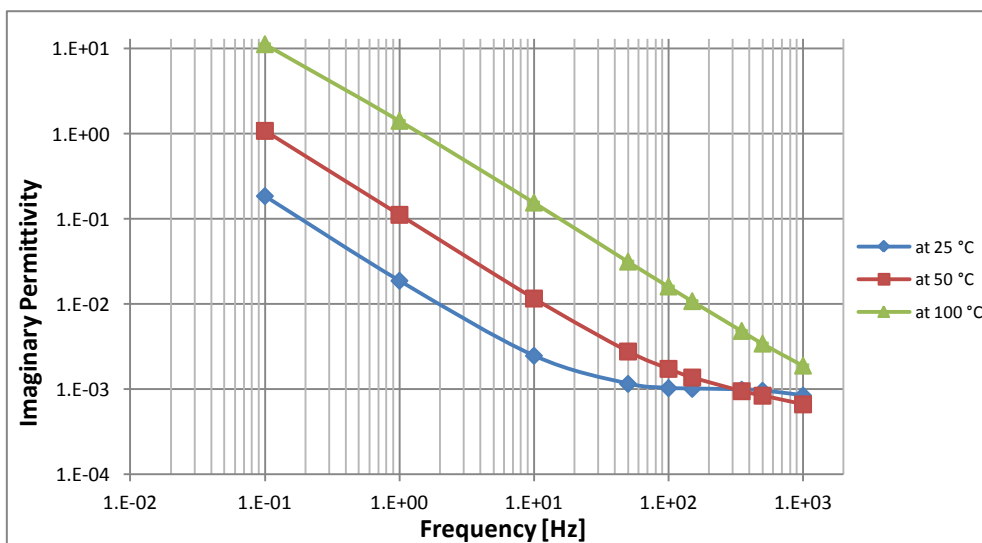


Fig. 4.38 BamB05 - Imaginary Permittivity

The specimen BamD04 provides the outcomes of the third protocol for the silicone **RT 601** and its results are reported from Tab. 4.31 to Tab. 4.33.

Tab. 4.31 BamD04 results, 25°C

Freq [Hz]	Temperature at 25 °C											
	C_x [pF]	$u(C_x)$ [pF]	$\tan\delta$	$u(\tan\delta)$	$\tan\delta_L$	$u(\tan\delta_L)$	$\tan\delta_{pol}$	$u(\tan\delta_{pol})$	ϵ_r'	$u(\epsilon_r')$	ϵ_r''	$u(\epsilon_r'')$
0.1	95.2	1.1	3.213E-03	4.2E-05	2.896E-05	6.4E-07	3.184E-03	4.2E-05	2.546	0.035	8.11E-03	1.5E-04
1	95.2	1.1	3.76E-04	1.4E-05	2.897E-06	5.7E-08	3.73E-04	1.4E-05	2.546	0.035	9.50E-04	3.7E-05
10	95.2	1.1	1.16E-04	1.1E-05	2.897E-07	5.7E-09	1.16E-04	1.1E-05	2.545	0.035	2.94E-04	2.9E-05
50	95.2	1.1	2.50E-04	1.2E-05	5.79E-08	1.1E-09	2.50E-04	1.2E-05	2.545	0.035	6.36E-04	3.3E-05
100	95.2	1.1	2.35E-04	1.2E-05	2.898E-08	5.7E-10	2.35E-04	1.2E-05	2.545	0.035	5.98E-04	3.2E-05
150	95.2	1.1	2.58E-04	1.3E-05	1.932E-08	3.8E-10	2.58E-04	1.3E-05	2.544	0.035	6.55E-04	3.3E-05
350	95.2	1.1	3.20E-04	1.3E-05	8.28E-09	1.6E-10	3.20E-04	1.3E-05	2.544	0.035	8.14E-04	3.5E-05
500	95.2	1.1	3.55E-04	1.4E-05	5.80E-09	1.1E-10	3.55E-04	1.4E-05	2.544	0.035	9.03E-04	3.7E-05
1000	95.1	1.1	4.10E-04	1.4E-05	2.899E-09	5.7E-11	4.10E-04	1.4E-05	2.543	0.035	1.043E-03	3.9E-05

Tab. 4.32 BamD04 results, 50°C

Freq [Hz]	Temperature at 50 °C											
	C_x [pF]	$u(C_x)$ [pF]	$\tan\delta$	$u(\tan\delta)$	$\tan\delta_L$	$u(\tan\delta_L)$	$\tan\delta_{pol}$	$u(\tan\delta_{pol})$	ϵ_r'	$u(\epsilon_r')$	ϵ_r''	$u(\epsilon_r'')$
0.1	91.2	1.1	8.796E-03	9.8E-05	7.39E-05	1.5E-06	8.722E-03	9.8E-05	2.437	0.034	2.126E-02	3.8E-04
1	91.2	1.1	6.97E-04	1.7E-05	7.39E-06	1.3E-07	6.89E-04	1.7E-05	2.437	0.034	1.679E-03	4.8E-05
10	91.2	1.1	1.57E-04	1.2E-05	7.39E-07	1.3E-08	1.57E-04	1.2E-05	2.437	0.034	3.81E-04	2.9E-05
50	91.1	1.1	2.50E-04	1.3E-05	1.478E-07	2.5E-09	2.50E-04	1.3E-05	2.436	0.034	6.09E-04	3.2E-05
100	91.1	1.1	1.25E-04	1.1E-05	7.39E-08	1.3E-09	1.24E-04	1.1E-05	2.436	0.034	3.03E-04	2.8E-05
150	91.1	1.1	1.40E-04	1.1E-05	4.928E-08	8.5E-10	1.39E-04	1.1E-05	2.436	0.034	3.40E-04	2.8E-05
350	91.1	1.1	1.80E-04	1.2E-05	2.112E-08	3.6E-10	1.80E-04	1.2E-05	2.436	0.034	4.39E-04	2.9E-05
500	91.1	1.1	1.92E-04	1.2E-05	1.479E-08	2.6E-10	1.92E-04	1.2E-05	2.436	0.034	4.68E-04	3.0E-05
1000	91.1	1.1	2.39E-04	1.2E-05	7.39E-09	1.3E-10	2.39E-04	1.2E-05	2.436	0.034	5.82E-04	3.1E-05

Tab. 4.33 BamD04 results, 100°C

Freq [Hz]	Temperature at 100 °C											
	C_x [pF]	$u(C_x)$ [pF]	$\tan\delta$	$u(\tan\delta)$	$\tan\delta_L$	$u(\tan\delta_L)$	$\tan\delta_{pol}$	$u(\tan\delta_{pol})$	ϵ_r'	$u(\epsilon_r')$	ϵ_r''	$u(\epsilon_r'')$
0.1	84.0	1.1	2.577E-02	2.7E-04	7.68E-05	1.6E-06	2.569E-02	2.7E-04	2.245	0.034	5.77E-02	1.1E-03
1	83.9	1.1	3.417E-03	4.4E-05	7.69E-06	1.4E-07	3.409E-03	4.4E-05	2.242	0.034	7.64E-03	1.5E-04
10	83.9	1.1	4.31E-04	1.4E-05	7.69E-07	1.4E-08	4.31E-04	1.4E-05	2.242	0.034	9.65E-04	3.5E-05
50	83.9	1.1	3.37E-04	1.3E-05	1.538E-07	2.8E-09	3.37E-04	1.3E-05	2.242	0.034	7.56E-04	3.2E-05
100	83.9	1.1	1.30E-04	1.1E-05	7.69E-08	1.4E-09	1.30E-04	1.1E-05	2.242	0.034	2.91E-04	2.6E-05
150	83.8	1.1	1.07E-04	1.1E-05	5.128E-08	9.2E-10	1.07E-04	1.1E-05	2.241	0.034	2.40E-04	2.5E-05
350	83.8	1.1	8.6E-05	1.1E-05	2.198E-08	3.9E-10	8.55E-05	1.1E-05	2.241	0.034	1.92E-04	2.4E-05
500	83.8	1.1	7.5E-05	1.1E-05	1.539E-08	2.8E-10	7.53E-05	1.1E-05	2.241	0.034	1.69E-04	2.4E-05
1000	83.8	1.1	8.6E-05	1.1E-05	7.69E-09	1.4E-10	8.62E-05	1.1E-05	2.241	0.034	1.93E-04	2.5E-05

The main characteristics of the RT 601 results are illustrated in the following charts, from Fig. 4.39 to Fig. 4.41.

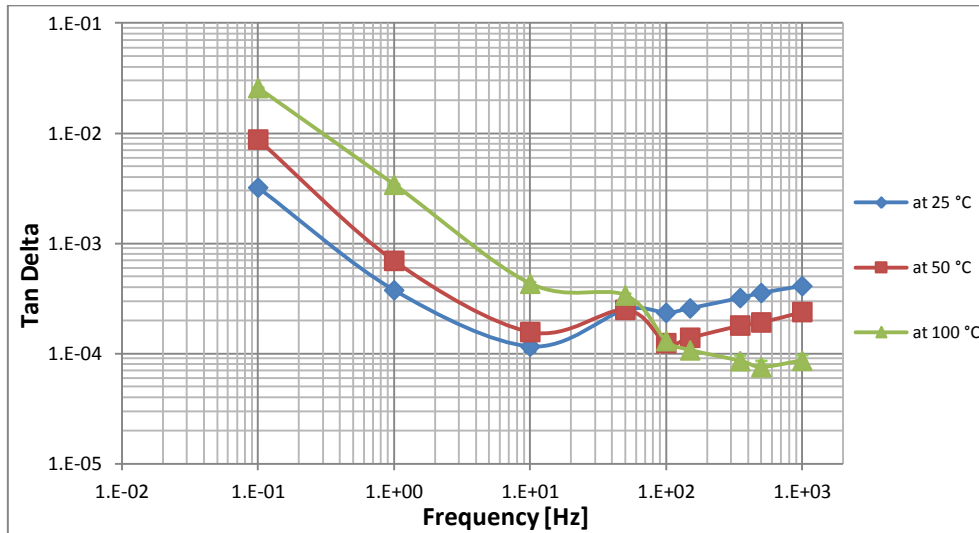


Fig. 4.39 BamD04 - Tan Delta

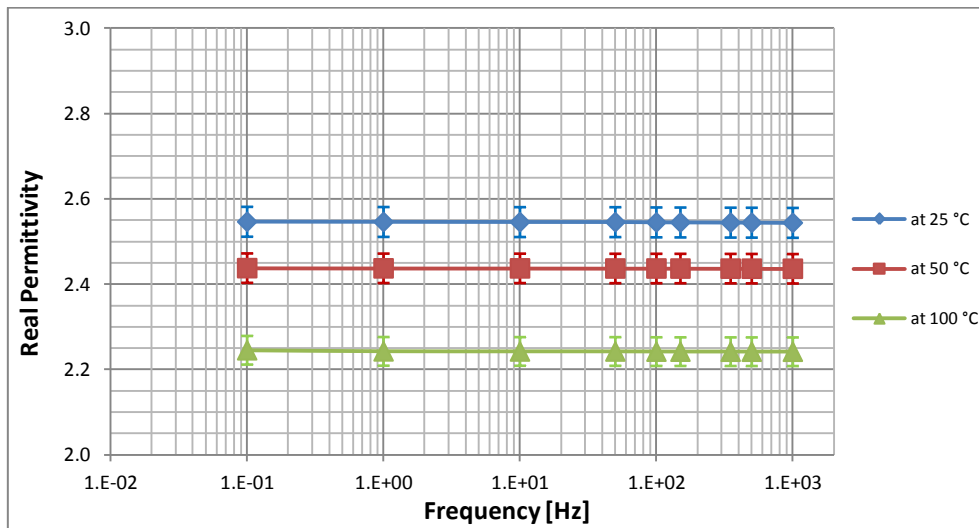


Fig. 4.40 BamD04 - Real Permittivity

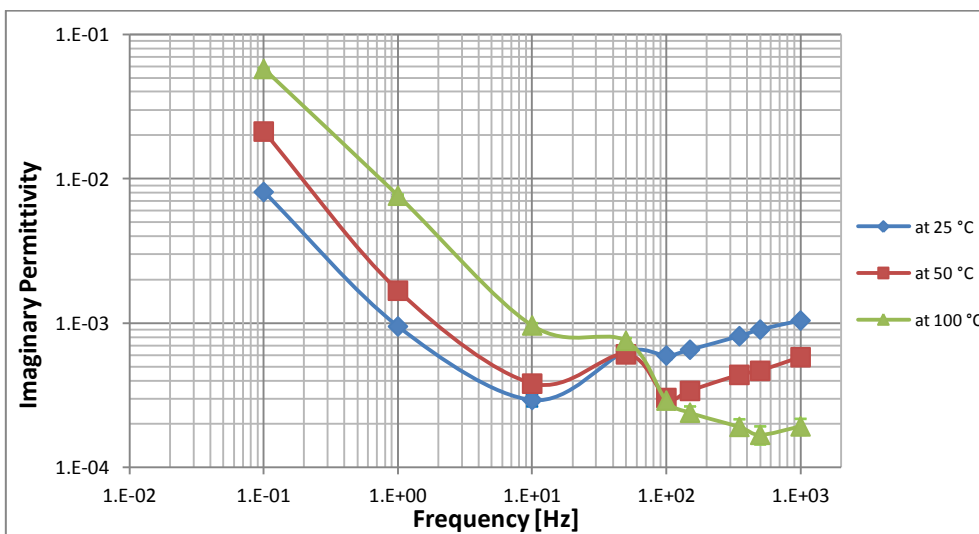


Fig. 4.41 BamD04 - Imaginary Permittivity

The sample of **Powersil 600** for the third protocol is the BamP02; its results are provided in the following three table, from Tab. 4.34 to Tab. 4.36.

Tab. 4.34 BamP02 results, 25°C

Freq [Hz]	Temperature at 25 °C											
	C_x [pF]	$u(C_x)$ [pF]	$\tan\delta$	$u(\tan\delta)$	$\tan\delta_L$	$u(\tan\delta_L)$	$\tan\delta_{pol}$	$u(\tan\delta_{pol})$	ϵ_r'	$u(\epsilon_r')$	ϵ_r''	$u(\epsilon_r'')$
0.1	92.4	1.1	2.072E-03	3.07E-05	1.723E-06	5.037E-08	2.070E-03	3.072E-05	2.122	0.041	4.39E-03	1.1E-04
1	92.1	1.1	2.075E-03	3.08E-05	1.730E-07	4.751E-09	2.075E-03	3.075E-05	2.114	0.041	4.39E-03	1.1E-04
10	91.9	1.1	1.025E-03	2.02E-05	1.733E-08	4.760E-10	1.025E-03	2.025E-05	2.109	0.040	2.162E-03	6.0E-05
50	91.8	1.1	6.03E-04	1.60E-05	3.469E-09	9.527E-11	6.03E-04	1.603E-05	2.108	0.040	1.272E-03	4.2E-05
100	91.8	1.1	5.00E-04	1.50E-05	1.735E-09	4.765E-11	5.00E-04	1.500E-05	2.107	0.040	1.054E-03	3.8E-05
150	91.8	1.1	4.50E-04	1.45E-05	1.157E-09	3.177E-11	4.50E-04	1.450E-05	2.107	0.040	9.48E-04	3.6E-05
350	91.8	1.1	3.58E-04	1.36E-05	4.96E-10	1.362E-11	3.58E-04	1.358E-05	2.107	0.040	7.53E-04	3.2E-05
500	91.8	1.1	3.34E-04	1.33E-05	3.471E-10	9.534E-12	3.34E-04	1.334E-05	2.107	0.040	7.04E-04	3.1E-05
1000	91.8	1.1	2.79E-04	1.28E-05	1.736E-10	4.768E-12	2.79E-04	1.279E-05	2.106	0.040	5.88E-04	2.9E-05

Tab. 4.35 BamP02 results, 50°C

Freq [Hz]	Temperature at 50 °C											
	C_x [pF]	$u(C_x)$ [pF]	$\tan\delta$	$u(\tan\delta)$	$\tan\delta_L$	$u(\tan\delta_L)$	$\tan\delta_{pol}$	$u(\tan\delta_{pol})$	ϵ_r'	$u(\epsilon_r')$	ϵ_r''	$u(\epsilon_r'')$
0.1	89.2	1.1	2.029E-03	3.03E-05	6.43E-06	1.869E-07	2.023E-03	3.029E-05	2.048	0.040	4.14E-03	1.0E-04
1	89.0	1.1	2.305E-03	3.31E-05	6.44E-07	1.760E-08	2.305E-03	3.305E-05	2.043	0.040	4.71E-03	1.1E-04
10	88.7	1.1	1.647E-03	2.65E-05	6.47E-08	1.766E-09	1.647E-03	2.647E-05	2.036	0.040	3.352E-03	8.4E-05
50	88.6	1.1	9.18E-04	1.92E-05	1.295E-08	3.536E-10	9.18E-04	1.918E-05	2.033	0.039	1.867E-03	5.3E-05
100	88.6	1.1	7.11E-04	1.71E-05	6.48E-09	1.769E-10	7.11E-04	1.711E-05	2.032	0.039	1.445E-03	4.5E-05
150	88.5	1.1	6.26E-04	1.63E-05	4.32E-09	1.179E-10	6.26E-04	1.626E-05	2.032	0.039	1.271E-03	4.1E-05
350	88.5	1.1	4.65E-04	1.47E-05	1.851E-09	5.056E-11	4.65E-04	1.465E-05	2.032	0.039	9.45E-04	3.5E-05
500	88.5	1.1	4.12E-04	1.41E-05	1.296E-09	3.540E-11	4.12E-04	1.412E-05	2.031	0.039	8.36E-04	3.3E-05
1000	88.5	1.1	3.04E-04	1.30E-05	6.48E-10	1.770E-11	3.04E-04	1.304E-05	2.031	0.039	6.17E-04	2.9E-05

Tab. 4.36 BamP02 results, 100°C

Freq [Hz]	Temperature at 100 °C											
	C_x [pF]	$u(C_x)$ [pF]	$\tan\delta$	$u(\tan\delta)$	$\tan\delta_L$	$u(\tan\delta_L)$	$\tan\delta_{pol}$	$u(\tan\delta_{pol})$	ϵ_r'	$u(\epsilon_r')$	ϵ_r''	$u(\epsilon_r'')$
0.1	83.2	1.1	8.626E-03	9.63E-05	5.73E-05	1.592E-06	8.568E-03	9.627E-05	1.908	0.038	1.635E-02	3.7E-04
1	83.0	1.1	1.942E-03	2.94E-05	5.74E-06	1.489E-07	1.936E-03	2.942E-05	1.904	0.038	3.688E-03	9.2E-05
10	82.8	1.1	2.248E-03	3.25E-05	5.75E-07	1.492E-08	2.247E-03	3.248E-05	1.900	0.038	4.27E-03	1.1E-04
50	82.6	1.1	2.016E-03	3.02E-05	1.154E-07	2.993E-09	2.016E-03	3.016E-05	1.895	0.038	3.820E-03	9.5E-05
100	82.5	1.1	1.590E-03	2.59E-05	5.77E-08	1.498E-09	1.590E-03	2.590E-05	1.894	0.038	3.010E-03	7.8E-05
150	82.5	1.1	1.360E-03	2.36E-05	3.850E-08	9.991E-10	1.359E-03	2.360E-05	1.893	0.038	2.573E-03	6.8E-05
350	82.4	1.1	9.51E-04	1.95E-05	1.651E-08	4.285E-10	9.51E-04	1.951E-05	1.892	0.038	1.799E-03	5.2E-05
500	82.4	1.1	8.13E-04	1.81E-05	1.156E-08	3.000E-10	8.13E-04	1.813E-05	1.892	0.038	1.537E-03	4.6E-05
1000	82.4	1.1	6.19E-04	1.62E-05	5.78E-09	1.501E-10	6.19E-04	1.619E-05	1.891	0.038	1.171E-03	3.9E-05

The next figures (from Fig. 4.42 to Fig. 4.44) illustrate the obtained outcomes of BamP02, according to the dissipation factor and the two components of permittivity.

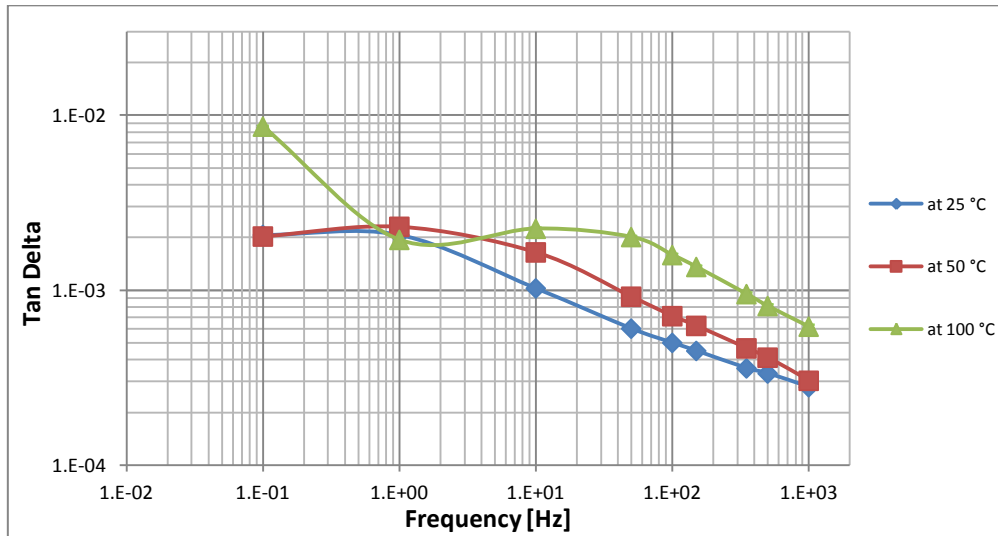


Fig. 4.42 BamP02 - Tan Delta

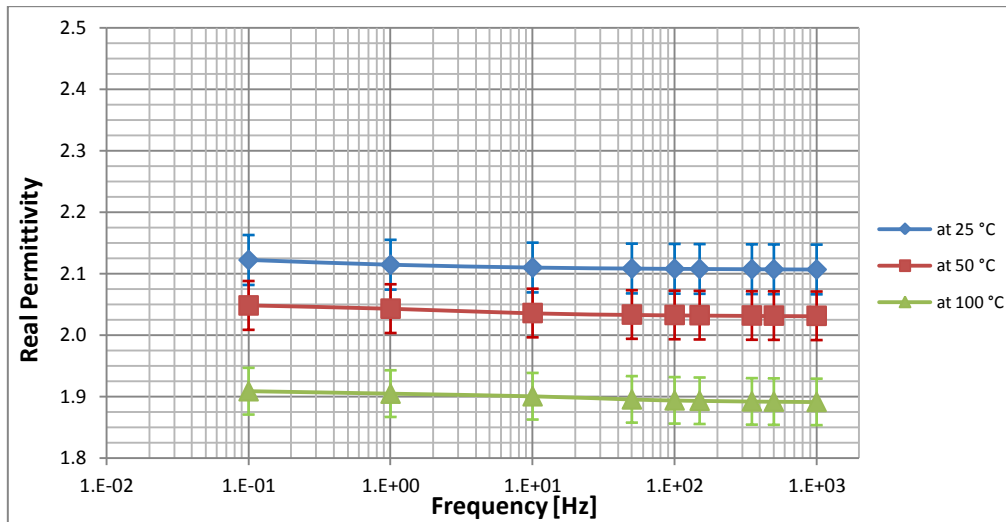


Fig. 4.43 BamP02 - Real Permittivity

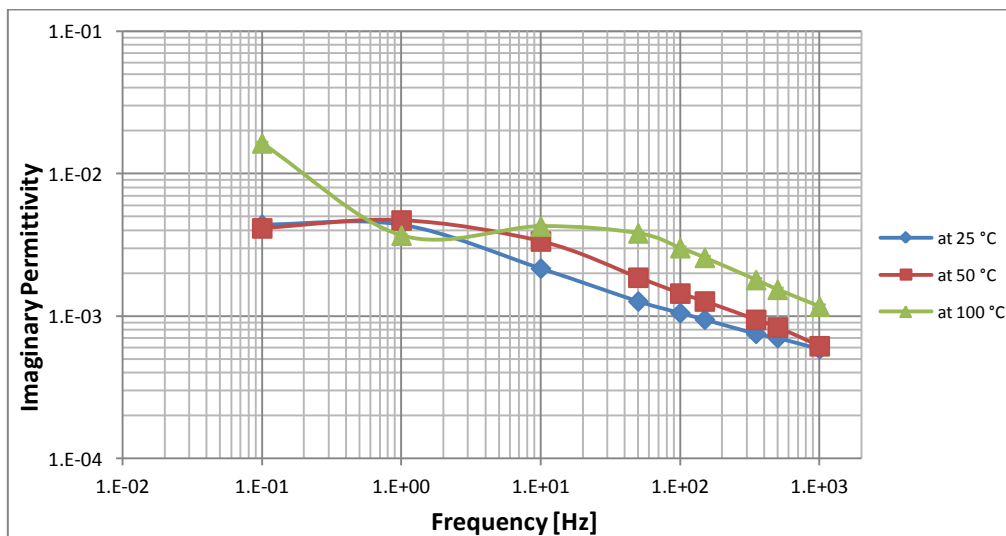


Fig. 4.44 BamP02 - Imaginary Permittivity

The figures from Fig 4.45 to Fig 4.47 compare the loss tangent of the different silicones.

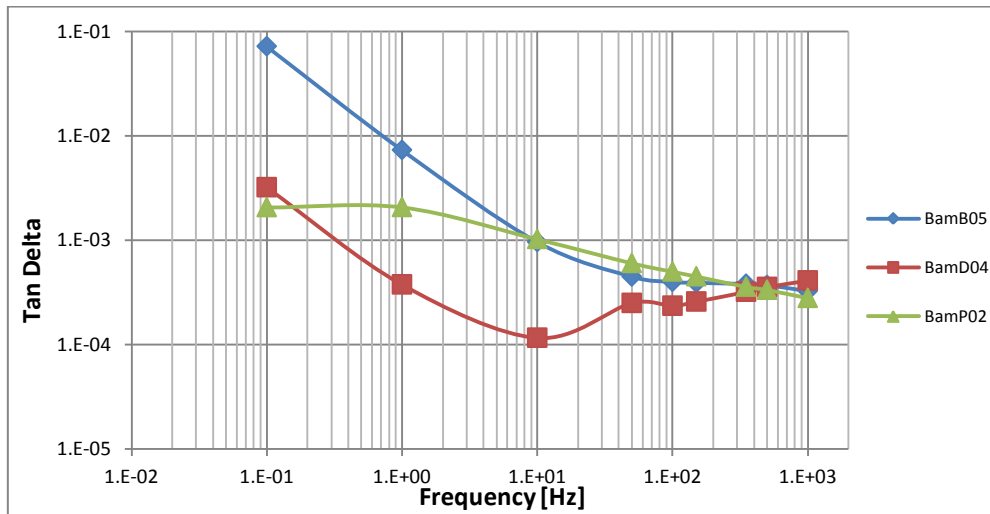


Fig. 4.45 Third protocol: Tan Delta comparison at 25° C

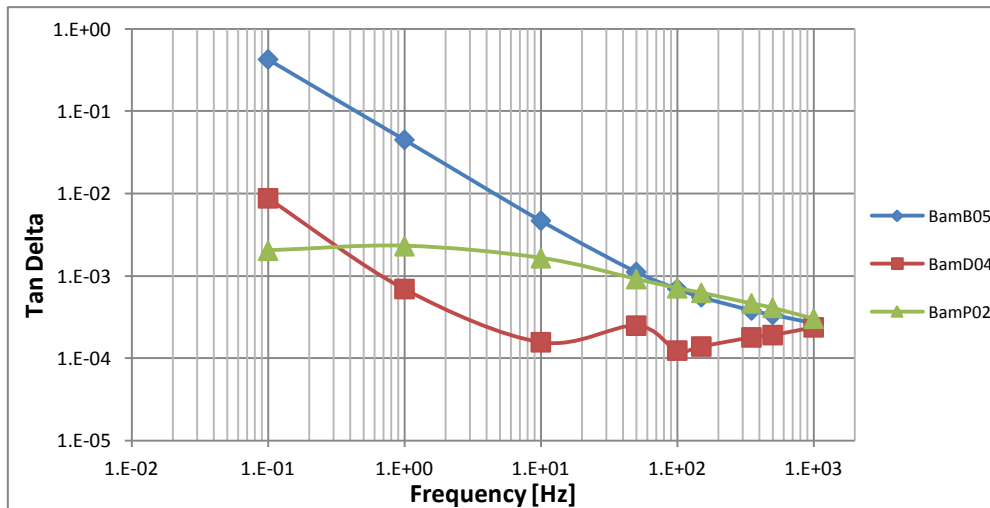


Fig. 4.46 Third protocol: Tan Delta comparison at 50° C

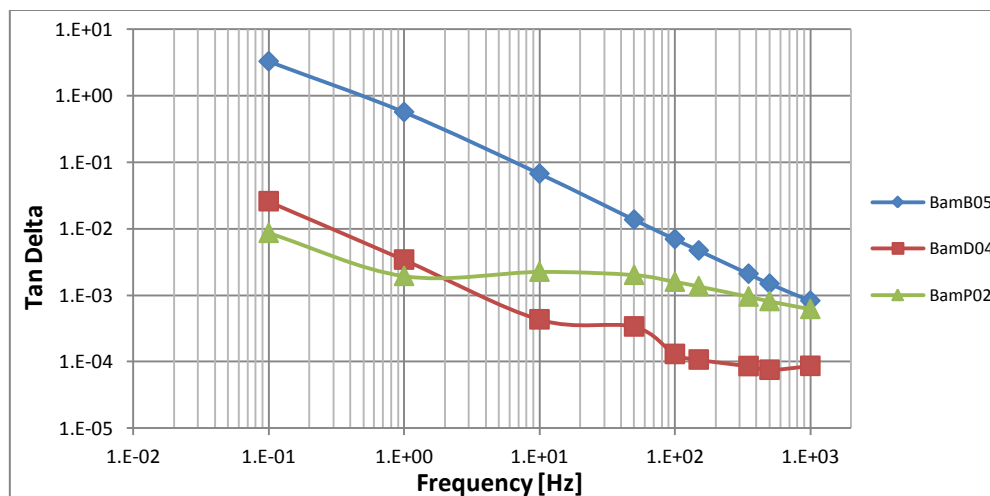


Fig. 4.47 Third protocol: Tan Delta comparison at 100° C

Considering the **dissipation factor**, it is noticed a general reduction with the frequency for all the materials and, in parallel, an increase when the temperature grows (from Fig. 4.45 to Fig. 4.47); in fact, the molecules are not influenced by a too fast electric field, together with the heat dissipation due to the thermal agitation.

For the ESA 7250, as in the previous protocol, at room temperature and high frequencies the loss tangent stabilizes toward a quite constant value. Whereas, at 50°C and 100°C, it continues to linearly decrease (Fig. 4.36); maybe, the thermal agitation involves other elements, which could follow the alternating field also at alternating frequency.

It is noticeable the value 3 assumed by the loss tangent, at 0.1 Hz and 100°C.

The $\tan\delta_L$ reduces when the frequency increases and with the growth of temperature it increases, due to modification of volume resistivity and ε_r' (as in the other materials).

About the RT 601, the graph of loss factor is quite particular (reported in Fig. 4.39): exactly at 50 Hz, the $\tan\delta$ values increase and assume the same quantity for all the temperature (like a resonance frequency), after which the order of temperatures disposition is inverted (the $\tan\delta$ at 100°C becomes the lowest one). Perhaps, a modification of the chemical structure is activated at high temperatures, involving different elements that react in a different way to the field alternation.

In this situation, the values covered by the 25°C curve are narrower than the 100°C ones, in which two orders of magnitude are involved.

In the Powersil 600, the temperature effect on the loss factor is quite small (Fig. 4.42).

The three curves cover a restricted area, more limited than the RT 601.

At 100°C and 1 Hz there is a sudden and unique decrease for which the particles minimize the dissipation of energy.

The figures from Fig. 4.48 to Fig. 4.50 show the real permittivity of all the tested samples.

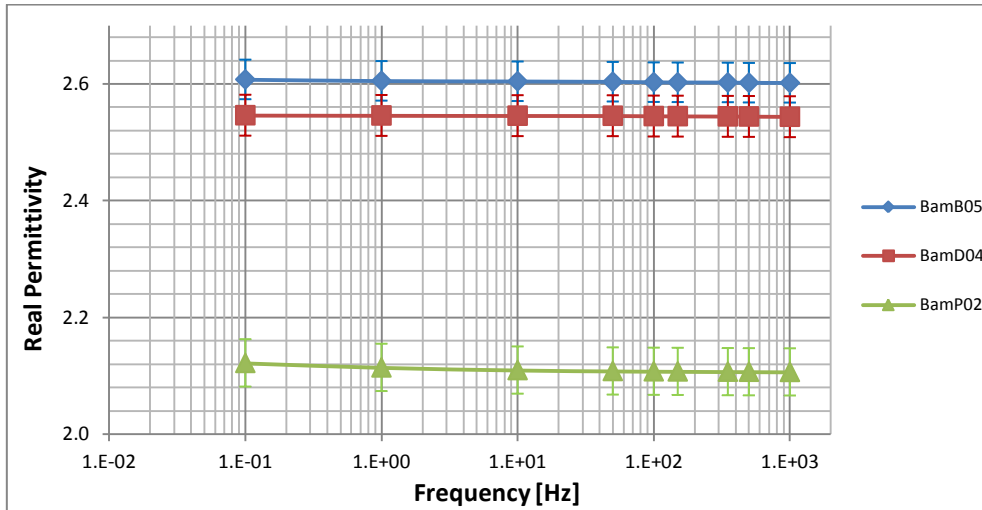


Fig. 4.48 Third protocol: Real Permittivity comparison at 25° C

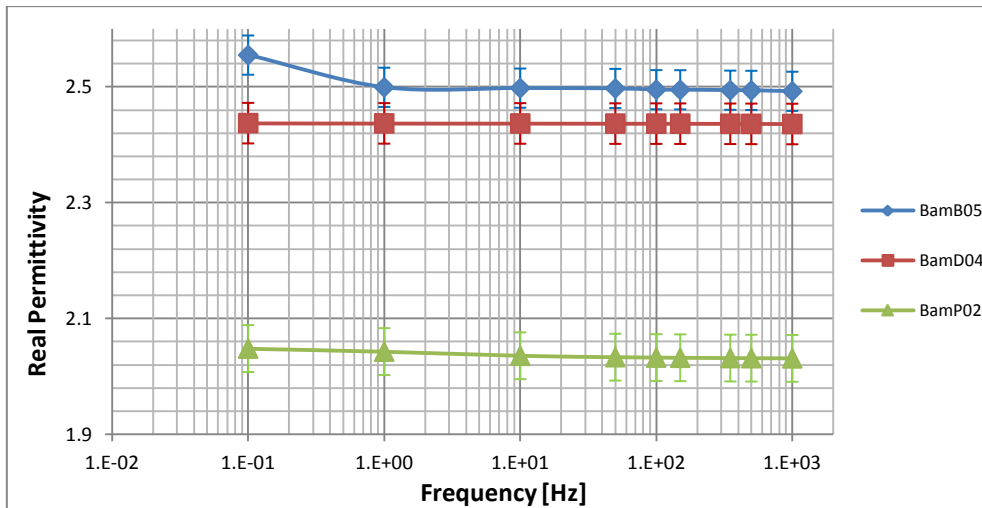


Fig. 4.49 Third protocol: Real Permittivity comparison at 50° C

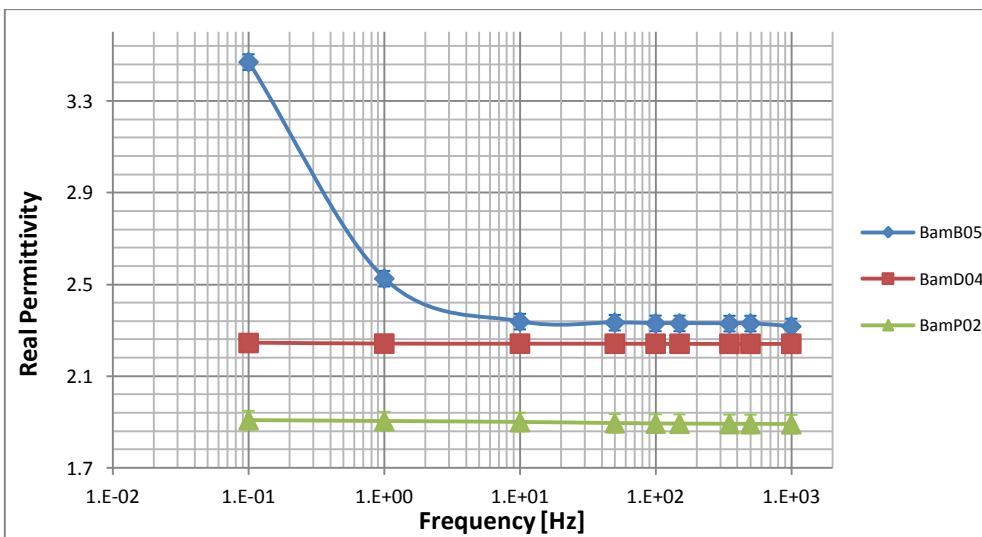


Fig. 4.50 Third protocol: Real Permittivity comparison at 100° C

Regarding the **real part of permittivity**, as reported in the last protocol, the dielectric constant is considered stable with the frequency. This happens also at higher temperatures, but the values at which they stabilize is lower (from Fig. 4.48 to Fig. 4.50).

It means that the molecules/dipoles that contributes to the polarization follow the alternating field in the whole range of frequencies with the same mechanism, but this is opposed by the thermal randomization of the medium.

The clear, unusual behavior is represented by the high temperatures of ESA 7250 (shown in Fig. 4.37). At 50°C it is already possible to distinguish an increase only for low frequencies, at 100°C there is a very huge value for 0.1 Hz that widely overcome the other temperature results, then the capacitance decreases with the frequency.

This outcome could be due to big/heavy molecules that are activated with high temperatures (maybe modification of silicone's chemical structure) but that cannot follow the field at high frequencies, because its weight or dimensions.

ESA 7250 and RT 601 experience a slightly stronger dependence on temperature than Powersil 600, which at 100°C arrives to the smallest value of 1.9, reported in Tab. 4.36.

In the figures from Fig. 4.51 to Fig. 4.53 the imaginary component of permittivity is illustrated at different temperatures, providing a comparison between the three specimens.

About the **imaginary part of permittivity**, it is noticeable the deep effect of temperature on ESA 7250, having the curves of different degrees that are well separated each other, (it is worthy of attention the value 11.2 reached at 100°C and 0.1 Hz). The other materials present curves that remain closer along the graph.

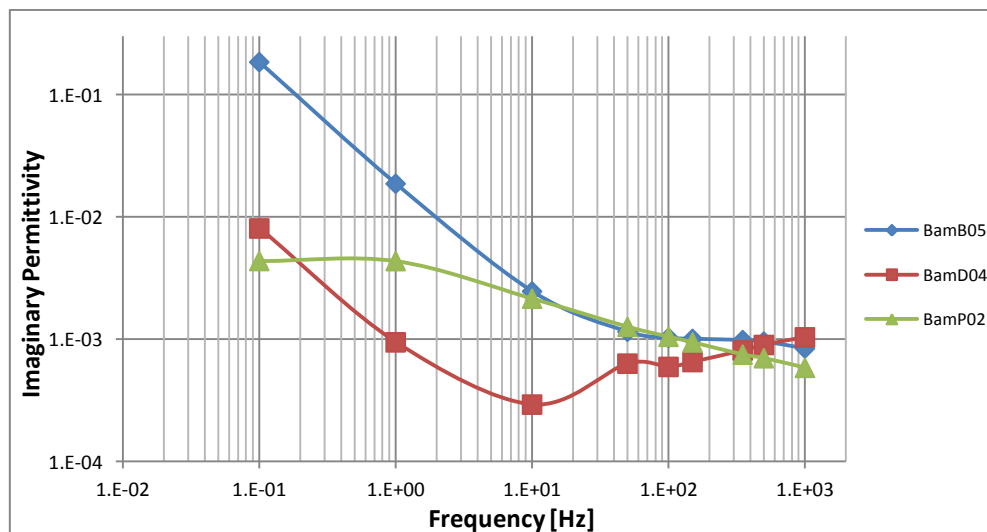


Fig. 4.51 Third protocol: Imaginary Permittivity comparison at 25° C

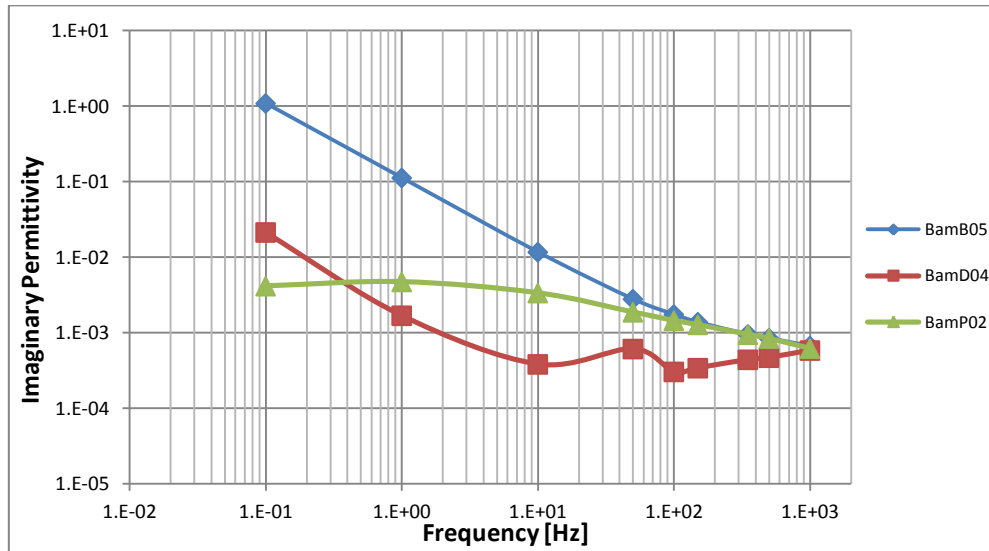


Fig. 4.52 Third protocol: Imaginary Permittivity comparison at 50° C

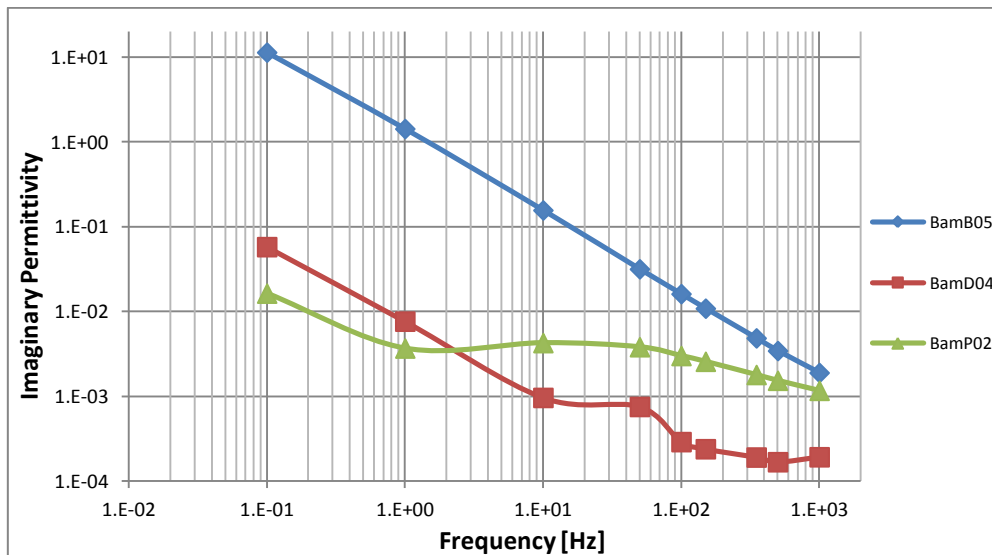


Fig. 4.53 Third protocol: Imaginary Permittivity comparison at 100° C

It is to be noted the correspondences of the results between the different protocols, at the same conditions.

Regarding the silicones analyzed in all the protocols (summarized by the graphs from Fig. 4.45 to Fig. 4.50), in general the ESA 7250 behaves higher losses and dielectric constant, together with a deep dependence on temperature and frequency (when it happens), whereas the Powersil 600 shows a weak subordination to the test variables.

The RT 601 has similarity with Powersil 600, accompanied by unusual behavior ($\tan\delta$ in the third protocol, Fig. 4.39) and an higher dielectric constant.

Apart from the specific considerations, these tests reveal how the dielectric constant is not linked to the dissipation factor (how it could be initially thought) and how different phenomena rule them.

4.5.1 ESA 7250 - Specimen D: air bubble effects

As disclosed in the third chapter, a circular specimen (named “Specimen D”) made by ESA 7250 has been manufactured with a small air bubble inside (2-3 mm in diameter), in order to detect its effects on dielectric properties.

The third protocol (constant voltage) has been applied, and the results are here reported. Without the volume resistivity values related to these specimens, it is not possible to distinguish the two $\tan\delta$ components (and the imaginary part of permittivity).

This specimen is compared with the BamB05, to which the same protocol has been applied, and, for a better understanding, its results are reported (with the designation: “without bubble”).

Tab. 4.37 Comparison with/without bubble, 25°C

Temperature at 25 °C												
Freq [Hz]	With Bubble						Without Bubble					
	C_x [pF]	uc(Cx) [pF]	$\tan\delta$	uc($\tan\delta$)	ϵ_r'	uc(ϵ_r')	C_x [pF]	uc(Cx) [pF]	$\tan\delta$	uc($\tan\delta$)	ϵ_r'	uc(ϵ_r')
0.1	113.1	1.1	3.114E-01	3.1E-03	2.492	0.031	97.4	1.1	7.214E-02	7.3E-04	2.607	0.034
1	111.2	1.1	3.345E-02	3.4E-04	2.450	0.031	97.3	1.1	7.315E-03	8.3E-05	2.605	0.034
10	111.1	1.1	3.591E-03	4.6E-05	2.448	0.031	97.3	1.1	9.60E-04	2.0E-05	2.604	0.034
50	111.1	1.1	9.96E-04	2.0E-05	2.447	0.031	97.3	1.1	4.47E-04	1.4E-05	2.603	0.034
100	111.1	1.1	6.92E-04	1.7E-05	2.447	0.031	97.2	1.1	3.98E-04	1.4E-05	2.603	0.034
150	111.1	1.1	5.98E-04	1.6E-05	2.447	0.031	97.2	1.1	3.90E-04	1.4E-05	2.602	0.034
350	111.0	1.1	4.94E-04	1.5E-05	2.446	0.031	97.2	1.1	3.81E-04	1.4E-05	2.602	0.034
500	111.0	1.1	4.67E-04	1.5E-05	2.446	0.031	97.2	1.1	3.71E-04	1.4E-05	2.602	0.034
1000	111.0	1.1	4.09E-04	1.4E-05	2.446	0.031	97.2	1.1	3.25E-04	1.3E-05	2.601	0.034

Tab. 4.38 Comparison with/without bubble, 50°C

Temperature at 50 °C												
Freq (Hz)	With Bubble						Without Bubble					
	C _x [pF]	uc(C _x) [pF]	tanδ	uc(tanδ)	εr'	uc(εr')	C _x [pF]	uc(C _x) [pF]	tanδ	uc(tanδ)	εr'	uc(εr')
0.1	119.4	1.1	1.067E+00	1.1E-02	2.630	0.032	95.5	1.1	4.278E-01	4.3E-03	2.555	0.034
1	108.3	1.1	1.302E-01	1.3E-03	2.386	0.031	93.4	1.1	4.517E-02	4.6E-04	2.499	0.033
10	107.8	1.1	1.340E-02	1.4E-04	2.375	0.031	93.3	1.1	4.700E-03	5.7E-05	2.498	0.033
50	107.8	1.1	2.892E-03	3.9E-05	2.375	0.031	93.3	1.1	1.121E-03	2.1E-05	2.497	0.033
100	107.8	1.1	1.591E-03	2.6E-05	2.374	0.031	93.2	1.1	7.01E-04	1.7E-05	2.495	0.033
150	107.8	1.1	1.163E-03	2.2E-05	2.374	0.031	93.2	1.1	5.54E-04	1.6E-05	2.495	0.033
350	107.7	1.1	6.70E-04	1.7E-05	2.374	0.031	93.2	1.1	3.82E-04	1.4E-05	2.494	0.033
500	107.7	1.1	5.53E-04	1.6E-05	2.374	0.031	93.2	1.1	3.39E-04	1.3E-05	2.494	0.033
1000	107.7	1.1	3.90E-04	1.4E-05	2.373	0.031	93.1	1.1	2.68E-04	1.3E-05	2.492	0.033

Tab. 4.39 Comparison with/without bubble, 100°C

Temperature at 100 °C												
Freq (Hz)	With Bubble						Without Bubble					
	C _x [pF]	uc(C _x) [pF]	tanδ	uc(tanδ)	εr'	uc(εr')	C _x [pF]	uc(C _x) [pF]	tanδ	uc(tanδ)	εr'	uc(εr')
0.1	252.6	1.3	3.263E+00	3.3E-02	5.566	0.052	129.6	1.1	3.276E+00	3.3E-02	3.469	0.038
1	112.6	1.1	8.967E-01	9.0E-03	2.482	0.031	94.4	1.1	5.658E-01	5.7E-03	2.525	0.034
10	101.6	1.1	1.123E-01	1.1E-03	2.239	0.030	87.4	1.1	6.705E-02	6.8E-04	2.338	0.033
50	101.3	1.1	2.288E-02	2.4E-04	2.231	0.030	87.2	1.1	1.362E-02	1.5E-04	2.333	0.033
100	101.2	1.1	1.154E-02	1.3E-04	2.230	0.030	87.1	1.1	6.955E-03	8.0E-05	2.330	0.033
150	101.2	1.1	7.747E-03	8.7E-05	2.230	0.030	87.1	1.1	4.686E-03	5.7E-05	2.330	0.033
350	101.2	1.1	3.405E-03	4.4E-05	2.230	0.030	87.0	1.1	2.094E-03	3.1E-05	2.329	0.033
500	101.2	1.1	2.414E-03	3.4E-05	2.230	0.030	87.1	1.1	1.485E-03	2.5E-05	2.330	0.033
1000	101.2	1.1	1.222E-03	2.2E-05	2.230	0.030	86.6	1.1	8.23E-04	1.8E-05	2.317	0.033

The figures from Fig. 4.54 to Fig. 4.56 illustrate the comparison between the dissipation factors of the two specimens at different temperatures.

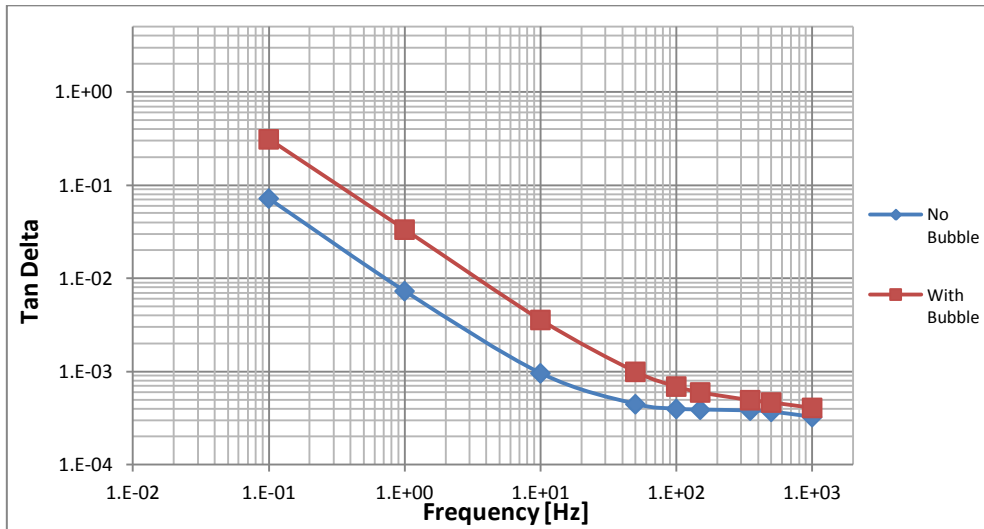


Fig. 4.54 Comparison air bubble: Tan Delta at 25°C

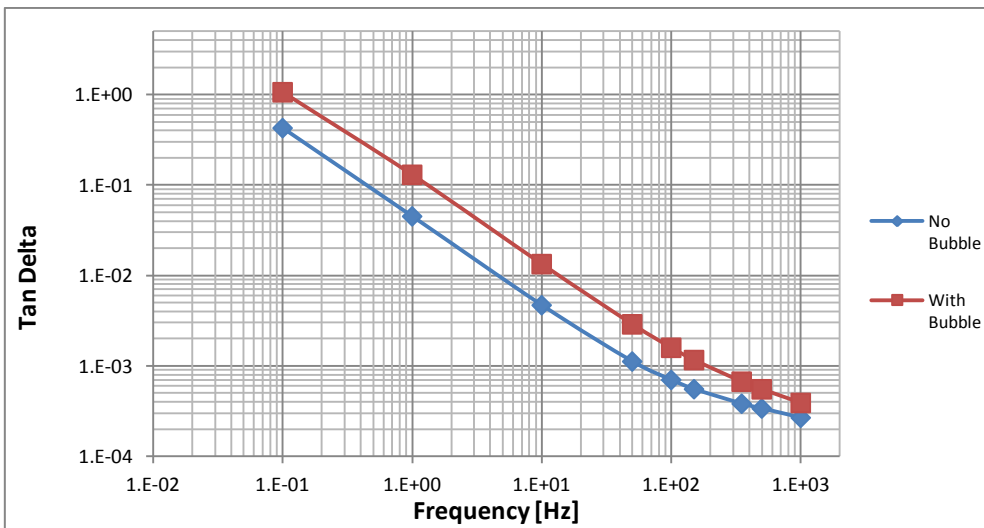


Fig. 4.55 Comparison air bubble: Tan Delta at 50°C

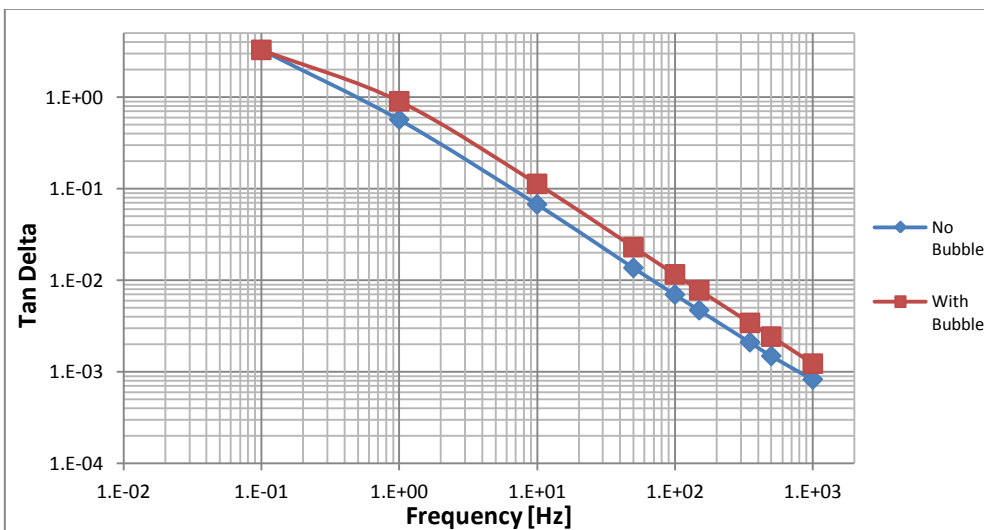


Fig. 4.56 Comparison air bubble: Tan Delta at 100°C

Considering the graphs related to the **dissipation factor**, from Fig. 4.54 to Fig. 4.56, it is to be noted that the losses in the specimen with the bubble are always higher than in the “standard” ones, reducing this difference when the temperature increases.

Anyway, the shape of these curves is similar at all the temperatures, for which the basic and dominant mechanism is the same for both the specimens.

At high frequencies and room temperature, the loss tangent of the two specimens gets closer, probably because there are more big/heavy elements in the air bubble that lose their effects at those frequencies.

Due to the high resistivity of air (reported in literature as $1.3 \cdot 10^{18} \div 3.3 \cdot 10^{18} \Omega \cdot \text{cm}$), it can be supposed that the disparity is due to the polarization component of $\tan\delta$, more intense in the Specimen D, and not to the electrical conduction. Hence, it can be stated that in the air bubble there are more (or different) elements that collide each other, dissipating their energy.

The **real part of permittivity** is shown in the next three figures (from Fig. 4.57 to Fig. 4.59), allowing a comparison between the two analyzed specimens.

The evident consideration is the preeminence of BamB05 with respect to the Specimen D: the air bubble reduces the total polarization of the medium at all the temperatures (for which the difference is always quite similar).

There is a correspondence between the reduction of the polarization and the increase of losses, perhaps involving the same chemical components of air bubble.

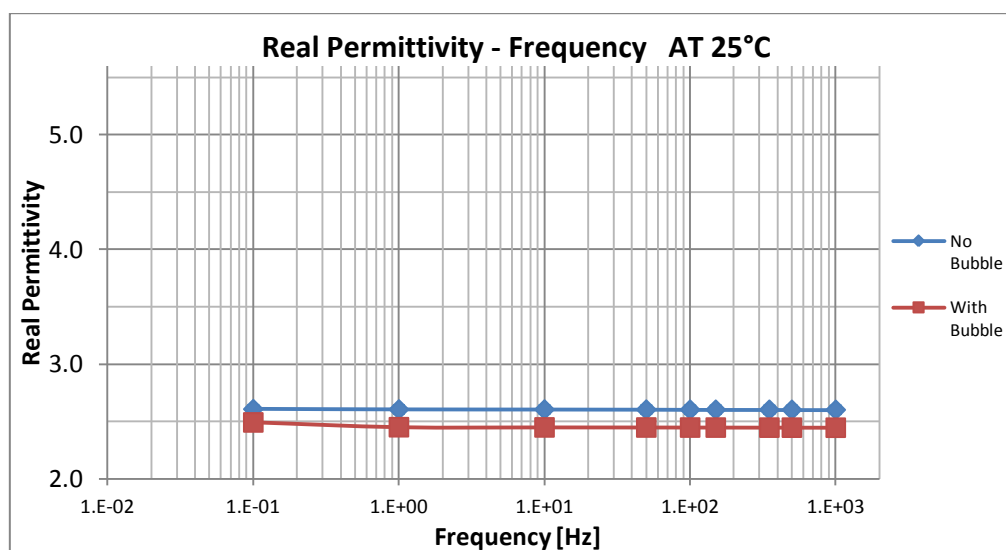


Fig. 4.57 Comparison air bubble: Real Permittivity at 25°C

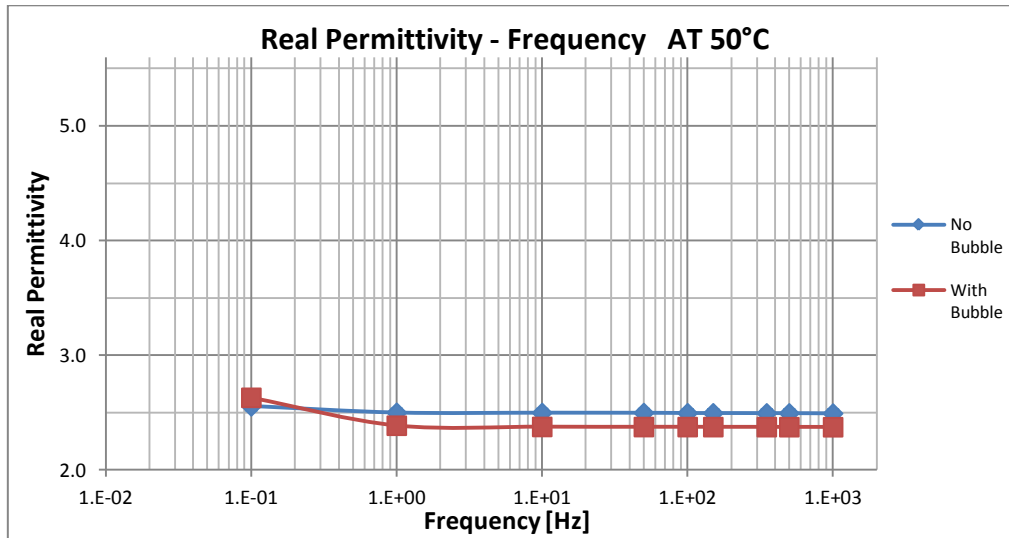


Fig. 4.58 Comparison air bubble: Real Permittivity at 50°C

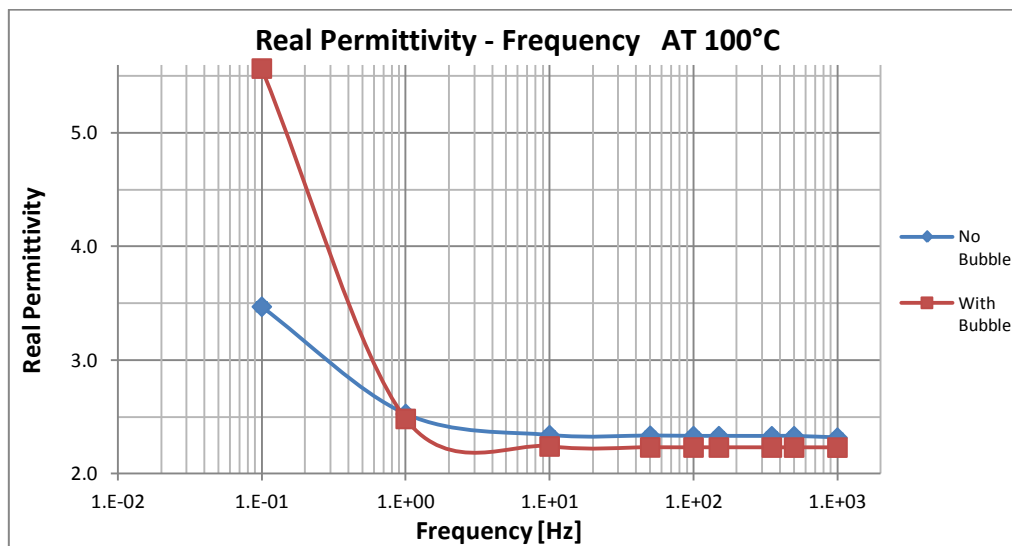


Fig. 4.59 Comparison air bubble: Real Permittivity at 100°C

This example shows the need to avoid defects or gas inclusions in the silicone products during the manufacturing, in order to prevent reduction in the quality and modification of dielectric properties, that could reduce the life time and entail additional costs.

5 VOLUME RESISTIVITY

5.1 Introduction

The purpose of electrical insulating materials is to isolate components of an electrical system from each other and from ground, while at the same time providing mechanical support for the components.

In these applications it is important that the dielectric materials be characterized by very high resistivities to prevent the conduction of electrical current and hence minimize the associated heating and energy losses.

Nevertheless, whatever the end-use or application, it is desirable to be able to characterize the DC conduction behavior of the insulating material in use to ensure that it meets the proper performance requirements.

The data may also be useful in determining whether the material has been subjected to deterioration in service, its moisture content, degree of cure and mechanical continuity.

In this chapter, the theory of volume resistivity is followed by the measurements carried out on three types of silicone rubbers, according to a temperature cycle. Their results are discussed, adding to considerations regarding their activation energy.

5.2 The Electrical Conduction in Insulating Materials

Arrangements of atoms or ions in real materials are never perfect, also as a requirement of thermal equilibrium.

In some cases, these particles are missing from sites at which they are supposed to be present. This creates a defect known as a vacancy.

In some other cases, introduced atoms or ions (inadvertently or not) may end up in the interstitial sites, originating a so-called interstitial defect.

Many solids have interstitial impurities which are often ionized or charged.

These interstitial ions can jump, from one interstitial site to another, and hence drift by diffusion in the presence of a field.

A positive ion at an interstitial site always prefers to jump into a neighboring interstitial site along the direction of the field because it experiences an effective force in this direction.

When an ion with charge q_{ion} jumps a distance d along the field E , its potential energy decreases by $q_{ion}Ed$. If it tries to jump in the opposite direction, it has to do work $q_{ion}Ed$ against the force of the field.

The conduction process is then essentially field-directed diffusion.

Deviations from stoichiometry in compound solids often lead to the generation of mobile electrons and point defects such as vacancies. Therefore, there are electrons, holes, and various mobile ions available for conduction under an applied field as depicted.

In addition, polymers may contain ions derived from the polymerization process, from the local degradation (dissociation) of the polymer itself, or from water absorption. Conductivity σ of the material depends on all the conduction mechanisms with each species of charge carrier making a contribution, so it is given by:

$$\sigma = \sum q_i n_i \mu_i$$

where n_i is the concentration, q_i is the charge carried by the charge carrier species of type i and μ_i is the drift mobility of these carriers.

The dominant conduction mechanism is often quite difficult to uniquely identify; further, it may change with temperature, composition, and ambient conditions such as the air pressure.

For many insulators, it has been found that, in the majority of cases, the conductivity follows an exponential or Arrhenius-type temperature dependence so that σ is thermally activated:

$$\sigma = \sigma_0 \cdot e^{-\frac{E_\sigma}{kT}}$$

where E_σ is the activation energy for conductivity and k is the Boltzmann constant, expressing the temperature T in Kelvin. This equation is useful in predicting the conductivity at different temperatures and evaluating the temperature stability of the insulator.

5.3 The Volume Resistivity

Resistivity, denoted by ρ , is the inverse of the conductivity and it is defined as the ratio between the electric field E inside the material and the generated current density J :

$$\rho = \frac{1}{\sigma} = \frac{E}{J}$$

The resistivity of an insulator is measured by sourcing a known voltage, measuring the resulting current, and calculating the resistance using Ohm's Law. From the resistance measurement, the resistivity is determined based on the physical dimensions of the test sample. Instruments called electrometers are used to make this measurement because of their ability to measure small currents.

Volume resistivity is an intrinsic property defined as the electrical resistance through a cube of insulating material. When expressed in $\Omega \cdot \text{cm}$, it would be the electrical resistance through a one-centimeter cube of insulating material.

Resistivity and resistance, denoted as R , are linked by the following equation:

$$\rho = R \frac{A}{d}$$

in which A is the cross-sectional area of the specimen and d its thickness.

5.3.1 The Standard Method

The standard way to characterize high-resistivity materials is to apply a step voltage, measure the current through the sample after a fixed time (usually 1 minute), then calculate the resistivity in accordance with Ohm's law and the last equation.

However, it's important to understand that the current measured in this way is a combination of background currents from many sources, the DC resistive current and the current charging the capacitance of the material, [28].

Any sample has capacitance, as well as resistance; a one-minute delay between the step voltage and the current's record is effectively a measurement of the material at the characteristic frequency of 8.3 mHz (that in many cases is perfectly adequate).

While one may or may not wish to include the low-frequency AC impedance in the sample measurement, the background currents are not an effect of the applied voltage and have no relevance in any impedance measurement.

Background currents can be produced by many different phenomena: from piezoelectric effects to temperature induced pole relaxation to discharging internal capacitive elements. These background currents decay over time at different rates, depending upon their individual time constants.

So, the standard method current is the sum of the step response stimulated current and the background current (Fig. 5.1).

The background currents can be large enough to swamp the stimulated current. In some cases, the negative background current would lead to the erroneous conclusion that the sample has negative resistance. Furthermore, uncertainty in the current can increase dramatically in the calculated resistance, where a known voltage is divided by a measured current that passes through zero.

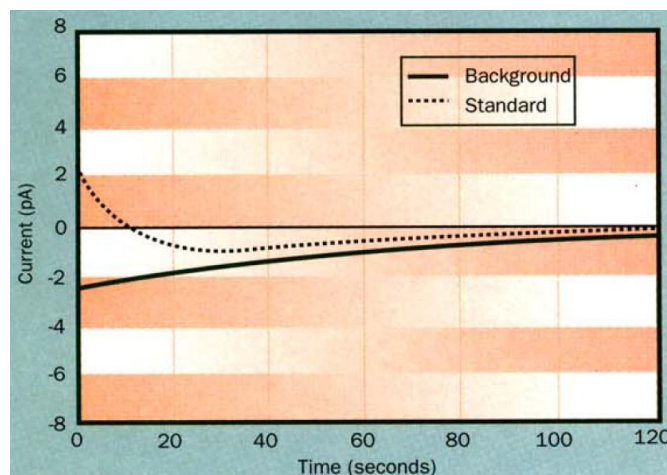


Fig. 5.1 Example of measured (standard) current and background one

5.3.2 The Alternating Polarity Method

The effects of the background current can be reduced by stimulating a sample with DC voltages of alternating polarity. This method consists of a two-step process (represented in Fig. 5.2 with the relative quantities).

Firstly, apply a positive voltage, wait a specified period of time and take a current measurement (I_1). Second, immediately after I_1 , apply a negative voltage of the same magnitude, wait the same period of time and take another current measurement (I_2).

Additional steps further improve the accuracy of the final resistance calculation.

To cancel out the first-order drift (slope in the background current) the first step is repeated, thereby obtaining a third current measurement (I_3). Repeating the second step, which provides a fourth measurement point (I_4), will cancel out the second-order drift (the curvature of the background current line).

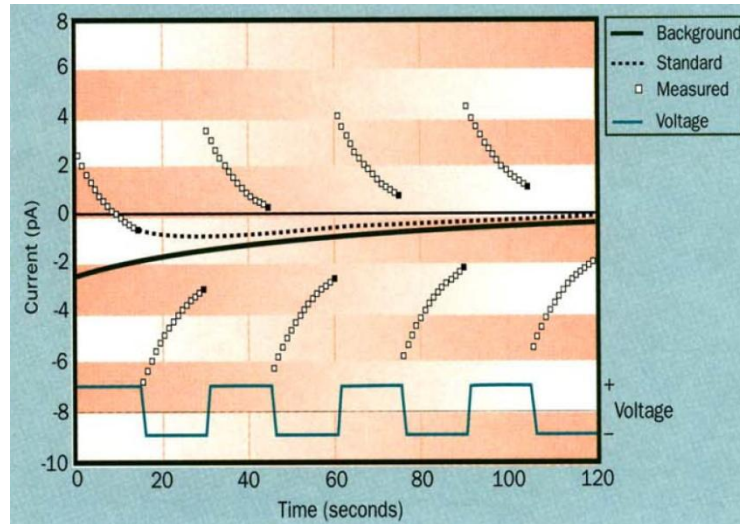


Fig. 5.2 Example of Alternating-Polarity Method's quantities

These extra steps can be used to determine a weighted—average current called I_{calc} , given by the following equation:

$$I_{calc} = \frac{I_1 + 3 \cdot (-I_2) + 3 \cdot I_3 + 4 \cdot (-I_4)}{8}$$

The sequence of weighted averages quickly converges to a very stable value. The first few measurements do not represent steady-state values, because of the finite time required for a sample's combination of resistance and capacitance (or RC circuit) to respond to the voltage stimuli.

This method provides much more repeatable results than measuring current directly, resulting deeply effective in investigating the high-resistance materials.

5.4 The Measurements

The analysis of volume resistivity has been conducted in the laboratories of Technische Universität in Berlin, by means of the electrometer “Keithley 6517B” (Fig. 5.3), suitable for low currents and high impedance resistivity measurements.

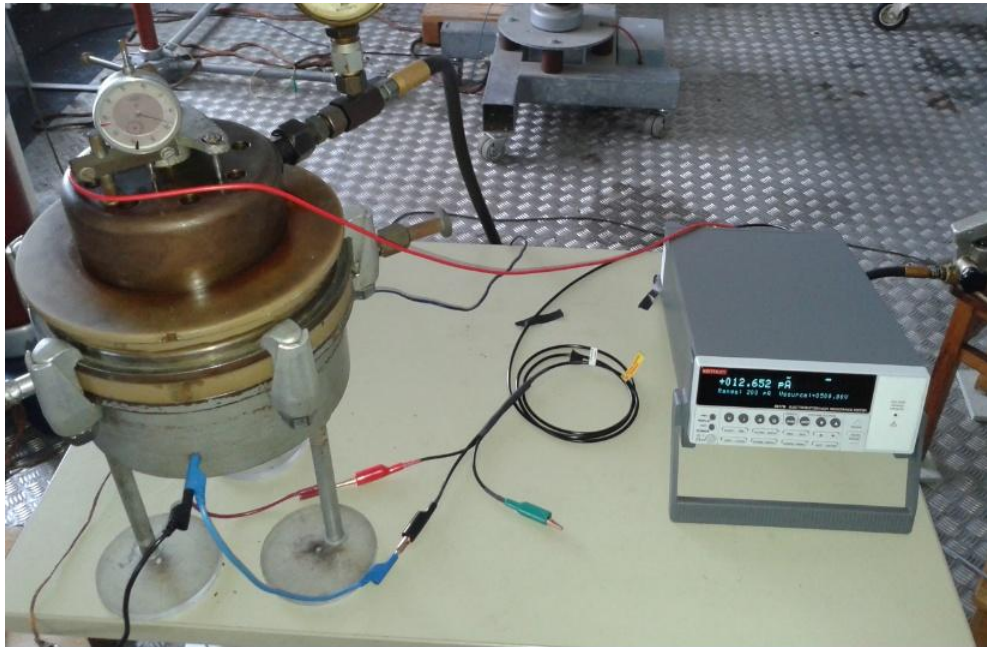


Fig. 5.3 The electrometer “Keithley 6517B” connected to the test cell

The silicone rubber specimens are inserted into the test cell, which has been connected to the electrometer.

Each test is conducted following a *temperature cycle*: the temperature is progressively increased from room temperature (25 °C) up to 100 °C; in this range five tests are conducted. Then, after a 30 minutes break, the temperature is decreased and the measurements are carried out at the same steps.

The temperature is managed using the relative controller previously introduced.

Initially, the standard method was implemented (to apply a step voltage for a fixed period of time and finally to record the volume resistivity) but, due to the background current problems already described (that led to useless outcomes), the alternating polarity method has been used.

Each step of applied voltage has a value of ± 500 V and lasts 20 seconds. The first five values (100 s) are discarded by the instruments and the first outcome is shown after

additional 80 s (necessary to compute I_{calc}); then, in order to reach the complete stability, the 10th result has been recorded.

The measurement uncertainty on the volume resistivity is obtained starting from the resistance, its relative uncertainty is given by the following formula (from the Keithley 6517B data sheet, [29]):

$$u_r(R) = \frac{u(V_{ALT}) + u(I_{MEAS}) \cdot R}{V_{ALT}}$$

In which $u(V_{ALT})$ is the uncertainty of the alternating polarity voltage (500 V), as $0.15\% \cdot V_{ALT} + 0.1\text{mV}$, whereas R is the resistance expressed by the instrument and $u(I_{MEAS})$ is the accuracy of the ammeter using $\frac{V_{ALT}}{R}$ as input, obtained with the table 5.1 (the current range depend on silicone material and temperature).

Tab. 5.1 The accuracy of the ammeter

Range	5½-Digit Resolution	Accuracy ±(%rdg + counts)
200 pA	1 fA	1+5
20 nA	100 fA	0.2+5
200 nA	1 nA	0.2+5

Then the volume resistivity uncertainty is obtained with the following expression:

$$u(\rho) = \rho \cdot \sqrt{\left(\frac{u(R)}{R}\right)^2 + \left(\frac{u(A)}{A}\right)^2 + \left(\frac{u(d)}{d}\right)^2}$$

Still considering A as the area of the inner electrode ($7853.9 \pm 4.5 \text{ mm}^2$).

The following silicone rubber materials are investigated:

- Bluesil ESA 7250
- Elastosil RT 601
- Powersil 600

For each kind of rubber three circular specimens (with 130 mm in diameter) have been tested, to which the applied oil pressure is still $20 \frac{\text{kg}}{\text{cm}^2}$.

Regarding the **Bluesil ESA 7250**, the tested specimens for the volume resistivity test assume the reduced thicknesses shown in Tab. 5.2.

Tab. 5.2 The thicknesses of the samples ESA 7250

Specimen	Reduced Thickness [mm]
BAMB03	1.946 ± 0.013
BAMB05	1.861 ± 0.012
BAMB06	1.826 ± 0.015

The three samples provided the outcomes reported in the Tab. 5.3.

Tab. 5.3 Volume resistivity results of ESA 7250

TEMP. [°C]	BAMB03		BAMB05		BAMB06	
	ρ [$\Omega\cdot\text{cm}$]	$u(\rho)$ [$\Omega\cdot\text{cm}$]	ρ [$\Omega\cdot\text{cm}$]	$u(\rho)$ [$\Omega\cdot\text{cm}$]	ρ [$\Omega\cdot\text{cm}$]	$u(\rho)$ [$\Omega\cdot\text{cm}$]
25	6.467E+13	5.0E+11	7.868E+13	5.8E+11	7.014E+13	6.2E+11
40	2.782E+13	2.2E+11	3.292E+13	2.4E+11	3.263E+13	2.9E+11
60	1.0777E+13	8.4E+10	1.1791E+13	8.8E+10	1.184E+13	1.1E+11
80	4.315E+12	3.3E+10	4.430E+12	3.3E+10	5.616E+12	5.0E+10
100	2.108E+12	1.6E+10	2.185E+12	1.6E+10	3.078E+12	2.7E+10
30 MINUTES BREAK						
100	1.845E+12	1.4E+10	2.072E+12	1.5E+10	2.755E+12	2.4E+10
80	3.099E+12	2.4E+10	3.431E+12	2.5E+10	4.427E+12	3.9E+10
60	7.016E+12	5.5E+10	7.856E+12	5.8E+10	8.485E+12	7.5E+10
40	1.834E+13	1.5E+11	2.065E+13	1.6E+11	2.213E+13	2.0E+11
25	4.976E+13	3.9E+11	6.726E+13	5.0E+11	6.306E+13	5.6E+11

Moreover, for the dissipation factor and permittivity test, the volume resistivity of BamB05 at 50 °C has been calculated, giving $(1.938 \pm 0.014) \cdot 10^{13} \Omega \cdot \text{cm}$, and the specimen BamB02 at room temperature: $(6.830 \pm 0.046) \cdot 10^{13} \Omega \cdot \text{cm}$.

These results are illustrated in five graphs (from Fig. 5.4 to Fig. 5.8), showing a comparison between the different specimens and their specific temperature cycles.

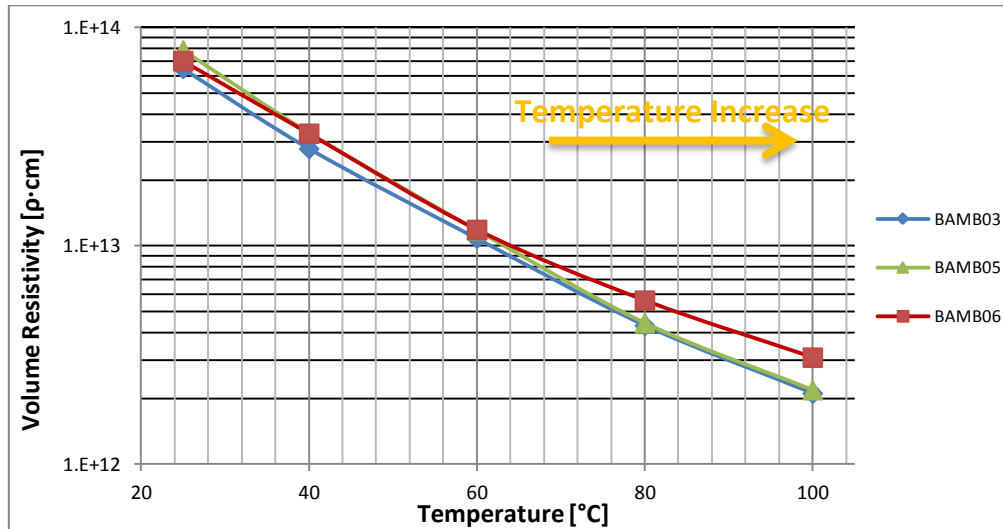


Fig. 5.4 Volume resistivity - Temperature increase: ESA 7250

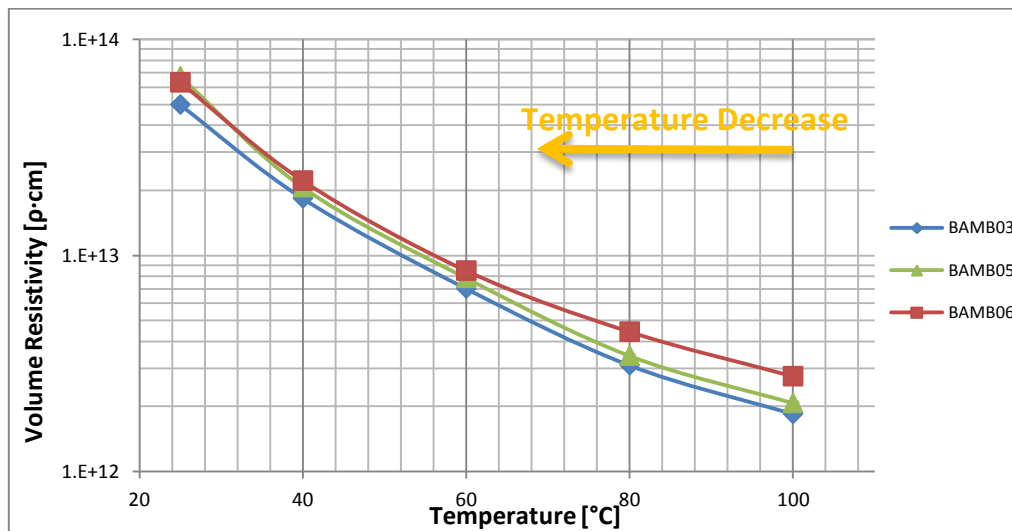


Fig. 5.5 Volume resistivity - Temperature decrease: ESA 7250

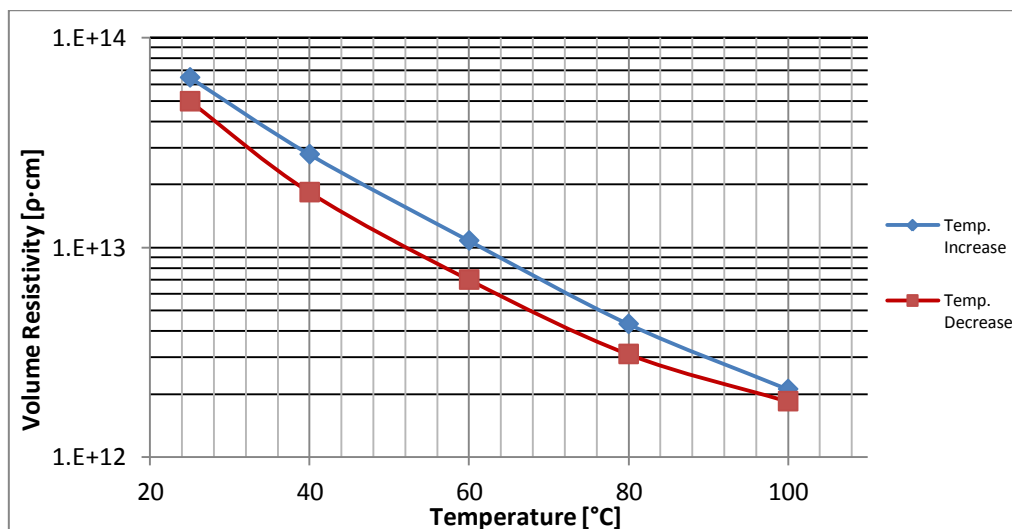


Fig. 5.6 Volume resistivity - Temperature cycle: BamB03

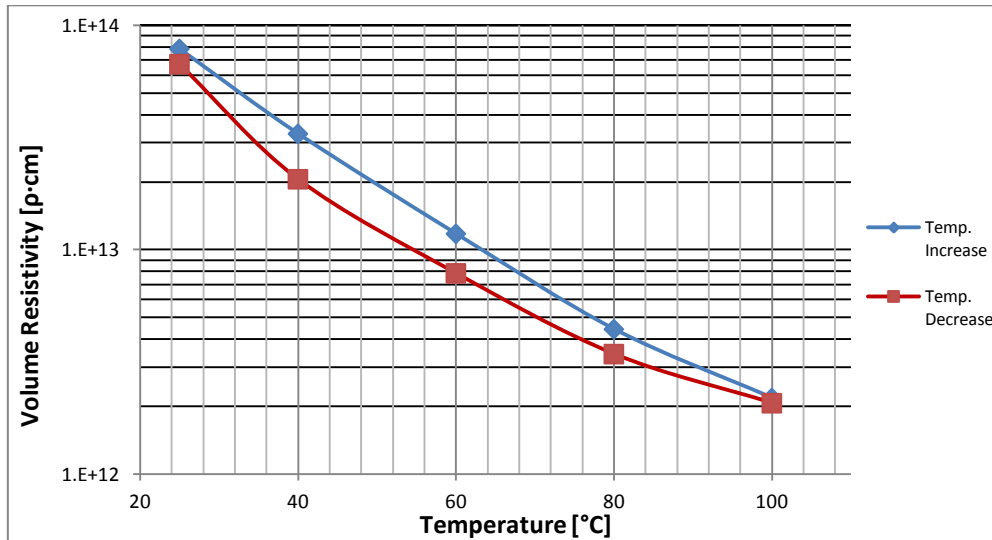


Fig. 5.7 Volume resistivity - Temperature cycle: BamB05

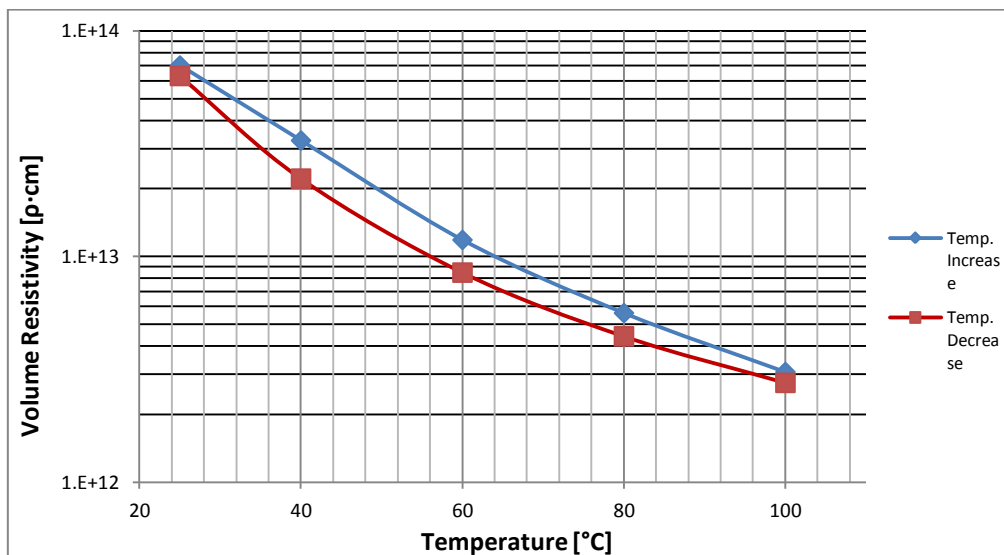


Fig. 5.8 Volume resistivity - Temperature cycle: BamB06

In ESA 7250, the different specimens have results such close to each other, particularly at low temperatures (Fig. 5.4 and Fig. 5.5).

The values decrease more exponentially in the growth of temperatures than in their reduction, in which the volume resistivities increase slower (with respect to the temperature) arriving to similar results at 25°C.

Considering the silicone **Elastosil RT 601**, the thicknesses of tested samples is reported in Tab. 5.4; whereas, their provided outcomes are found in Tab. 5.5.

In addition, for the calculations of permittivity in Chapter 4, the volume resistivity of BamD04 at 50 °C has been calculated, giving $(9.980 \pm 0.098) \cdot 10^{14} \Omega \cdot \text{cm}$.

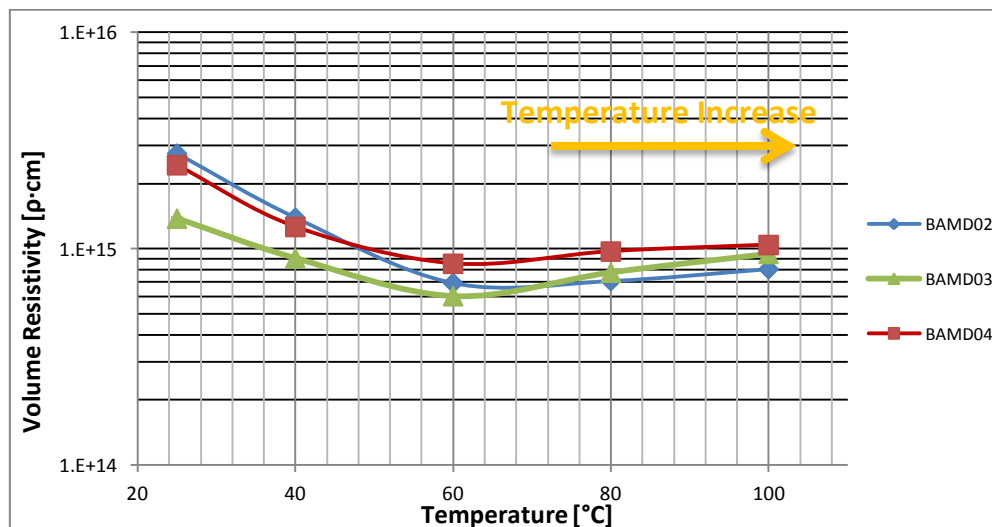
Tab. 5.4 The thicknesses of the samples RT601

Specimen	Reduced Thickness [mm]
BAMD02	2.021 ± 0.013
BAMD03	2.000 ± 0.012
BAMD04	1.859 ± 0.014

Tab. 5.5 Volume resistivity results of RT 601

TEMP. [°C]	BAMD02		BAMD03		BAMD04	
	ρ [$\Omega\cdot\text{cm}$]	$u(\rho)$ [$\Omega\cdot\text{cm}$]	ρ [$\Omega\cdot\text{cm}$]	$u(\rho)$ [$\Omega\cdot\text{cm}$]	ρ [$\Omega\cdot\text{cm}$]	$u(\rho)$ [$\Omega\cdot\text{cm}$]
25	2.758E+15	3.7E+13	1.380E+15	1.8E+13	2.438E+15	3.4E+13
40	1.394E+15	1.3E+13	9.047E+14	7.7E+12	1.263E+15	1.3E+13
60	6.951E+14	5.8E+12	6.046E+14	4.8E+12	8.535E+14	8.2E+12
80	7.103E+14	6.0E+12	7.769E+14	6.5E+12	9.723E+14	9.5E+12
100	8.062E+14	6.9E+12	9.479E+14	8.2E+12	1.043E+15	1.0E+13
30 MINUTES BREAK						
100	7.955E+14	6.8E+12	9.208E+14	7.9E+12	9.732E+14	9.5E+12
80	8.695E+14	7.5E+12	9.107E+14	7.8E+12	1.011E+15	1.0E+13
60	1.0900E+15	9.9E+12	1.116E+15	1.0E+13	1.384E+15	1.4E+13
40	2.375E+15	3.2E+13	2.169E+15	2.9E+13	2.789E+15	3.9E+13
25	5.876E+15	7.9E+13	3.704E+15	4.9E+13	6.913E+15	9.8E+13

The obtained outcomes are shown in the graphs, from Fig. 5.9 to Fig. 5.13

**Fig. 5.9** Volume resistivity - Temperature increase:RT 601

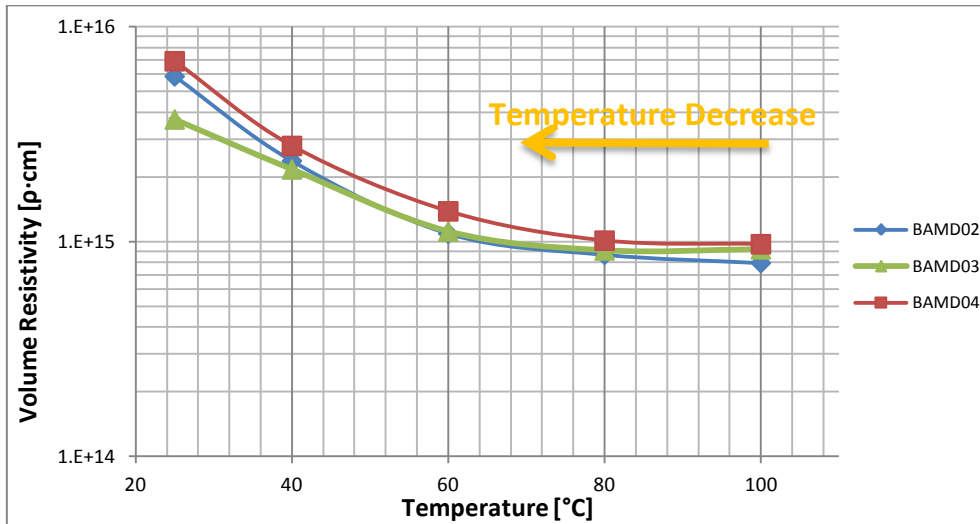


Fig. 5.10 Volume resistivity - Temperature decrease:RT 601

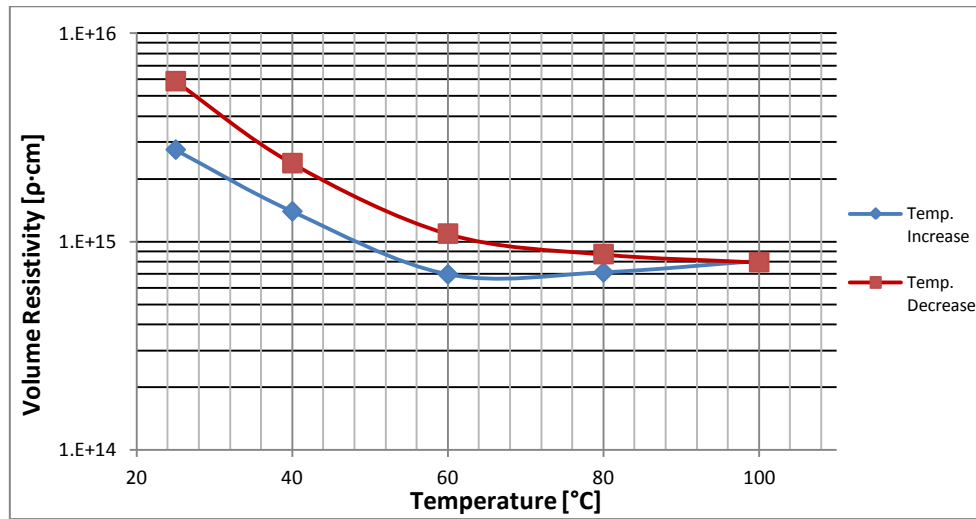


Fig. 5.11 Volume resistivity - Temperature cycle: BamD02

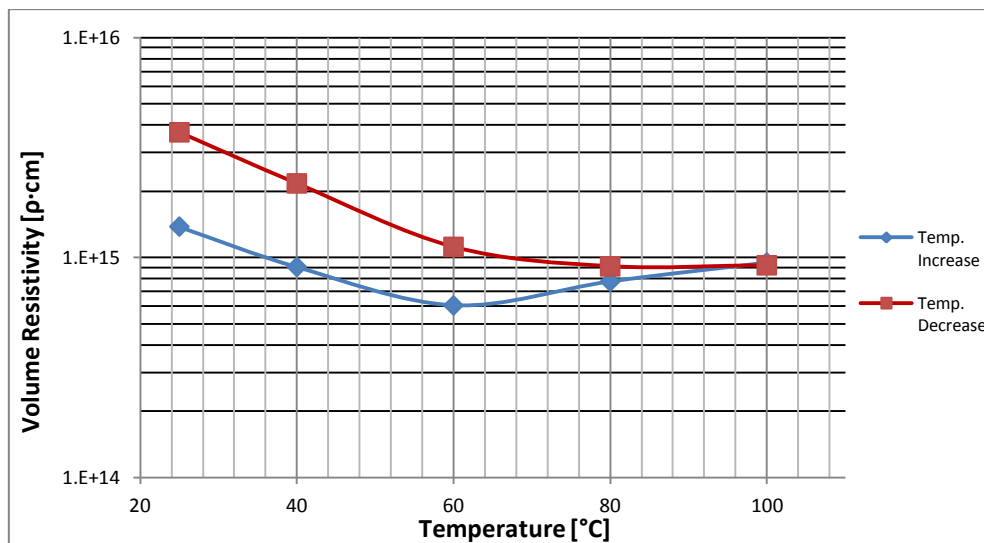


Fig. 5.12 Volume resistivity - Temperature cycle: BamD03

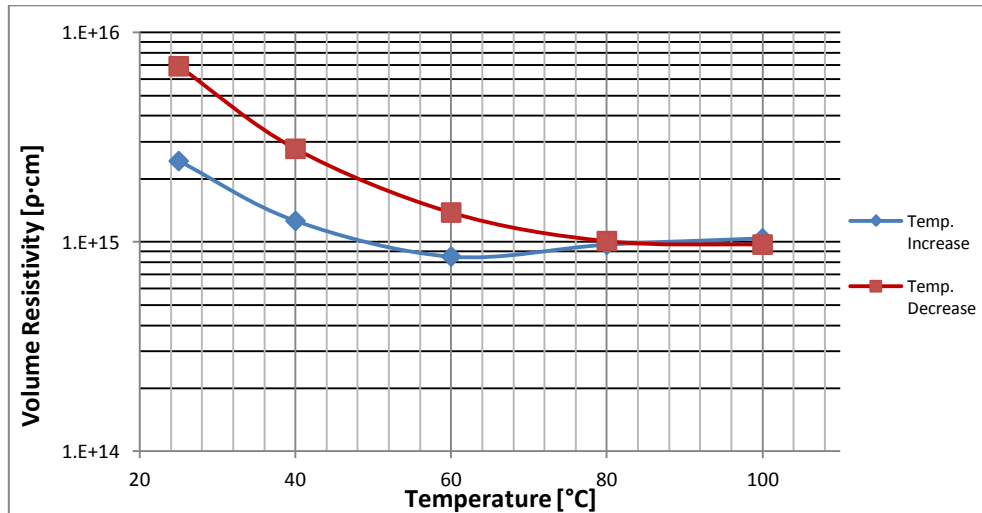


Fig. 5.13 Volume resistivity - Temperature cycle: BamD04

The material RT 601 presents a particular and unusual behavior (followed by all the specimens): during the increase of temperature (Fig. 5.9) the volume resistivity reduces until $60 \div 70$ °C, after which it slightly grows; whereas, during the reduction of temperatures (Fig. 5.10) the resistivity increases continuously, in particular very strongly below 60°C, and arriving a room temperature's value much higher than the initial one.

In order to investigate this behavior, the volume resistivity of BamD03 and BamD04 is computed at room temperature two days after the original record, the new results are $1.395 \cdot 10^{15} \Omega \cdot \text{cm}$ and $2.019 \cdot 10^{15} \Omega \cdot \text{cm}$, respectively. These values are very close to the initial ones.

The resistivity of this material shows a sensitivity for the temperature that needs some time to be exhibited, tending to increase more than the normality.

It is a temporary phenomenon (as proved by the successive results) and it can be due to modifications inside the chemical structure, which after some time at high temperatures undergoes some kind of alteration.

The last analyzed silicone rubber is the **Powersil 600**. Its tested specimens and their thicknesses are found in Tab. 5.6

Tab. 5.6 The thicknesses of the samples Powersil 600

Specimen	Reduced Thickness [mm]
BAMP01	1.660 ± 0.026
BAMP02	1.596 ± 0.024
BAMP03	1.612 ± 0.023

The acquired results are reported in the Tab. 5.7.

Tab. 5.7 Volume resistivity results of Powersil 600

TEMP [°C]	BAMP01		BAMP02		BAMP03	
	ρ [$\Omega\cdot\text{cm}$]	$u(\rho)$ [$\Omega\cdot\text{cm}$]	ρ [$\Omega\cdot\text{cm}$]	$u(\rho)$ [$\Omega\cdot\text{cm}$]	ρ [$\Omega\cdot\text{cm}$]	$u(\rho)$ [$\Omega\cdot\text{cm}$]
25	5.89E+16	1.2E+15	4.916E+16	9.7E+14	4.645E+16	8.8E+14
40	3.047E+16	6.0E+14	2.022E+16	3.9E+14	2.067E+16	3.8E+14
60	1.261E+16	2.5E+14	1.093E+16	2.1E+14	7.78E+15	1.4E+14
80	4.693E+15	9.1E+13	3.604E+15	6.9E+13	3.632E+15	6.7E+13
100	1.946E+15	3.4E+13	1.644E+15	2.7E+13	1.958E+15	3.1E+13
30 MINUTES BREAK						
100	1.890E+15	3.3E+13	1.619E+15	2.7E+13	2.004E+15	3.2E+13
80	3.419E+15	6.6E+13	3.126E+15	6.0E+13	3.202E+15	5.9E+13
60	1.185E+16	2.3E+14	7.76E+15	1.5E+14	5.94E+15	1.1E+14
40	2.304E+16	4.5E+14	1.941E+16	3.7E+14	1.298E+16	2.4E+14
25	4.055E+16	8.1E+14	3.577E+16	7.0E+14	3.855E+16	7.2E+14

Due to the employment in the dissipation factor and permittivity test, the volume resistivity of BamD04 has been calculated at 50 °C, giving $(1.366 \pm 0.026) \cdot 10^{16} \Omega \cdot \text{cm}$.

The graphs of Powersil 600 results are reported from Fig. 5.14 to Fig. 5.18, showing the comparison between the three samples' values and their specific temperature cycles.

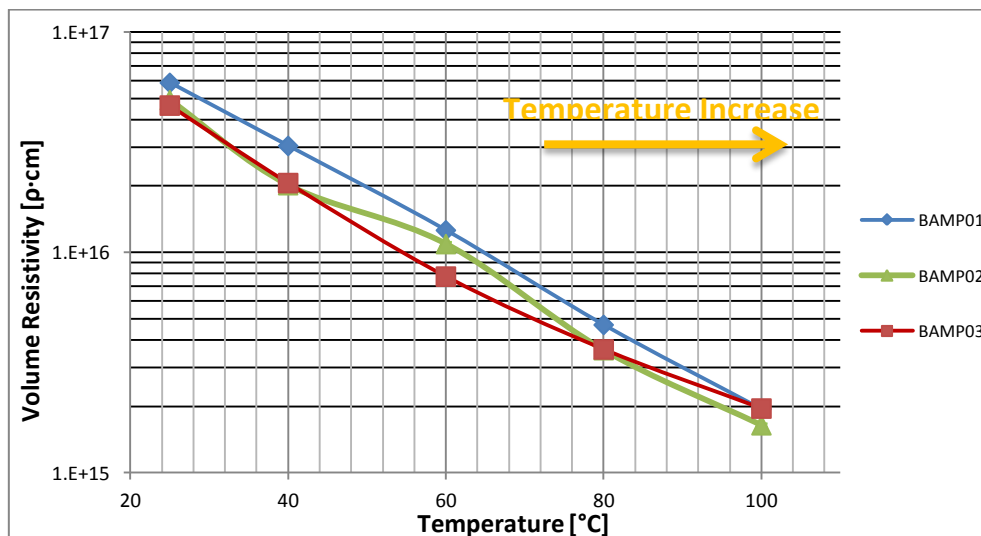


Fig. 5.14 Volume resistivity - Temperature increase: Powersil 600

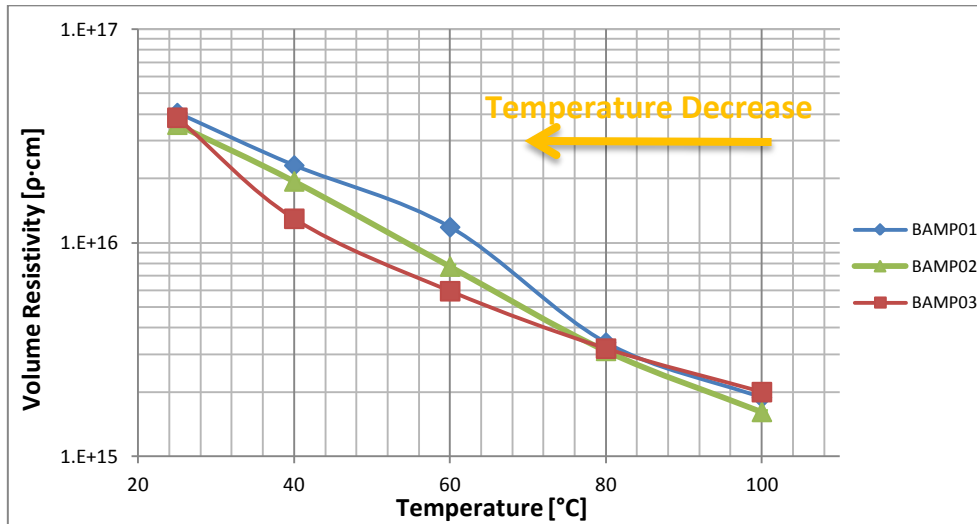


Fig. 5.15 Volume resistivity - Temperature decrease: Powersil 600

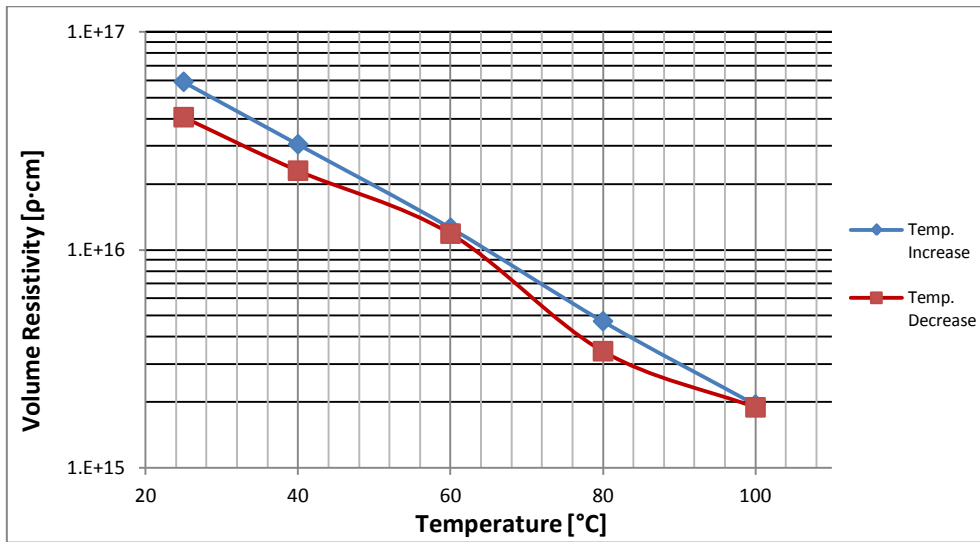


Fig. 5.16 Volume resistivity - Temperature cycle: BamP01

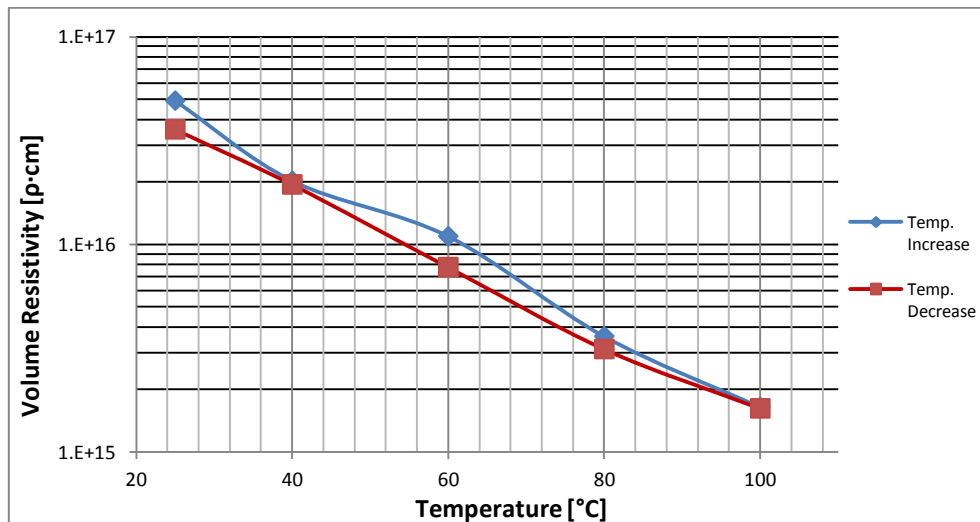


Fig. 5.17 Volume resistivity - Temperature cycle: BamP02

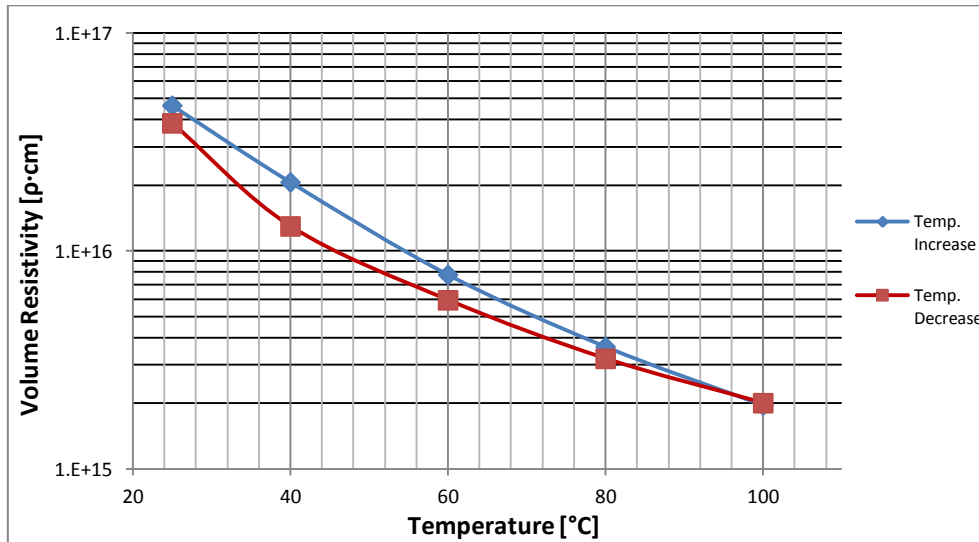


Fig. 5.18 Volume resistivity - Temperature cycle: BamP03

The silicone Powersil 600 (from Fig. 5.16 to Fig. 5.18) exhibits a behavior similar to ESA 7250 (from Fig. 5.6 to Fig. 5.8), regarding the exponential dependence on temperature and the lower values during the second part of thermal cycle. Particular outcomes are sometimes revealed around $40 \div 60$ °C, in which the specimens assume a deflected value from the curve's tendency.

In order to have a complete comparison between all the different silicone materials, the results are reported in two graphs, one for the increase of temperature (Fig. 5.19) and the other one for its decrease (Fig. 5.20).

Looking at them, it is noticeable the well distinction between the three materials.

The Powersil 600 presents the highest volume resistivity at all the temperatures, whereas the ESA 7250 owns the lowest one. These two silicones show an exponential decrease with the temperature (linear in the reported graphs); on the other hand, the volume resistivity of RT 601 depends to a lesser extent on the temperature, approaching the Powersil 600's value at 100°C (although at room temperature the three materials are equally separated in the logarithmic scale).

When the materials are considered together, between the increase and decrease of temperature the global difference is not pronounced, the exception is found in the low temperatures of RT 601.

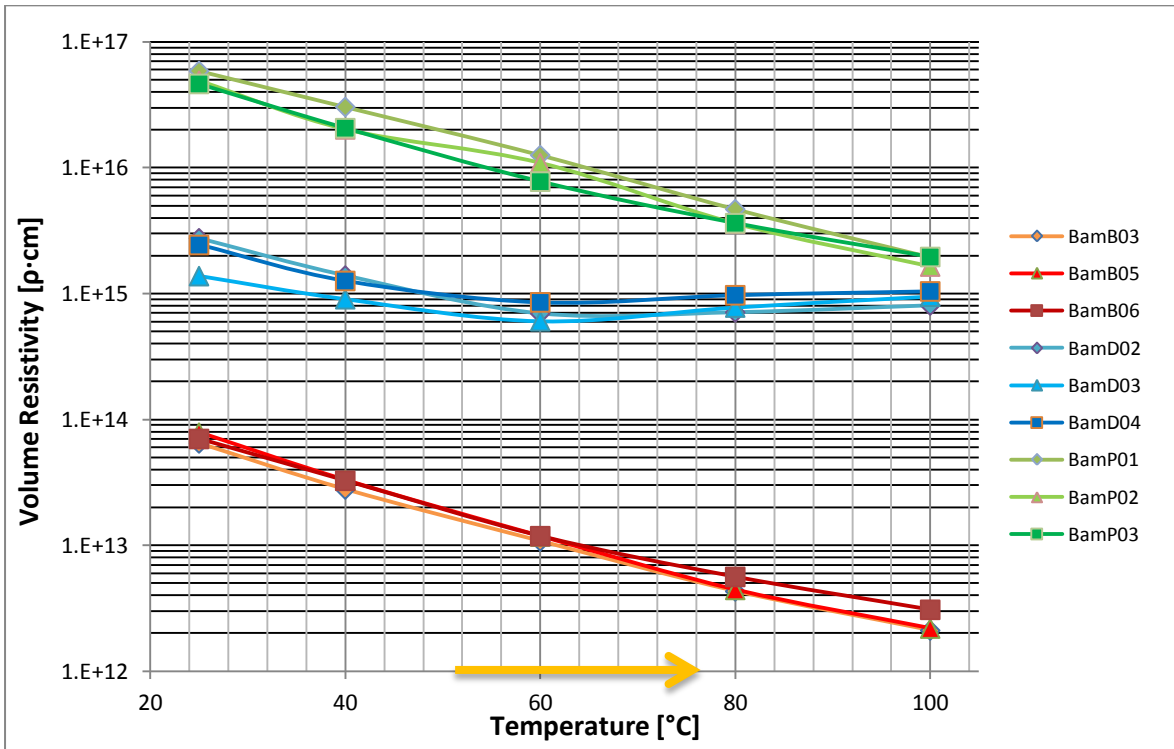


Fig. 5.19 Volume resistivity: temperature increase

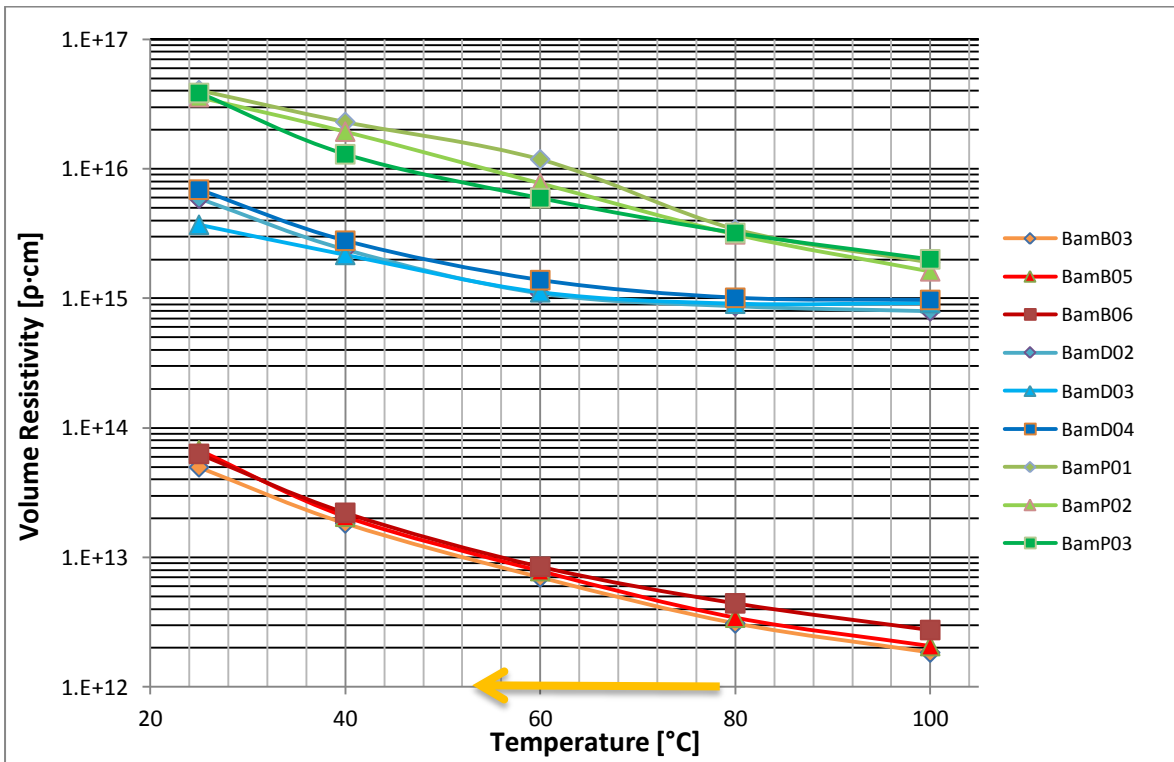


Fig. 5.20 Volume resistivity: temperature decrease

5.5 Computation of Activation Energy

Following the temperature dependence of conductivity introduced in the paragraph 5.2, the computation of its activation energy for the tested silicones has been proposed.

In addition, this calculation indicates if the ideal exponential behavior is fulfilled or not, by checking the regularity of computed activation energy at different temperatures.

The basic expression is:

$$\sigma = \sigma_0 \cdot e^{-\frac{E_\sigma}{kT}}$$

That can be recombined, obtaining:

$$\ln\left(\frac{\sigma}{\sigma_0}\right) = -\frac{E_\sigma}{kT}$$

When $\ln\left(\frac{\sigma}{\sigma_0}\right)$ is plotted against $\frac{1}{T}$, the result is a straight line with slope $-\frac{E_\sigma}{k}$.

If the conductivity at temperatures T_1 and T_2 are σ_1 and σ_2 , respectively, then the slope of the straight line is:

$$\frac{\ln\left(\frac{\sigma_2}{\sigma_0}\right) - \ln\left(\frac{\sigma_1}{\sigma_0}\right)}{\frac{1}{T_2} - \frac{1}{T_1}} = \frac{\ln\left(\frac{\sigma_2}{\sigma_1}\right)}{\frac{1}{T_2} - \frac{1}{T_1}} = -\frac{E_\sigma}{k}$$

Finally, expressing the activation energy with eV unity (dividing the energy in Joule by the charge of the electron, e) and substituting the volume resistivities to the conductivities, it is obtained:

$$E_\sigma = -\frac{\ln\left(\frac{\rho_1}{\rho_2}\right) \cdot k}{\left(\frac{1}{T_2} - \frac{1}{T_1}\right) \cdot e}$$

In our specific case, E_σ has been computed for each temperature interval (in thermal increase and decrease); then, the average value for every specimen is computed.

The measurement uncertainty is computed on each activation energy (denoted as E_σ^i), applying the following formula:

$$u(E_\sigma^i) = \sqrt{\left(\frac{\partial E_\sigma}{\partial \rho_1} \cdot u(\rho_1)\right)^2 + \left(\frac{\partial E_\sigma}{\partial \rho_2} \cdot u(\rho_2)\right)^2 + \left(\frac{\partial E_\sigma}{\partial T_1} \cdot u(T_1)\right)^2 + \left(\frac{\partial E_\sigma}{\partial T_2} \cdot u(T_2)\right)^2}$$

In which the partial derivatives are:

$$\frac{\partial E_{\sigma}}{\partial \rho_1} = \frac{-k}{\left(\frac{1}{T_2} - \frac{1}{T_1}\right) \cdot e \cdot \rho_1}$$

$$\frac{\partial E_{\sigma}}{\partial T_1} = \frac{-k \cdot \ln\left(\frac{\rho_1}{\rho_2}\right)}{\left(\frac{1}{T_2} - \frac{1}{T_1}\right)^2 \cdot e \cdot T_1^2}$$

$$\frac{\partial E_{\sigma}}{\partial \rho_2} = \frac{k}{\left(\frac{1}{T_2} - \frac{1}{T_1}\right) \cdot e \cdot \rho_2}$$

$$\frac{\partial E_{\sigma}}{\partial T_2} = \frac{-k \cdot \ln\left(\frac{\rho_1}{\rho_2}\right)}{\left(\frac{1}{T_2} - \frac{1}{T_1}\right)^2 \cdot e \cdot T_2^2}$$

In which the uncertainties on the temperatures are estimated considering a triangular distribution and supposing a resolution of ± 2 °C, obtaining $u(T_1) = u(T_2) = 0.82$ °C.

With the error propagation theory, the uncertainty of the specimen's average is expressed by their specific uncertainties' combination, obtaining the following formula:

$$u_c(E_{\sigma}) = \sqrt{\frac{1}{8^2} \cdot \sum_{i=1}^8 (u(E_{\sigma}^i))^2}$$

The obtained results for Bluesil ESA 7250 are summarized in the Tab. 5.8

Tab. 5.8 Activation energies for ESA 7250

TEMPERATURE INTERVAL [°C]	BAMB03		BAMB05		BAMB06	
	E_{σ} [eV]	$u(E_{\sigma})$ [eV]	E_{σ} [eV]	$u(E_{\sigma})$ [eV]	E_{σ} [eV]	$u(E_{\sigma})$ [eV]
25 - 40	4.52E-01	3.6E-02	4.67E-01	3.7E-02	4.10E-01	3.2E-02
40 - 60	4.26E-01	2.5E-02	4.61E-01	2.7E-02	4.55E-01	2.7E-02
60 - 80	4.63E-01	2.8E-02	4.96E-01	2.9E-02	3.78E-01	2.3E-02
80 - 100	4.06E-01	2.4E-02	4.01E-01	2.4E-02	3.41E-01	2.1E-02
100 - 80	2.94E-01	1.8E-02	2.86E-01	1.8E-02	2.69E-01	1.7E-02
80 - 60	4.14E-01	2.5E-02	4.19E-01	2.5E-02	3.29E-01	2.0E-02
60 - 40	4.31E-01	2.6E-02	4.34E-01	2.6E-02	4.30E-01	2.6E-02
40 - 25	5.35E-01	4.2E-02	6.33E-01	4.9E-02	5.61E-01	4.4E-02
	0.428 ± 0.010		0.449 ± 0.011		0.3967 ± 0.0097	

It is noticeable that, considering Tab. 5.8, the results of silicone ESA 7250 are quite close each other, particularly during the temperature increase (suggesting the respect of ideal exponential behavior), and the minimum activation energies are concentrated in the interval 100 – 80 °C.

The silicone RT 601 presents a behavior that is visibly far off from the Arrhenius type equation of conductivity, particularly at high temperatures (as pointed out in Fig. 5.9 and Fig. 5.10); in fact, some negative activation energies have been obtained (leading to an average value quite small).

These computed quantities are reported in Tab. 5.9.

Tab. 5.9 Activation energies for RT 601

TEMPERATURE INTERVAL [°C]	BAMD02		BAMD03		BAMD04	
	E_{σ} [eV]	$u(E_{\sigma})$ [eV]	E_{σ} [eV]	$u(E_{\sigma})$ [eV]	E_{σ} [eV]	$u(E_{\sigma})$ [eV]
25 - 40	3.66E-01	3.0E-02	2.26E-01	1.9E-02	3.52E-01	2.9E-02
40 - 60	3.12E-01	1.9E-02	1.81E-01	1.2E-02	1.76E-01	1.2E-02
60 - 80	-1.10E-02	6.0E-03	-1.27E-01	9.4E-03	-6.60E-02	8.0E-03
80 - 100	-7.18E-02	8.0E-03	-1.13E-01	9.4E-03	-3.95E-02	8.2E-03
100 - 80	5.05E-02	7.5E-03	-6.28E-03	6.9E-03	2.16E-02	8.0E-03
80 - 60	1.14E-01	9.2E-03	1.03E-01	8.7E-03	1.59E-01	1.2E-02
60 - 40	3.50E-01	2.2E-02	2.98E-01	1.9E-02	3.15E-01	2.0E-02
40 - 25	4.85E-01	3.9E-02	2.87E-01	2.4E-02	4.86E-01	3.9E-02
	0.1994 ± 0.0074		0.1061 ± 0.0052		0.1755 ± 0.0071	

Finally, the activation energies of Powersil 600 are presented in Tab. 5.10.

Tab. 5.10 Activation energies for Powersil 600

TEMPERATURE INTERVAL [°C]	BAMP01		BAMP02		BAMP03	
	E_{σ} [eV]	$u(E_{\sigma})$ [eV]	E_{σ} [eV]	$u(E_{\sigma})$ [eV]	E_{σ} [eV]	$u(E_{\sigma})$ [eV]
25 - 40	3.53E-01	3.1E-02	4.76E-01	4.0E-02	4.34E-01	3.6E-02
40 - 60	3.96E-01	2.6E-02	2.76E-01	2.0E-02	4.39E-01	2.8E-02
60 - 80	5.00E-01	3.2E-02	5.62E-01	3.5E-02	3.85E-01	2.6E-02
80 - 100	4.99E-01	3.3E-02	4.45E-01	3.0E-02	3.50E-01	2.5E-02
100 - 80	3.36E-01	2.4E-02	3.73E-01	2.6E-02	2.66E-01	2.1E-02
80 - 60	6.29E-01	3.9E-02	4.60E-01	3.0E-02	3.13E-01	2.2E-02
60 - 40	2.99E-01	2.1E-02	4.12E-01	2.7E-02	3.50E-01	2.4E-02
40 - 25	3.03E-01	2.8E-02	3.28E-01	2.9E-02	5.83E-01	4.7E-02
	0.414 ± 0.011		0.416 ± 0.011		0.390 ± 0.011	

With respect to ESA 7250 (Tab. 5.8), in the Powersil 600 (Tab. 5.10) the outcomes are more separated (indicating a less exponential dependence on the temperature), in particular during the temperature decrease (as can be noticed in the Fig. 5.14 and Fig. 5.15).

6 POLARIZATION AND DEPOLARIZATION CURRENT TEST

6.1 Introduction

Recently more attention has been directed to assessment of condition of electrical apparatus such as transformer, cable and rotating machine as they are the important units in power system. Indeed, these equipments insulation system should be monitored frequently to prolong their life time and to reduce the maintenance cost.

For obtaining a more clear and focused information on insulation health, newer diagnostic testing and analytical techniques are investigated in recent times. Over the last 10 years, several sophisticated approaches have been implemented.

In particular, the need to assess the insulation system nondestructively and reliably has driven the development of dielectric response diagnostic tools based on changes of the dielectric properties of the insulation. Among these non-destructive monitoring techniques the Polarization and Depolarization Current (PDC) measurement is gaining exceptional importance to the utility professionals. This method, based on the principle of dielectric response on time domain, has been widely used as the diagnostic tool for the moisture content and ageing condition evaluation of mentioned electrical apparatus.

In this chapter this method is presented and the test results are related; the measurements have been conducted on the silicone rubber varying the temperature, providing considerations regarding the utilized instruments and the obtained outcomes.

6.2 Theory of PDC

PDC assessment technique has widely been accepted by most researchers as a genuine technique for assessing electrical insulation materials based on the accepted quantum mechanics and Maxwellian Distribution theory of the behavior of a linear insulating system.

The principle of measurement of polarization and depolarization current is based on application of a DC voltage across a test object for a long time.

During this time the current, arising from the activation of the polarization process with different time constants corresponding to different mechanism in the material and due to the conductivity of the object, is measured.

Then the voltage is removed and the object is short-circuited. The previously activated polarization process now gives rise to the discharging current in the opposite direction, where no contribution of the conductivity is present.

The schematic diagram of the PDC measuring set-up is shown in Figure 6.1, in which the switch implements the transition from polarization to depolarization phase and the electrometer has the task of measuring the current in both stages.

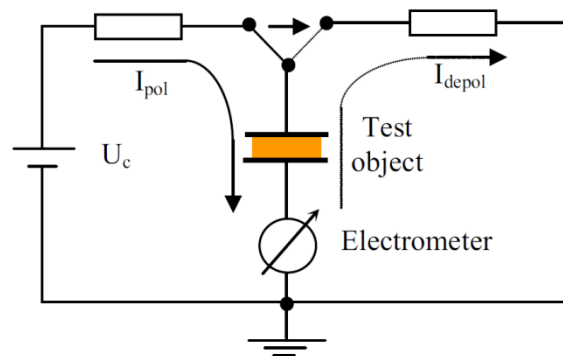


Fig. 6.1 Scheme of the PDC measurements

Charging and discharging currents (polarization and depolarization ones) are influenced by the properties of the insulating materials as well as by the geometric structure of the insulating system, [35].

Assuming a homogeneous electric field $E(t)$ is applied to the dielectric material, the current density through the surface of the material can be written as:

$$J(t) = \sigma E(t) + \frac{dD(t)}{dt}$$

The current density $J(t)$ is the sum of the conduction current and the displacement current, where σ is the DC conductivity and $D(t)$ is the electric displacement as given below:

$$D(t) = \varepsilon_0 E(t) + \Delta P(t)$$

where ε_0 is the vacuum permittivity, ε_r is the relative permittivity of the insulation at power frequency and $P(t)$ is the dielectric polarization. In the PDC test, a relevant role is played by the dielectric response function $f(t)$, related to the dielectric polarization by the following relationship:

$$\Delta P(t) = \varepsilon_0 \int_0^{\infty} f(t - \tau) \cdot E(\tau) d\tau$$

The response function $f(t)$ describes the fundamental memory property of the dielectric system and can provide significant information about the insulating material.

The function $f(t)$ can be determined experimentally as the response of the dielectric to a step-function charging field.

As said, in order to investigate the polarization process, the polarization and depolarization currents are measured. Combining the previous equations, we obtain:

$$J(t) = \sigma E(t) + \varepsilon_0 \frac{dE(t)}{dt} + \varepsilon_0 \frac{d}{dt} \int_0^t f(t - \tau) \cdot E(\tau) d\tau$$

For a homogeneous material, the field strength $E(t)$ can be considered as generated by an external voltage $U(t)$; the current through a test object with geometric capacitance C_0 (measured capacitance at or near power frequency, divided by ε_r) can be written as:

$$i(t) = C_0 \left[\frac{\sigma}{\varepsilon_0} U(t) + \frac{dU(t)}{dt} + \frac{d}{dt} \int_0^t f(t - \tau) \cdot U(\tau) d\tau \right]$$

Assuming that the test object is totally discharged and that a step voltage is applied with the following characteristics:

$$U(t) = \begin{cases} 0 & t < 0 \\ U_c & t_0 \leq t \leq t_c \\ 0 & t > t_c \end{cases}$$

This will give zero current for times before $t = 0$, and the so-called polarization currents for times $t_0 \leq t \leq t_c$.

The polarization current is built up in three parts:

- the first part is related to the conductivity of the test object, the direct or quasi-direct conduction current
- the second is the capacitive current, associated with the charging of the geometric capacitance of the specimen. After a constant voltage jump is applied to the sample, the capacitive current decays exponentially.
- the last one is associated to the activation of the different polarization processes within the dielectric, called absorption current.

The polarization (charging) current through the object can thus be expressed as:

$$i_p(t) = C_0 U_C \left[\frac{\sigma}{\epsilon_0} + \delta(t) + f(t) \right]$$

In which $\delta(t)$ is the Dirac function arising from the suddenly applied step voltage at $t = t_0$. The capacitive current component can be dominant for the first few seconds but the absorption current components of the polarization / depolarization currents and the direct conduction current dominate after tens of seconds, [32].

The delta component is usually neglected, because it is fast and not measured by the instruments, so the polarization current assumes the formulation below:

$$i_p(t) = C_0 U_C \left[\frac{\sigma}{\epsilon_0} + f(t) \right]$$

Once the step voltage is replaced by a short circuit, a depolarization current is built up. The magnitude of the depolarization current assumes the following relationship:

$$i_d(t) = C_0 U_C [f(t) - f(t + t_c)]$$

Where t_c is the time during which the voltage has been applied to the test object.

The typical nature of these currents due to a step charging voltage U_C is represented in Figure 6.2.

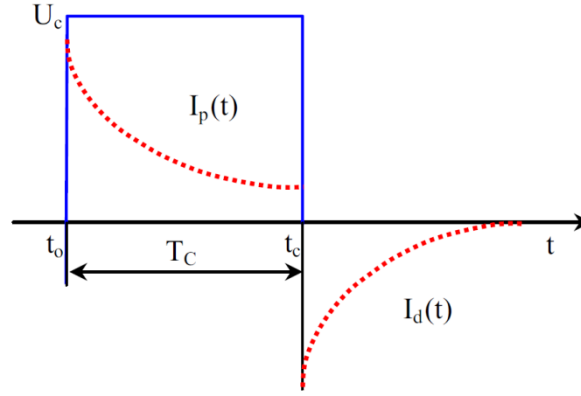


Fig. 6.2 Polarization and depolarization currents due to a step charging voltage

Polarization and depolarization current both decrease in magnitude with measuring time, and polarization current tends to a stable value, while depolarization current goes to zero. This is because the magnitudes of initial part of polarization currents depend on relaxation currents. The potential redistributes inside medium with the increase of polarization time. Then relaxation currents decrease, and polarization currents converge to a fixed value, that is DC conduction current.

The medium begins to depolarize when voltage is removed. Dipoles inside medium gradually rearrange until disordered state, and the medium becomes electrically neutral as a whole. This procedure shows that depolarization currents decayed with time, approaching the zero value.

In order to estimate the dielectric response function $f(t)$ from a depolarization current measurement it is assumed that the dielectric response function is a continuously decreasing function in time, then if the polarization period is sufficiently long, so that $f(t + t_c) \cong 0$, the dielectric response function $f(t)$ is proportional to the depolarization current, with the following relationship:

$$f(t) = \frac{i_p(t)}{C_0 U_c} - \frac{\sigma}{\varepsilon_0} \cong \frac{-i_d(t)}{C_0 U_c}$$

From the measurements of polarization and depolarization currents, it is possible to evaluate the DC conductivity σ of the test object.

Taking into account $f(t + t_c) \cong 0$, the previous equations can be combined to express the DC conductivity of the composite dielectric as:

$$\sigma = \frac{\varepsilon_0}{C_0 U_c} (i_p(t) - i_d(t))$$

The average conductivity for a given insulation system, thus, is found to be dependent upon the difference between the polarization and depolarization current values. For a linear dielectric, it is expected that the difference between the polarization and depolarization current is equal to the time-independent direct current.

However, practical dielectric systems inevitably have certain non-linearity in their dielectric response. As a result, the difference between the polarization and depolarization current is found to vary with time depending upon the condition of the dielectric material. The conductivity of the medium computed using the last equation would thus be dependent on time.

6.3 The measurement circuit

The test have been carried on in the laboratories of Technische Universität Berlin.

The test fixture was set up in the same university; it consists essentially of the following industrial components: the PC, the DSP, the DC high voltage power source, the sensors (including the electrometer Keithley 617), several relays and a control unit.

The relative scheme is shown in Figure 6.3.

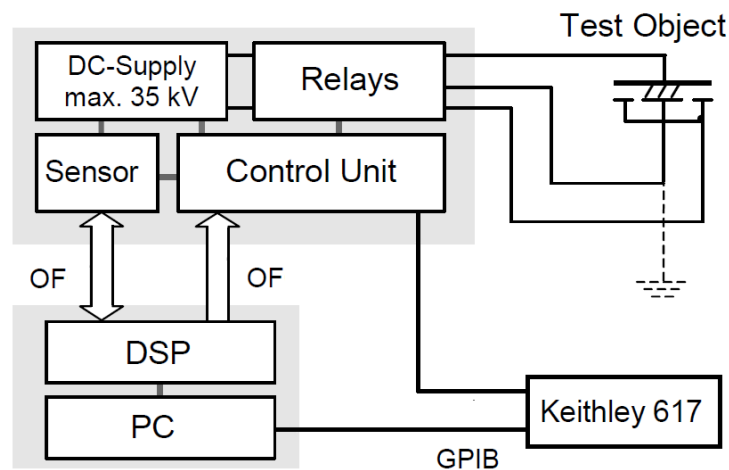


Fig. 6.3 Scheme of PDC measuring system

With respect to the theory explained in the paragraph 6.2, between the polarization and depolarization phase there is the presence of a short-circuit period of the test object.

The desired test parameters (load voltage level, charging time, short-circuit time, depolarization time, etc.) are largely free adjustable and set into the PC, via the software “DSMess 3.11”, which represents the interface for the DSP unit.

The DSP transmits all the PC instructions to the control unit and the remaining components via optical fibers and constitutes the time basis for all the shifts.

The polarization current is computed by the internal sensor (with a measuring range between 1 μA and about 10 pA), during the charging period of the DC power source (at maximum 35 kV for 1 hour); then, after the short-circuit phase (at minimum 1 second), the depolarization current is calculated by the external electrometer, the Keithley 617.

The measured data are processed and stored in the DSP and finally the PC shows them graphically.

The circuit configuration of each phase is now pointed out:

- **Polarization phase** (Fig. 6.4)

The path followed by the polarization current, through the relays and switches, is underlined. After the DC source, the voltage divider is present (up to 10 V), necessary in computing the voltage level, and the resistance R_E is used to ground the HV part with the switch S2.

The guard electrode is denoted by the letter G; on the other hand, the measuring electrode is indicated by the letter M. They are both connected to the system via a coaxial cable.

During operation, the switch S9 is closed, connecting the guard electrode to ground.

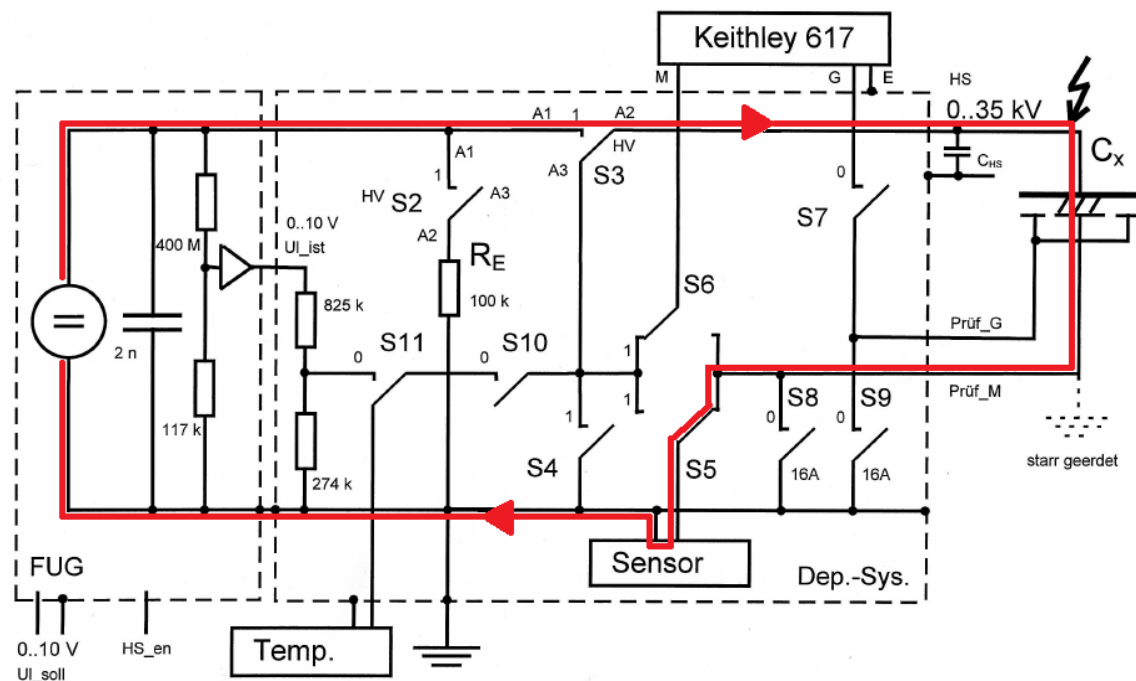


Fig. 6.4 The polarization circuit

- **Short-circuit phase** (Fig. 6.5)

The switches S8 and S4 close; meanwhile, S3 changes its position (from A1 to A3), short-circuiting the test object.

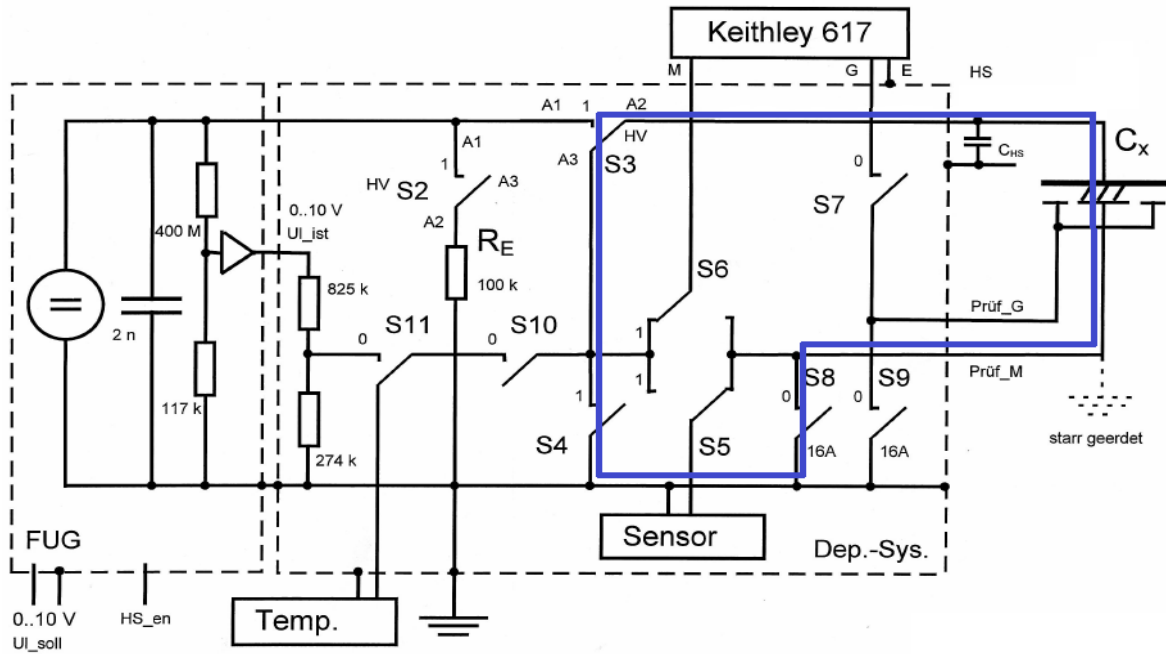


Fig. 6.5 The short-circuit circuit

- **Depolarization phase** (Fig. 6.6)

The switches S8 and S5 open and S6 changes its position; the closure of S7 allows the connection to ground of Keithley 617. In this way the depolarization current is measured.

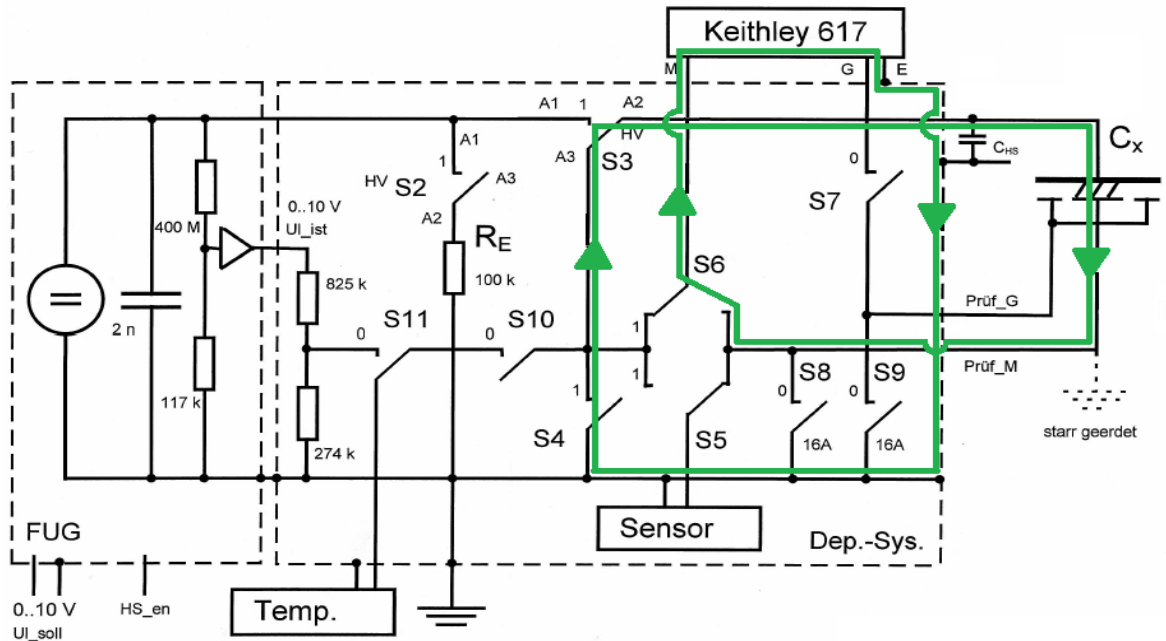


Fig. 6.6 The depolarization circuit

6.4 The Results

The effects of polarization and depolarization on the silicone material ESA 7250 is analyzed with respect to different temperatures, chosen as 25°C, 50°C and 100°C.

In need of completing the inspection on a specimen (conclude the PDC test at every temperature in one day), it has been necessary to decide the duration of the two phases, also considering the time to heat up the sample.

In the polarization phase, the applied voltage is set at 1 kV with a duration of 2000 s, whereas the acquirement of depolarization current lasts 4000 s, separated by a short-circuit phase for 1 s. During the temperature increase, for 45 minutes, the specimen is short-circuited, in order to discharge additionally it.

The uncertainty computation is applicable only to the depolarization current (for which the external electrometer has been used), considering the product specifications (Table 6.1).

Tab. 6.1 The accuracy of the ammeter

Range	4½ -Digit Resolution	Accuracy ±(%rdg + counts)
2 pA	100 aA	1.6 + 66
20 pA	1 fA	1.6 + 7
200 pA	10 fA	1.6 + 1
2 nA	100 fA	0.25 + 5
20 nA	1 pA	0.25 + 1
200 nA	10 pA	0.25 + 1

Three circular specimens have been tested, with the thicknesses reported in Table 6.2, always due to 20 $\frac{kg}{cm^2}$ of oil pressure.

Tab. 6.2 The thicknesses of the samples ESA 7250

Specimen	Reduced Thickness [mm]
BAMB07	1.922 ± 0.013
BAMB09	1.960 ± 0.016
BAMB10	1.975 ± 0.010

The reported graphs constitute the results of the PDC tests. The three specimens are shown together at different temperatures, initially for the polarization phase (from Fig. 6.7 to Fig. 6.9) and then for the depolarization one (from Fig. 6.10 to Fig. 6.12).

It is worthy of attention the deep difference between the polarization curves and the depolarization ones, for which the involved dipoles/molecules seem to respond differently in the two phases; in particular, the recombination of these elements tends to be more intensive in the depolarization, whereas in the polarization the recombination appears slighter.

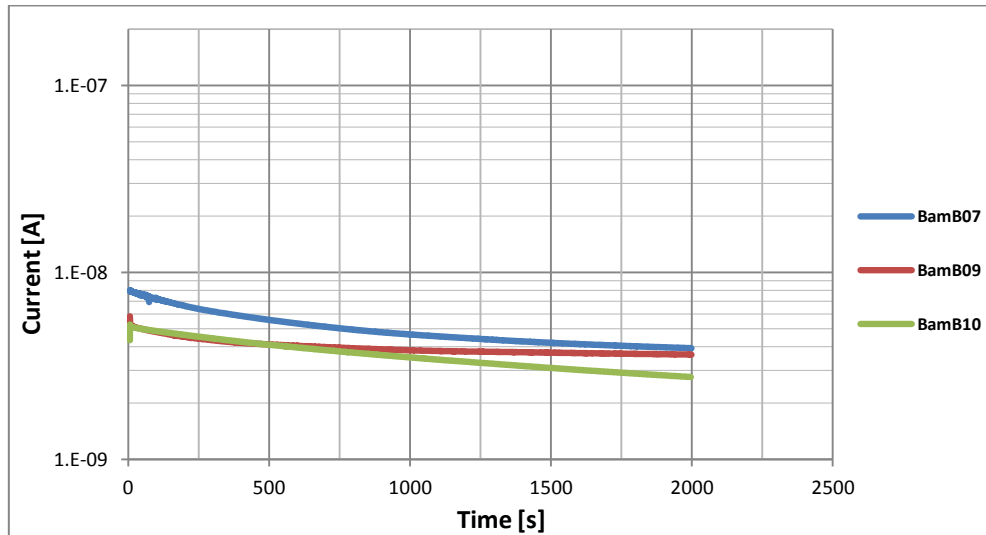


Fig. 6.7 PDC test - Polarization: 25 °C

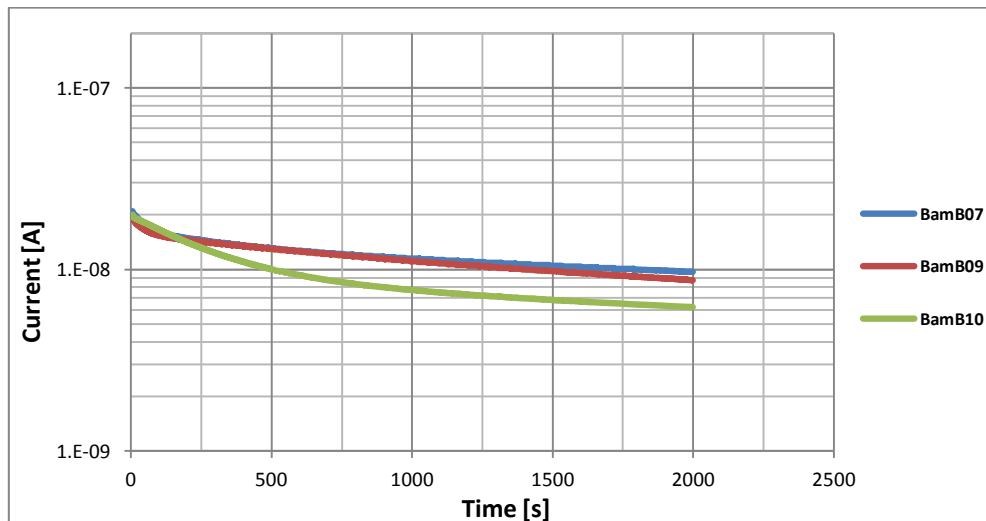


Fig. 6.8 PDC test - Polarization: 50 °C

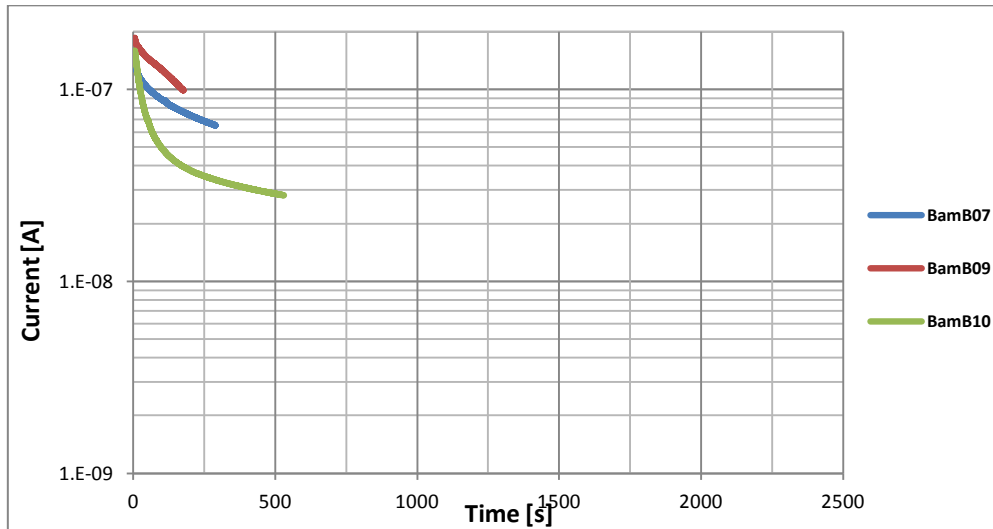


Fig. 6.9 PDC test - Polarization: 100 °C

In the polarization phase, the current reaches an almost stable value at around 1000 s, in particular BamB07 and BamB09 (noticeable only in Fig. 6.7 and Fig. 6.8), and, in general, it does not decrease very much from the initial seconds.

In addition, the different specimens report similar results, except the initial part of the measurement at 100°C (Fig. 6.9).

As it would be expected, when the temperature increases the curves move upwards, due to the resistivity reduction; in addition, the difference between the initial current and the steady state value grows (as it is seen in the 100°C graph).

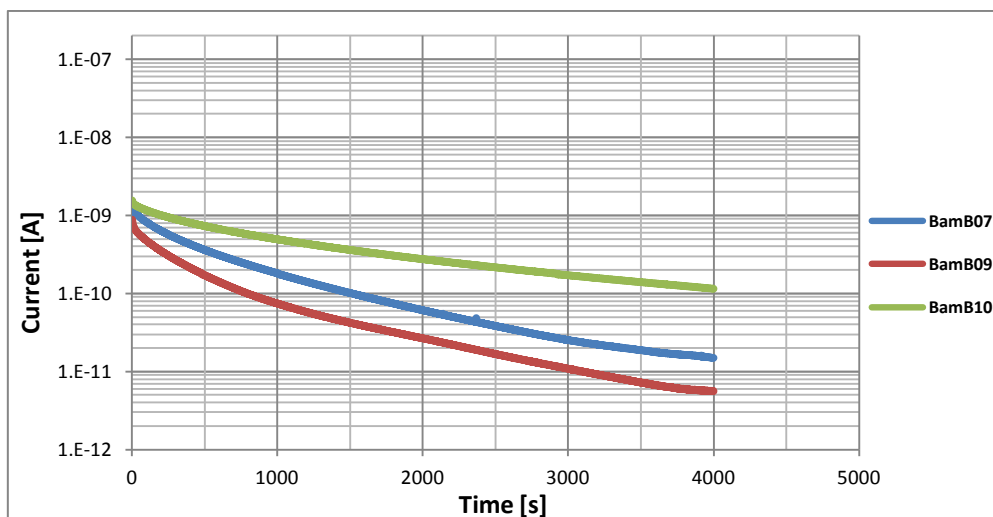


Fig. 6.10 PDC test - Depolarization: 25 °C

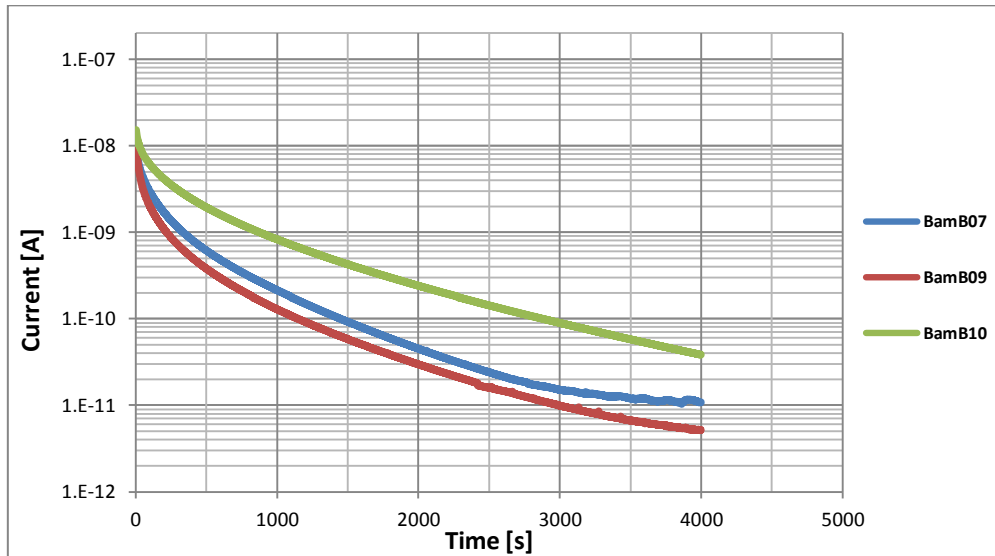


Fig. 6.11 PDC test - Depolarization: 50 °C

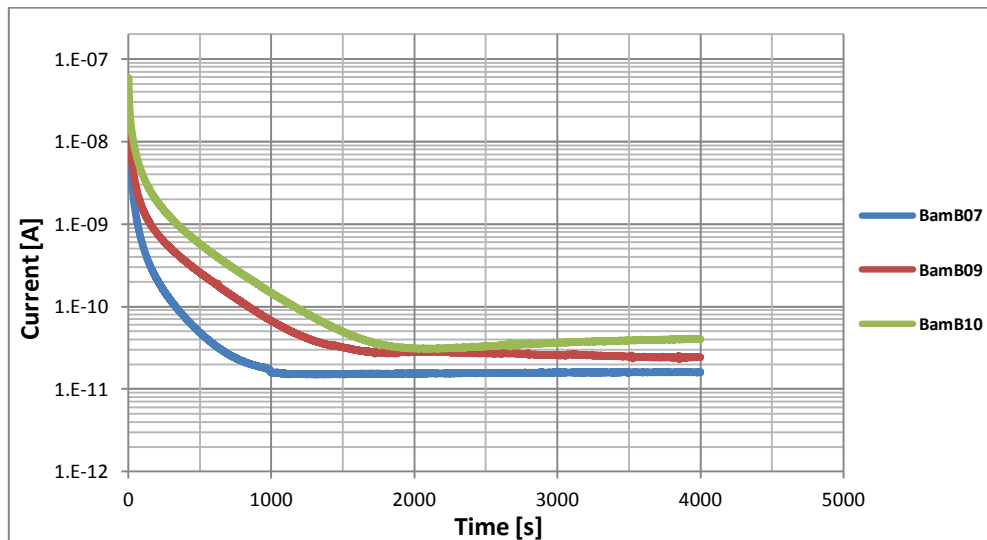


Fig. 6.12 PDC test - Depolarization: 100 °C

On the contrary, in the depolarization phase (from Fig. 6.10 to Fig. 6.12), the specimens present currents well separated, at whichever temperature. The curves go ideally to zero; anyway, at the end of the measurement (4000 s) this situation is not reached yet.

According to a temperature increase, the initial value of current increases, due to the higher final measure in the polarization phase, and the curves decrease faster (with a bigger slope): the cause could be in the temperature dependence of relaxation phenomena, for which the elements can recombine easier at high temperatures (helped by thermal agitation). The decrease is noticed more linear at room temperature, becoming more curved at 50°C and 100°C.

An unexpected situation takes place at 100°C (Fig. 6.12): for each specimen the current stops to decrease at different moments, stabilizing at steady state values or, as the BamB10, it also seems to slightly increase. The repetition of this behavior for all the specimens makes it such peculiar. It is difficult to find the cause in the natural behavior of the silicone, in particular for BamB10, because the polarization must be accompanied by an electric field.

Considering the expression of the dielectric response function, $f(t) \cong \frac{-i_d(t)}{c_0 U_c}$, it should be noted that, being the voltage and the geometric quantities regarded as equal for all the specimens, the depolarization current graphs represent, in a different scale, also the response functions.

As anticipated in the paragraph 6.2, in practical tests, the difference between the polarization and depolarization current hardly remains constant over time, but the dielectric response function is modified by additional phenomena.

Now, the issue regarding the polarization at 100°C is discussed. At a certain instant of time, the software blocks and no more measures are registered, as evinced in Fig. 6.9

Anyway, it has been verified that, even if the values during the polarization phase are not recorded, the voltage is correctly applied, polarizing the specimen without distorting the depolarization curve.

The total amount of charge, corresponding to the area below the polarization current curve, is computed. The software “DSMess 3.11” generates the recorded value of current with the corresponding time instant. Considering two successive instant t_i and t_{i+1} , to which the current values i_i and i_{i+1} correspond, respectively, the average charge is:

$$q_i = \frac{(t_{i+1} - t_i) \cdot (i_{i+1} + i_i)}{2}$$

The total charge is obtained by the sum of all the average charges, for all the recorded current values. The results with the 100°C condition provide higher results than with other temperatures (even if the duration is much shorter); in addition, the amounts of charge at which the instrument blocks are very similar:

- BamB07 : $2.40 \cdot 10^{-5}$ C
- BamB09 : $2.25 \cdot 10^{-5}$ C
- BamB10 : $2.23 \cdot 10^{-5}$ C

This results express the faults dependence on the recorded charge. Thus, the cause is identified in the operational amplifier integrator used for the current measurement, its capacitor becomes completely charged and the device experiences the block state.

In order to solve the problem, it is necessary to substitute the component; furthermore, the measurement circuit could be modified, in order to measure also the polarization current with the external electrometer “Keithley 617”, applying suitable protections against unexpected breakdowns.

Considering the expression of conductivity presented in paragraph 6.2, the volume resistivity of the tested specimens is computed, utilizing the PDC results of ESA 7250.

In doing it, the condition $f(t + t_c) \cong 0$ is considered as respected.

Deriving the previous formula, the volume resistivity is obtained:

$$\rho = \frac{U_c \cdot A}{d' \cdot (i_p(t) - i_d(t))}$$

In which A is the area of the inner electrode and d' is the reduced thickness, according to the values of Table 6.3.

It is worth noting that this volume resistivity, computed with PDC test, should be written as $\rho(t)$, in order to specify its dependence on the time.

The results are presented in Fig. 6.13; they are obtained by applying the last expression to a determined number of PDC results (polarization and depolarization values).

The curves are well separated according to the temperature, for which the volume resistivity decreases. They generally increase with time, as the polarization current reduces and the depolarization one becomes too small, losing its influence.

The initial variable values (before 100 s) are due to the high depolarization current (25°C and 50°C) or to the fast decrease of polarization one (100°C).

The specimen BamB10 is well detached from the other samples, presenting a pronounced higher resistivity; besides the effective higher resistivity, it can be noticeable that BamB07 and BamB09 show a more completed achievement of steady state condition at the end of polarization time.

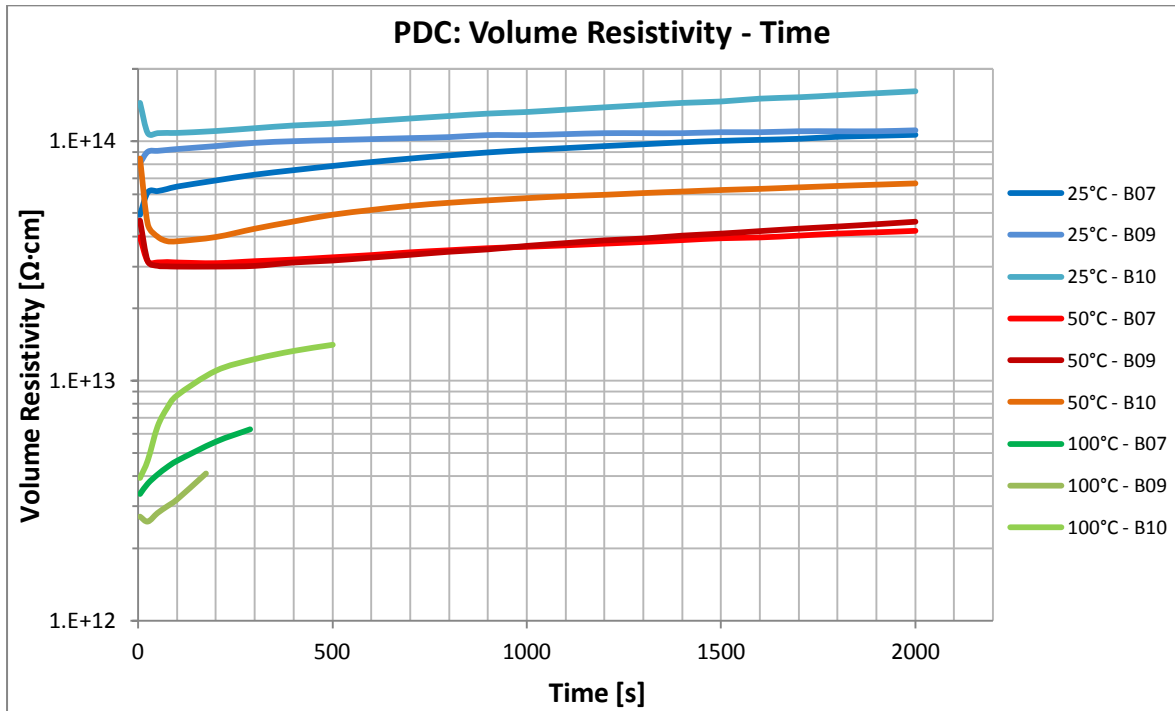


Fig. 6.13 Volume resistivity obtained from PDC test

Due to the non ideal behavior, the complete respect of $f(t + t_c) \cong 0$, and the unstable conditions at high temperatures, the volume resistivity obtained from PDC tests depends on time, increasing with it.

Considering the results obtained in the fifth chapter (the direct measurement with the electrometer, Tab. 5.3), the volume resistivities are similar to these obtained from PDC test (according to Fig. 6.13) by BamB07 and BamB09, in particular in the initial period (below 500 s) at 25°C and 50°C.

7 CONCLUSIONS

The aim of this thesis is the analysis of silicone rubber, according to mechanical and electrical characterizations.

This material is widely used in multiple applications, because of its important and useful qualities. In electrical engineering, its excellent insulating properties, together with its chemical stability and the immunity to contamination, bestow a central role on it, overcoming other classic materials.

In this work, different kinds of silicones are considered, allowing a comparison between them. Their manufacturing is explained, together with the production of samples that are used in the performed tests, according to the direct experience in the laboratories of “Polymeric GmbH Berlin”.

The mechanical measurement consists in the tensile strength test. It is an important tool in determining the mechanical properties of materials, assuming a fundamental role in the industrial manufacturing, when the decision regarding the implementation of different materials is carried out.

The tensile strength test provides results regarding the behavior of the material due to an applied force together with its maximum elongation and stress; clear differences in the analyzed materials are located and discussed.

Furthermore, the outcomes' goodness is evinced with the “statistical process control” and the Young's modulus is calculated, furnishing an important basis for the successive tests.

During the dielectric tests, it is important to prevent external interferences; in order to assure the absence of partial discharge phenomena, the silicone rubber undergoes a partial discharge test in the “Technische Universität Berlin”, in order to determine the inception voltage level of PD occurrences.

The first dielectric test is the dissipation factor test, connected to the permittivity theory of a dielectric material. The loss tangent of silicone rubber is determined, together with other relevant quantity, by comparing the test object with an ideal capacitor. This test is performed according to different variables: the temperature, the frequency and the voltage

level. In addition, the results allow the determination of the two components of permittivity: the real and imaginary parts.

In order to enhance the analysis, a specimen containing an air bubble is tested and compared with the standard results, providing additional considerations.

The second electrical test consists in the determination of the volume resistivity. The silicone rubbers are tested with a dedicated electrometer, implementing the alternating polarity method, obtaining precise results in the low current measurements. The materials are tested following a temperature cycle, from room temperature to 100°C and backward. In addition to the result analysis of the different materials, the calculation of activation energy is proposed.

This thesis concludes with the polarization depolarization current test, in which the test object is subjected to a constant applied voltage and, successively, a short circuit phase. The current measurement allows the evaluation of the dielectric response in the time domain. The test is conducted at three different temperatures, providing result considerations on the different conditions.

These tests and analysis constitute an effective characterization of different silicone rubbers according to different conditions. The goal always remains the understanding of outcomes' causes and the physical behavior.

The results can constitute the decision of practical fulfillments or the basis for a further inspection of silicone rubber.

REFERENCES

- [1] R. Allen Bernstorff, David Ryan, “*Silicone compounds for high-voltage insulators: compounding silicone rubber*”, Hubbell Power Systems Inc.
- [2] Jim Goudie, “*Silicone rubber for electrical insulators*”, Dow Corning Corporation, Rubber Technology International, 1998
- [3] “*Characteristic properties of silicone rubber compounds*”, Shin-Etsu, 2005
- [4] “*Elastomer engineering guide*”, James Walker
- [5] Zulkifli Ahmad, “*Polymeric dielectric materials*”, Intech, 2012
- [6] G. Sala, L. Di Landro, A. Airoidi, P. Bettini , “*Tecnologie e materiali aerospaziali: Cap.23 – Tipologie degli elastomeri*”
- [7] S.O. Kasap, “*Principles of electronic materials and devices – third edition*”, Mc Graw Hill, 2006
- [8] Pradeep Fulay, “*Electronic, magnetic and optical materials*”, Advanced materials and technologies series, CRC Press, 2010
- [9] Roger Brown, “*Handbook of polymer testing – short term mechanical tests*”, Rapra technology, 2002
- [10] J.R. Davis, “*Tensile testing*”, Davis & Associates, ASM International, 2004
- [11] G.M. Swallowe, “*Mechanical properties and testing of polymers, an A-Z reference*”, Kluwer academic publishers, 1999
- [12] International Standard: “*Rubber, vulcanized or thermoplastic - Determination of tensile stress-strain properties*”, ISO 37:2011 (E)
- [13] “*Tensile testing basics, tips and trends*”, ADMET, 2005
- [14] “*Instruction manual for material testing machines BZ1-MM14450.ZW06*”, Zwick Roell, 2012

-
- [15] European standard: “*Kabel, isolierte Leitungen und Glasfaserkabel – Prüfverfahren für nichtmetallene Werkstoffe – Teil 501: Mechanische Prüfungen – Prüfungen zur Bestimmung der mechanischen Eigenschaften von Isolier- und Mantelwerkstoffen*”, EN 60811-501
- [16] F. H. Kreuger, “*Partial discharge detection in high-voltage equipment*”, Butterworths, 1989
- [17] König, Narayana Rao, “*Partial discharges in electrical power apparatus*”, VDE-Verlag, 1993
- [18] Wolfgang Hauschild, Eberhard Lemke, “*High-voltage test and measuring techniques*”, Springer, 2014
- [19] Roger F. Harrington, “*Introduction to electromagnetic engineering*”, Courier Dover Publications, 2003
- [20] R. Bartnikas, “*Engineering dielectrics – Volume II B*”, ASTM STP 926, 1987
- [21] Andreas Küchler, “*Hochspannungstechnik: Grundlagen - Technologie - Anwendungen*”, Springer, 2009
- [22] “*Bestimmung der dielektrischen Eigenschaften*”, DIN 53 483, 1969
- [23] International standard: “*Recommended methods for the determination of the permittivity and dielectric dissipation factor of electrical insulating materials at power, audio and radio frequencies including metre wavelengths*”, IEC 250
- [24] “*IEEE standard techniques for high voltage testing*”, IEEE Std 4 – 1995
- [25] Luciano Simoni, “*Proprietà dielettriche e scarica dei materiali isolanti elettrici*”, CLUEB, 1996
- [26] Luciano Simoni, “*Resistenza alle sollecitazioni dei materiali isolanti elettrici*”, CLUEB, 1996
- [27] Kornhuber, Markalous, Muhr, Strehl, Sumereder, “*Comparison of methods for the dissipation factor measurements at practical examples*”, 16th international symposium on high voltage engineering, 2009
- [28] Adam Daire, “*Improving ultra-high-resistance measurements*”, American Institute of Physics, 1996
-

- [29] *“Reference Manual: Electrometer model 6517B”*, Keithley Instruments Inc. 2009
- [30] Sudha, Sukumar Roy, Uma Rao, *“Evaluation of activation energy (E_a) profiles of nanostructured alumina polycarbonate composite insulation materials”*, International journal of materials, mechanics and manufacturing, 2014
- [31] Jamail, Piah and Muhamad, Kamarudin, *“Comparative study on conductivity and moisture content using polarization and depolarization current (PDC) test for HV insulation”*, Transactions on electrical and electronic materials, 2014
- [32] Bernier, Parpal, David, Jean, Lalancette, *“Dielectric response of laboratory aged PE cables”*, IEEE, 2008
- [33] Fofana, Hemmatjou, Farzaneh, Gockenbach, Borsi, *“Polarization and depolarization current measurements of oil paper impregnated insulation system under thermal runaway”*, International conference on solids dielectrics, IEEE, 2010
- [34] David, Lamarre, Nguyen, *“Measurements of polarization/depolarization currents for modern epoxy-mica bars in different conditions”*, IEEE, 2007
- [35] Suleiman, Bashir, Muhamad, Jamail, Kamarudin, *“Polarization & depolarization current (PDC) measurement in cellulose insulating materials”*, Annual report conference on electrical insulation and dielectric phenomena, 2013
- [36] Muhamad, Phung, Blackburn, Lai, *“Polarization and depolarization current (PDC) tests on biodegradable and mineral transformer oils at different moisture levels”*, University of New South Wales